Annual Report 2024

Chair for Functional Materials
with the
Soft Matter Physics Group

Technical University of Munich
TUM School of Natural Sciences
Physics Department

Prof. Dr. Peter Müller-Buschbaum
Chair for Functional Materials
muellerb@ph.tum.de
www.ph.nat.tum.de/functmat

Prof. Christine M. Papadakis, PhD
Soft Matter Physics Group
papadakis@tum.de
www.ph.nat.tum.de/softmatter

Technical University of Munich
TUM School of Natural Sciences
Physics Department
James-Franck-Str. 1
85748 Garching

Secretaries/Administration:
Marion Waletzki: marion.waletzki@ph.tum.de
Sanja Ulrich: sanja.ulrich@tum.de

Tel.: +49(0)89 289-12452
Fax: +49(0)89 289-12473

Cover page picture:

The artwork on the cover illustrates the main research activities of the chair, i.e., the study of functional soft matter in condensed films and in solution using light, X-ray and neutron scattering methods to characterize the structure-function relationship of the material at the nanoscale. "E13 & E59" are the internal administrative descriptions of the Chair for Functional Materials and the Soft Matter Physics Group, respectively.

Editor: Dr. Julian Eliah Heger

Preface

It is a great pleasure to present the annual report for the year 2024 in the name of the staff of the Chair for Functional Materials and the Soft Matter Physics Group. It provides an overview of our teaching, research, and development activities. Our research activities are focused on functional materials and cover a broad range from soft matter physics to developments of methods and instrumentation. We examine the fundamental physics of material properties using mainly scattering methods (neutron, x-ray, and light scattering). The general goal of our research is to explain the functional characteristics of soft condensed matter from the knowledge of its nanostructure, molecular dynamics and kinetics.

In 2024, the research activities covered the specific areas of polymer solutions and gels, responsive thin films, functional thin films, photovoltaics, polymer-hybrid systems, materials for energy storage, real-time characterizations, and the development of instrumentation and software. In 2024, we had many guests visiting us in Garching and presenting their research work. We also traveled to numerous conferences and workshops, both in Germany and abroad, to interact with international scientists and present our results.

The activities in the fields of polymer films for application in photovoltaics and polymer-hybrid systems were successfully continued. With *"TUM.solar"*, the Keylab in the network of in the Bavarian Collaborative Research Project *"Solar Technologies go Hybrid"* (SolTec) headed by Prof. Müller-Buschbaum was running in its twelfth year of funding. Research activities covered a broad area of next-generation solar cells, including organic solar cells, dye-sensitized solar cells, hybrid solar cells, perovskite solar cells, and quantum dot solar cells. Moreover, thermoelectric materials and energy storage materials with a focus on lithium-ion battery technology were investigated. In addition, we investigated novel self-assembling responsive polymers, also under high pressure, orthogonally switchable polymers, and polymeric hydrogels for medical applications such as 3D bioprinting for tissue engineering.

The in-house experiments available in the laboratories of the chair were supplemented by many activities at large-scale facilities, comprising synchrotron radiation and neutron scattering experiments. Also, the in-house x-ray scattering experiments for SAXS/WAXS/GISAXS/GIWAXS as well as XRR/XRD, were heavily booked.

In 2024, the Chair for Functional Materials and the Soft Matter Physics Group comprised 1 professor emeritus, 1 visiting professor, 1 PostDoc, 5 fellows, 59 PhD students, 31 master students, 29 bachelor students, 1 student assistant, and 5 administrative and technical staff members. 10 PhD theses were accomplished; moreover, 20 master theses as well as 21 bachelor theses were finished. We were happy to have hosted 7 guests.

Also, in 2024, we held our internal summer school. It took place in the TUM Science & Study Center Raitenhaslach, the former Cistercian monastery near Burghausen, and was dedicated to selected experimental techniques relevant to the group. The excursion to Königssee was definitely a highlight of the event. With the MLZ-organized conference "Machine Learning Conference for X-Ray and Neutron-Based Experiments" in the Bürgerhaus Garching, a follow-up of the workshop at Lawrence Berkeley National Laboratory, took place in April 2024. Perhaps the most exciting event was the "Sino-German Workshop Exploration of Structure and Morphology in Polymers by Advanced Scattering Techniques (ExpAdvScaTech)" in Hangzhou, China, in October 2024, which we co-organized with Qi Zhong from Zhejiang Sci-tech Univer-

sity. Another highlight was the eighth European Conference on Neutron Scattering (ECNS) being organized by the MLZ in Garching. 538 participants from all around the world joined a very lively atmosphere.

Regarding teaching activities of the chair, we offered the lectures "Materials science" (Papadakis). Special lectures comprised *"Polymer physics"* (Papadakis), *"Nanostructured soft materials"* (Müller-Buschbaum) and *"Measurement and sensor technology"* (Müller-Buschbaum). Prof. Papadakis acted again as a deputy women's representative of the Physics Department, and Prof. Müller-Buschbaum started serving in the *"TUM Sustainability Board"*. Moreover, Prof. Müller-Buschbaum headed the activities in the *"Network Renewable Energies (NRG)"* in the MEP. As a service to the community, Prof. Müller-Buschbaum served as Deputy Editor at *"ACS Applied Materials & Interfaces"*.

This annual report comprises a selection of the different research topics and projects carried out in the individual groups of the chair. It highlights the dedicated and successful research activities and collaborations with other groups and large-scale facilities. We wish all chair members a fruitful continuation and a very successful year 2025.

Peter Müller-Buschbaum and Christine M. Papadakis April 2025

Contents

1 Polymer solutions and gels

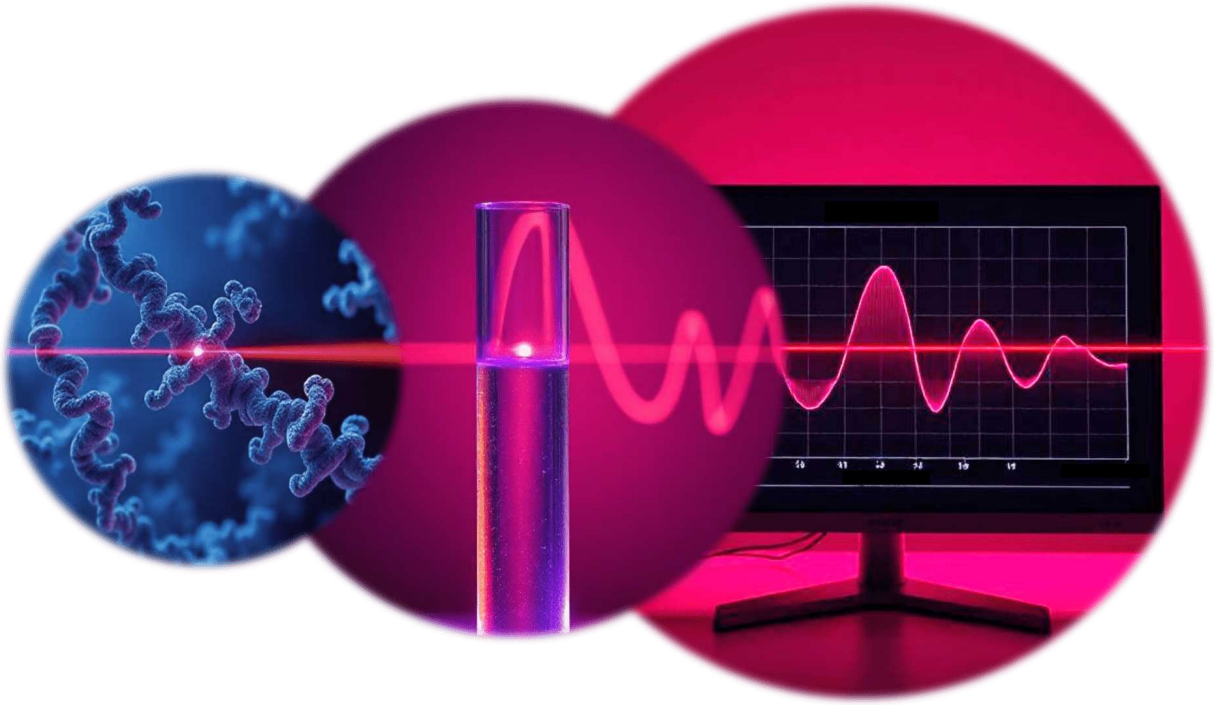

1.1 Thermoresponsivity in poly(*N*-isopropylmethacrylamide) in neat water and in water/methanol mixtures

C.-H. Ko, P. Wastian, D. Schanzenbach[1], P. Müller-Buschbaum, A. Laschewsky[1,2], C. M. Papadakis

[1] Universität Potsdam, Germany

[2] Fraunhofer IAP, Potsdam-Golm, Germany

Thermoresponsive polymers with lower critical solution temperature (LCST) behavior in aqueous solution have been proposed, among others, for sensor and switching applications. In spite of the fact that these applications require specific switching behavior, most fundamental investigations have focused on poly(*N*-isopropyl acrylamide) (PNIPAM). The polymer under study here, poly(*N*-isopropyl methacrylamide) (PNIPMAM), is very similar to PNIPAM, except that it features an additional α-methyl group on the backbone (inset of Figure 1.1a). In aqueous solution, it is thermoresponsive with LCST behavior, but its cloud point temperature T_{cp} is unexpectedly higher than the one of PNIPAM. This shift was explained by differences in the hydration behavior and to steric hindrances. In our previous studies [1], we found that, in the one-phase state, the chain conformation of PNIPMAM is more compact than the one of PNIPAM. Moreover, large-scale inhomogeneities due to physical crosslinks were detected already in the one-phase state, even at very low polymer concentrations. Hence, the effect of the α-methyl group on the behavior of PNIPMAM in aqueous solution is complex and deserves further investigation. In the present study, we focus on the effect of the cosolvent methanol. We map out the phase diagram and use dynamic light scattering (DLS) to investigate the collective dynamics of PNIPMAM in water/methanol mixtures. These reflect the chain conformation and are sensitive to the presence of aggregates.

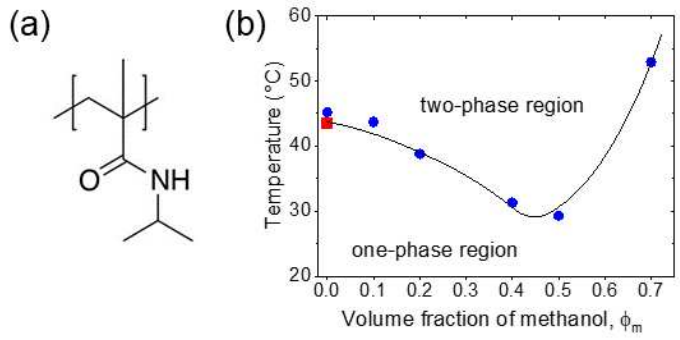

Figure 1.1:
(a) The chemical structure of the repeating unit of PNIPMAM. (b) Cloud point temperatures from turbidimetry (red square) and DSC (blue circles) in dependence on the volume fraction of methanol. The line guides the eye.

In detail, a PNIPMAM homopolymer with a molar mass of 17 kg mol^{-1} was investigated. As solvents, heavy water (D_2O) and fully deuterated methanol (CD_3OD) were used at methanol volume fractions $\Phi_m = 0 - 0.7$. 30 g L^{-1} solutions were prepared by adding the solvent mixture to the pre-weighed polymer, shaking at room temperature and filtering. The T_{cp}-values in dependence on Φ_m were determined by turbidimetry and differential scanning calorimetry (DSC). DLS was carried out using an instrument from ALV (Langen, Germany), a HeNe laser having a power of 35 mW and a wave length $\lambda = 632.8$ nm, and a goniometer. The solutions were filled into cylindrical cuvettes, that were mounted in a thermostated index-matching vat. Temperature-dependent measurements were carried out at a scattering angle $\theta = 90$ °C between room temperature and the respective cloud point. At each temperature, 10 measurements having a duration of 30 s were carried out after careful thermal equilibration. The resulting intensity autocorrelation functions $G_2(t)$ were analyzed using the REPES algorithm, which calculates the distribution functions of relaxation times τ, $A(\tau)$.

The phase diagram shows overall the expected behavior (Figure 1.1b): T_{cp} decreases from 45 °C in neat D_2O to 29 °C at $\Phi_m = 0.5$ and increases strongly above. Figure 1.2 shows intensity autocorrelation functions and the corresponding distribution functions for $\Phi_m = 0$ and 0.5 at different temperatures in the one-phase region. The latter feature two peaks for all samples, reflecting a fast and a slow process. The amplitude of the slow mode decreases strongly with increasing Φ_m. This decrease indicates that the solutions become more homogeneous at large length scales, as the methanol content is increased, and/or that the large clusters contain more solvent, and hence, contribute less to the overall scattering.

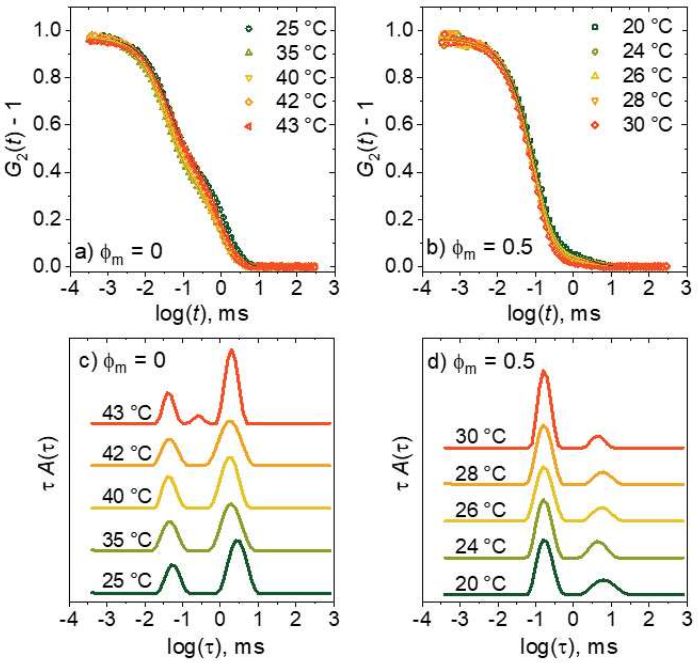

Figure 1.2:
Representative intensity autocorrelation functions $G_2(t) - 1$ from DLS (top) and the corresponding distribution functions $\tau A(\tau)$ (bottom) for $\Phi_m = 0$ (left) and 0.5 (right) at the temperatures indicated in the graphs, measured at $\theta = 90$ °C. The distribution functions are shifted vertically.

The temperature dependencies of the overall intensities are shown for all Φ_m-values in Figure 1.3a. They follow scaling behavior $I(T) \propto (T_c - T)^{-\gamma}$, where T is the absolute temperature and T_c the critical temperature, as evident from the goodness of the fits. However, the scaling exponent γ shows peculiar behavior: It decreases abruptly from 0.38 at $\Phi_m = 0$ to 0.14 at $\Phi_m = 0.1$, then increases steadily to 0.39 at $\Phi_m = 0.5$ Figure 1.3b. The reason for this non-monotonous behavior is at present unclear. In the entire range, the values are far below the value predicted by mean-field theory ($\gamma = 1$). The behavior of PNIPMAM in water/methanol mixtures is thus significantly more complex than predicted by mean-field theory.

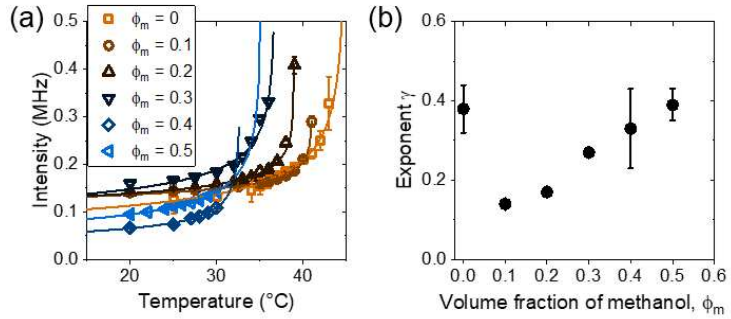

Figure 1.3:
(a) Scattered intensities in dependence on temperature for the Φ_m-values given (symbols). The lines are fits of scaling laws. (b) Resulting scaling exponents γ in dependence on the volume fraction of methanol, Φ_m.

[1] C.-H. Ko, C. M. Papadakis et al., *Macromolecules* **53**, 6816-6827 (2020)

1.2 PNIPAM mesoglobules in dependence on pressure

B.-J. Niebuur, A. Schulte[1], C. M. Papadakis

[1] University of Central Florida, Orlando, U.S.A.

Thermo-responsive polymers are important from a fundamental perspective as well as for applications, such as sensors and switches. While they are water-soluble below the cloud point temperature T_{cp} , they are water-insoluble above and undergo a coil-to-globule transition. For the thermo-responsive model system poly(*N*-isopropylacrylamide) (PNIPAM) in aqueous solution, the collapsed and water-insoluble polymers form aggregates, which are long-lived and of mesoscopic size; hence, they are commonly named "mesoglobules". Pressure has a significant effect on T_{cp}: The coexistence line of aqueous solutions of PNIPAM in the temperature-pressure frame has the shape of an ellipse, i.e., T_{cp} increases with pressure by a few degrees, before it decreases again. Inside the ellipse, i.e., at low temperatures and pressures, resides the one-phase state, while the solution is in the two-phase state outside [1]. The size and water content of the PNIPAM mesoglobules depend strongly on pressure: Whereas heating the PNIPAM solution to the two-phase state at atmospheric pressure results in small and compact mesoglobules having a radius of about 0.5 μm, large, water-rich aggregates with sizes of 1-2 μm are formed around 100 MPa [2]. We refer to these distinct states as the low- (LP) and the high-pressure (HP) regime. Here, we address the nature of the transition from small and compact mesoglobules to larger, water-rich aggregates and back [3]. We carried out small-angle scattering studies of the size and water-content of the mesoglobules formed in a semidilute aqueous solution of PNIPAM in dependence on pressure in the two-phase region, i.e., at temperatures above the coexistence line. At this, we performed isothermal pressure scans between 10 and 110 MPa, i.e., from the LP to the HP regime and back.

In detail, PNIPAM with a molar mass $M_n = 36000$ g/mol was dissolved at a concentration of 3 wt% in an 80:20 v/v mixture of D_2O and H_2O. Very small-angle neutron scattering (VSANS) measurements were performed at the instrument KWS-3 at the Heinz Maier-Leibnitz Zentrum (MLZ), Garching, Germany. The sample was mounted in a temperature-controlled custom-made pressure cell, where it was placed between sapphire windows and had a thickness of 1 mm. The structures of the mesoglobules were characterized in isothermal pressure scans above the coexistence line: After heating the sample at 10 MPa from 20 °C to 35.4, 36.2 or 37.0 °C, pressure scans were carried out at these temperatures from 10 to 110 MPa and back. The background-corrected and normalized scattering profiles were modeled using one or two Beaucage form factors, which give the radius of gyration R_g of the mesoglobules. The invariant Q^* was calculated as well, which is indicative of the water content.

Figure 1.4a and b displays representative scattering curves. At 10 MPa, a shoulder is discernible. With increasing pressure, the overall intensity decreases, which points to an increased hydration of the mesoglobules. Between 40 and 50 MPa, the shoulder abruptly moves to lower values of the momentum transfer (Figure 1.4a). Thus, a transition from small and compact mesoglobules having a size of a few 100 nm to large aggregates having a size in the micrometer range is observed. When pressure is decreased again, the transition is observed as well, but it is not as pronounced, and the original shape is not fully recovered (Figure 1.4b).

As obtained from fitting a Beaucage form factor, R_g increases abruptly from 0.24 μm at 40 MPa to 0.78 μm at 50 MPa and continues to increase strongly, i.e., there is a transition at 45 MPa (Figure 1.4c). The invariant Q^* decreases discontinuously at 45 MPa (Figure 1.4d). Thus, at the transition pressure of 45 MPa, the mesoglobules grow abruptly and take up water, which we assign to the coalescence of the mesoglobules. When pressure is decreased again, the large aggregates persist down to the lowest pressure. However, at 40 MPa and below, an additional small structure is discerned, in the range of 0.4-0.6 μm. These values are similar to the ones of the

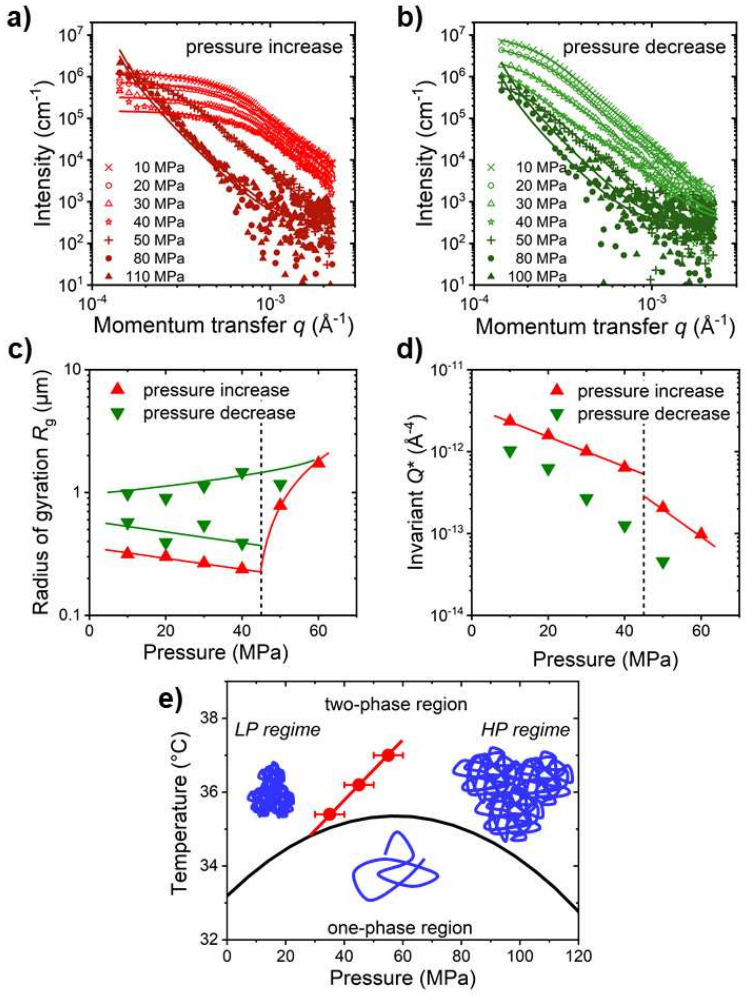

Figure 1.4:
(a, b) Representative VSANS curves obtained during a pressure increase from 10 to 110 MPa (a) and back (b) at 36.2 °C. Symbols: experimental data. Solid lines: model fits. Light and dark colors indicate the LP and the HP regimes. (c, d) Pressure-dependent structural parameters obtained from model-fitting the VSANS data: (c) Radii of gyration, (d) invariant Q^*. The vertical dashed lines indicate the transition pressures. The full lines guide the eye. (e) Phase diagram including the new transition line between the low-pressure and the high-pressure regime (red symbols and line) and the coexistence line between the one-phase and the two-phase region (black line). The PNIPAM chains and their aggregates are depicted in blue.

initial mesoglobules. The invariant Q^* follows the trend of the pressure increase, but does not recover the initial value. We conclude that, during the pressure increase, the mesoglobules take up water, and at 45 MPa, their water content is sufficiently high to enable coalescence, which results in large water-rich aggregates at higher pressures. On the way back, these large aggregates shrink, and small, compact structures are formed again, but they cannot fully separate from each other.

The transition pressures between the compact mesoglobules at low pressures and swollen large aggregates at high pressures, as obtained from the three scans, lie on a tilted line (Figure 1.4e). While the transition between mesoglobules and aggregates is continuous at the highest temperature and mainly due to swelling, it becomes more and more abrupt as temperature is decreased, and here, coalescence dominates [3]. We attribute this difference to the higher degree of hydration and the resulting enhanced chain mobility at the lower temperatures, enabling coalescence. The transition is, however, not completely reversible, because the compact mesoglobules cannot fully separate from each other. These findings may be of importance for the disintegration of microplastics and of polymeric nanoparticles used for drug delivery.

[1] C. M. Papadakis, B.-J. Niebuur, A. Schulte, *Langmuir* **40**, 1-20 (2024)

[2] B.-J. Niebuur, A. Schulte, C. M. Papadakis et al., *ACS Macro Lett.* **6**, 1180-1185 (2017)

[3] B.-J. Niebuur, A. Schulte, C. M. Papadakis et al., *Langmuir* **40**, 22314-22323 (2024)

1.3 Star-like Molecular Brushes with Poly(2-oxazoline)-based Amphiphilic Diblock Side Arms

W. Xu, L. Fietzke[1], D. Soloviov[2], R. Jordan[1], C. M. Papadakis

[1] TU Dresden, Dresden, Germany
[2] EMBL at DESY, Hamburg, Germany

Poly(2-oxazoline)s (POx) are a class of biocompatible polymers that have gained significant attention in recent years due to their versatile properties and various potential applications in biomedicine. Various POx-based molecular brushes have been investigated, focusing on the overall brush conformation [1, 2]. In the current study, we investigate the structure and the behavior of aqueous solutions of molecular brushes, in which diblock copolymers from hydrophilic methyl(2-oxazoline) (MeOx) and hydrophobic *n*-butyl(2-oxazoline) (BuOx) are grafted onto star-shaped poly(methyl methacrylate) (PMMA) backbones. The functionality of the PMMA backbone ranges from 2 to 5 (Fig. 6.25).

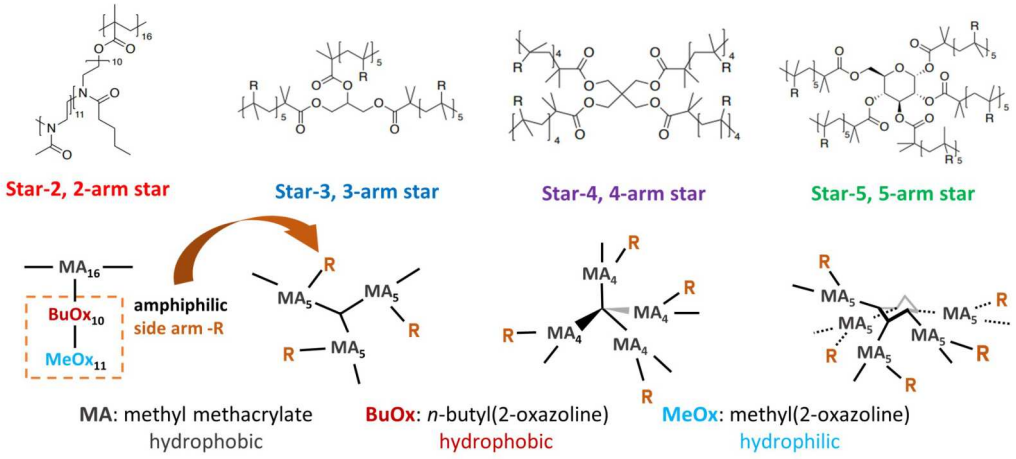

Figure 1.5: Structures of the star-shaped molecular brushes

To investigate the hydrodynamic radii of the molecular brushes using dynamic light scattering (DLS), they were dissolved at a concentration of 10 g/L in water. Scattering experiments were carried out with a LS Spectrometer (LS Instruments) equipped with a 660 nm laser. Samples were measured at room temperature (20 °C). To probe the chain conformation of the molecular brushes in detail, synchrotron small-angle X-ray scattering (SAXS) was performed at beamline P12, EMBL, DESY, also at 20 °C on the identical solutions.

Fig. 6.26 (a) shows the intensity autocorrelation functions from DLS. While the autocorrelation function for Star-3 is a single decay, an additional slow decay is observed for the other samples. It is attributed to the large particles in the solution, which coexist with the small particles. Fig. 6.26 (b) shows the distribution of the hydrodynamic radii of the particles in the solution. First, a sharp peak at around 8 nm hydrodynamic radius can be seen for all samples. Exclusively for Star-2, Star-4 and Star-5, there exists a second peak which refers to particles of a size of a few hundreds nanometers. We assign these to the individual brushes and the aggregates formed by individual brushes. DLS indicates that only small amount of aggregates exist in the aqueous solution of Star-3.

Fig. 6.26 (c) shows the SAXS intensities of the molecular brushes. Except for Star-3, strong scattering signals are found in the low q-value region of the curve, i.e., forward scattering. Apart

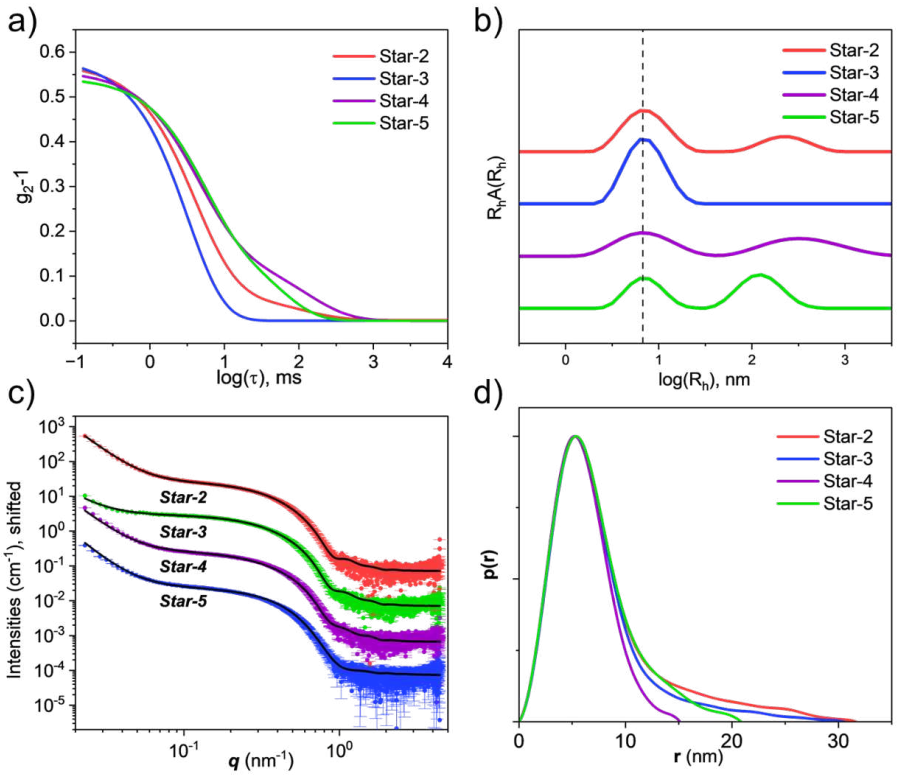

Figure 1.6:
(a) Autocorrelation functions of the molecular brushes from DLS. (b) Distributions of the hydrodynamic radii. (c) SAXS intensities of the molecular brushes, from bottom to top, the curves are offset by 20, 200 and 2000. Black solid lines represent the model fits. (d) Pair distribution functions derived from SAXS intensities.

from that, the shapes of the curves are very similar in the medium to high q-value region, featuring first a plateau and then a decay. The forward scattering signals, which exist only in Star-2, 4, 5, are due to the presence of aggregates, which is in agreement with DLS. The medium to high q-value parts of the curves, which are largely identical, comprise the shape information of individual brushes. Therefore, all the brushes have a very similar shape, which is demonstrated by model fits: the intensity curves are accurately reproduced using homogeneous ellipsoid form factor models with comparable size parameters. Fig. 6.26 (d) are the pair distribution functions $p(r)$. They generally feature a slightly asymmetrical peak centered around 8 nm, whereas the positions of the right edge range from 15 nm to 30 nm. The main peak, which is attributed to the distance distributions within the individual molecular brushes, is the same for all samples, which supports the idea that all brushes have the same shape in solution. The difference in the flanks may be due to the different degrees of elongation of the ellipsoids and the interference of the aggregates. We conclude that all star-shaped molecular brushes are ellipsoids with a hydrodynamic radius of around 8 nm in their aqueous solutions. The number of backbone arms does not strongly affect the conformation of the brush but may have an impact on their tendency to form aggregates.

[1] J. -J. Kang, C. M. Papadakis et al., *Langmuir* **38**, 5226-5236 (2022)

[2] J. -J. Kang, C. M. Papadakis et al., *Colloid Polym. Sci.* **299**, 193-203 (2021)

1.4 Self-assembly of thermo- and pH-responsive amphiphilic triblock terpolymers

F. Zheng, C. Jeffries[1] L. Wang[2], T. K. Georgiou[2], C. M. Papadakis

[1] EMBL, Hamburg, Germany
[2] Imperial College, London, UK

Amphiphilic block copolymers self-assemble into micelles of different shapes in aqueous solution and form hydrogels if the polymer concentration is sufficiently high [1]. While the micellization of diblock copolymers with permanently hydrophilic and hydrophobic blocks has been extensively studied, less is known about the micelle and gel formation of triblock terpolymers with pH- and thermoresponsive blocks. The use of functional segments in block copolymers increases the tunability of the nanostructures even further. Triblock terpolymers with a hydrophobic block (A) and two thermo- and pH-responsive blocks (B and C) form micelles whose self-assembly and hydrogel structures can be expected to depend strongly on pH and temperature values.

Here, the effect of temperature and pH values on the self-assembly of the dual responsive terpolymer featuring three different blocks is addressed. This consists of the hydrophobic poly(methyl methacrylate) (PMMA, A), the pH- and thermoresponsive poly(2-(dimethylamino)ethyl methacrylate) (PDMAEMA, B) with a pK_a of 7.6, and the pH- and thermoresponsive poly(N-(2-methacryloyloxyethyl)pyrrolidone) (PNMEP, C) with a pK_a of 5.2, a hitherto uninvestigated type of block. More specifically, a PMMA$_{21}$-*b*-PDMAEMA$_{32}$-*b*-PNMEP$_{18}$ (ABC) triblock terpolymer was synthesized by RAFT polymerization. Both B and C blocks exhibit LCST behavior in aqueous solution, i.e., they become water-insoluble when heated through their cloud point (CP). Moreover, a change in pH influences the degree of ionization of the basic groups of the B and C blocks, which leads to an extension of the blocks by ionic interactions and hence the change of solubility in solution.

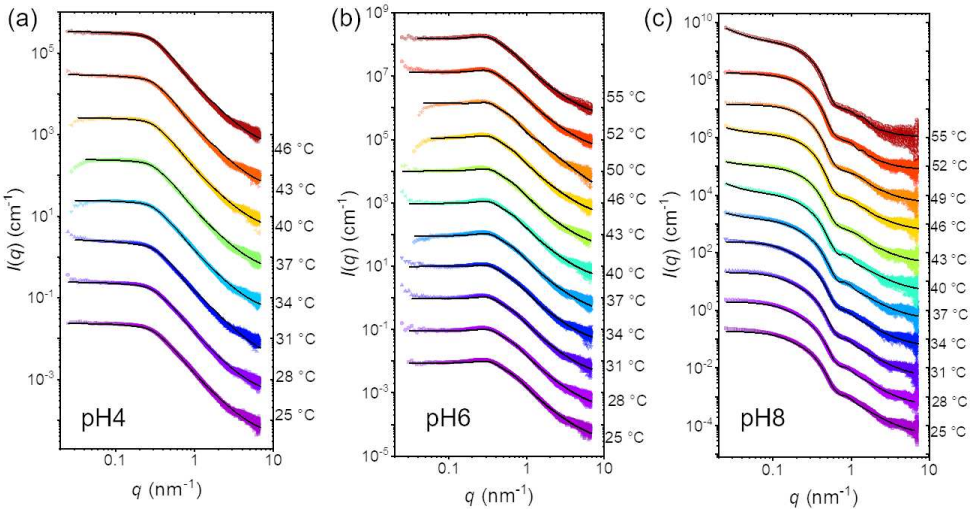

Figure 1.7:
SAXS curves of 1 wt% solution of ABC in H_2O with increasing temperatures at pH values of (a) 4, (b) 6, and (c) 8. Solid black lines are the best model fits. The curves are shifted vertically for better visibility.

To gain insight about the shape and size of micelles, an ABC triblock terpolymer was investigated in a 1 wt% solution in H_2O by small-angle X-ray scattering (SAXS) at beamline P12 at EMBL. The polymer solutions at pH 8, i.e., above the pK_a of both responsive blocks;

at pH 6, which is below the pK_a of PDMAEMA; and at pH 4, below the pK_a of PNMEP, were measured from 25 to 55 °C in steps of 3 °C. The X-ray wavelength was 0.12 nm. The sample-detector-distance of 3 m was used to cover the q range of 0.03–7 nm^{-1}.

The obtained SAXS curves are shown in Figure 1.7. The SAXS curves from pH 4 and pH 6 show similar shapes and vary weakly with temperature, featuring a plateau at low q value and exhibiting shoulders at $q \cong$ 0.2-0.3 nm^{-1}, which are attributed to form factor scattering from single micelles. The scattering curves from ABC at pH 8 exhibit more rounded shoulders at $q \cong$ 0.2 nm^{-1} compared to the ones from lower pH values. At 43 °C and above, the curves show an increase in forward scattering in the low q region, indicating the presence of clusters.

From the fitting results, we propose the self-assembled solution structures schematically shown in Figure 1.8. At pH 4 and pH 6, spherical core-shell micelles are formed at both pH values, featuring the hydrophobic A block as the core and the B and C blocks as the shell. Strong stretching and electrostatic repulsion of the chains prevent aggregation of micelles, leading to extended chain conformation and increased solubility. Even when the temperature is above CP_{PNMEP}, ABC shows no size or shape change at both pH values. At pH 8 , both B and C blocks are uncharged and flexible. The B block shows a CP at $\sim$ 43 °C while the C block is fully hydrophilic. ABC self-assembles into cylindrical micelles at 25 °C. The cylinder length becomes shorter with increasing temperature, while the cross-sectional radius stays constant. At 43 °C, the thermoresponsive PDMAEMA block becomes more hydrophobic, leading to the formation of aggregates of spherical micelles.

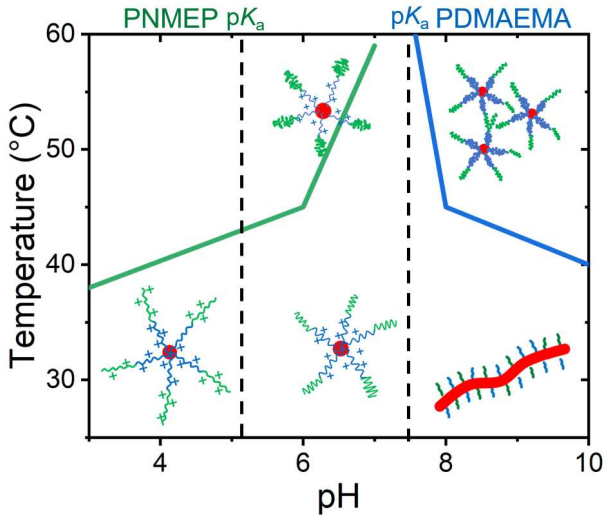

Figure 1.8:
Schematic drawing of the proposed most prominent self-assembled structures of ABC in aqueous solution at different pH values. The green and blue solid lines represent the CPs of PNMEP and PDMAEMA, respectively. Red, blue, green colors denote the PMMA, PDMAEMA, and PNMEP blocks, respectively.

In summary, the synchrotron SAXS measurements on solutions of pH- and thermoresponsive triblock terpolymers elucidate the effect of charges and temperature on the self-assembly of micelles. When the pH value is lower than pK_a of either of the responsive blocks, the micellar structure shows only a weak temperature dependence, where charges hinder the coil-to-globule transition even when the temperature is above the CP. When the pH is above both pK_a values, flexible and uncharged chains allow a cylinder-to-sphere shape change of micelles with increasing temperature. Thus, the self-assembly behavior of the block copolymer in aqueous solution is largely governed by the water solubilities and the charge states of the blocks.

[1] A. P. Constantinou, B. Zhan, T. K. Georgiou, *Macromolecules* **54**, 1943-1960 (2021)

1.5 Photoswitching of thermoresponsive poly(*N*,*N*-dimethylacrylamide) containing amino acid-modified azobenzene side groups

P. Zhang, R. Steinbrecher[1], Feifei Zheng, Wenqi Xu, David Kohsbahn, C. M. Jeffries[2], A. Laschewsky[1,3], P. Müller-Buschbaum, C. M. Papadakis

[1] University of Potsdam, Potsdam-Golm, Germany

[2] European Molecular Biology Laboratory, DESY, Hamburg, Germany

[3] Fraunhofer IAP, Potsdam-Golm, Germany

Endowing thermoresponsive polymers with additional photoresponsivity is of interest for applications such as drug delivery, owing to the non-invasive nature of these stimuli. The lower critical solution temperature (LCST) behavior in aqueous solution, characterized by a coil-to-globule transition at the cloud point (CP), can be fine-tuned by incorporating photoswitches. Among these, azobenzene (AB) is the most widely used due to its pronounced *trans-cis* isomerization without side reactions. However, due to the weak change of its dipole moment, its influence on the CP is only small [1]. To address this, we introduced amino acids as linkers between the thermoresponsive polymer backbone and the AB, aiming to enhance this photoresponse effect. In this context, beta-alanine (β-Ala) was used as the linker to connect AB to the thermoresponsive poly(*N*,*N*-dimethylacrylamide) (PDMA). Here, we present results on a PDMA random copolymer, in which 11.8% of the repeating groups carry an AB group linked by β-Ala (Fig. 1.9a). The conversion from the *trans*- to the *cis*-state was achieved by irradiating with a 365 nm UV LED light (Fig. 1.9b).

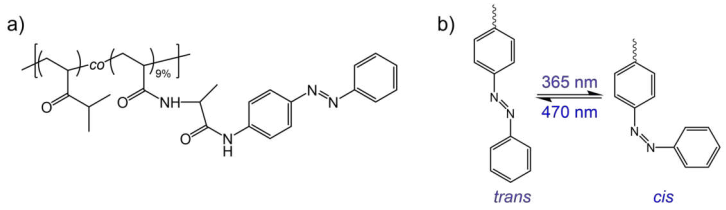

Figure 1.9:
a) Structural formula of **PDMA-βAla$_{11.8\%}$**
b) *trans-cis* isomerization of the AB group.

To determine the temperature dependences on the hydrodynamic radii (R_h) and CPs of **PDMA-βAla$_{11.8\%}$**, dynamic light scattering (DLS) was performed. To investigate the inner structure of it, synchrotron small-angle X-ray scattering (SAXS) were conducted at beamline P12, DESY. The wavelength used was 0.124 nm, and the sample-detector distance was 3.0 m.

First, the intensity autocorrelation functions G_2-1 obtained from DLS exhibit single decays at about 10^{-4} ms for both states (Fig. 1.10a and b), indicating that the copolymers are molecularly dissolved in water. Meanwhile, both states have comparable R_h values. The difference between them is the temperature dependence: the *trans*-state exhibits an initial increase followed by a subsequent decrease, while the *cis*-state displays a continuous increase. From the sudden increased R_h and the reduction of the intercept from G_2-1 due to the multiple scattering, the CPs of the *trans*- and *cis-state* are found to be at 31 °C and 27 °C, respectively. Further away above the CPs, the single chains start to aggregate strongly, resulting in sizes too large to be characterized by DLS.

The scattering curves obtained from SAXS are depicted in Fig. 1.11a and b. First, we see shoulders from 0.1 and 1 nm^{-1}, which can be attributed to the copolymer chain scattering. According to the strong forward scattering starting from 40 °C for both states, we determined the CPs to be 40 °C for both. To describe the shape of the copolymer, we used cylinder form factor, with the parameters cross-sectional radius R_{cs} and length L. In addition, the power law term and

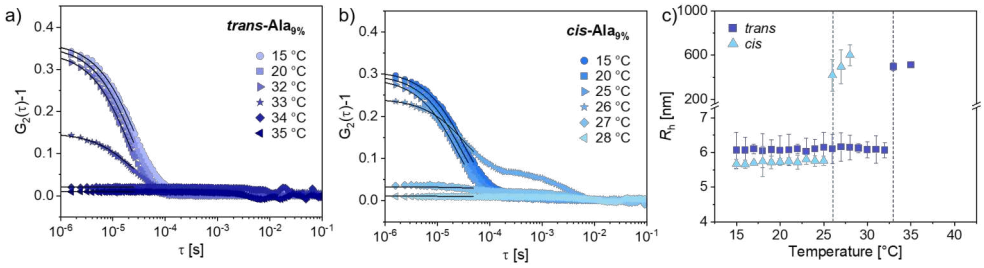

Figure 1.10:
DLS results with intensity auto-correlation functions G_2-1 for the a) *trans*- and b) *cis*-state and R_h for c) both states of **PDMA-βAla$_{11.8\%}$** in 5 g/L aqueous solutions in dependence on temperature. CPs are indicated by red dashed lines.

the Ornstein-Zernike structure factor is used to describe the aggregates and the concentration fluctuations between the chains, respectively. From the cylinder dimensions as shown in Fig. 1.11c, we obtain a decreased L for the *trans*- and increased L for the *cis*-state with the increased temperature, while the R_{cs} stays almost unchanged, suggesting that the copolymer single chains are gathering together to form cylindrical aggregates, and the *trans*-state contracts while the *cis*-state extends in axial direction (Fig. 1.11e), respectively. This is consistent with DLS results. Fig. 1.11d shows an increased correlation length for the *trans*- and nearly unchanged for the *cis*-state, where the *trans*-state shows a lower correlation length and thus a stronger spatial correlation between the PDMA chains due to the more hydrophobic nature of the AB group in the *trans*-state which makes the chains less extended.

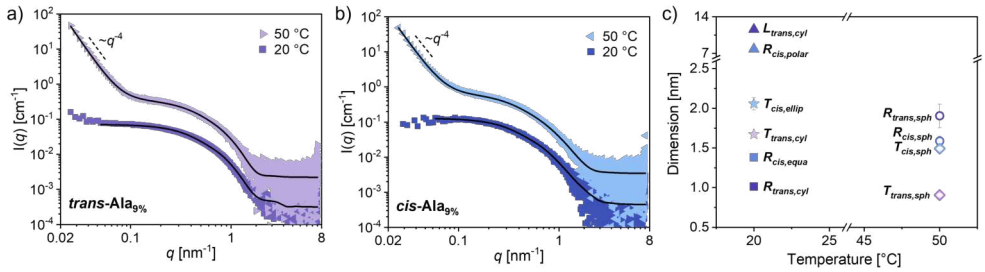

Figure 1.11:
SAXS results with scattering curves for a) *trans*- and b) *cis*-state of PDMA-β**Ala$_{11.8\%}$**, cylinder dimensions in nm c) and correlation length in nm d), sketches of copolymer chain conformation for *trans*- and *cis*-state in dependence on temperature. CPs are indicated by red dashed lines.

In summary, both states of the PDMA-β**Ala$_{11.8\%}$** exhibit a cylindrical shape, but show different LCST transition behaviors, with shortened *trans*- and longer *cis*-state in their axial direction.

[1] A. Miasnikova, C. A. Benítez-Montoya, A. Laschewsky, *Macromol. Chem. Phys.* **214**, 1504 (2013)

2 Responsive thin films

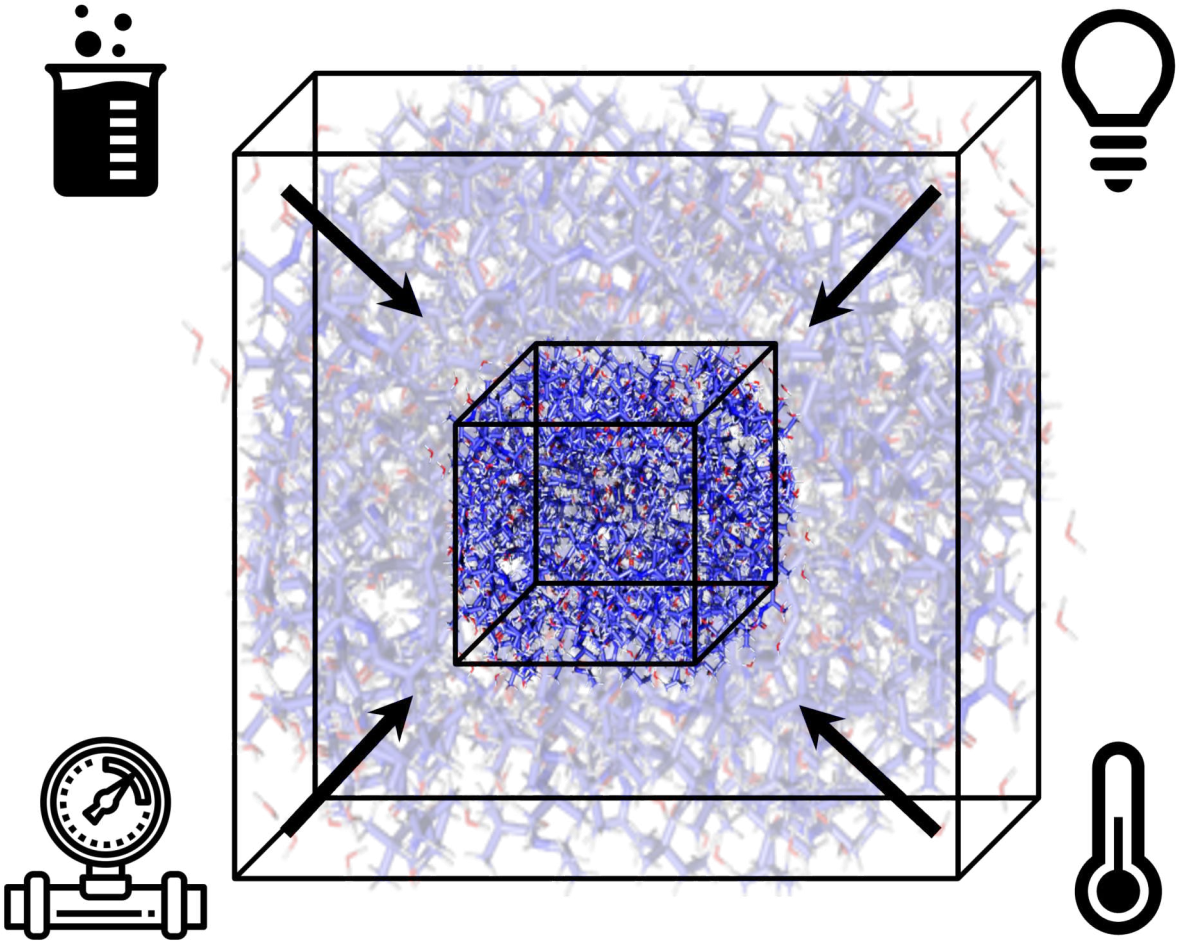

2.1 Morphologies in thin films of charged pentablock terpolymers during solvent vapor annealing

Y. Gu, C. Tsitsilianis[1], C. M. Papadakis

[1] University of Patras, Greece

Stimuli-responsive block copolymers with charged segments have emerged as versatile platforms for designing adaptive nanomaterials, owing to their ability to undergo reversible structural transitions under external triggers such as pH, temperature, and solvent environments [1]. Among these systems, ABCBA pentablock terpolymers are particularly promising due to their interplay between hydrophobic and ionizable blocks. However, the precise control of nanoscale morphologies through combined pH modulation and solvent vapor annealing (SVA) has not been fully exploited yet. This study focuses on a symmetric pentablock terpolymer system comprising poly(methyl methacrylate) (PMMA), poly(2-(dimethylamino)ethyl methacrylate) (PDMAEMA), and poly(2-vinylpyridine) (P2VP), arranged in an MDVDM architecture. The pH-responsive nature of PDMAEMA (pKa = 7.5) and P2VP (pKa = 5.5) enables tunable electrostatic interactions, while the hydrophobic PMMA endblocks provide structural stability. By leveraging both pH variation and solvent selectivity during solvent vapor annealing, we aim to achieve fine control over nanoscale self-assembly.

Thin films were prepared by spin-coating 2 wt% MDVDM aqueous solutions (pH adjusted from 5.5 to 8.0) onto acid-treated silicon substrates. The polymer composition, expressed in volume fractions, was $f_{\mathrm{PMMA}} = 0.04$, $f_{\mathrm{PDMAEMA}} = 0.68$ and $f_{\mathrm{P2VP}} = 0.28$. SVA was conducted in a controlled humidity chamber (19 °C, relative humidity 0–90%), using water vapor as the annealing medium. The evolution of the film thickness was monitored in real-time via in-situ spectral reflectometry. Morphological characterization was carried out using atomic force microscopy (AFM) in tapping mode, with periodic domain spacings determined by fast Fourier transform analysis of the height images.

Figure 2.1 shows AFM height images in dependence on the pH-value of the solution used for film preparation. At pH 5.5 (Figure 2.1 (a)), the film exhibits a disordered structure with minimal height variations. At pH 6.5 (Figure 2.1 (b)), distinct structural features begin to emerge, indicating the onset of microphase separation. At pH 7.0 (Figure 2.1 (c)), well-defined domains with clear boundaries are observed, reflecting an ordered morphology. At pH 8.0 (Figure 2.1 (d)), the domains are larger and exhibit increased height variations, demonstrating further coarsening of the structure.

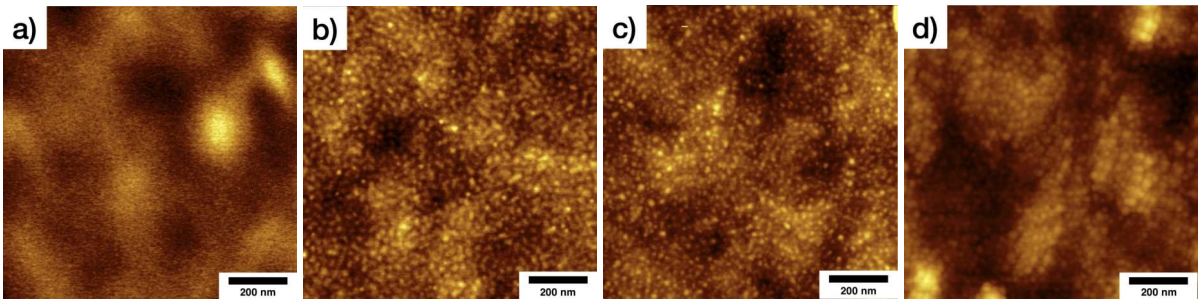

Figure 2.1: AFM height images of as-prepared thin films from MDVDM. a): pH 5.5; b): pH 6.5; c): pH 7.0; d): pH 8.0. The scale bar represents 200 µm, and the height range increases from 2.5 nm in (a) to 50 nm in (d).

Figure 2.2 illustrates the dependence of the height of the protrusions and periodic domain spacing on pH. The main plot shows that the height of the protrusions increases significantly with pH, transitioning from a disordered state to an ordered morphology at higher pH values. In contrast, the periodic domain spacing, measured using AFM, is plotted against pH in the ordered regime, indicating that the domain spacing is almost independent of the pH-value. These results reflect the enhanced microphase separation and structural organization of the thin films at higher pH values.

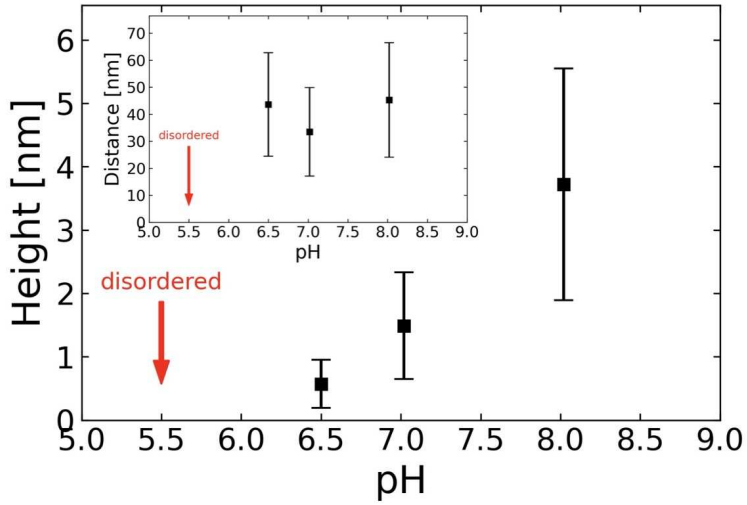

Figure 2.2:
The main plot shows the average height of thin films as a function of pH. The inset illustrates the periodic domain spacing of the films as a function of pH.

Figure 2.3 illustrates the swelling behavior of these films as a function of the relative humidity at two pH values (5.5 and 7.0). The main plot provides a detailed view of the step-wise swelling process over time at pH 7.0 by controlling the gas flow rate of the water vapor, where distinct swelling plateaus are observed, indicating the progressive absorption of water into the film structure. The inset shows the gradual increase in swelling ratio with relative humidity, highlighting the pH-dependent swelling behavior of the films. Maximum swelling ratios of 1.6 and 2.4 are obtained at pH 5.5 and pH 7.0, respectively.

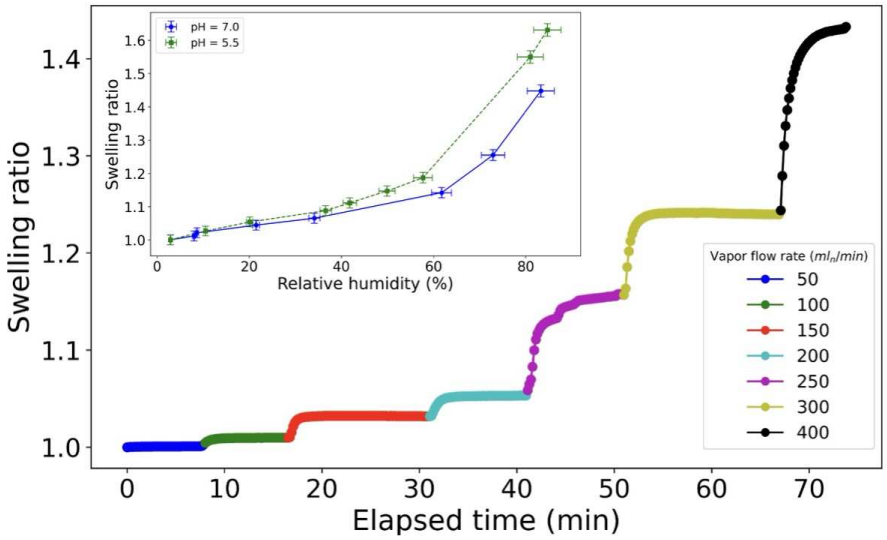

Figure 2.3:
Film thickness of a film prepared at pH 7.0 for different relative humidities. The inset shows the swelling ratios, i.e. the film thickness divided by the initial thickness, in dependence on the relative humidity for films prepared at pH 5.5 (green symbols) and 7.0 (blue symbols).

Future studies will use in-situ AFM to investigate real-time structural responses under controlled ionization and solvent conditions. These efforts will elucidate how pH-modulated charge density influence the surface morphology.

[1] F. A. Jung, C. M. Papadakis, *Adv. Funct. Mater.* **31**, 2102905 (2021)

2.2 Azobenzene: impact on swelling in thermoresponsive polymer films under UV irradiation

D. P. Kosbahn, R. Cubitt[1], R. Steinbrecher[2], A. Laschewsky[2], C. M. Papadakis, P. Müller-Buschbaum

[1] ILL, Grenoble, France
[2] University of Potsdam, Potsdam-Golm, Germany

Thin polymer films capable of reversible coil-to-globule transitions in response to external stimuli have garnered significant attention for their potential use in functional materials such as sensors, nanoswitches, and responsive coatings. Stimuli like temperature, pH, cation addition, or consolvent addition can induce structural and morphological changes in these films, affecting their swelling behavior under varying levels of relative humidity. Among these, light stands out as a non-invasive, high-resolution trigger. This functionality is enabled by photoswitchable molecules, such as azobenzene and azopyrazole, which undergo reversible double-bond isomerization upon irradiation with specific wavelengths of light. The process can be reversed either by exposure to a different wavelength or through thermal relaxation [1].
In this study, we synthesized statistical copolymers by combining azobenzene-acrylamide (AzAm) with the lower critical solution temperature (LCST) polymer poly(dimethylacrylamide) (pDMAm). While aqueous solutions of these polymers have demonstrated LCST shifts upon irradiation, their behavior in thin films remains unexplored. Here, we examine the swelling characteristics of p(AzAm-co-DMAm) thin films in both isomeric states of the photoswitchable azobenzene (Az). The impact of UV irradiation on the film swelling behavior in water vapor is investigated, with the aim of controlling film thickness and water content.
Using reflectance UV-vis spectroscopy, we examine the effect of the isomerization and subsequent thermal relaxation on the optical absorption properties of the polymer film. Fig. 2.4 shows the reflectance spectra of the thin polymer film before irradiation and at different times after irradiation, showing the thermal relaxation of the *cis*-molecules back to their stable *trans*-state. It can be seen that the reflectance in the region around $\lambda = 350$ nm increases after irradiation, due to lower absorption by the azobenzene, and subsequently decreases as the azobenzene molecules thermally relax to their stable state. The results show successful photoswitching of the polymer and give information about the effect of the thin film geometry on the kinetics of the thermal relaxation.

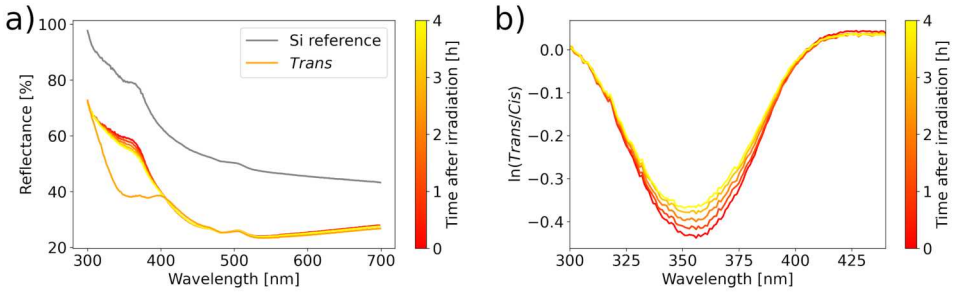

Figure 2.4:
a) Reflectance spectra of the thin polymer films before and after irradiation and the reference spectrum of a silicon wafer. b) Logarithmic ratios of the reflectance curves showing the thermal relaxation of the moieties. The minimum is proportional to the amount of moieties that have relaxed from the unstable *cis*-state to the stable *trans*-state.

Using *in situ* Fourier-transform infrared (FTIR) spectroscopy during swelling of the film under water vapor combined with UV-irradiation, we probe the effect of the azobenzene moieties on

the interaction between water and polymer. Fig. 2.5 shows the wavenumber evolution of the absorption bands ν_{as}(C-H_2) and amide I during swelling, irradiation (lamp on) and thermal relaxation (lamp off) of the polymer film. During swelling, the peak position of the ν_{as}(C-H_2) band shifts to higher wavenumbers, as the vibration of the CH_2 units in the polymer backbone increases in frequency due to confinement by water molecules. The amide I band moves towards lower wavenumbers as vibration is impeded by the formation of hydrogen bonds. After irradiation, there is a further shift towards higher and lower wavenumbers, respectively, indicating that the isomerization results in higher water uptake by the polymer.

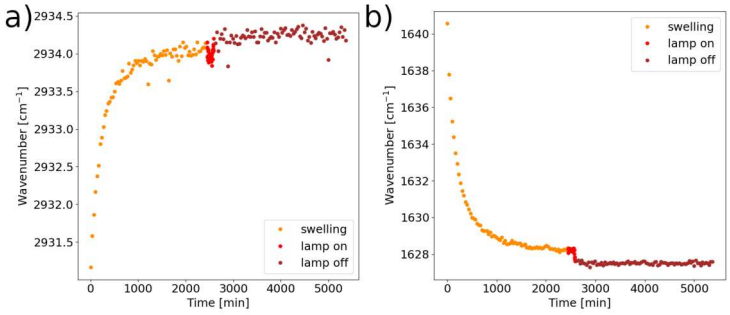

Figure 2.5:
a) Peak position of the ν_{as}(C-H_2) band over time. b) Peak position of the amide I band over time.

Using time-of-flight neutron reflectometry (ToF-NR) at the D17 instrument at Institute Laue-Langevin (ILL), we obtain depth-resolved information about the solvent distribution in the thin film in dry and swollen state, before, during and after irradiation, using a custom-made sample environment [2]. Fig. 2.6 shows the static measurements of the thin film in the aforementioned states. While there is a decrease in thickness and SLD when the lamp is switched on, the film returns back to near its previous state after irradiation, indicating that the effect of the UV-light on the water uptake is less pronounced in the thin film used for ToF-NR measurements.

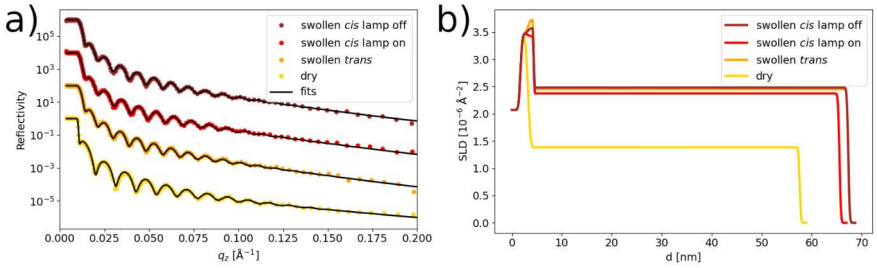

Figure 2.6:
a) Static ToF-NR curves (symbols) and fits (lines). b) SLD profiles of the models used for fitting the data.

In summary, the results show a successful isomerization of the photoactive moieties when irradiated with light. The isomerization seems to increase water uptake by the polymer, although this effect is more pronounced in thicker films. Our results reveal insights on how photoswitchable moieties affect the microscopic properties of thin polymer films.

[1] A. Goulet-Hanssens, F. Eisenreich, S. Hecht, *Adv. Mater.* **32**, 1905966 (2020)

[2] T. Widmann, L. P. Kreuzer, G. Mangiapia, M. Haese, H. Frielinghaus, P. Müller-Buschbaum, *Rev. Sci. Instrum.* **91**, 113903 (2020)

2.3 Study of the swelling behavior of poly(*N*-vinylisobutyramide): a strutural Isomer of poly(*N*-isopropylacrylamide)

M. P. Le Dû, R. Cubitt[1], C. Henschel[2], A. Laschewsky[2,3]

[1] ILL, Grenoble, France
[2] University of Potsdam, Potsdam-Golm, Germany
[3] Fraunhofer-Institut für Angewandte Polymerforschung, Potsdam-Golm, Germany

Poly(*N*-isopropylacrylamide) (PNIPAM) is one of the most outstanding thermoresponsive polymers and has been studied for its sharp and reversible phase transition at around 30 °C in water. However, the acrylamide-based monomers used to synthesize NIPAM-based polymers pose toxicity risks, and their intensive use has brought substantial traces of acrylamides in food and water wastes.[1] Hence, alternative polymers such as poly(*N*-vinylisobutyramide) (PNVIBAM), are investigated. PNVIBAM is known to be water soluble and have a transition temperature of 39 °C in water.[2] These are two attractive features when used as a controlled drug delivery system or smart skin coating in the medical field.
This research project aims to study the swelling behavior of PNVIBAM thin film and to compare it to that of the well-known PNIPAM. The investigation is carried out on several length scales, ranging from the mesoscopic to molecular scale. First, the water absorption of the PNVIBAM film under water vapor is studied with respect to the swelling of the PNIPAM film. Fig. 2.7 shows the recorded spectral reflectance data of the polymer films under water vapor. Both samples are first dried under N_2 atmosphere before exposure to high relative humidity. The PNIPAM thin film reaches a higher thickness than PNVIBAM, which translates to a higher swelling capacity of PNIPAM films.

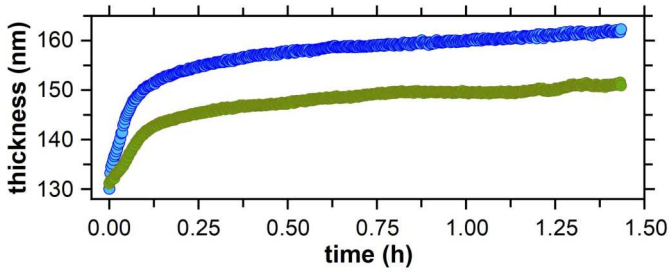

Figure 2.7:
Thickness evolution of PNIPAM (blue) and PNVIBAM (green) films under H_2O vapor exposure.

Then, the solvent distribution within the films is studied by time-of-flight neutron reflectometry (ToF-NR). The scattering length density (SLD) distribution along the normal direction of the substrates in the dry state, shown in Fig. 2.8 a) and b) reveals an enrichment layer of solvent (D_2O) at the substrate interface in the PNIPAM sample. In contrast, the PNVIBAM film does not present this solvent-rich layer. The swelling kinetics are studied as shown in Fig. 2.8 c), where the swelling ratio of the polymer films is plotted against the volume fraction of solvent within the samples. It is observed that a volume fraction of (D_2O) of 3.8 % is required to cause the PNVIBAM film vertical expansion, while 6 % is needed for the PNIPAM sample. Such observation is linked to a difference in free volume accessible by the solvent's molecules within the films. Finally, *in situ* Fourier transform infrared (FTIR) spectroscopy under water vapor is used to probe the interaction with the polymers and the solvent. Fig. 2.9 shows the peak position shift over the time of some characteristic absorption bands of the polymers. The position of the Amide I bands shifts towards lower values, characteristic of hydrogen bond formation. This shift is stronger in the case of PNIPAM, which translates to a more hydrophilic behavior than

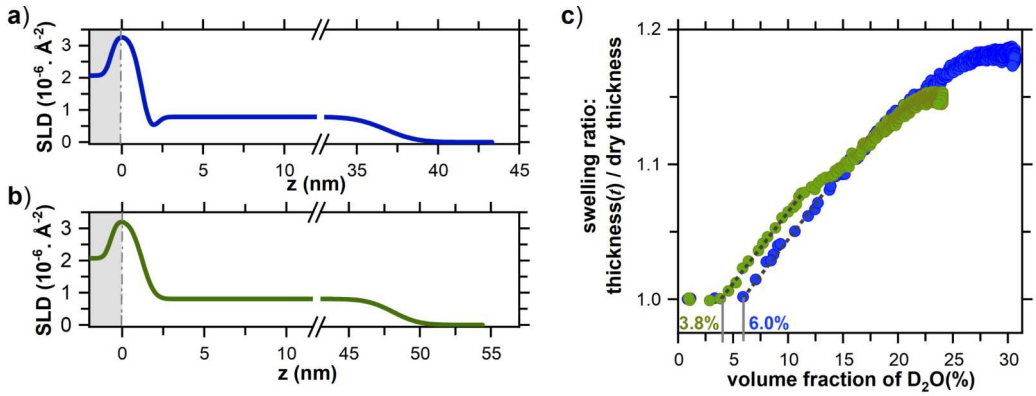

Figure 2.8:
ToF-NR investigation of PNIPAM (blue) and PNVIBAM (green) thin films under D_2O vapor exposure; a) and b) SLD profile of the polymer thin films; c) evolution of the swelling ratio as a function of the volume fraction of D_2O

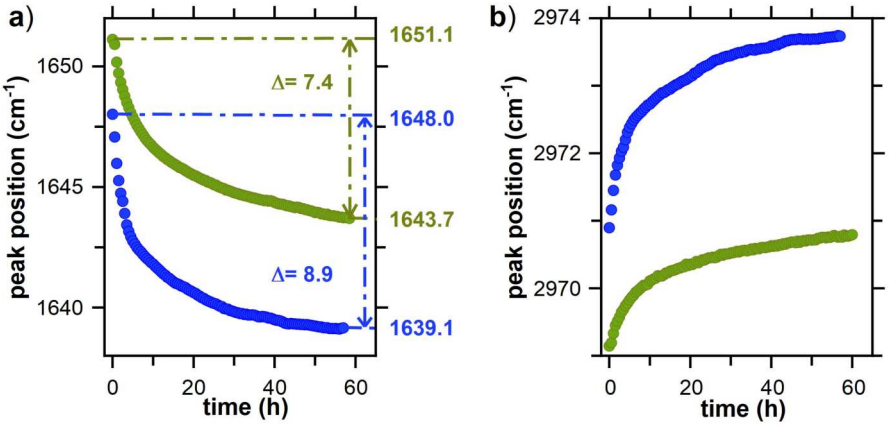

Figure 2.9:
In situ FTIR investigation under H_2O vapor exposure. Peak position shift of the a) amide I band and the b) -C-H_3 asymmetric stretching absorption band of PNIPAM (blue) and PNVIBAM (green).

PNVIBAM despite its lower transition temperature. The peak positions of the -C-H_3 asymmetric stretching vibrations of the isopropyl side groups shift towards higher values. Such behavior is characteristic of confinement from water clathrates around those hydrophobic units.[3] This shift is bigger in the case of PNIPAM, meaning that the induced confinement is weaker in PNVIBAM. It has been deduced that the hydrophobic interaction in PNVIBAM is stronger than in PNIPAM, which sterically hinders the absorption of more water molecules.
Despite the isomeric relationship between PNIPAM and PNVIBAM, those two polymers, in thin film geometry, have different swelling behaviors when exposed to water vapors. Such differences need to be accounted for when bringing these materials into applications.

[1] H. Vihola, A. Laukkanen, L. Valtola, H. Tenhu, J. Hirvonen, *Biomater.* **26(16)**, 3055-3064 (2005)

[2] C. Henschel, D. Schanzenbach, A. Laschewsky, C. .H. Ko, C. M. Papadakis, P. Müller-Buschbaum, *Colloid Polym. Sci.* **301(7)**, 703-720 (2023).

[3] M. L. Galbraith, J. D. Madura, *J. Mol. Graphics Modell.* **78**, 168-175 (2017)

2.4 Salt-mediated tuning of the swelling degree of PNIPMAM thin films

J. Reitenbach, R. Cubitt[1], D. Schanzenbach[2], A. Laschewsky[2], C. M. Papadakis, P. Müller-Buschbaum

[1] ILL, Grenoble, France

[2] Universität Potsdam, Potsdam-Golm, Germany

Stimuli-responsive polymers have gained significant interest due to their ability to change their properties in response to external triggers. Among them, thermoresponsive polymers are particularly important for applications such as targeted drug delivery, sensors, and smart coatings. These polymers undergo reversible phase transitions when exposed to changes in temperature. A key factor found to influence the transition temperature of thermoresponsive polymers are specific ion effects, where ions alter polymer behavior by modifying hydrogen bonding and solvation dynamics. Depending on the type of ion, the polymer response can be either enhanced or suppressed, significantly affecting its ability to swell and contract. Another intriguing phenomenon in thermoresponsive polymers is the cononsolvency effect, where a polymer that is soluble in the individual solvents becomes insoluble in their mixture at certain compositions. The origin of this counterintuitive behavior is still under debate, with theories ranging from complex formation to competitive binding effects and preferential adsorption. However, an understanding of the cononsolvency effect is essential for designing advanced polymer-based materials with a controlled response in complex solvent environments. Inspired by the specific ion and cononsolvency effect, the influence of salts on the swelling degree of poly(*N*-isopropylmethacrylamide) (PNIPMAM) thin films is investigated. The introduction of salts into these thin films is aimed at evaluating their role in modifying polymer-solvent interactions and controlling the film response under different vapor atmospheres.

To study the effect of salts on the swelling and cononsolvency-induced collapse, PNIPMAM thin films containing either $Mg(ClO_4)_2$ or $NaClO_4$ are fabricated on silicon substrates. The films are first swollen in a D_2O atmosphere, followed by exposure to a D_2O-acetone vapor mixture atmosphere in a defined ratio to induce the collapse transition. The experiment is conducted at a constant temperature to exclude thermal effects originating from the intrinsic thermoresponsive behavior of PNIPMAM. Using time-of-flight neutron reflectometry (ToF-NR) and Fourier-transform infrared spectroscopy (FTIR) the macroscopic film changes as well as the underlying molecular interactions are investigated. The ToF-NR measurements provide insights into the film thickness evolution over time and the vertical solvent distribution inside the films during the vapor exchange process. FTIR spectroscopy further allows for the analysis of molecular interactions occurring within the polymer film, and subjecting the FTIR data to correlation analysis allows to deduce the sequence of solvation events. In Fig. 2.10 the film thickness evolution as well as the change of the scattering length density (SLD) are shown for the $NaClO_4$- (green) and $Mg(ClO_4)_2$-containing (orange) PNIPMAM thin films obtained from the ToF-NR analysis. The results reveal that the swelling behavior of the films depends strongly on the type of salt. In a pure D_2O vapor atmosphere, both systems exhibit an increase in film thickness, with $NaClO_4$-containing PNIPMAM thin films swelling by 177%, whereas $Mg(ClO_4)_2$-containing films exhibit a more moderate swelling of 39%. This striking difference indicates that sodium perchlorate significantly enhances the water uptake ability. Upon exposure to a D_2O-acetone vapor mixture atmosphere (90:10 volume ratio), the films undergo a cononsolvency-driven contraction. The $NaClO_4$-containing films show a thickness decrease of over 50%, while the $Mg(ClO_4)_2$-containing films contracts by only 9%. This finding indicates that $NaClO_4$ enhances not only the swelling capacity but also the subsequent collapse behavior. FTIR analysis provides mechanistic insights into the solvation process and the corresponding FTIR spectra are shown in Fig. 2.11. During swelling, amide-D_2O hydrogen bonds form, stabilizing the hydrated state of

the polymer. Upon vapor exchange, these hydrogen bonds are perturbed, leading to solvent release. The incorporation of acetone reduces D_2O-amide interactions, while amide-amide interactions increase, promoting film collapse. The different response behaviors between $NaClO_4$- and $Mg(ClO_4)_2$-containing films highlight the influence of specific ion effects, with $NaClO_4$ enhancing swelling and contraction responses more effectively than $Mg(ClO_4)_2$. The pronounced differences in solvent uptake and release behaviors indicate that the cation type plays a crucial role, even when the anion remains constant. By systematically varying salt types and concentrations, further research can lead to the optimization of smart coatings, drug delivery systems, and other stimuli-responsive applications.

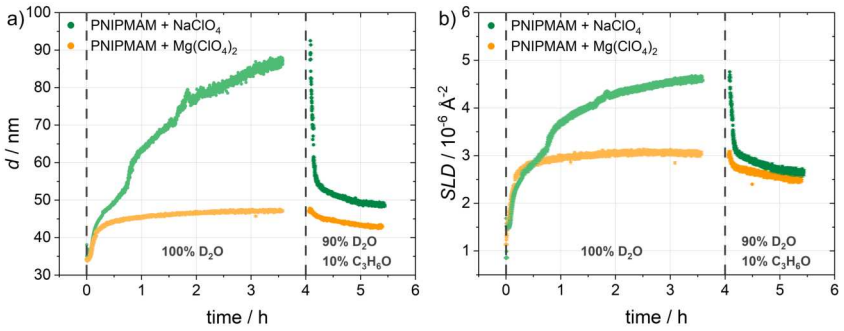

Figure 2.10:
a) Thickness and b) SLD evolution over time for the PNIPMAM thin films containing either $NaClO_4$ (green) or $Mg(ClO_4)_2$ (orange) [1].

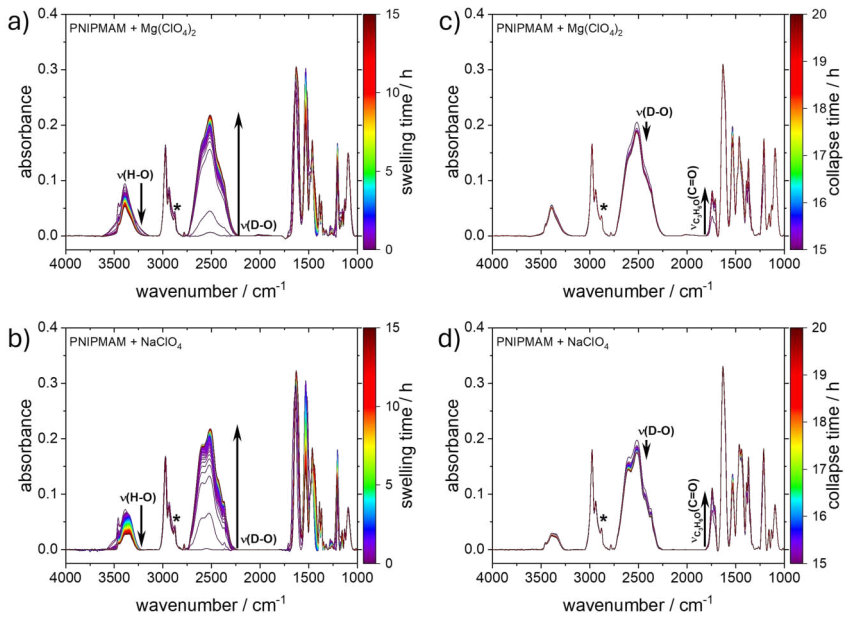

Figure 2.11:
FTIR spectra measured during the a,b) swelling and c,d) collapse of a PNIPMAM film containing either $Mg(ClO_4)_2$ (top) or $NaClO_4$ (bottom). Black arrows indicate the intensity trends of the signals originating from solvent molecules over time [1].

[1] J. Reitenbach, P. Wang, L. F. Huber, S. A. Wegener, R. Cubitt, D. Schanzenbach, A. Laschewsky, C. M. Papadakis, P. Müller-Buschbaum, *Macromolecules* **57**, 10635-10647 (2024)

3 Functional thin films

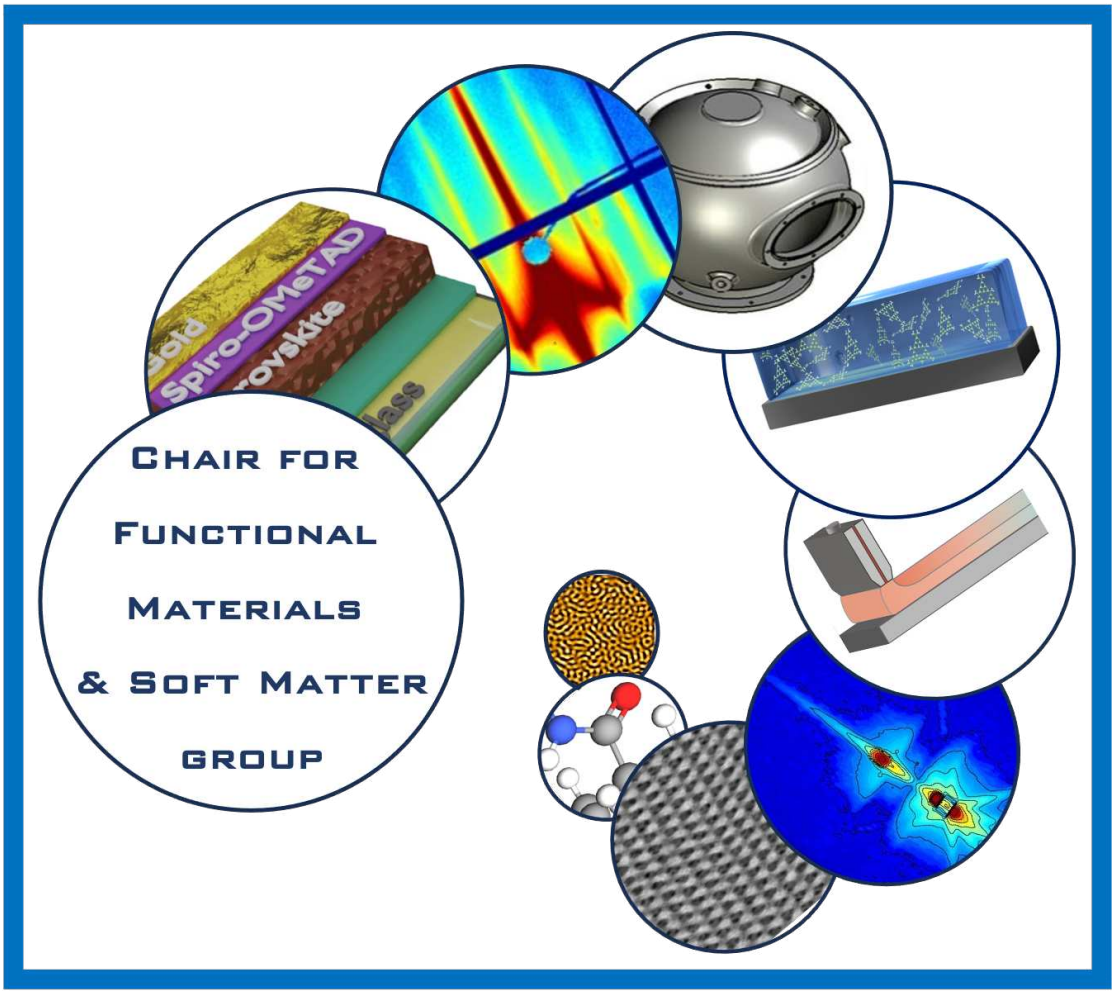

3.1 Influence of salt addition on the ionic conductivity, hydration behavior, and structure of poly(sulfobetaine) hydrogels for electrolyte applications

F. Ganster, A. Stephan[1], P. Müller-Buschbaum, L. P. Kreuzer[1]

[1] MLZ, Garching, Germany

Polyzwitterionic hydrogels are promising candidates as electrolytes in aqueous solid-state batteries, such as zinc-ion batteries (ZIBs), due to their ability to retain water molecules, facilitating ionic transport [1]. The proportional addition of zinc salts induces the formation of so-called ion migration channels, driven by electrostatic interactions and acid-base concepts. Specifically, Zn^{2+} ions coordinate with the negatively charged groups of the polyzwitterion, forming Zn^{2+}-rich channels. Within these channels, retained water acts as a lubricant, coordinating with the charged groups of the polyzwitterion while reducing interactions with mobile Zn^{2+} ions. Eventually, this promotes ion pair dissociation and enhances ion mobility [2]. By adding anions, e.g., cosmotropic SO_4^{2-} and chaotropic CH_3COO^- (acetate), the interactions between water and the polyzwitterion can be tuned, which in turn impacts on the formation and structure of the ion channels and thus, on the overall ionic conductivity. The underlying mechanisms, i.e., the hydration behavior of the polyzwitterionic hydrogel in the presence of different salts, and the consequences for the hydrogel structure and ionic conductivity are the subject of this research project.

The first step explores the impact of salt addition on the ionic conductivity of the zwitterionic polysulfobetaine methacrylate (PSBMA) hydrogel (Fig. 3.1 a)). Salt-free and salt-containing [$ZnSO_4$ and Zn(acetate)] hydrogels are sandwiched (via the drop-casting technique) between two steel plates and assembled into a coin cell before assessing the ionic conductivity by measuring the electrochemical impedance.

The results demonstrate that all three samples exhibit significantly different ionic conductivities. While adding salt—regardless of the type—generally leads to an increased ionic conductivity, distinct differences between the salt types are also observed. This is shown in Fig. 3.1 b) for a salt concentration of 1 M with respect to the retained water. These variations are attributed to salt-type-specific hydration of the zwitterionic polymer and structural changes in the hydrogel. FTIR spectroscopy is used to investigate the hydration behavior of the hydrogel upon adding different types and even small amounts of salt. Fig. 3.1 c) presents the FTIR spectra of three hydrogels: one salt-free, one containing $ZnSO_4$, and one containing Zn(acetate), each at a 1:1 molar ratio relative to the number of repeating units in the polymer.

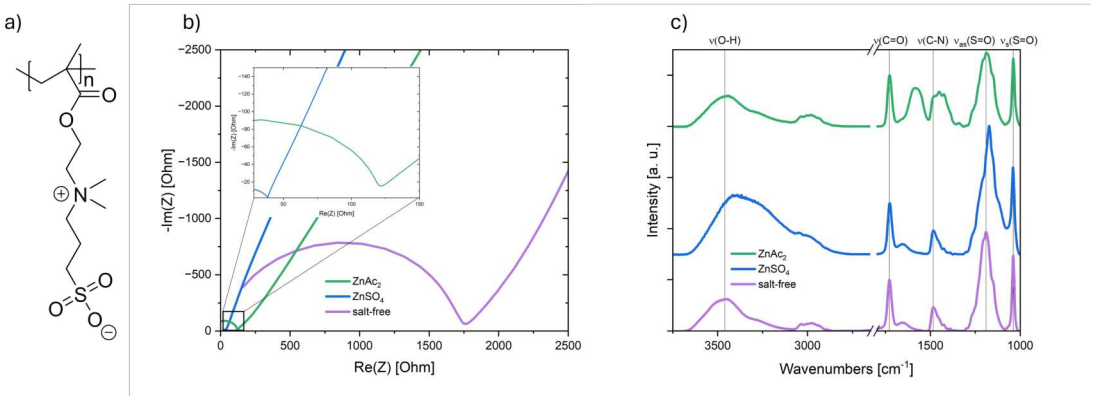

Figure 3.1:
Chemical structure of PSBMA (a) as well as impedance spectra (b) and FTIR spectra (c) of salt-free, $ZnSO_4$- and Zn(acetate)-containing PSBMA hydrogels.

Notably, the peak positions assigned to the functional groups in the hydrogel are not equally affected by the addition of salt. In particular, the C=O stretching vibration at 1728 cm^{-1} and the symmetric S=O stretching vibration at 1039 cm^{-1} appear to remain constant. Slight changes can be observed in the asymmetric S=O stretching vibration at 1190 cm^{-1} and in the O-H stretching vibration (around 3460 cm^{-1}). These measurements confirm that the characteristic functional groups of the hydrogel are clearly identifiable in the FTIR spectrum. Consequently, this approach provides a reliable basis for conducting further hydration studies. In-situ FTIR measurements are presently being conducted to investigate the effects of varying relative humidity and temperature conditions.
Besides the hydration behavior, the hydrogel morphology also seems to depend on the chaotropic/cosmotropic nature of the added salt as preliminary results from GISAXS measurements performed at the Elettra Sincrotone Trieste indicate.
While FTIR spectroscopy provides valuable insights into the functional groups of the polymer, Raman spectroscopy is integrated into the project due to its ability to study water dynamics in detail. Understanding hydration water dynamics is crucial for optimizing ionic transport and conductivity in zwitterionic hydrogels. In addition, an experimental setup is developed to simultaneously measure water dynamics (via Raman spectroscopy) and ionic conductivity (via impedance spectroscopy). At the same time, parameters such as relative humidity and temperature can be varied. Therefore, a custom sample holder is designed as shown in Fig. 3.2 a). The design includes a steel ring that contacts the hydrogel-coated steel plate. Both are then pressed together at the center of the holder, where two bridges extending from the center facilitate verification of the hydrogel thickness. Electrical contacts on either side of the steel plates are integrated to enable connection to a potentiostat, while the ring electrode and the opening in the holder ensure that the Raman laser can access the hydrogel. The holder is tailored to fit into an existing humidity chamber (Fig. 3.2 b)). This chamber was originally developed for simultaneous Raman spectroscopy and quasi-elastic neutron scattering (QENS) measurements and precisely controls temperature and humidity. Recently, it was successfully commissioned at the FOCUS instrument at Paul Scherrer Institut (Switzerland). This chamber will be utilized in upcoming QENS experiments using the IRIS instrument at the ISIS Neutron and Muon Facility (UK) to study the role of water dynamics in zwitterionic hydrogels.

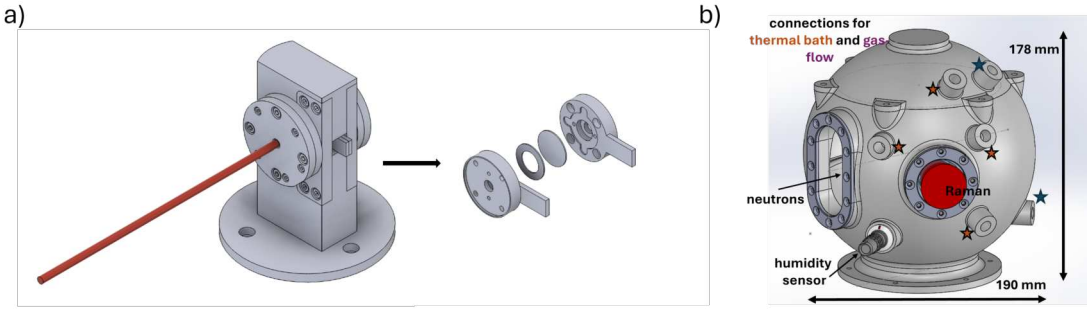

Figure 3.2:
Schematic representations of the custom holder and its centerpieces for simultaneous Raman spectroscopy and impedance measurements (a) and the humidity chamber (b). The Raman laser is indicated in red.

[1] P. Yang, J.-L. Yang, K. Liu, H. J. Fan, *ACS Nano* **16**, 15528-15536 (2022)

[2] Y. Wang, Q. Li, H. Hong, S. Yang, R. Zhang, X. Wang, X. Jin, B. Xiong, S. Bai, C. Zhi, *Nat. Commun.* **14**, 3890 (2023)

3.2 Water-uptake in Zn-loaded polysaccharide films

J. E. Heger, H. Amenitsch[1], C. M. Papadakis, P. Müller-Buschbaum

[1] ELETTRA, Basovizza, Italy

Aqueous Zn-ion batteries have recently gained increasing interest due to their low cost of fabrication, which is made possible by the abundance of involved materials, the low toxicity of the materials used, and the specific energy density of the batteries. In order for Zn-ion batteries to become a serious candidate to replace Li-ion batteries and to overcome the associated economic and environmental issues in handling the Li precursors, research is focused, in particular, on the electrolyte architecture used in Zn-ion batteries. The use of hydrogel-based quasi-solid electrolytes offers the combined advantages of liquid and solid electrolytes, including enhanced mechanical flexibility and ion conductivity [1].
Solvent vapor treatment (SVT) has frequently been used to manipulate the structures of thin polymer films. Here, we investigate films from biopolymers that are loaded with ions which are expected to become mobile in the solvent-swollen state. These films are prepared by spin-coating on silicon substrates. For SVT, a custom-made, temperature-controlled chamber is used, which allows placing of a solvent reservoir inside and provided bubblers as well as monitors for temperature and relative humidity (Fig. 3.3) [2].

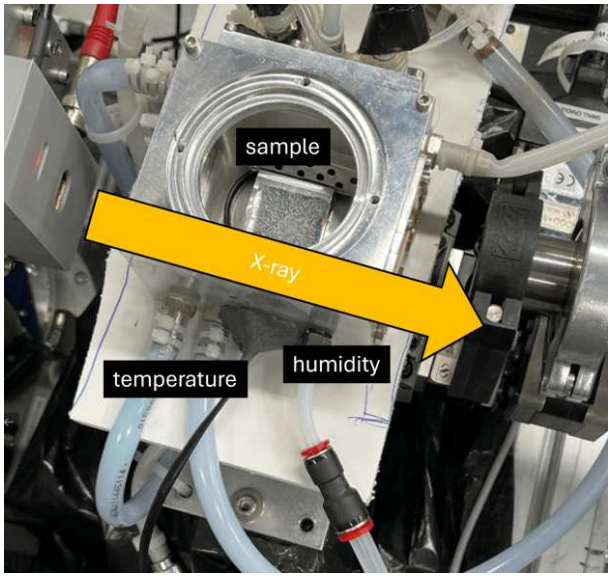

Figure 3.3:
Experimental setup at the Austrian SAXS beamline, ELETTRA. A cooling water circuit controls the sample temperature, and a stream of nitrogen through water containing bubblers controls the relative humidity inside the chamber during in situ GISAXS measurements.

The film structures are investigated using grazing-incidence small-angle X-ray scattering (GISAXS) at the Austrian SAXS beamline to get information on the lateral structure. Simultaneously, the spectral reflectance (SR) is measured to track the film thickness during the swelling and drying experiments. A 2D detector is mounted at a sample-detector distance of 1.8 m. From the 2D GISAXS maps, horizontal 1D line cuts are taken at the Yoneda peak position, which give information about the mesoscopic lateral film structure.
We investigate hydrogels based on environmentally friendly polysaccharides, specifically agar and pectin. The hydrogels are loaded with 1 M $ZnSO_4$, and thin films are prepared. To reveal the effect of water uptake and release and of elevated temperature on the nanoscale morphology of the Zn-ion loaded hydrogels, we conduct in-situ GISAXS measurements at an incident angle of

0.45° every 60 s with an exposure time of 30 s for in total 0.5 h per measurement spot. This is well below the maximum radiation dose that was experimentally quantified before the experiments. Initially, the samples are subjected to a relative humidity of 15–17% at 21 °C. Then, the relative humidity is increased to approximately 79–81%. Subsequently, the samples are heated to 65 °C at this elevated relative humidity. Lastly, the samples are cooled to 22 °C, and the relative humidity is reduced again to 15–17%. Each step lasts for 0.5 h, and simultaneous SR measurements monitor the occurring changes in film thickness, which varies from 356 nm to 395 nm (agar-based) and from 43 nm to 67 nm (pectin-based). The horizontal line cuts obtained from selected 2D GISAXS maps are shown in Fig. 3.4a and b for the pectin-based and the agar-based hydrogels, respectively. A qualitative comparison indicates that, at length scales of 30–50 nm, the pectin-based hydrogels exhibit a more pronounced morphological response to variations in ambient conditions than the agar-based hydrogels. These length scales correspond to the diameter of ion-diffusion channels within the network, which are expected to directly impact the electrolyte performance in Zn-ion batteries [3].
A more quantitative understanding is currently being developed through the modelling of GISAXS data with established models and the correlation of the structural variation with the one of the film thickness. The analyzed data will be discussed in the context of complementary electrochemical measurements.

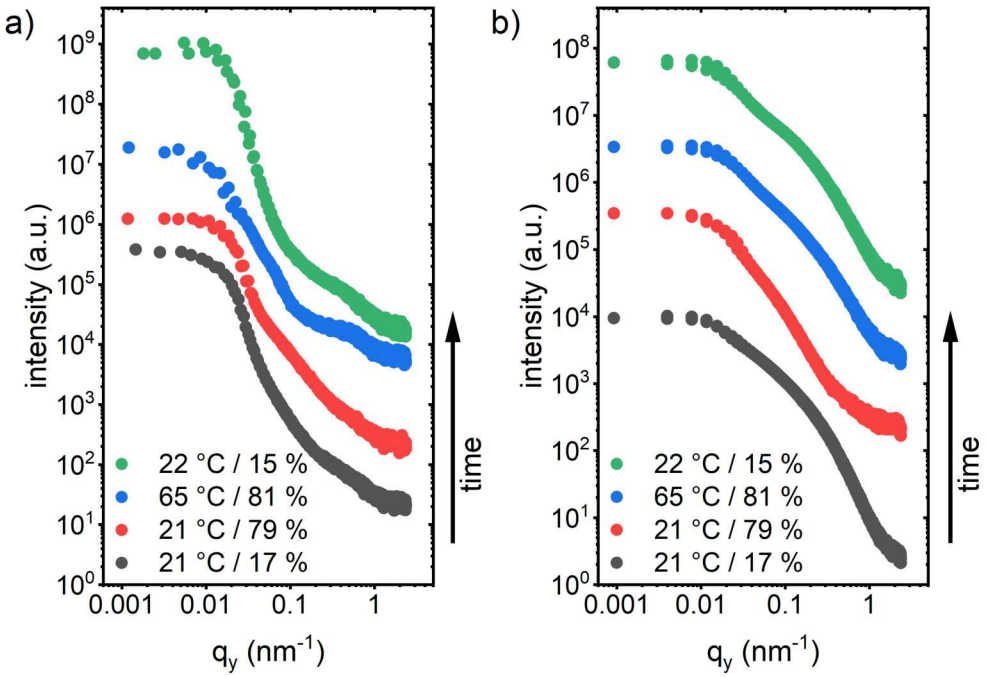

Figure 3.4:
Results from the $ZnSO_4$-loaded polysaccharide thin films. Horizontal line cuts taken at the Yoneda peak position of (a) the pectin-based hydrogel, and (b) the agar-based hydrogel.

[1] L. Li, S. Jia, S. Yue, C. Wang, H. Qiu, Y. Ji, M. Cao, D. Zhang, *Green Chem.* **26**, 6404-6422 (2024)

[2] A. V. Berezkin, F. A. Jung, D. Posselt, D.-M. Smilgies, C. M. Papadakis, *Adv. Funct. Mater.* **28**, 1706226 (2018)

[3] L. Yan, Q. Zhang, Z. Zhang, G.-J. Li, Y. Jin, X.-L. Zhang, Y.-Y. Sun, *J. Membr. Sci.* **690**, 122243 (2024)

3.3 Towards latex film formation investigated via GISAXS

S. Schraad[1], H. M. Salvador[2], N. Tomozeiu[2], P. Müller-Buschbaum, S. V. Roth[1,3]

[1] DESY, Hamburg, Germany
[2] Canon Prod. Print., Venlo Netherlands
[3] KTH, Stockholm, Sweden

Printing with water based inks is a complex process representing the physical-chemical interactions between a complex fluid and a porous paper. Directly after deposition of the inks, the solvent evaporates, and colloids in the ink start to self-assemble. Print quality is the result of these stages and the interaction of the different components between each other and the substrate. A sketch showing the different stages, from deposition to final film formation, is shown in Fig. 3.5 for a non-porous substrate and a porous substrate. This topic is investigated by industry and academics since a long time, a full understanding could not be gathered by now. Especially in-situ measurements on latex film formation are rarely published [1,2].

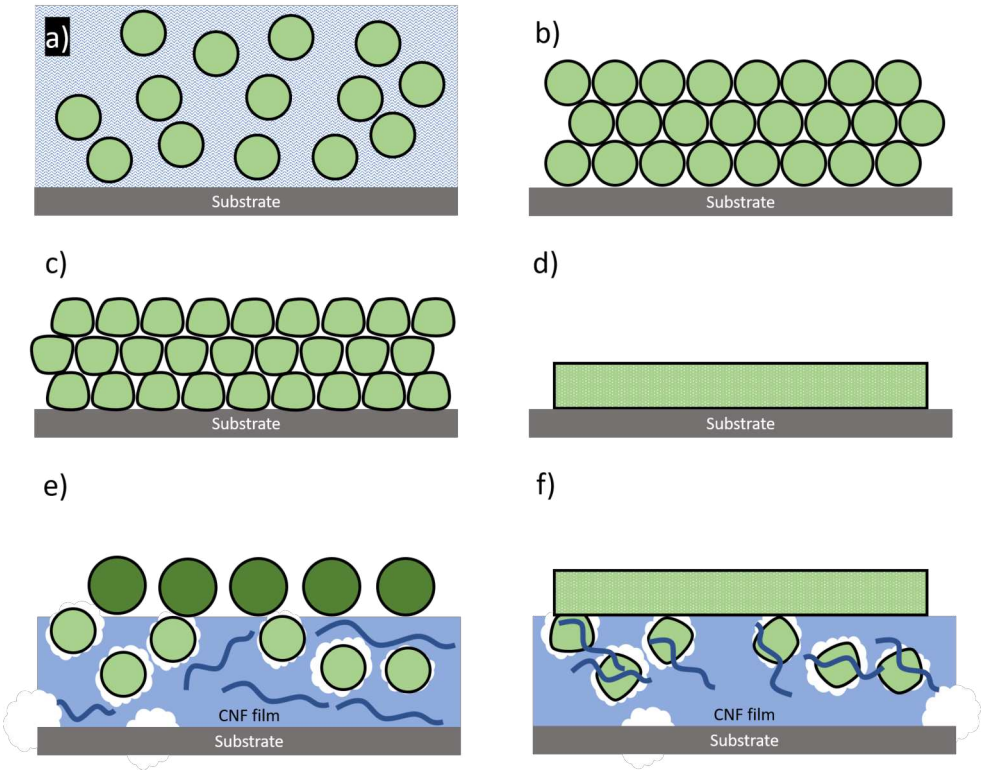

Figure 3.5:
Different stages of typical latex ink film formation on non-porous substrate (a-d), and imbibition of latex colloids into porous substrate before (e) and after annealing (f). a) An aqueous suspension containing polymeric micro- or nanospheres is deposited onto a substrate. b) The solvent evaporates, leading to the second stage of closely and in-contact colloid particles. c) The latex particles deform, resulting in the third stage. d) A mechanically stable film is formed after aging or annealing. e) Colloidal latex fill voids of cellulose nanofibrils (CNF) films, when their size is smaller than the voids. f) Deformation of colloids and entanglement with CNF after annealing or aging.

Ultrasonic spray deposition (USD) is used to produce CNF thin films and deposit the latex colloids. Like other spray deposition techniques, USD has a high material utilization and is scalable. USD nozzles create micrometer-sized droplets that are carried by nitrogen gas from

the nozzle tip onto the (heated) substrate. The formation of a continuous wetting layer is crucial to obtain homogeneous films. The wetting behavior is governed by the surface energy of the substrate.
The droplets are usually smaller and have a lower velocity than droplets created during air-brush spray deposition (ASD). Droplet size can be modified by choosing the nozzle frequency for USD. In ASD, droplets are created by pressing the solution with the help of a carrier gas through a small orifice, while USD utilizes a piezoelectric generator to atomize the dispersion.
Generally, USD leads to more homogeneous films with a smooth surface due to the low kinetic energy of the droplets impinging onto the substrate [3]. Therefore, USD is used instead of ASD to fabricate CNF thin films and latex colloid-coated CNF thin films, with a layer thickness aiming between 500 nm and 2 µm. Here, the idea is to prepare ultra-smooth thin films as a model substrates to mimic printing on paper. For comparison, non-porous substrates, i.e. silicon wafers, will be used as well.

An experimental chamber is currently designed, which allows to investigate the latex film formation via combined grazing incidence X-ray scattering (GISAXS) and spectral reflectance. Spectral reflectance is recorded by a white light interferometer (WLI). To observe the later stages of solvent evaporation, coalescence and deformation, it is necessary to use in-situ GISAXS during film formation. Here, focus is on analyzing structural changes during the different stages quantitatively.
The chamber will include the possibility to deposit the colloids or later latex inks onto the CNF films, then the sample will be moved into the X-ray beam and focal point of the white light interferometer. Here, reduction of vibrations are crucial, due to the sensitivity of the WLI. The enclosed chamber then also allows to monitor temperature and relative humidity, which can influence the latex film formation process [4-6]. By including a fan the convection rate can be controlled, which also influences film structure [7].

Ex situ spectroscopic ellipsometry is used to determine film thickness and optical properties of ultrasonically sprayed CNF thin films and latex colloid coated CNF films. Literature suggest graded films, meaning film density changes from top to bottom [4]. This graded layer model will be used for colloid coated CNF films, as it proved to be successful to distinguish if colloids imbibe into the CNF layer or not [4].
Another crucial parameter is the colloid size, because during the deformation phase mechanical forces acting on the particles depend on the radius of curvature of the latex particles, which is governed by the particle size. Also comparing non-deforming silica nanoparticles with the aforementioned deformable, polymeric colloid particles, will give valuable insight into the film formation process.

[1] I. Martin-Fabiani, D. K. Makepeace, P. G. Richardson, J. Lesage de la Haye, D. Alba Venero, S. E. Rogers, F. D'Agosto, M. Lansalot, J. L. Keddie, *Langmuir*, **35/10**, 3822-3831 (2019)

[2] M. A. Winnik, *COCIS*, **2** , 192-197 (1997)

[3] S. Liu, X. Zhang, L. Zhang, W. Xie, *Sci Rep*, **6**, 37402 (2016)

[4] C. Harder, M. Betker, A. E. Alexakis, Y. Bulut, B. Sochor, L. D. Söderberg, E. Malmström, P. Müller-Buschbaum, S. V. Roth, *ACS Appl. Nano Mater.*, **7**, 10840-10851 (2024)

[5] X. Chen, S. Fischer, Y. Men, *Langmuir*, **27**, 12807-12814, (2016)

[6] C. J. Brett, N. Mittal, W. Ohm, M. Gensch, L. P. Kreuzer, M. Månsson, H. Frielinghaus, P. Müller-Buschbaum, L. D. Söderberg S. V. Roth, *ACS Macromolecules*, **52**, 4721-4728 (2019)

[7] S. V. Roth, *J. Phys.: Condens. Matter*, **28**, 403003 (2016)

4 Photovoltaics

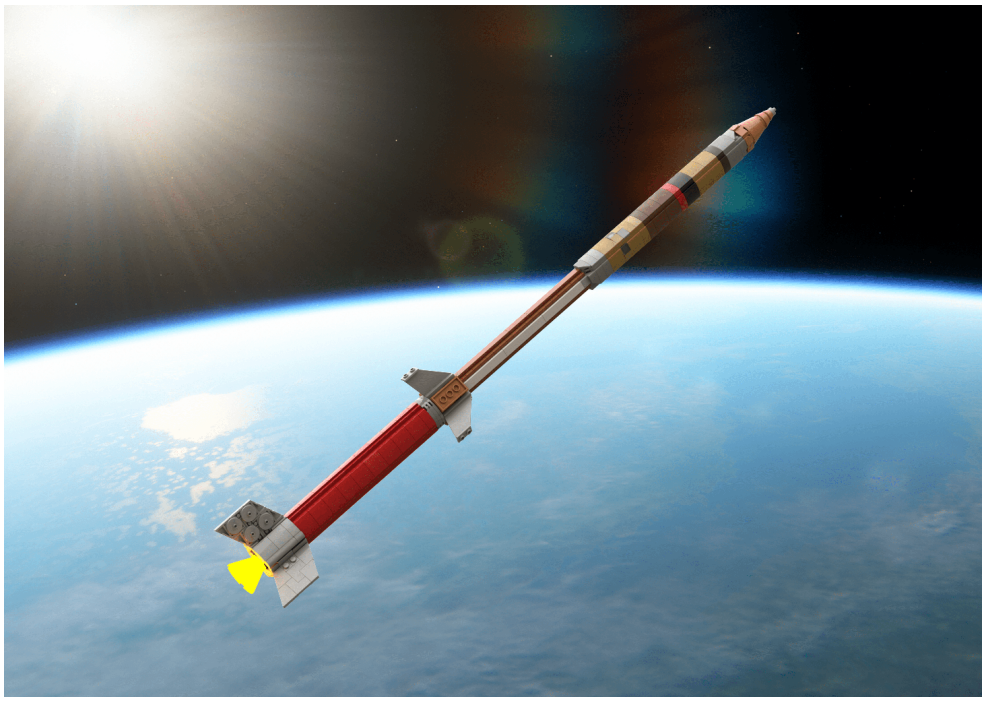

4.1 Influence of solid state ligand exchange on perovskite nanocrystals

T. Baier, M. Schwartzkopf[1], P. Müller-Buschbaum

[1] DESY, Hamburg, Germany

The global energy demand has been steadily increasing in recent years, a trend expected to persist. Therefore, harnessing solar energy through photovoltaic technologies is becoming increasingly important. Perovskite nanocrystals have emerged as a promising active layer material in perovskite solar cells (PSCs) due to their tunable bandgap properties facilitated by quantum confinement effects, potential for multi-exciton generation, and compatibility with various solution-based deposition techniques, such as spin-coating and slot-die coating. These attributes contribute to the enhanced power conversion efficiency of PSCs. Notably, the current record for solar cells utilizing perovskite nanocrystals as the active material demonstrates a power conversion efficiency of 17.4%, comparable to that of conventional solar cells. [1]
One reason for perovskite being used as active material within the PSC is the great advantage of being a group of materials having the ABX_3 structure. Therefore, the bandgap of the final layer can be tuned by exchanging the atoms but keeping the structure. By reducing the size of the bulk perovskite crystals to a region below the Bohr radius, which is for $FAPbI_3$ roughly $r_B \approx 5\,\mathrm{nm}$ [2], the quantum confinement regime is reached and the crystals are called perovskite quantum dots (PQD) or above that regime perovskite nanocrystals (PNc). Because of that, they have no longer continuous conduction and valence bands; they are quantized, and therefore, multiple exciton generation is enabled. So-called ligands ensure that the crystals are kept within their size.
Within this work, perovskite nanocrystals are synthesized using the in reference [3] described hot-injection method to obtain cesium-formamidinium lead iodide perovskite nanocrystals ($FAPbI_3$). These nanocrystals are deposited onto an indium tin oxide (ITO) substrate using the large scalable slot-die coating method. Slot-die coating is chosen because there are further advantages as it is material efficient and compatible with solution-based precursors, which leads to cheap and light final layers.
As the perovskite nanocrystal layers have a rather small thickness after one deposition, there are several deposition steps necessary to ensure a sufficient thickness and absorbance for solar cells. It is of great importance to understand the influence of the amount of depositions steps onto the crystallinity of the final films. Therefore, grazing-incidence wide-angle scattering (GIWAXS) measurements are done to observe the crystal structure of the thin film, as can be seen in Fig. 4.1.
To analyze the 2D GIWAXS data, a so-called cake-cut is performed, which means that the intensity is integrated azimuthically, as visualized in Fig. 4.1a). The obtained line data is called pseudo-X-ray diffraction (p-XRD), which is shown in Fig. 4.2a). Here can be seen that the $FAPbI_3$ is mainly within the δ-phase, which is unfortunately photoinactive. The lead iodide (PbI_2) and the ITO are in the trigonal phase.
In Fig. 4.1c) an azimuthal tube-cut at one specific $q-$value is performed to obtain the crystal orientation. For the obtained (100) δ-$FAPbI_3$ peak this is done at $q = 0.8\,\mathrm{Å}^{-1}$. The data shows two intensity peaks, one at $\chi = 0\,^\circ$ (face-on) and one at $\chi \approx \pm 45\,^\circ$ (edge-on). Therefore, a double Gaussian distribution is fit to the data after removing the background. The area underneath the peaks is Lorentz-corrected (sin χ), and the orientation distribution is obtained. This is shown in Fig. 4.2b). The major amount of the crystals is isotropically orientated independently of the number of deposition steps. Similar behavior is observed with the edge-on orientation. The most visible changes are within the share of face-on orientation, which decreases while increasing the deposition number.

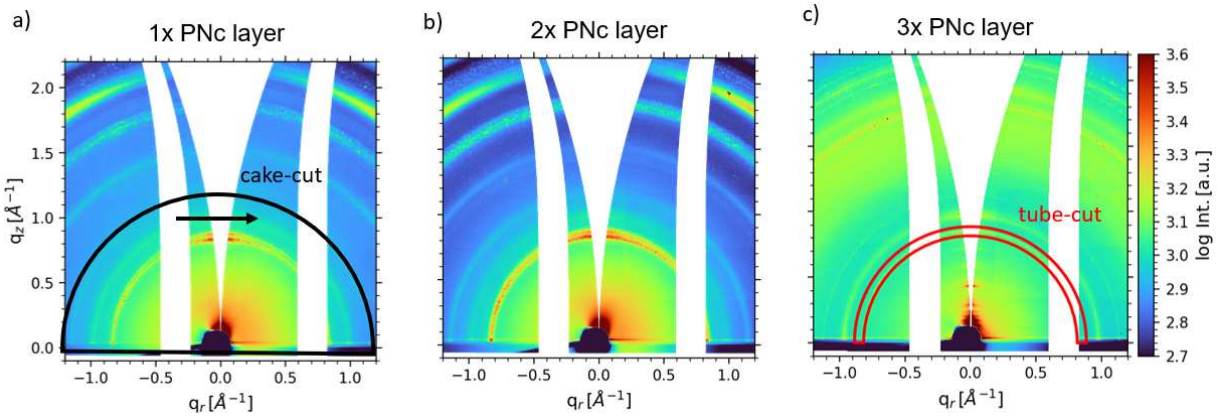

Figure 4.1:
2D GIWAXS data of $FAPbI_3$ perovskite nanocrystals with different number of deposition steps: (a) 1x deposition, b) 2x depositions, c) 3x depositions).

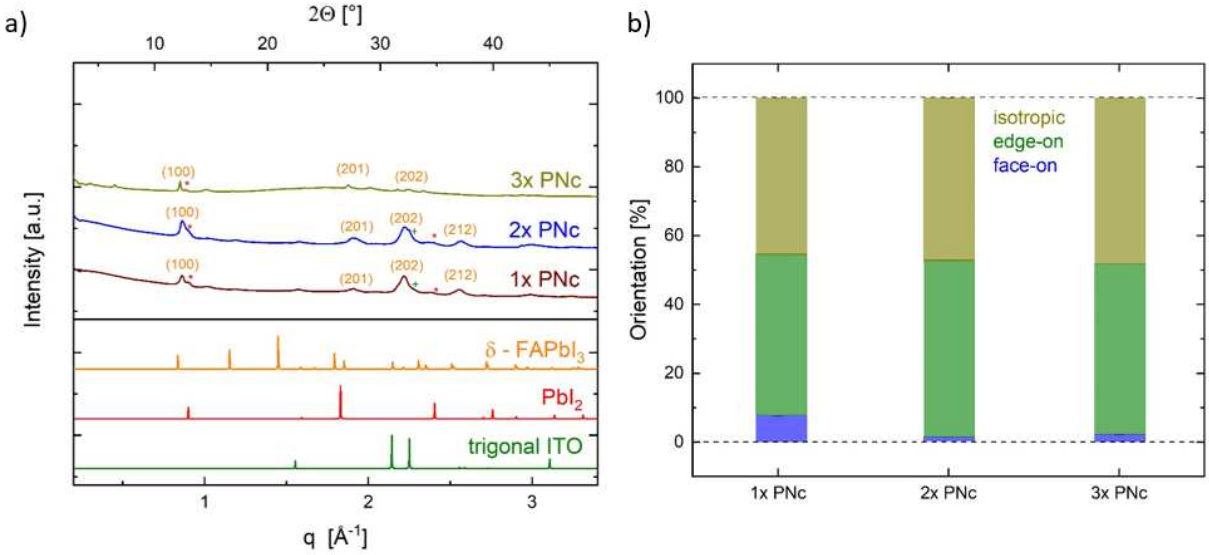

Figure 4.2:
a) Pseudo-XRD data of $FAPbI_3$ nanocrystal films printed with a different number of deposition steps and simulated scattering data of ITO, PbI_2, and δ-$FAPbI_3$. b) Percentage of face-on, edge-on, and isotropic orientated $FAPbI_3$ perovskite nanocrystals with a different number of deposition steps.

Further investigations address the crystallization behavior of perovskite nanocrystal layers and its difference between printing on a pure ITO substrate instead of already redeposited PNc layers. Differences can be expected due to the different surface roughnesses of both films as well as different surface energies.

[1] Q. Zhao, A. Hazarika, X. Chen, S. P. Harvey, B. W. Larson, G. R. Teeter, J. Liu, T. Song, C. Xiao, L. Shaw, M. Zhang, G. Li, M. C. Beard, J. M. Luther, *Nat. Commun.* **10**, 2842 (2019)

[2] K. Galkowski, A. Mitioglu, A. Miyata, P. Plochoka, O. Portugall, G. E. Eperon, J. T. W. Wang, T. Stergiopoulos, S. D. Stranks, H. J. Snaith, *Energy Environ. Sci.* **9**, 962-970 (2016)

[3] Q. A. Akkerman, L. Martínez-Sarti, L. Goldoni, M. Imran, D. Baranov, H. J. Bolink, F. Palazon, L. Manna, *Chem. Mater.* **30**, 6915-6921 (2018)

4.2 Pre-aggregation engineering for morphology optimization in organic solar cells

T. M. Bohnen, J. Zhang, P. Müller-Buschbaum

Organic solar cells (OSCs) have created strong interest in the green sustainable research area due to their potential regarding light weight and flexibility [1]. In the active layer, the electrons in the valence band are excited to form electron-hole pairs, so-called exitons. For classical solar cells like silicon, the dielectric constant is high enough to allow for a spontaneous exciton dissociation at room temperature. The organic materials used in OSCs typically have a much lower dielectric constant resulting in a stronger Coulomb bonding of hole and electron. These exitons can only dissociate if they diffuse to a donor-acceptor interface, otherwise they recombine. Hence, the inner interface in an active layer is crucial for the charge generation, which determines the final performance of OSCs. Bulk heterojunctions (BHJ), a mixing of donor and acceptor molecules at the nanoscale, can increase the number of donor-acceptor interfaces. Yet too many interfaces can break the continuity of donor and acceptor phases which will hinder the charge carrier transport. Morphology optimization is a key strategy for finding a balance between the interface and the transport network. This results in an optimization of the device performance and stability. Due to the solution-processing method, the selection of solvents for precursor solutions is crucial, as it directly affects the morphology of the active layer. Recent research demonstrates that donor and acceptor molecules form aggregates of varying sizes already in the precursor solutions, subsequently inducing different phase separation structures, domain developments, and crystallization behaviors during the drying process [2].
Here, the used materials are BTP-4F-24 acting as the non-fullerene small molecule acceptor and PBDB-TF-TTz as the donor. Their respective structural formulas are shown in Fig. 4.3 (a) and (b).

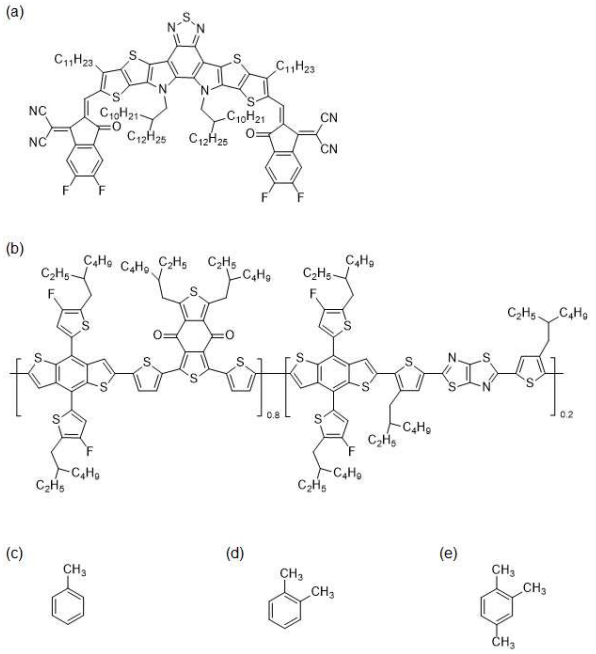

Figure 4.3:
Structural formulas of (a) BTP-4F-24, (b) PBDB-TF-TTz, (c) toluene, (d) o-xylene, and (e) 1,2,4-trimethylbenzene

We use toluene, o-xylene, and 1,2,4-trimethylbenzene as solvents for the precursor solutions for the active layer fabrication. Their respective structural formulas are shown in Fig. 4.3 (c) - (e).

These solvents are chosen due to their similar structure featuring an aromatic benzene ring, differentiated by the number and positioning of attached methyl groups. This structural similarity provides a controlled basis for investigating how slight variations in molecular structure of the solvent influence the film-forming process and the resulting film morphology.
Initial resulting films fabricated by spin-coating are shown in Fig. 4.4 with the films using toluene in the left column, o-xylene in the middle column, and 1,2,4-trimethylbenzene in the right column. All spin-coating processes are performed at room temperature to ensure consistent processing conditions across the different solvents. The films produced by using toluene and 1,2,4-trimethylbenzene show many streak-like defects. This suggests poor solubility at room temperature in these solutions. The films produced using o-xylene have a more uniform morphology, suggesting that o-xylene is a good solvent at room temperature. Further inquiries at different temperatures are needed to determine the solubility behavior for the used polymers in different temperature regimes. In future work, the pre-aggregation behavior in precursor solution will be probed by small-angle X-ray scattering (SAXS), while the final morphology will be investigated via atomic force microscopy (AFM), grazing incidence small- and wide-angle X-ray scattering (GISAXS and GIWAXS).

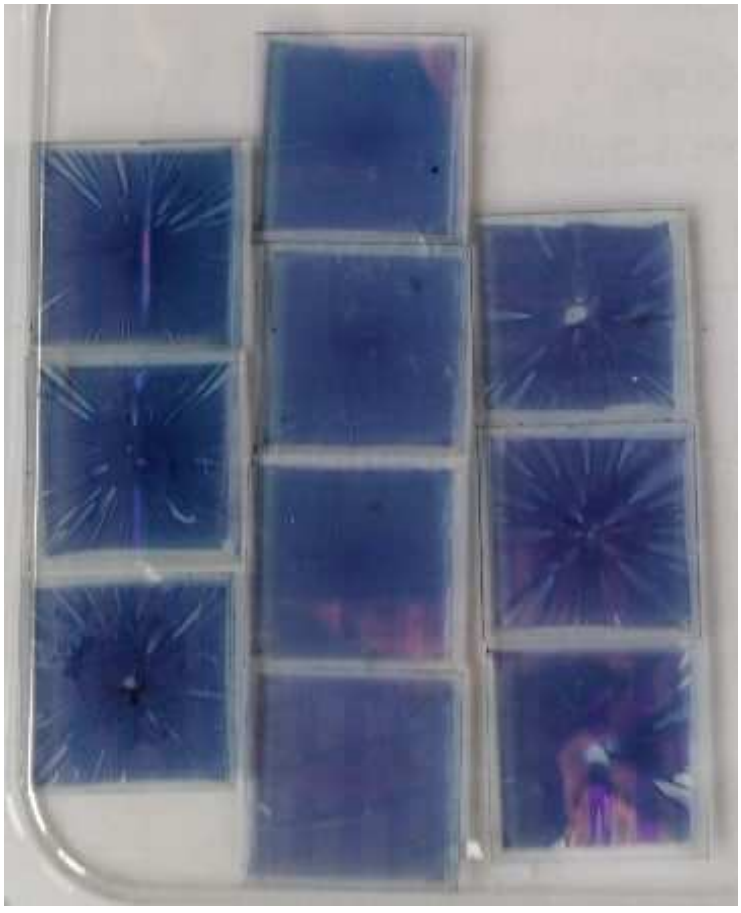

Figure 4.4:
Spin-coated BHJ films made with toluene, o-xylene, and 1,2,4-trimethylbenzene (left column to right column)

[1] C. An, J. Hou, *Acc. Mater. Res.* **3**, 540-551 (2022)

[2] M. Gao, C. Sun, Y. Li, N. Li, H. Jiang, C. He, Y. Chen, W. Zhao, J. Hou, L. Ye, *Adv. Mater.* **36**, 10795-10804 (2024)

4.3 $CsPbBr_3$ nanocrystal seeds for improved perovskite thin film morphology

A. Buyan-Arivjikh, M. Schwartzkopf[1], S. L. Vayalil[1,2], P. Müller-Buschbaum

[1] DESY, Hamburg, Germany

[2] UPES, Dehradun, India

Organic-inorganic halide perovskites have gained significant interest in the scientific community owing to their favorable optoelectronic properties combined with their ease of production and abundance of raw materials [1]. The combination of the aforementioned factors makes the class of hybrid halide perovskites attractive for low-cost manufacturing of optoelectronic devices such as lasers, photodetectors, and solar cells [1]. Most fabrication methods for perovskite thin films are based on laboratory-scale techniques such as spin coating or drop- casting. For real-world applications, low-cost, scalable coating methods are required [2]. Amongst the various large-scale fabrication methods, the slot-die coating technique is a promising way as it offers a stable coating window with tuneable thin film thicknesses via adapting the respective printing parameters. Key factors for the performance of a perovskite- based device are the respective thin film's crystallinity and microstructure, which is affected by the thin film's processing conditions; specifically the nucleation & growth behavior in these fast crystallizing systems. In this context, we utilized $CsPbBr_3$ nanocrystals as seed crystals for more tuneable growth behavior by reducing the number of spontaneous nucleation sites. To investigate the seeding effect on the thin film during- and after growth, we built an in-situ optical spectroscopy set-up able to switch from transmission mode UV-vis- to photoluminescence (PL) spectroscopy mode and vice versa. The synthesized $CsPbBr_3$ nanocrystals are cubic in shape as shown in the SEM measurement (Fig. 4.5 a) and exhibit a PL emission close to 2.4 eV with a full width at half maximum (FWHM) of 70 meV (Fig. 4.5 b).

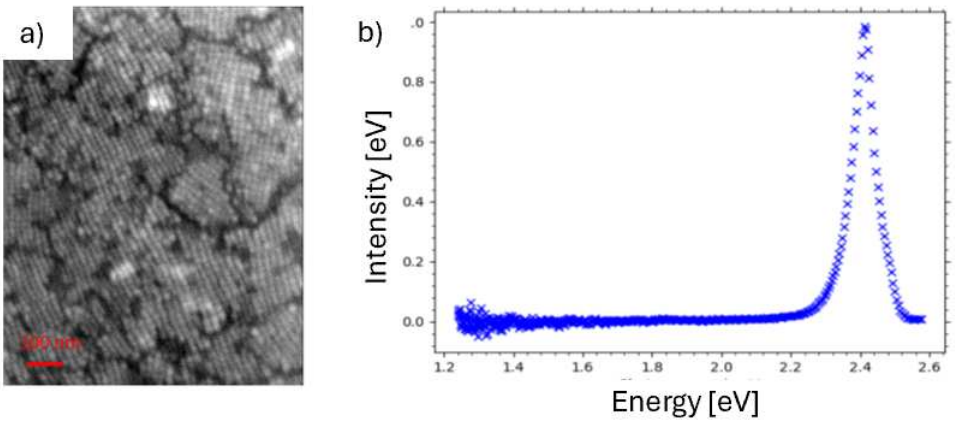

Figure 4.5:
a) SEM image of the perovskite nanocrystal thin film. b) PL measurement of $CsPbBr_3$ nanocrystals on substrate

In-situ transmission mode UV-vis spectroscopy measurements while coating the main perovskite solution reveal superior absorbance of the seeded perovskite thin film in comparison to the seed-free control film. Furthermore, the perovskite's phase transition from intermediate phase to photoactive phase occurs in a faster manner for the seed crystal mediated thin film (Fig. 4.6). An increase in the absorption should reflect in superior photovoltaic properties for seed crystal- mediated thin films, which we attribute to a superior active layer morphology. In addition to in-situ UV-vis measurements, in-situ PL spectroscopy reveals the photoactive phase growth pathways for the seeded thin film (Fig. 4.7 a) and highlights the different growth

mechanisms compared to a seed crystal-free thin film (Fig. 4.7 b). Specifically, the seed crystal mediated thin film exhibits a second PL emission larger than 1.7 eV in the early stages of film growth. The second peak gradually diffuses into the main perovskite PL peak around 1.6 eV. We attribute the second, high energy PL peak to the $CsPbBr_3$ seed crystals that have red-shifted from 2.4 eV to 1.6 eV throughout the thin film growth process as the seed crystal surrounding medium is a perovskite solution that is rich in iodide. Hence, the bromide rich perovskite crystals will increase their iodide content, which is accompanied by a red-shift in the respective PL emission.

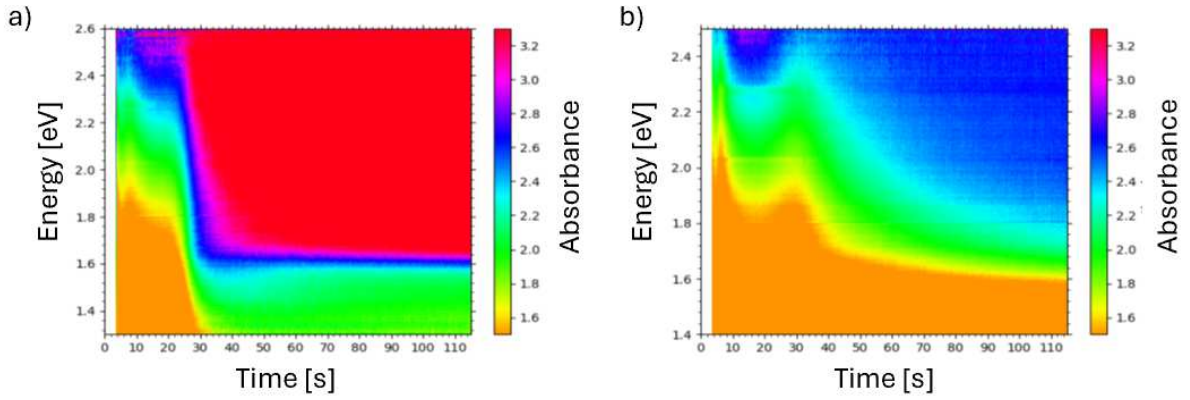

Figure 4.6:
Transmission mode in-situ UV-vis spectroscopy measurement of a seed crystal mediated perovskite thin film a) and a control film without seed crystals b).

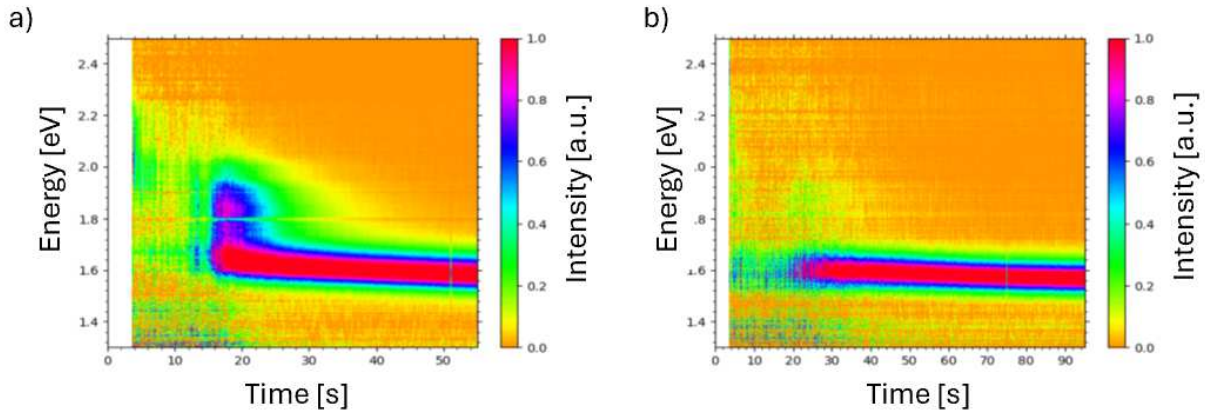

Figure 4.7:
Normalized in-situ PL spectroscopy measurement for a seed crystal mediated thin film a) and a control film without seed crystals b).

[1] CY. Lin, SS. Li, JW. Chang, HC. Chia, YY. Hsiao, CJ. Su, BJ. Lian, CY. Wen, SK. Huang, WR. Wu, DY. Wang, AC. Su, CW. Chen, US. Jeng, *Adv. Funct. Mater.* **29**, 1902582 (2019)

[2] N. Xiuxiu, L. Nengxu, C. Qi, Z. Huanping, *Adv. Energy Sustainability Res.*, **2.2**, 2000046, (2021)

4.4 Revealing the effect of solvent vapor annealing on the morphology of non-fullerene organic solar cells

L. Chu, J. Zhang, P. Müller-Buschbaum

Morphology optimization has been a highly effective strategy to improve the performance of organic solar cells (OSCs) via enhancing charge generation and transport [1]. Among the various methods for optimizing the morphology, solvent vapor annealing (SVA) is a post-deposition treatment used to modify the morphology of thin films, particularly organic solar cells with non-fullerene small molecules. The basic principle involves exposing a deposited thin film to the vapor of a good solvent for at least one of the components in the film (typically the polymer in a polymer donor: small molecule acceptor system). The diffusion of solvent vapor into the film enables the swelling and rearranging of the components, leading to the altered phase separation structure and crystallinity [2]. The extent of swelling and rearrangement depends on several factors such as the annealing time, the selection of the solvent vapor, among others. However, the kinetic mechanisms about the effect of annealing time and solvent selection on SVA are still unknown to large extent [3]. Herein, PBDB-TF-TTz and BTP-4F-24 are selected as the polymer donor and non-fullerene small molecule acceptor, respectively, which are further dissolved in o-xylene to prepare the precursor solution.

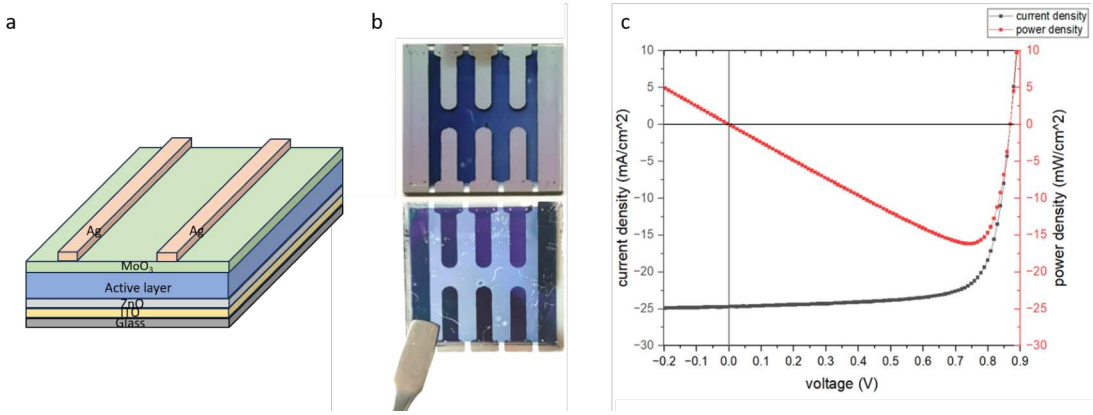

Figure 4.8:
a) Organic solar cells with an inverted device structure of glass/ITO/ZnO/PBDB-TF-TTz:BTP-4F-24/MoO3/Ag as used in the present study. b) Photographs of frontside and backside views of a typical fabricated as-cast device. c) Corresponding J-V curve (red) and output power (blank) of an initial device measured under AM1.5G conditions.

We firstly fabricate the as-cast devices to investigate the feasibility of this combination. Specifically, the ITO-glass substrate is cleaned as the bottom transparent conductive electrode. Next, an hole blocking layer (HBL), ZnO, is deposited to facilitate electron extraction, which is followed by the spin-coated active layer consisting PBDB-TF-TTz and BTP-4F-24. Finally, MoO_3 and silver are sequentially evaporated as the electron blocking layer (EBL) and anode. Fig. 4.8a shows the frontside and backside view of a typical as-cast device. The active layer is uniform and smooth without any obvious aggregations, which is beneficial for the performance. Subsequently, the devices are measured by the solar simulator under AM1.5G irradiation to obtain the corresponding current-voltage (J-V) curves, as exemplarily depicted in Fig. 4.8b. The shape of curve indicates that the device exhibits the ideal characteristics of a pn junction. The short-circuit current density (J_{sc}), representing the ability to generate current when no external load is applied, is approximately 24.7 mA/cm². The open-circuit voltage (V_{oc}) is around 0.85

V, which indicates the excellent ability to generate a potential difference between its terminals. The fill factor (FF) is 75.38% and P_{max} is the maximum output power. Finally, the power conversion efficiency (PCE) reaches 16.16%. Our results demonstrate that this structure of as-cast organic solar cells works well, which can be further used for the investigation on SVA.

In future work, we will focus on the fundamental understanding of the effect of different solvents for the SVA on the morphology and the associated kinetic processes during this treatment. As the schematic diagram (Fig. 4.9) shows, the active layer film is put into the petri dish sealed with a cap, which contains a specifically the solvent vapor atmosphere. To avoid the influence of temperature on the SVA, the petri dish will be constantly kept at 25 °C. Three solvents (cyclohexane, benzene, 2-methyltetrahydrofuran) are selected for the SVA, which have similar boiling points but different solubility parameters. We systemically investigate the impact of the SVA by these three solvents on the morphological properties of non-fullerene OSCs using atomic force microscopy (AFM), as well as grazing incidence small- and wide angle X-ray scattering (GISAXS and GIWAXS). Furthermore, we will also provide real-time insights into the morphological evolution during SVA through in situ UV-Vis absorption spectroscopy and in situ photoluminescence measurements. Finally, we will correlate the solubility parameters and annealing time with phase separation and crystalline characters of active layer and provide the valuable guideline for the optimization of morphology though SVA.

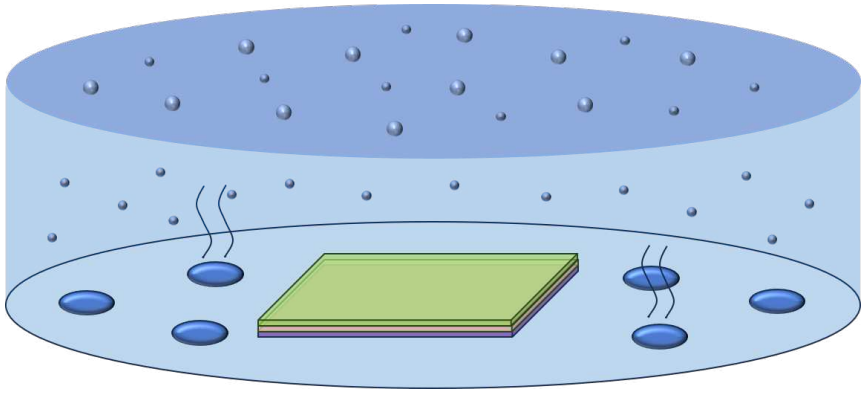

Figure 4.9:
Schematic diagram of the solvent vapor annealing (SVA). The active layer is put in the middle of the petri dish before evaporating MoO_3 and Ag. The solvent with a fixed volume is dropped around the active layer. Finally, the petri dish is sealed with a cap and kept 25 °C for different annealing time.

[1] J. Zhang, K. Jiang, G. Yang, T. Ma, J. Liu, Z. Li, J.Y.L. Lai, W. Ma, H. Yan, *Adv. Energy Mater.* **7**, 1602119 (2017)

[2] C. Jin, B.C. Olsen, E.J. Luber, J.M. Buriak, S. V. Roth, *Chem. Mater.* **29**, 176-188(2017)

[3] Y. Zhang, S. Li, D. Zheng, J. Yu, *Org. Electron.* **15**, 2647-2653(2014)

4.5 Facet-dependent photovoltaic efficiency and stability variations in mixed Sn-Pb perovskite solar cells

X. Ci, P. Müller-Buschbaum

Metal halide perovskite photovoltaic devices, with a certified power conversion efficiency (PCE) of more than 26%, have become one of the most attractive light-harvesting applications. The prevalent facet orientations in perovskite polycrystalline films are (001), (111), and (011). The surface chemical state is directly related to the facet orientation due to the different atomic arrangements and spacings on different facets. The facet-dependent anisotropy of the optoelectronic properties of perovskites has been reported in single-crystal particles, whereas a unified view is still lacking in preferential oriented polycrystalline films. Ma et al. discovered that the optoelectronic properties, such as charge carrier mobility and the dielectric constant, differ significantly across the (001), (111), and (011) facets in polycrystalline perovskite films. Furthermore, different facets exhibit different resistance to moisture-induced degradation. [1] Moreover, in previous reports, preferentially oriented films have been obtained by introducing additives to induce crystallization. It is difficult to exclude the interference of the introduced chemicals in the resulting photovoltaic performance. Besides, most previous pieces of literature use XRD to detect the orientation of the perovskite films, which is limited and cannot detect the specific orientation angles of different crystal planes of perovskite.

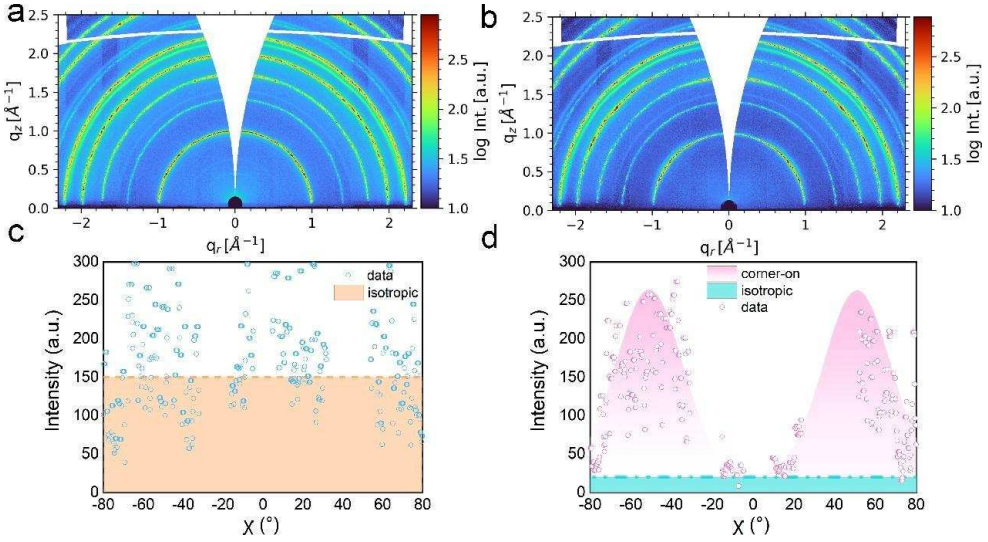

Figure 4.10:
2D GIWAXS data for perovskite films a) without annealing and b) with annealing. Azimuthal tube cuts (points) with fits (lines) of the 2D GIWAXS data of perovskite films c) without annealing (001) and d) with annealing (001).

In this work, we have first successfully tailored two different orientations of perovskite films by a two-step inter-diffusion solution method through delicate component modulation without introducing any additives. Here, we monitor the perovskite structure change by two-dimensional grazing-incidence wide-angle X-ray scattering (GIWAXS) and track the performance evolution of solar cells simultaneously to precisely detect the perovskite film orientation changes in the microscale. Compared with the devices fabricated out of perovskite films without annealing Fig. 4.10a and Fig. 4.10c), the (001) plane of the perovskite films with annealing (Fig. 4.10b and Fig. 4.10d) display a different orientation distribution showing a small isotropic part and two corner-on Gaussian-shaped peaks. This finding means that the samples with annealing show a

higher orientation of the crystallites.

A p-i-n device structure of ITO/PEDOT:PSS/perovskite/PCBM/BCP/Ag is used in this work (Fig. 4.11a). Fig. 4.11b and 4.11c show the PCE for the champion devices without annealing and with annealing, respectively. The without annealing device shows a lower PCE value (18.65%), and the PCE of the annealing device is improved to 19.87%. For further measurements of the stability of solar cells, we track the performance evolution of PSCs under an air atmosphere and one-sun solar illumination (ISOS-L-1I) for 250 min. The normalized photovoltaic parameters are shown in Fig. 4.11d. The device with annealing exhibits lower stability than the device without annealing. The PCE of the devices without annealing remains at 95% of their initial value, while the higher orientation device shows a decrease of 23%. To reveal the perovskite structure evolution, the operando GIWAXS method is used during the device operation at 120 °C temperature for 120 min. To better understand the perovskite crystal structure changes happening during the operando measurement,we further investigate the microstrain evolution by the Williamson-Hall analysis applied to the pseudo-XRD data. During the first 100 min of operation, the microstrain in the perovskite of the sample with annealing is sharply increased (Fig. 4.11e). In contrast, for the without annealing sample, the microstrain in the perovskite only displays a slight fluctuations rather than a sharp increase. Such microstrain relaxation of the active layer is beneficial for slowing down the crystal structure degradation and a related PCE decrease. [2] In conclusion, the perovskite solar cells without annealing display outstanding efficiency and the perovskite solar cells with annealing display excellent stability.

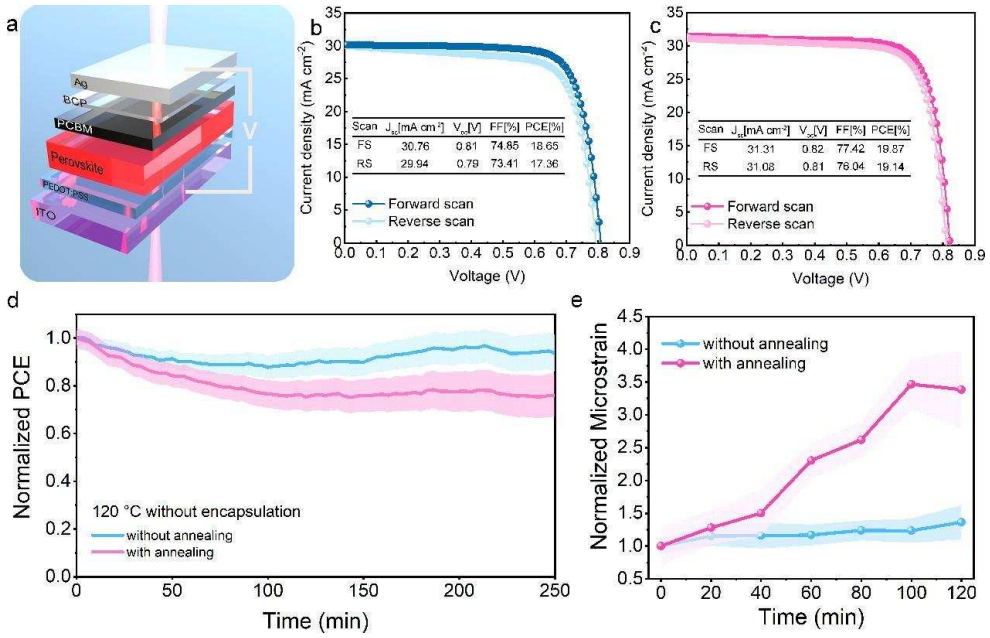

Figure 4.11:
a) Device structure diagrams. J-V curves of the champion device for b) without annealing sample and c) with annealing sample. d) Temporal evolution of PCE e) Device microstrain analysis from Williamson-Hall analysis.

[1] F. Gao, H. Li, B. Jiao, L. Tan, C. Deng, E. Debroye, Y. Peng, Y. Yang, C. Yi, Q. Zhao, *Joule* (2024)

[2] X. Jiang, J. Zeng, K. Sun, Z. Li, Z. Xu, G. Pan, R. Guo, S. Liang, Y. Bulut, B. Sochor, M. Schwartzkopf, K. Reck, T. Strunskus, F. Faupel, S. V. Roth, B. Xu, P. Müller-Buschbaum, *Nano Energy* **132**, 110360 (2024)

4.6 Gas quenching under ambient conditions for efficient and stable perovskite solar cells with surface passivation

Z. Jin, P. Müller-Buschbaum

Perovskite solar cells (PSCs) have emerged as a promising photovoltaic technology due to their remarkable power conversion efficiencies (PCEs) and potential for low-cost fabrication. However, PSCs experience still significant challenges, especially concerning operational stability under ambient conditions, where moisture, oxygen, and thermal stresses can degrade the perovskite structure. To address these issues, innovative processing techniques and surface passivation strategies are essential. The preparation of uniform and pinhole-free perovskite films is crucial for achieving high-performance, large-area PSCs. The processes of nucleation and crystal growth are critical to the film formation. Consequently, the selection of an appropriate quenching technique to induce a supersaturation state plays a vital role in controlling nucleation and crystal growth. Gas quenching is a method using an inert gas flow to facilitate solvent evaporation and induce perovskite precipitation, enabling uniform crystallization and reducing defect density. The controlled formation process of the perovskite layer minimizes undesirable defects that act as non-radiative recombination centers and further enhances the optoelectronic properties. In the experimental preparation process of perovskite films, there are different types of defects appearing in the films. Since the poor film and interface quality can be the main reason of unsatisfying PCE values of devices. It can be a solution to introduce some small molecules as surface passivation to reduce the chemical activity of the perovskite and transport layer interface. Surface passivation plays a pivotal role in stabilizing the perovskite layer by mitigating surface trap states and improving moisture resistance. This approach offers a feasible pathway to overcome the challenges associated with PSC fabrication under ambient conditions, paving the way for their practical application.

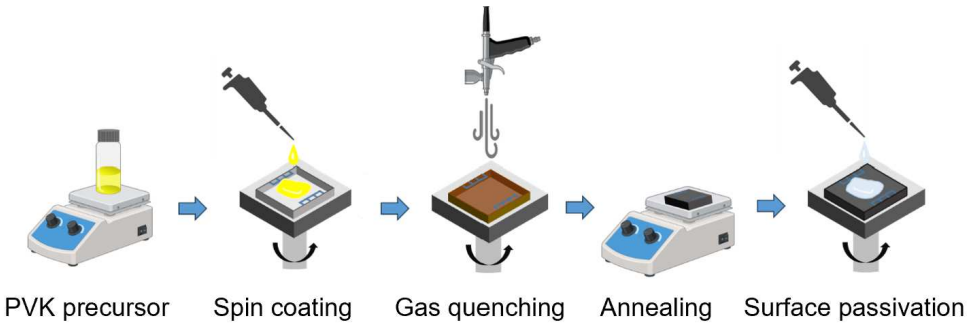

Figure 4.12: Experimental process of perovskite films with surface passivation.

In this study, perovskite layer are fabricated using gas quenching method. In addition, organic amines and their halides: PEAI (phenethyl ammonium iodide), BAI (n-butylammonium iodide) and OAI (n-octylammonium iodide) are used as surface passivation materials to figure out their impacts on defects passivation and performance improvement. The experimental fabrication process of perovskite films with surface passivation is shown in Fig. 4.12

Schematic diagrams of 3D perovskite crystal structure and XRD spectra of perovskite films with/without surface passivation are shown in Fig. 4.13, where strong diffraction peaks of (100) orientation, indicating 3D perovsikte structure, are dominating. After passivation with PEAI, BAI and OAI, the peak position slightly shifts to smaller 2θ values, which indicates that the distance between (100) planes inside the 3D perovskite lattice becomes smaller with passivation. Smaller (100) plane distances can be attributed to the pressure release of 3D perovskite structure

after surface passivation. Besides scattering peaks of the 3D perovskite, there are also intensity peaks appearing at smaller 2θ values, which suggests the presence of a 2D perovskite structure.

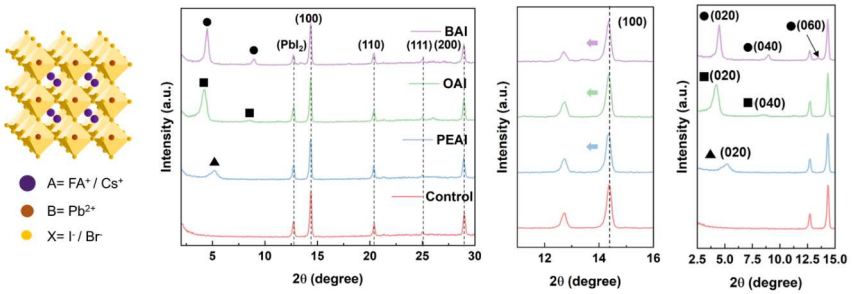

Figure 4.13:
Crystal structure of 3D perovskite and XRD spectrum of perovskite films with/without surface passivation.

From the experimental peak positions obtained in this study, it can be conclusively confirmed that thin 2D perovskite layers of $(PEA)_2PbI_4$, $(BA)_2FAPb_2I_7$, and $(OA)_2PbI_4$ form on the top surface of the underlying 3D perovskite layer. This structural configuration highlights the capability of these 2D layers to act as protective and passivating barriers, which is a desirable feature in enhancing the stability of 3D perovskites. The interlayer distance of the 2D perovskites is determined from the XRD patterns by applying Bragg's Law, as depicted in Fig. 4.14.

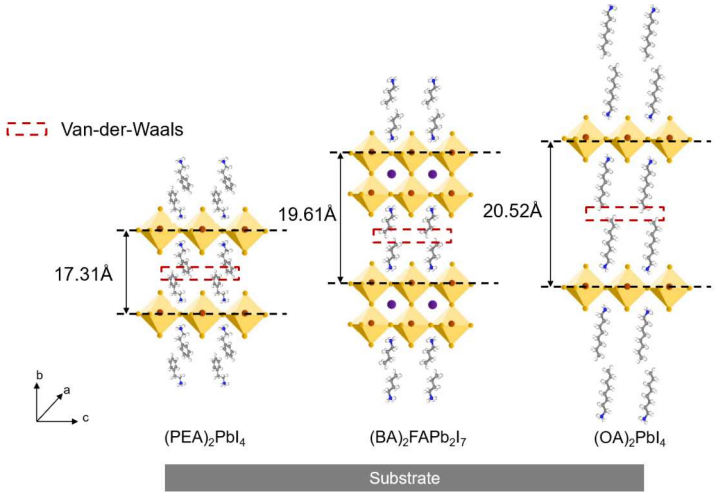

Figure 4.14:
Schematic of crystal structures of $(PEA)_2PbI_4$, $(BA)_2FAPb_2I_7$ and $(OA)_2PbI_4$ showing interlayer distance obtained from XRD patterns.

Among the studied compounds, $(OA)_2PbI_4$ exhibits the largest interlayer distance, which is attributed to long alkyl chain length of the OAI molecules. In contrast, $(PEA)_2PbI_4$ features the shortest interlayer distance, attributed to the comparatively shorter phenethylamine (PEA) molecule. This compact structure may lead to stronger interlayer interactions and distinct optoelectronic behaviors.

[1] G. iu, C. Qiu, B. Tian, X. Pan, D. Ding, Y. Chen, C. Ren, T. He, Y. Shi, C. Su, Y. Li, Y. Gao, D. Fan, *ACS Appl. Electron. Mater.* **1**, 2253-2259 (2024)

4.7 Homogeneous $FACsPbI_3$ for efficient and stable perovskite solar cells prepared via a two-step deposition method

X. Jiang, P. Müller-Buschbaum

Despite the significant advancements in the power conversion efficiency (PCE) of $FAPbI_3$-based perovskite solar cells (PSCs), their commercialization remains hindered by stability issues [1,2]. These challenges arise primarily from the phase transition of the α-phase to the δ-phase under operation. Alloying $FAPbI_3$ with cesium to form FA-Cs perovskite ($FACsPbI_3$) has emerged as a promising approach to enhance both phase and thermal stability [3].

We fabricate perovskite thin films via a sequential deposition method, as shown in Fig. 4.15. The CsMA (CsI + MACl) is used as a Cs source to dope the $FAPbI_3$ perovskite into $FACsPbI_3$ perovskite. In this study, we demonstrate that adding a cesium source to the PbI_2 solution promotes the formation of a structurally stable α-phase in the PbI_2 film. This stabilization reduces cation diffusion but leads to cesium accumulation at the top surface of the perovskite layer, resulting in in-homogeneous perovskite (i-perovskite). To address this issue, we construct a δ-phase into the PbI_2 film by pre-depositing the cesium source prior to PbI_2 deposition. This approach facilitates the uniform vertical distribution of FA and Cs cations, resulting in a homogeneous perovskite (h-perovskite) device.

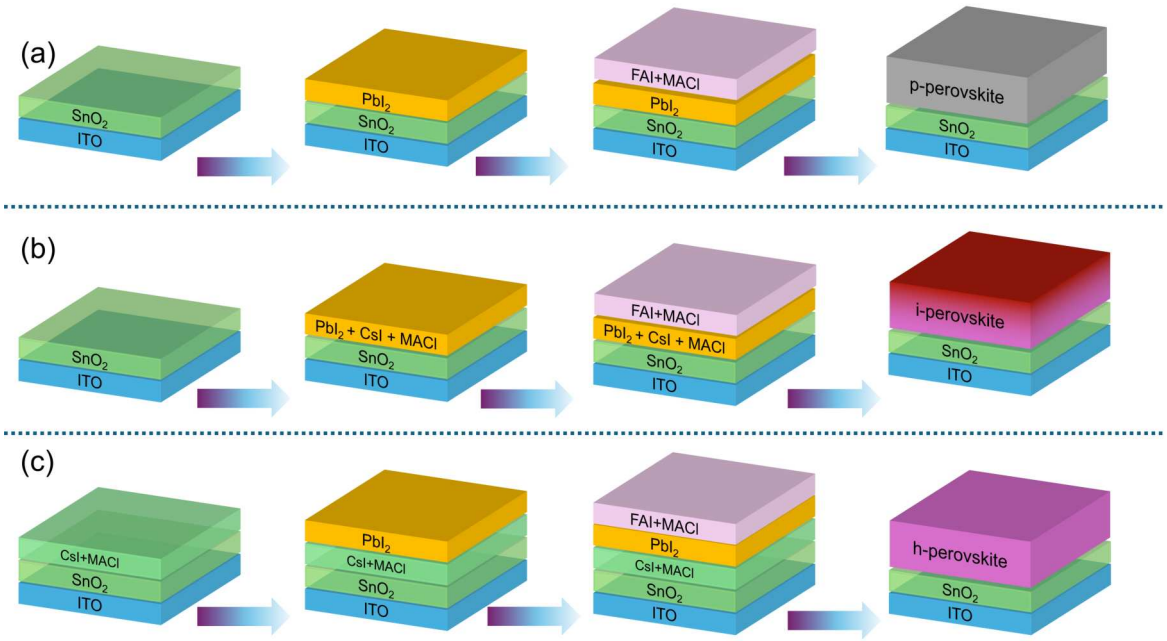

Figure 4.15:
Schematic diagram of sequential deposition of (a) p-perovskite, (b) i-perovskite, and (c) h-perovskite.

To investigate the effect of Cs distribution in $FACsPbI_3$ perovskite on the photovoltaic performance, both i-perovskite and h-perovskite are used in regular planar PSCs. The device structure is ITO/SnO_2/$FACsPbI_3$/Spiro/Au, as shown in Fig. 4.16a. According to the investigation of PCE distribution with different concentrations of CsI: MACl, both the i-perovskite and h-perovskite show the highest PCE at the concentration of CsI: MACl = 10: 1 mg. Thus, this optimized concentration (10: 1) be used for the later investigation of the effect of Cs distribution

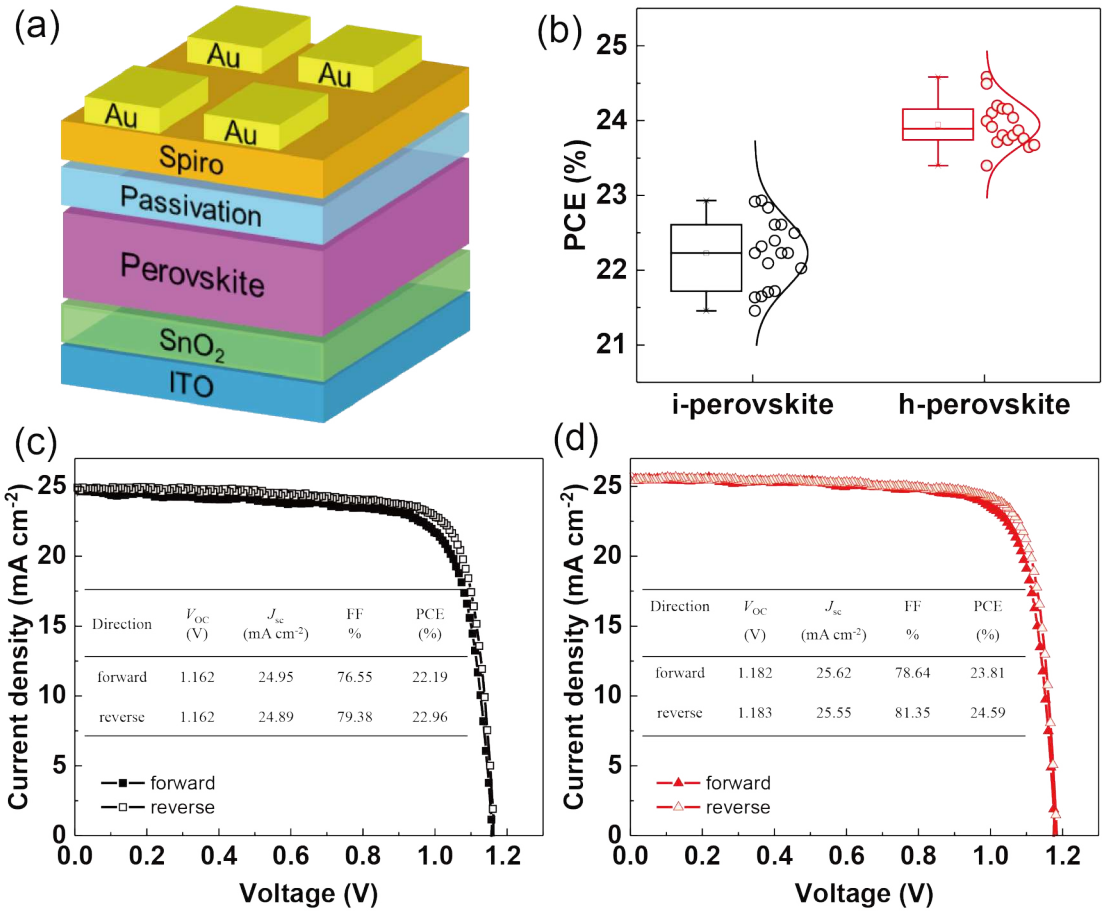

Figure 4.16:
(a) Regular device structure used in this work. (b) PCE distribution of i-perovskite and h-perovskite devices collected from 18 individual solar cells. The J-V curves of (c) i-perovskite champion device and (d) h-perovskite champion device with forward and reverse scans from - 0.2 V to 1.2 V. The insert table is the corresponding photovoltaic parameters.

on perovskite thin film and device. The PCE distribution of i-perovskite and h-perovskite are plotted in a box plot, as shown in Fig. 4.16b. The h-perovskite device exhibits a much higher average PCE and narrower PCE distribution of 23.95% $\pm$ 0.30% than the i-perovskite of 22.23% $\pm$ 0.45%, indicating a higher reproducibility for h-perovskite. To further investigate the effect of Cs distribution on the photovoltaic parameters, the J-V curves of the champion device for both i-perovskite and h-perovskite are shown in Figs. 4.16c and d, respectively. The photovoltaic parameters extracted from the J-V curve are presented in the inserted table. As expected, the h-perovskite exhibits an improved PCE of 24.59% with a V_{OC} of 1.183 V, a J_{SC} of 25.55 mA cm^{-2}, and an FF of 81.35% under reverse scan. Its hysteresis index is 3.17%. In comparison, the i-perovskite shows a slightly higher hysteresis index of 3.35% and a lower PCE of 22.96% with a V_{OC} of 1.162 V, a J_{SC} of 24.89 mA cm^{-2}, and an FF of 79.38%. The higher PCE of h-perovskite than i-perovskite can be attributed to the simultaneous improvement in V_{OC}, J_{SC}, and FF. We achieve a significant improvement in PCE by homogenize the Cs distribution in FACsPbI$_3$ film.

[1] H. Chen, Y. Chen, T. Zhang, X. Liu, X. Wang, Y. Zhao, *Small Structures* **2**, 2000130 (2021)

[2] H.S. Kim, and N.G. Park, *Adv. Energy Mater.*, 2400089 (2024)

[3] W. Li, M. Hao, A. Baktash, L. Wang, J. Etheridge, *Nat. Commun.* **14**, 8523 (2023)

4.8 Temperature-dependent Thermal Behavior of BTP-4F-12 based Organic Solar Cells

Z. Li, M. Schwartzkopf[1], S. K. Vayalil[1,2], P. Müller-Buschbaum

[1] DESY, Hamburg, Germany
[2] UPES, India, Germany

Heat is one key factor contributing to the performance decreases of organic solar cells, which would lead to inevitable morphological changes in the active layers. Common research with ex-situ characterizations hinders comprehensive insights into the underlying thermal degradation mechanisms. In this study, the device thermal stability of BTP-4F-12-based solar cells is investigated with operando tracking to provide a deep understanding of temperature-dependent degradation processes. Fig. 4.17 a) shows the experimental setup illustration. The molecular structures, energy level diagram as well as the UV-vis spectra are shown in Fig. 4.17 b) to d), respectively. PBDBTCl-DTBT and PBDB-TF-T1 are selected as donors to compare the thermal stability. The solar cells are aged in a nitrogen atmosphere to exclude the influence of air or oxygen, ensuring that any observed device performance changes are primarily due to thermal effects. The *J-V* curves of the devices are measured with the temperature increasing from 10 °C to 130 °C. Then, the solar cells are cooled down to 10 °C as a final aged state.

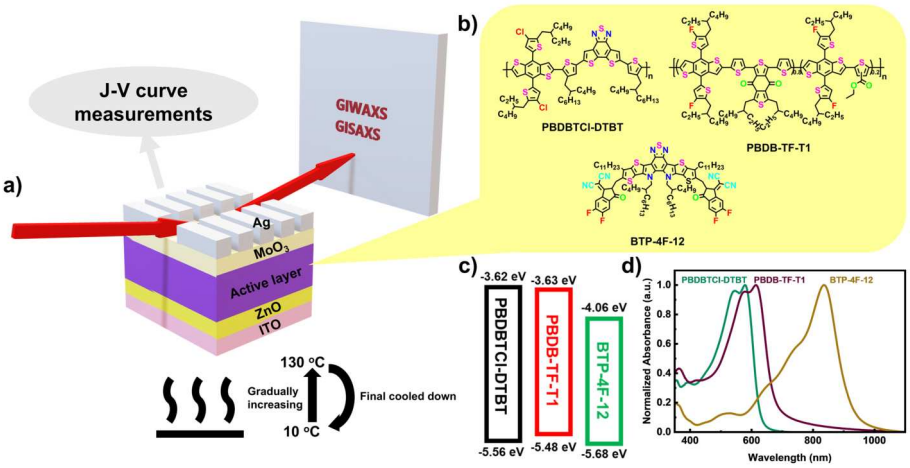

Figure 4.17:
a) Schematic of the operando measurement setup. b) Chemical structures, c) Energy Level diagram and d) UV-vis absorption spectra of the materials utilized in this report

Fig. 4.18 a) and b) shows the *J-V* curves evolution of these two solar cells. Both solar cells exhibit a notable decrease in V_{OC} under elevated temperatures, while the PBDB-TF-T1-based cell maintains stable J_{SC} and FF values compared to the PBDBTCl-DTBT-based solar cell. Furthermore, the solar cells undergo a rapid cooling back to 10 °C to assess their final aged state, with the performance results shown in Fig. 4.18 c) and d). Interestingly, both solar cells show a recovery in V_{OC} upon cooling, suggesting that it is highly linked to temperature-dependent charge carrier recombination or broadening of the density of states (DOS), which are general phenomenon in photovoltaics cells. While the J_{SC} and FF values, however, exhibit slight decreases after cooling. In general, the PBDB-TF-T1-based solar cell exhibits a remarkable thermal stability.

Fig. 4.19 a) and b) illustrate the UV-vis absorbance spectra of active layer films recorded at different temperatures. The data do not show significant changes in shape as reported already

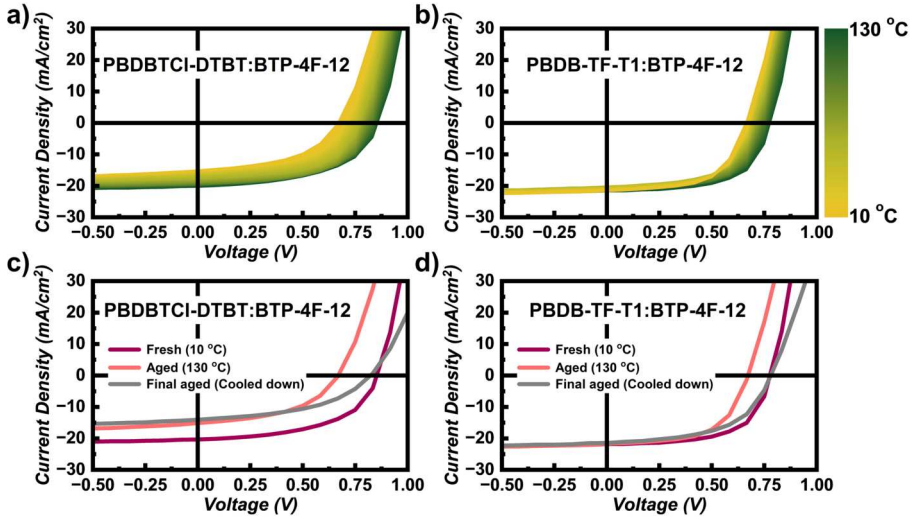

Figure 4.18:
J-V curve evolution of a) PBDBTCl-DTBT:BTP-4F-12 solar cells and b) PBDB-TF-T1:BTP-4F-12 solar cells as the temperature increases from 10 °C to 130 °C. *J-V* curves of c) PBDBTCl-DTBT:BTP-4F-12 solar cells and d) PBDB-TF-T1:BTP-4F-12 solar cells at their fresh, 130 °C, and final aged state.

in the light-induced interfacial degradation study of non-fullerene OSCs, indicating that thermal aging does not cause a chemical decomposition of the materials. In both cases, the 0-0 peak of the polymer donor weakens gradually with increasing aging temperature. Specifically, the PBDBTCl-DTBT-based film exhibits more pronounced changes, which is strongly linked to changes in molecular aggregation.

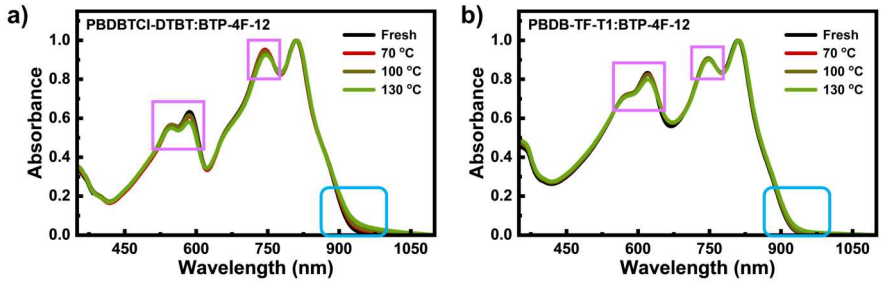

Figure 4.19:
Evolution of UV-vis spectra at different temperatures aging of a) PBDBTCl-DTBT:BTP-4F-12 films and b) PBDB-TF-T1:BTP-4F-12 films.

In summary, the temperature-dependent thermal behavior of PBDBTCl-DTBT:BTP-4F-12 and PBDB-TF-T1:BTP-4F-12 solar cells are investigated in this report, where the loss of V_{OC} under high temperature is reversible, while the loss of J_{SC} couldn't get recovered. PBDB-TF-T1 based cells demonstrate a superior thermal stability compared to PBDBTCl-DTBT cells. The detailed analysis about the evolution of morphological change in the active layer would be illustrated in the future.

[1] L. Duan, A. Uddin, *Adv. Sci.* **7**, 1903259 (2020)

4.9 Investigation of wide-bandgap inverted perovskite solar cells

X. Tian, X. Jiang, P. Müller-Buschbaum

Metal halide perovskite has desirable optoelectronic and mechanical properties such as strong light absorption [1], long charge carrier diffusion length, and versatile processability using solution-based manufacturing techniques and ambient-temperature vapor phase deposition. With the development of perovskite solar cells (PSCs), the power conversion efficiency (PCE) has increased from 3.8% to 26.1% [2], which has attracted widespread research and commercialization attention. In addition to the PCE, the long-term stability of PSCs is also a crucial factor to satisfy industrial requirements for photovoltaic devices. Inverted PSCs with a p-i-n architecture have great potential for application due to their competitive efficiency and stability [3]. Therefore, inverted PSCs are fabricated and investigated in our work.

The planar p-i-n perovskite solar cells are fabricated with the architecture of glass/ITO/2PACz/perovskite/C_{60}/BCP/Ag. The PACz solution is spin-coated at the top of the ITO layer and annealed in an N_2-filled glove box. The perovskite precursor solution is dropped onto the 2PACz coated substrate. Then 200 μL ethyl acetate is slowly dropped onto the film at different time points during spin coating. Then the sample is annealed and further evaporated with C_{60}, BCP, and Ag, sequentially. The theoretical bandgap of $FA_{0.8}Cs_{0.2}PbI_{1.8}Br_{1.2}$ is 1.77 eV. In this work, the crystallographic and optical properties of perovskite thin film are measured with X-ray diffraction (XRD), photoluminescence (PL) spectroscopy, and ultraviolet-visible (UV-Vis) spectroscopy. The dropping time of antisolvent is crucial for the perovskite quality. To investigate the influence of dropping time on the perovskite thin film properties, different dropping time of 15, 17, 20, and 22 s are applied. We measure a series of PL and UV-Vis data based on different time of antisolvent dropping before the end of spin-coating. As we can see from the Fig. 4.20, the PL peak position and the absorption edge of perovskite shift with the dropping time variation, indicating the significant influence of the dropping time on the bandgap of the perovskite. The bandgap is close to the theoretical value of the $FA_{0.8}Cs_{0.2}PbI_{1.8}Br_{1.2}$ perovskite for 20 s dropping time.

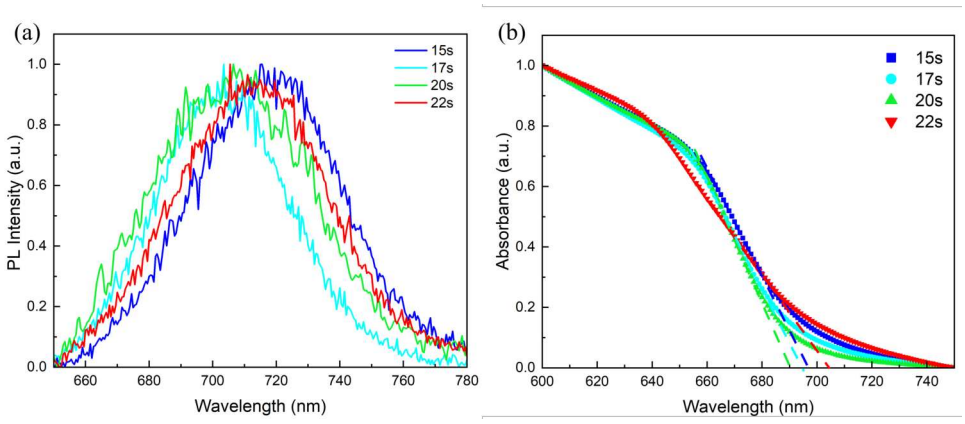

Figure 4.20:
(a) Photoluminescence (PL) spectroscopy and (b) ultraviolet-visible (UV-Vis) spectroscopy of different samples with different antisolvent dropping time before the end of spin-coating.

After the determination of the antisolvent dropping time, which is 20 seconds before the end of the spin-coating, we also measure the corresponding X-ray diffraction (XRD) of the perovskite

film to investigate the crystallographic properties of perovskite films. As we can see from the Fig. 4.21, there are only little PbI_2 residues remaining, and the intensity of (001) peak is much stronger than that corresponding to the δ-phase. The existence of δ-phase inside the perovskite film will cause the low PCE and stability, indicating the dropping time or antisolvent still needed to be optimized to get a pure α-phase perovskite.

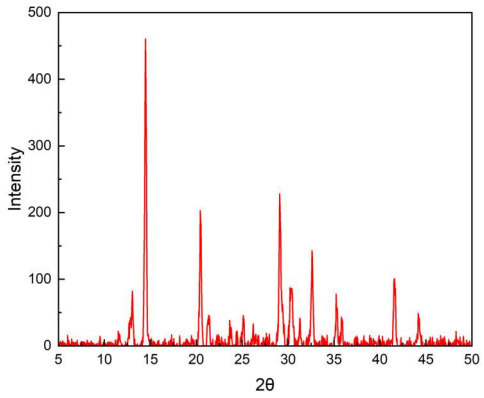

Figure 4.21:
X-ray diffraction (XRD) of the perovskite film with antisolvent dropping at 20 s before the end of spin-coating.

The result of optoelectronic performance test is shown in Fig. 4.22. We measure the J-V curves of the PSCs, with the power conversion efficiency (PCE) 1.18%, fill factor 26.7%, and open circuit voltage 0.89 V. There are many reasons which may cause the low PCE of the PSC. The first reason is concerned about the spin-coating process, which includes the dropping time of antisolvent, the annealing temperature and duration, which result in the existence of δ-phase perovskite. The second reason is the unoptimized thickness of the C_{60} and BCP. In the future, we will optimize the spin-coating process and thicknesses of different layers to realize better optoelectronic performance, which includes PCE, fill factor, operation stability, etc.

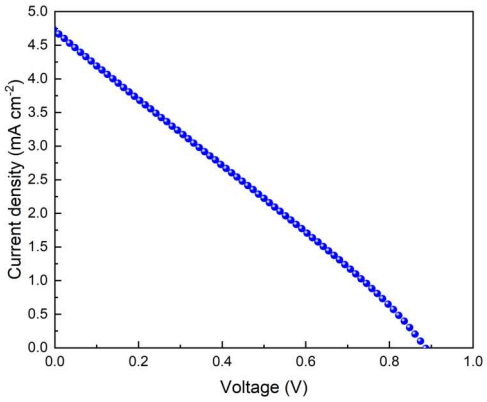

Figure 4.22: J-V curve of the perovskite solar cell.

[1] M. A. Green, A. Ho-Baillie, H. J. Snaith, *Nat. Photonics* **8**, 506 (2014)

[2] X. Shen, B. M. Gallant, P. Holzhey, J. A. Smith, K. A. Elmestekawy, Z. Yuan, etc, *Adv. Mater.* **35**, 2211742 (2023)

[3] W. Zhang, X. Guo, Z. Cui, H. Yuan, Y. Li, W. Li, X. Li, J. Fang, *Rev. Sci. Instrum.* **36**, 2311025 (2024)

4.10 Perovskite solar cell temperature dependence under space-like conditions

A. Vizcaino, M. Pfaller, S. A. Wegener, P. Müller-Buschbaum

Nowadays, satellites and space exploration play a crucial role in human civilization as one field that promotes research and technological development. Without going too far, a clear example of the application of this technology is GPS and telecommunications, which did not exist years ago but are used every day [1]. However, to maintain this infrastructure, it is necessary to supply energy to the satellites, but since they are in orbit, the best way to do so is through solar energy, which is abundant in space.

This is where solar cells emerge as the main energy supply, which needs a photovoltaic material to produce electrical energy through the photoelectric effect. Over the years, efforts have intensified to improve solar cells, especially to harness solar radiation and obtain the greatest amount of electric energy. Si solar cells and gallium arsenide based multi-junction solar cells have been used for many years with big success. These solar cell techniques are mature and well-commercialized. However, the solar modules are very heavy and with the development of novel solar cell technologies also new possibilities arise. Recently, it has been observed that perovskite solar cells have similar properties but with greater potential, due to their strong light absorption, which enables significantly thinner devices and thereby much higher power densities. In addition, perovskites demonstrate a high energy particle irradiance tolerance, can be produced at low temperatures, and are cheaper to synthesize. Therefore, recent investigations have developed around this material as a promising candidate for space applications [2]. Something that should not be forgotten is that there is also strong interest in improving the space technology sector in the low earth orbit (LEO), where most satellites are located. LEO corresponds to an altitude of 1600 km to 2000 km. In this region, equipment will be affected by high radiation, degradation, high vacuum, and fast temperature changes, so our devices must overcome these conditions.

Therefore, this project studies how temperature affects perovskite solar cells (PSC) in a space-like environment, using a setup built in our chair before. It consists of a vacuum chamber connected to a heater to increase temperature, and to a container with liquid nitrogen to achieve lower temperatures. To simulate the sunlight we use an LED. With this setup, it is possible to obtain a vacuum of 1.2×10^{-2} mbar to 1.8×10^{-2} mbar, which provides thermal insulation on the system and allows us to get preliminary results of the solar cells behavior in space [3][4]. Important parameters such as temperature and pressure are controlled by a temperature sensor and pressure indicator located inside the chamber.

As test samples, we synthesize n-i-p and p-i-n solar cells with a layered structure similar to Fig. 4.23a for the case of n-i-p solar cell. Once the manufacturing process was completed, we get solar cells as can be seen in Fig. 4.23b. Then, our solar cells are subjected to temperature cycling in the range of $-100°$C to $100°$C, and at the same time we perform I-V measurements of the n-i-p and p-i-n PSCs
To understand what happens to our solar cells under these conditions it is necessary to analyze important variables such as open-circuit voltage (V_{OC}), short-circuit current (J_{SC}), and fill factor (FF) that indicate how much power is generated. The power conversion efficiency (PCE) indicates how much of the power provided by the light source has been converted to electrical power.

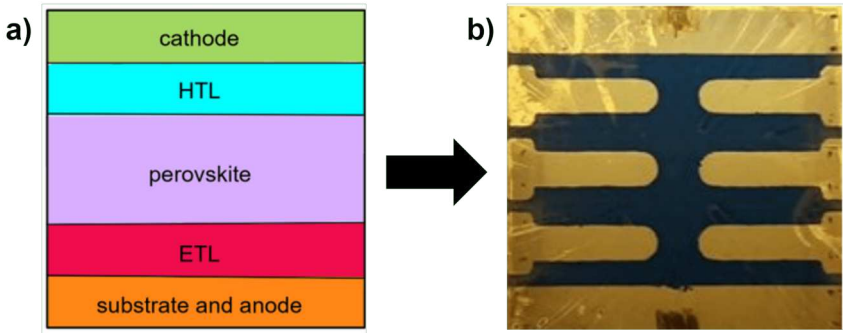

Figure 4.23:
a) a) Typical device architecture for a PSC in n-i-p structure and b) photograph of an example n-i-p PSC fabricated within this project.

From all the tested solar cells in this project, the p-i-n perovskite solar cell is the more efficient one having a PCE value of around 23% as shown in Fig. 4.24 which can be considered good because nowadays the perovskite solar efficiency is typically above 25% in single junction devices [5]. In addition, this configuration shows lower degradation compared with the other tested solar cells.

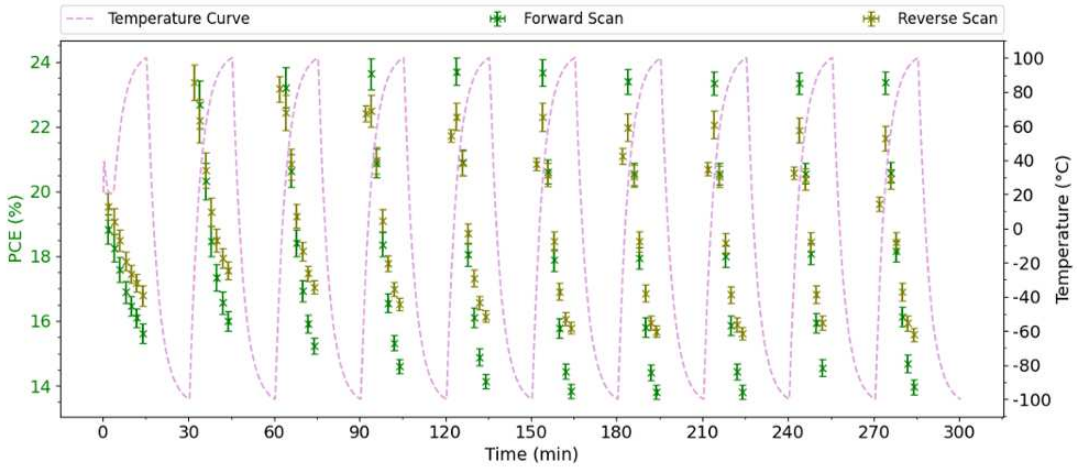

Figure 4.24: Mean of P CE for p-i-n PSC during thermal cycling between $-100°$ C to $100°$ C

To get as close as possible to the space conditions of LEO, which is where most satellites are located, the experiment can be done using an LED light with a spectrum closer to solar spectra. In this direction more work is ongoing.

[1] Z. Shi, A.H. Jayatissa, *Materials* **11**, (2018)

[2] V. Romano, A. Agresti, R. Verduci, G. D'Angelo, *ACS Energy Letters* **7**, 2490-2514 (2022)

[3] T. Patrick *Vacuum* **31**, 351-357 (1981)

[4] J. Yang, Q. Bao, L. Shen, L. Ding *Nano Energy* **76**, (2020)

[5] N.K. Elangovan, R. Kannadasan, B. Beenarani, M.H. Alsharif, M.K Kim, Z. Hasan *Energy Reports* **11**, 1171-1190 (2024)

4.11 Novel Thin-Film Solar Cells on a Rocked Flight

S. A. Wegener, C. Dreißigacker[1], T. Voigtmann[1], P. Müller-Buschbaum

[1] DLR, Oberpfaffenhofen, Germany

Perovskite solar cells representing an emerging class of solar cells that are named according to the crystal structure of their active layer. This perovskite active layer is commonly composed of lead, halides such as iodide, chloride, and bromide, and cation that is represented by cesium or molecules like formamidinium or methylammonium. Together they build the perovskite ABX_3 structure.
The perovskite active layer is what gives the solar cell its unique properties. Due to the direct bandgap the material has a very high optical absorbance, which enables a solar cell thickness of less than one micrometer. The active layer is surrounded by two blocking layers and electrodes. With this structure combined with optimal matched layer properties, perovskite solar cells have already achieved up to 25% efficiency [1]. This is comparable to top state of the art silicon solar cells.
Because of their low thickness and from this resulting superior power to weight ratio these solar cells also gained attention for space applications. Besides, several experiments showed a high tolerance against radiation.

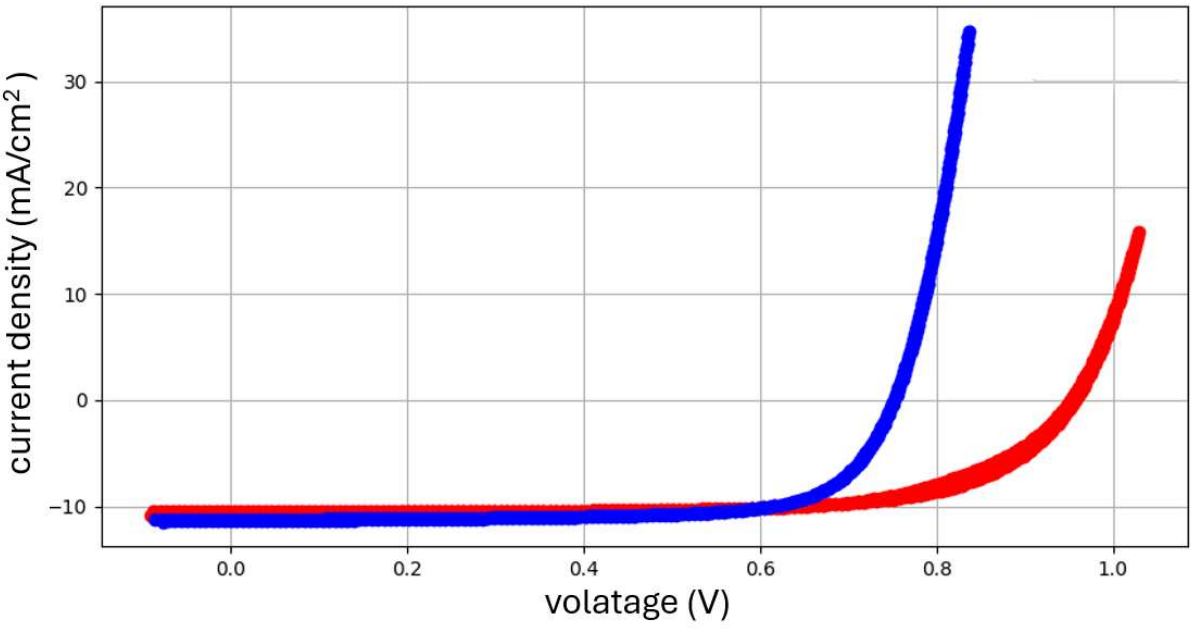

Figure 4.25: I-V-scan of perovskite (red) and organic (blue) solar cell collected during the flight.

In November 2024 we performed in space testing of the mentioned perovskite and also organic solar cells for the third time at our chair [2, 3]. The experiment was done on the MAPHEUS-15 sounding Rocket from German Aerospace Center (DLR). The cells were electrically characterized during the flight that took about 8 minutes and reached an altitude of 308 km. This is already close to a low earth orbit. For the first time, we used four optical spectrometers to measure the absorbance of the solar cells. The full measurement setup was in-house developed at the TUM physics department.

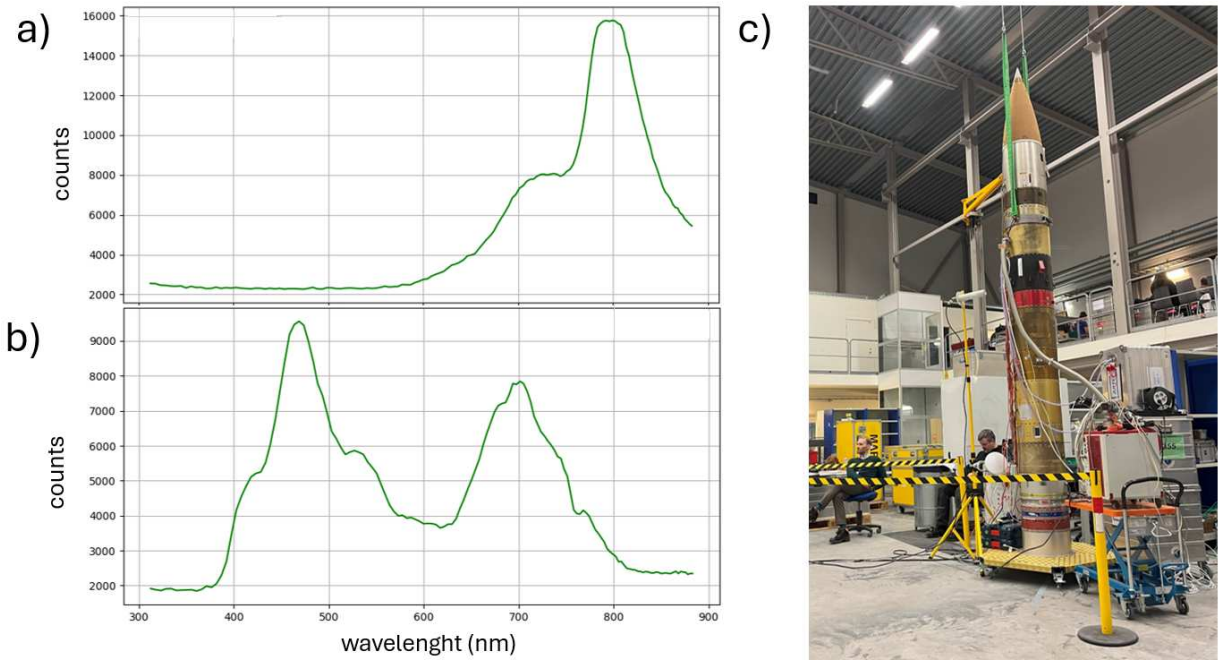

Figure 4.26:
Measuremnets of transmited light through a) perovskite and b) organic Solar cell, c) picture of rocked during communication tests.

The setup consists of eight similar modules that each contain two solar cell samples. Each sample has eight solar cell pixels. So, 128 solar cells were measured overall. Every second module contained a spectrometer. So also, each of the four evaluated solar cell types was characterized by its optical absorbance. To protect the solar cells from aerodynamic pressure during the launch they are mounted behind quartz glass windows. These windows caused some challenges during the first two flights. The high velocity of the rocket in the atmosphere causes the nosecone of the rocket to produce soot, which accumulates at the glass windows. This soot coverage could be significantly reduced due to a new more aerodynamic window design.
Figure 4.25 shows the measured I-V-curves for an organic and a perovskite solar cell measured during the space flight. The perovskite cell shows the higher PCE, which is mainly caused by the higher voltage. Additionally, the measured light spectrum behind the solar cells shows a high absorption of the light with a wavelength lower than 700nm (figure 4.26). The organic solar cell in contrast showed a higher transparence on a broader spectrum with is caused by the different external quantum efficiencies of Perovskite and organic solar cells.
The next steps for the Project will be a full reconstruction of the trajectory of the rocket to calculate the sun inclination angle on the solar cells and a detailed precharacterization of the samples.

[1] J. Jeong, M. Kim, J. Seo, H. Lu, P. Ahlawat, A. Mishra, J. Y. Kim and others, *Nature* **592**, 381-385 (2021).

[2] L. K. Reb, M. Böhmer, B. Predeschly, S. Grott, C. L. Weindl, G. I. Ivandekic, P. Müller-Buschbaum and others, *Joule* **4**, 1880-1892 (2020).

[3] L. K. Reb, M. Böhmer, B. Predeschly, S. Grott, C. Dreißigacker, J. Drescher, P. Müller-Buschbaum and others, *Rev. Sci. Instrum.* **92** (2021).

4.12 p-i-n-type perovskite solar cell for space applications

R. Yang, S. A. Wegener, P. Müller-Buschbaum

Solar cells convert sunlight into electrical energy, making them one of the primary energy sources for space applications. Today, silicon is the most researched material for solar cells. Perovskite solar cells (PSCs) utilize light-absorbing materials with a specific crystal structure, denoted as ABX_3. This structure comprises cubo-octahedral A cations, smaller octahedral B cations, and 12 surrounding X anions. The performance of PSCs has significantly improved over the years, achieving a power conversion efficiency (PCE) of up to 26.0% [1]. PSCs offer a high power-to-weight ratio compared to conventional silicon solar cells, which is a critical advantage for space applications.

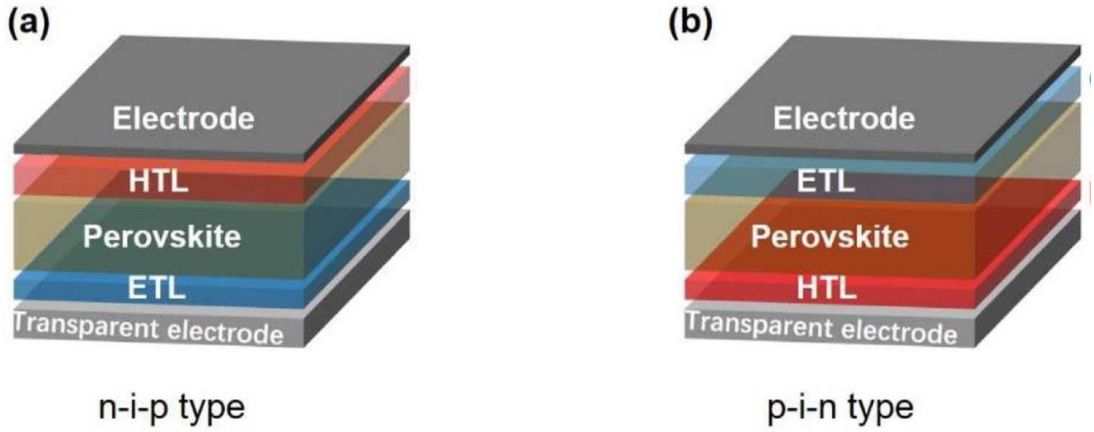

Figure 4.27: Structures of n-i-p and p-i-n-type PSCs. [2]

PSCs can be categorized into two types based on their stacking order: The regular PSC, also known as the negative-intrinsic-positive (n-i-p) type, and the inverted PSC, known as the positive-intrinsic-negative (p-i-n) type. Fig. 4.12 illustrates these two structures. The p-i-n type PSC has advantages such as a long-term stability of the devices. Solar cells in space environment present significant challenges, including radiation exposure, thermal expansion, material degradation, and efficiency losses. Radiation, such as solar cosmic radiation (SCR) and galactic cosmic radiation (GCR), is a critical concern. SCR primarily consists of protons, electrons, α-particles, and ions, while GCR is mainly composed of atomic nuclei. These radiation types interact with magnetic fields in low Earth orbit (LEO), forming complex radiation belts that cause ionization and displacement damage to spacecraft components. Thermal expansion poses another challenge, as varying thermal expansion coefficients between materials induce mechanical stresses, increasing the likelihood of crack formation. Additionally, chemical degradation exacerbates these issues. Changes in material properties, such as increased brittleness and potential phase transitions, further compromise structural stability. The goal of this project is to investigate the performance of p-i-n type PSCs for space applications and to optimize the manufacturing process to address challenges in the space environment.

To evaluate the feasibility of PSCs, batches of samples are fabricated using indium tin oxide (ITO) substrates, PTAA as the hole transport layer (HTL), $FAPbI_3$ as the perovskite absorber, C_{60} as the electron transport layer (ETL), BCP as a buffer layer, and Ag as the electrode. The solar cell assembly is performed inside a glovebox, providing an N_2-rich environment with minimal H_2O and O_2. The ITO-coated glass substrates are pre-cleaned with Hellmanex 1 and 2-propanol in an ultrasonic bath for 15 minutes before spin-coating. The HTL layer is spin-coated onto the

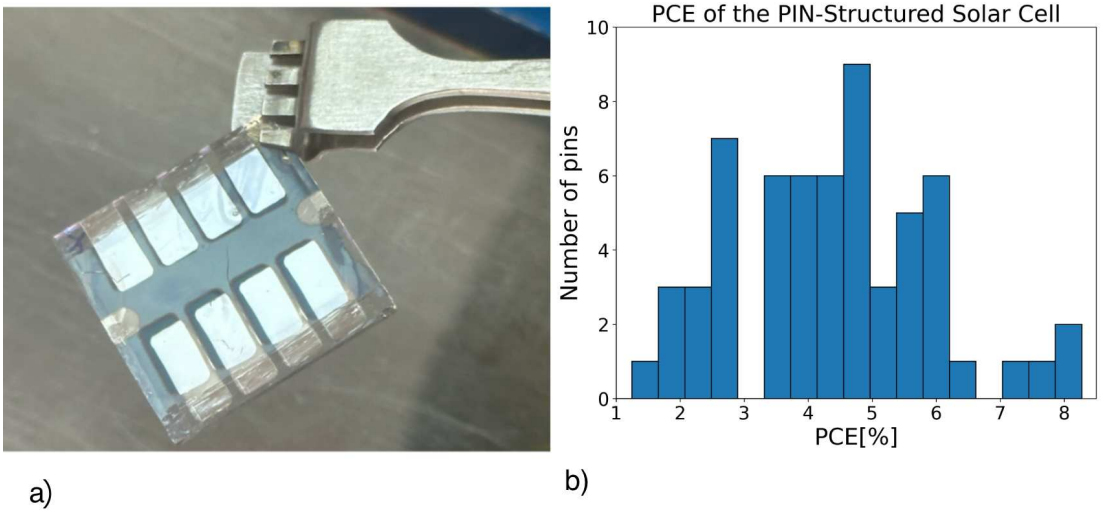

Figure 4.28:
a) Example of a freshly fabricated PSC module comprising eight individual solar cells and b) PCE distribution of PSC samples.

ITO layer after a 10-minute O_2 plasma treatment to enhance its hydrophilicity. Two candidates for the HTL in p-i-n structured PSCs, 2PACz and PTAA, are considered; PTAA is chosen due to its superior compatibility with DMF/DMSO [3]. The selected perovskite material, $FAPbI_3$, has a band gap of 1.41–1.51 eV. The perovskite layer is prepared using the two-step method: PbI_2 and FAI are sequentially spin-coated onto the substrate. The ETL layer and the electrode is thermal evaporated on top of the peorvskite layer, followed by layers in the order of C_{60}, BCP and silver. An example of a freshly fabricated sample is presented in Fig. 4.12.
The fabricated PSCs are tested using a solar simulator at room temperature. Under a simulated light source, the solar cells are scanned with a voltage range of -1.2 V to 0.2 V. Fig. 4.12 displays the PCE results of different PSCs. The solar cells achieve an average PCE of 4.58%, with the best performing cell reaching 8.28%. The fill factor ranged between 13% and 67%, demonstrating the need for further improvements in the device fabrication process. In summary, the results show a great potential for further measurements and to continue optimizing the fabrication techniques of the p-i-n type PSCs. The PSCs with the highest PCE will undergo additional testing in a thermal cycling system to assess its performance and stability under space-like conditions. Further experiments with the one-step perovskite deposition method are also planned.

[1] F. Ma, Y. Zhao, Z. Qu, J. You, *Acc. Mater. Res.* **4**, 716-725 (2023)

[2] H. Zhang, N. Park, *DeCarbon* **3**, 100025 (2024)

[3] Y. Wang, L. Duan, M. Zhang, Z. Hameiri, X. Liu, Y. Bai, X. Hao, *Solar RRL* **6**, 2200234 (2022)

4.13 Revealing the solvent effect on the morphology in printed organic solar cells

J. Zhang, M. Schwartzkopf[1], S. Koyiloth Vayalil[1,2], P. Müller-Buschbaum

[1] DESY, Hamburg, Germany

[2] UPES, Dehradun, India

Organic solar cells (OSCs) have obtained significant attention due to their inherent advantages, including light weight, flexibility, and solution-process capability, among others. Although the power conversion efficiency (PCE) of OSCs has surpassed 20%, morphology optimization remains crucial for further enhancing both performance and stability.[1] Owing to the solution-process method, the choice of processing solvents significantly impacts the final morphology, particularly in printing-based device fabrication, making it essential to understand how different solvents affect phase separation and crystallization in the active layer. Herein, we choose PBDB-TF-TTz and BTP-4F-24 as donor and acceptor due to their superior solubility, using o-xylene (XY) and chlorobenzene (CB) as the processing solvents, respectively.

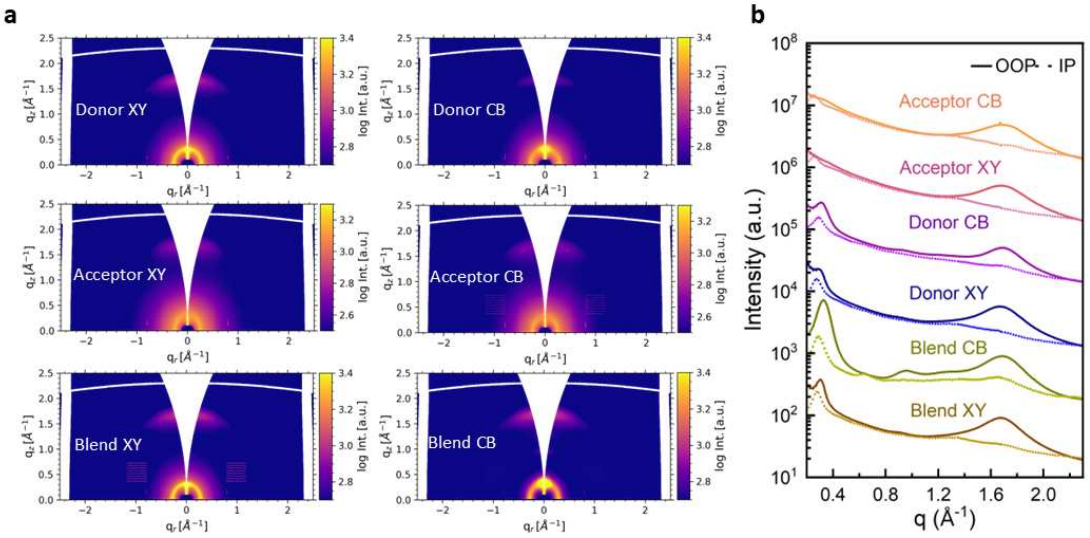

Figure 4.29:
a) Ex situ 2D GIWAXS data, and b) the corresponding radial cake cuts of the blend film, individual PBDB-TF-TTz (donor), and individual BTP-4F-24 (acceptor) with o-xylene or chlorobenzene.

Subsequently, we fabricate the active layer via slot-die coating and perform grazing-incidence wide-angle X-ray scattering (GIWAXS) to investigate solvent effects on the crystalline characteristics.[2] Fig. 4.29a shows the corresponding the 2D GIWAXS data. For PBDB-TF-TTz processed with o-xylene, a more pronounced (010) Bragg peak is seen in the out-of-plane (OOP) direction, indicating predominantly face-on oriented crystallites. This orientation is further supported by the weaker (100) peak in the in-plane (IP) direction. The enhanced π-π stacking and face-on orientation are beneficial for charge transport in the active layer. In contrast, BTP-4F-24 shows minimal differences in their GIWAXS patterns between o-xylene and CB processing, suggesting a limited solvent influence on its crystallization. The scenario for the blend films is the similar with that for the individual PBDB-TF-TTz, which is stronger π-π stacking and predominated face-on orientation. Furthermore, we conduct radial cake cuts on the 2D GIWAXS data of Blend XY and Blend CB in the OOP and IP directions (Fig. 4.29b) and then use Gaussian fit to extract π-π stacking and crystallite size of PBDB-TF-TTz and BTP-4F-24. The results

suggest that o-xylene processing leads to larger crystallite sizes and stronger intensity for PBDB-TF-TTz, while BTP-4F-24 maintain similar crystallite intensity across both solvents. These findings demonstrate that the crystallization behaviors in these systems are dominated by polymer-donor molecules.

To obtain deeper insights into the phase separation, we carry out grazing-incidence small-angle X-ray scattering (GISAXS) for the blend and individual films processed with different solvent (Fig. 4.30a). PBDB-TF-TTz exhibits distinct GISAXS textures between solvents, while BTP-4F-24 shows nearly identical patterns regardless of solvent choice. Additionally, the horizontal line cuts on GISAXS are conducted at the Yoneda peak position (Fig. 4.30b). Subsequently, the corresponding line cuts are fitted by the model including three cylindrical substructures with varying radii based on the effective interface approximation of the distorted-wave Born approximation.[3] The results signify smaller radii for all three structures in donor XY compared to donor CB, while acceptor XY and acceptor CB shows similar domain size. In blend films, CB processing results in larger domains compared to o-Xylene. These GISAXS results align with our GIWAXS findings, confirming that the polymer donor predominantly determines solvent-induced morphology.

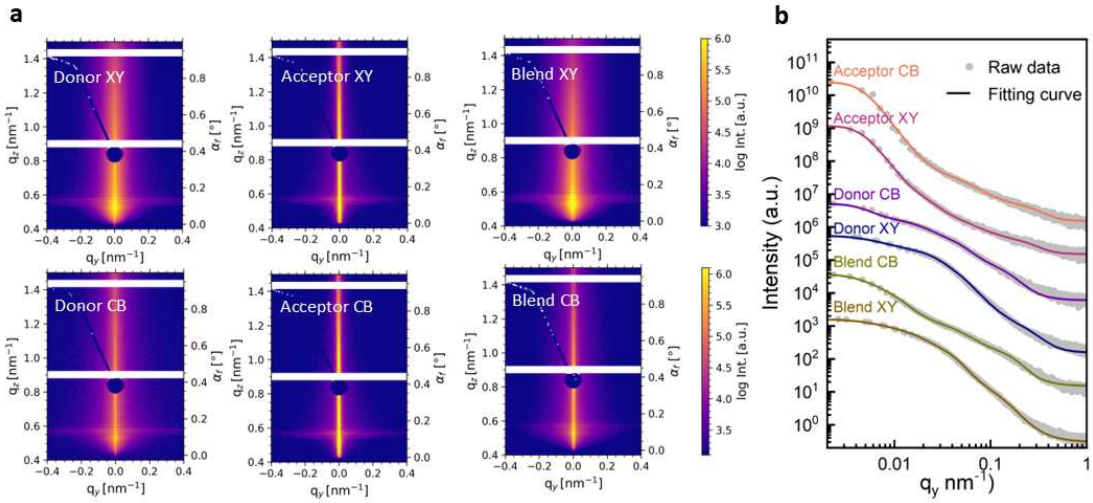

Figure 4.30:
a) Ex situ 2D GISAXS data, and b) the corresponding horizontal line cuts of the 2D GISAXS data of the blend film, individual PBDB-TF-TTz (donor), and individual BTP-4F-24 (acceptor) with o-xylene or chlorobenzene at the Yoneda region.

[1] P. Ding, D. Yang, S. Yang, Z. Ge, *Chem. Soc. Rev.* **53**, 2350 (2024)

[2] C. McDowell, M. Abdelsamie, M. F. Toney, G. C. Bazan, *Adv. Mater.* **30**, 1707114 (2018)

[3] P. Müller-Buschbaum, *Adv. Mater.* **26**, 7692 (2014)

4.14 p-type PbS quantum dot ink realization via modulated solvation

H. Zhong, F. Talib, W. Chen[1], P. Vezzoni[2], P. Müller-Buschbaum

[1] SZTU, Pingshan, China

[2] TUM, Garching, Germany

PbS colloidal quantum dots (CQDs) are promising materials for optoelectronic devices, including lasers, photodetectors, field-effect transistors (FETs) and solar cells, which is predominantly attributed to the tunable bandgap that allows absorption/emission wavelength ranging from near-infrared (NIR) to mid-wavelength infrared (MWIR), and solution processability that enables CQDs film on any substrates for large-scale device fabrication. To aim for the device application, the surface functionalization of CQDs is indispensable. Nowadays, n-type PbS CQDs ink passivated with inorganic halide ionic ligands is widely used to achieve high-performance devices, thanks to the solution ligand exchange (SLX) method, which is based on the Derjaguin, Landau, Verwey, and Overbeek (DLVO) theory. [1,2]

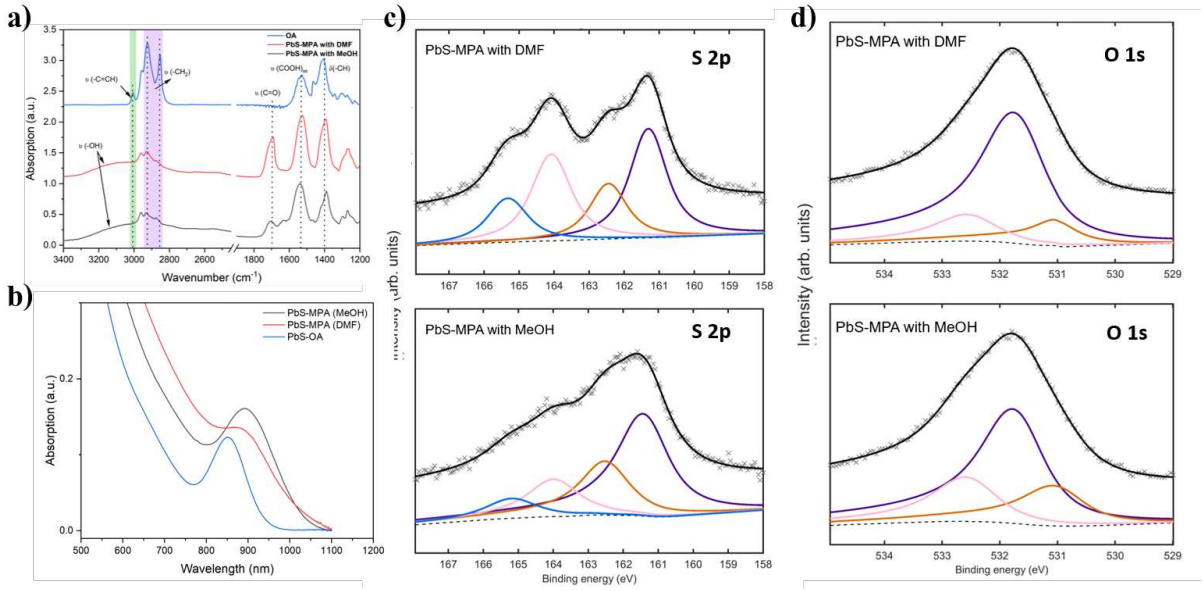

Figure 4.31:
a) UV-Vis spectroscopy and b) FTIR spectra of CQDs solids. XPS c) S 2p and d) O 1s spectra of the CQDs solids.

Compared to n-type ink, there are only a few works focused on p-type CQDs inks. In recent years, 1,2-ethanedithiol capped PbS CQDs (PbS-EDT), prepared with solid-state ligand exchange (SSLE) process via layer-by-layer deposition (LBL), has been the dominant p-type materials for PbS CQDs based optoelectronic devices. Apart from the tedious repetition of LBL steps and cracked films this method caused, SSE impedes the scalable devices fabrication for commercialization. Therefore, a few works have devoted on p-type PbS CQDs ink prepared by liquid-state ligand exchange (LSLE). A doping strategy is used to obtain a p-type ink where the surface of PbS QDs is initially treated with halides and then with cysteamine with thiolate ligands.[3] Another ligand 3-mercaptopropionic acid (MPA), which confers solubility in polar liquids with the carboxylic acid group, has also been a focus for developing PbS QD inks.[4,5] Lately, 2-mercaptoethanol (ME), which can form the robust hydrogen bonding with N,N- dimethylformamide (DMF)/DMSO solvent, is also applied for preparing p-type PbS CQD inks. [6,7]

To obtain the p-type PbS CQDs ink with short-chain molecular thiol ligands, the lack of a stable solvation mechanism in solution hinders the scalable commercialization for PbS CQDs devices. The colloidal stability of CQDs in solution depends on the solvation of surface ligands. In this work, we investigate the solvation behaviour of PbS-MPA p-type CQDs in DMF and methanol (MeOH), which is denoted as CQDs-DMF and CQDs-MeOH, respectively. As is seen in Fig. 4.31, the p-type ink is prepared via LSLE based on the modified methods [4,5]. Noticeably, the ink preparation and film deposition are conducted in the ambient environment. In Fourier-transform infrared (FTIR) spectroscopy (Fig. 4.31a.), the reduction of the CH2 stretching peak confirms the removal of oleic acid ligands, and the emergence of the C=O stretching peak indicates the bonding of the PbS CQDs surface with thiol groups of MPA ligands. In UV-Vis absorption spectroscopy (Fig. 4.31b.), both methods can successfully obtain the p-type CQDs film with pronounced exciton peaks. The more confined and red-shifted peak in the CQDs-MeOH sample indicates a stronger electronic coupling and more monodisperse CQDs compared to the CQDs-DMF sample. Additionally, X-ray photoelectron spectroscopy (XPS) reveals the surface passivation of CQDs. As is seen in Fig. 4.31c, the unbound thiol at 164 eV indicates that MeOH solvent can offer a better surface passivation for the (100) facets in the PbS QDs. Moreover, the lower intensity of the Pb-OH species at 532 eV implies fewer surface defects in the CQDs-MeOH samples (Fig. 4.31d). The device performance of PbS CQDs can be further investigated to connect its relations to the chemical passivation and inner structure.

[1] M.A. Boles, D. Ling, T. Hyeon, D.V. Talapin, *Nat. Mater.* **15**, 364-364 (2016).

[2] M. Liu, O. Voznyy, R. Sabatini, F.P. García de Arquer, R. Munir, A.H. Balawi, E.H. Sargent, *Nat. Mater.* **16**, 258-263 (2017).

[3] M.J. Choi, S.W. Baek, S. Lee, M. Biondi, C. Zheng, P. Todorovic, E.H. Sargent, *Adv. Sci.* **7**, 2000894 (2020).

[4] H. Aqoma, S.Y. Jang, *Energy Environ. Sci.* **11**, 1603–1609 (2018).

[5] F. Ahmed, J.H. Dunlap, P.J. Pellechia, A.B. Greytak, *Chem. Commun.* **57**, 8091–8094 (2021).

[6] C. Wang, Q. Wu, Y. Wang, Z. Wang, H. Li, X. Li, X. Zhang, *Adv. Funct. Mater.* **34**, 2315365 (2024).

[7] M.J. Choi, S.W. Baek, S. Lee, M. Biondi, C. Zheng, P. Todorovic, E.H. Sargent, *Adv. Sci.* **7**, 2000894 (2020).

4.15 Ternary organic solar cells for space application

I. A. Zitzmann, L. V. Spanier, P. Müller-Buschbaum

It has been demonstrated that organic solar cells (OSCs) are capable of achieving high gravimetric power densities, rendering them interesting for space applications where the use of lightweight materials is imperative. However, they still exhibit insufficient long-term stability, and there are few studies on their performance under space-like conditions.
The OSC's photon-absorbing active layer (AL) typically comprises a donor, such as a conjugated polymer, and an acceptor. The ternary strategy involves the incorporation of a third component into the active layer, either a second donor or a second acceptor, with the objective of increasing the OSC's performance, i.e., its power conversion efficiency (PCE) or its stability. It can, for example, increase the range of absorption of ternary organic solar cells (TOSC), optimize its morphology, or lead to suppressed non-radiative energy loss. [1]
In this study, an active layer system with two acceptors is investigated, with PBDB-T-2F (PM6) serving as the conjugated polymer donor and the primary acceptor being the non-fullerene small molecule BTP-eC9. The third component is the fullerene small moleculs acceptor $PC_{71}BM$, which acts as dopant for the acceptor material.
The UV-Vis absorption spectrum of the AL is depicted in Fig. 4.32. This measurement reveals that the AL materials, particularly PBDB-T-2F and BTP-eC9, exhibit complementary absorption spectra in regard to their absorbed photon energies, while the contribution of $PC_{71}BM$ to the overall absorption is expectantly found to be negligible. The slight blue shift of the primary

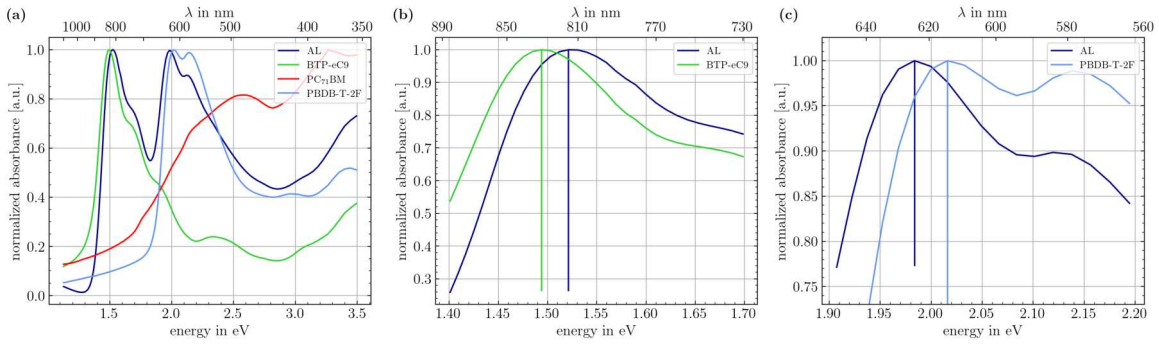

Figure 4.32:
(a) Normalized UV-Vis spectrum of the active layer (navy) and PBDB-T-2F (light-blue), BTP-eC9 (green) and $PC_{71}BM$ (red). (b) Zoomed-in view of the main absorption peak of BTP-eC9, and (c) zommed-in to the PBDB-T-2F maximum.

absorption peaks in the active layer compared to the pure materials can be explained by contributions to the absorption of the other substances and their influence on the intermolecular structure, which might also lead to a shift of the energy bands [2].
In order to simulate space conditions, the TOSCs are characterized with a solar simulator in a nitrogen-filled glovebox with AM0 irradiation. The AM0 spectrum is similar to the one outside Earth's atmosphere, which contains more UV radiation than the usually used AM1.5 spectrum. A systematic investigation was conducted to identify the optimal parameters enhancing the efficiency, including annealing time and temperature, AL-thickness, and the introduction of additives, such as 1,3,5-trichlorobenzene (TCB) and 1,8-diiodooctane (DIO). Selected results, measured with an AM0 spectrum and depicted in Fig. 4.33, reveal that the addition of DIO leads to a reduction in the open circuit voltage (U_{OC}) while concurrently enhancing the fill factor (FF). The TOSCs achieve peak performances in PCE of $13.0\,\%$ under AM0 irradiation, with some demonstrating even higher PCEs of up to $16.4\,\%$ with an AM1.5 spectrum.

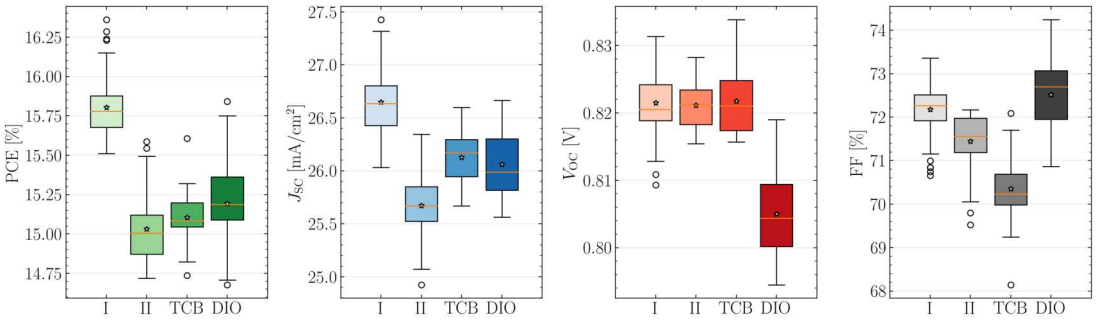

Figure 4.33:
Influence of additives on the photovoltaic parameters (PCE, short-circuit-current I_{SC}, open-circuit-voltage U_{OC} and fill factor FF) measured with an AM1.5 spectrum. The solar cells of I and II contain no additive, the active layers of DIO and TCB contain the respective additive. Star symbols show the average of the distribution, the orange lines show the median.

Notably, time evolution measurements (Fig. 4.34 (a)) suggest an initial increase in performance a few hours after the completion of fresh cells. The FF and, in particular, the U_{OC} improve, resulting in PCEs that are $\approx 19\,\%$ PCEs higher than the initial measurement. Further tests are necessary to investigate this phenomenon.

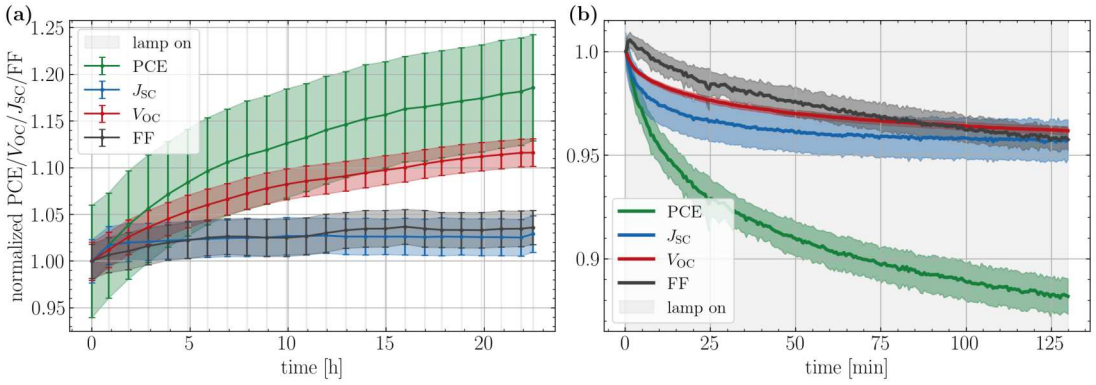

Figure 4.34:
(a) A fresh cell is illuminated approximately every hour and left in the dark in between.
(b) An older cell is measured continuously for 2 hours. The data is normalized to the beginning. Shaded areas show the $1\,\sigma$ statistical error of the measured cells.

The stability of the TOSCs under two hours of continuous illumination is examined in Fig. 4.34 (b), which shows that they retain $87\,\%$ of their initial PCE. All parameters undergo a decrease, with the fill factor contributing the most to the drop in PCE after two hours.
These TOSCs have recently also been successfully operated in space on a suborbital rocket flight, highlighting their potential for space applications in the future.
In subsequent studies, the structure of the AL will be examined using grazing incidence small- and wide-angle X-ray scattering techniques. Furthermore, the stability of TOSCs under thermal cycling will be tested, given the significant temperature variations present in space.

[1] X. Ding, Z. Li, *J. Polym. Sci.* **61**, 3022-3038 (2023)

[2] D. Kroh, F. Eller, K. Schötz, S. Wedler, L. Perdigón-Toro,G. Freychet, Q. Wei, M. Dörr, D. Jones, Y. Zou, E. M. Herzig, D. Neher, A. Köhler, *Adv. Funct. Mater.* **32**, 2205711 (2022)

5 Polymer-hybrid systems

5.1 Biopolymer-templated deposition of hierarchical 3D-structured graphene oxide/gold nanoparticle hybrids for surface-enhanced Raman scattering

Y. Guo[1], P. Müller-Buschbaum, S. V. Roth[1,2]

[1] DESY, Hamburg, Germany
[2] KTH, Stockholm, Sweden

Cellulose has emerged as a promising bio-based template for sensors, smart windows, and bioelectronics [1]. Typically, Surface-Enhanced Raman Scattering (SERS), an advantageous analytical technique, allows for the rapid detection and structural analysis of biological and chemical compounds through their spectral patterns in nanotechnology [2]. Thus far, two main mechanisms of SERS have been identified: electromagnetic enhancement (EM) and chemical enhancement (CM). CM is closely related to charge transfer between the substrate and molecules. EM arises from the amplified electromagnetic field induced by localized surface plasmon resonance (LSPR) around noble metal nanoparticles (NPs). Strong near-field coupling, i.e., hot spots, can occur between two metal NPs and the SERS signal can be improved by increasing the density of hot spots. In this work, we present a route for fabricating cellulose nanofibril (CNF) films loaded with gold nanoparticles (Au NPs) and graphene oxide (GO) to serve as SERS substrates. All layers are fabricated subsequently by layer-by-layer spray-coating followed by annealing. Compared to two-dimensional (2D) SERS substrates, incorporating CNF substrates as three-dimensional (3D) templates ensures a more uniform distribution of Au NPs, and thermal annealing further induces more hotspots by partial sintering. These hybrid 3D structures composed of Au NPs/GO significantly enhance the SERS sensitivity due to the synergistic effects of EM and CM. Therefore, our approach introduces an effective and scalable strategy for fabricating sensitive SERS substrates.

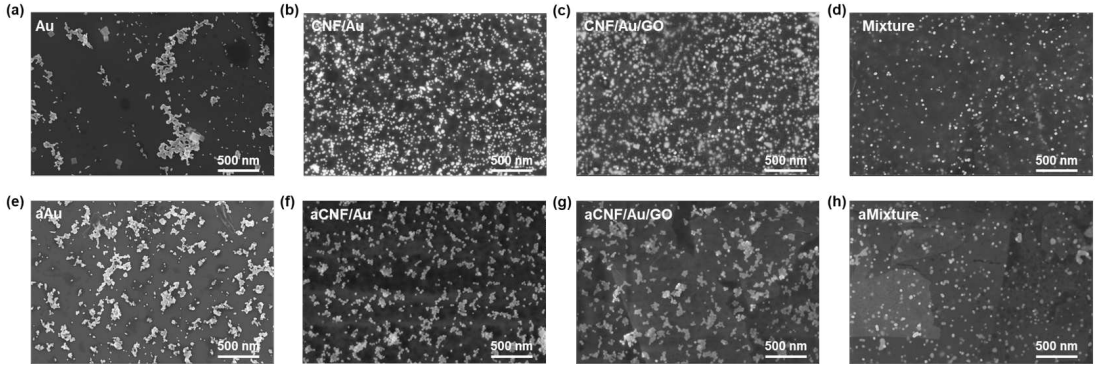

Figure 5.1:
SEM images of pristine Au NP sprayed on silicon and CNF-based thin films: a,e)Au NP on sprayed Si ("Au"); b,f) Au NP on CNF film ("CNF/Au"); c,g) GO and Au NP on CNF film ("CNF(Au/GO"); d,h) mixture of Au NP, GO and CNF on Si ("Mixture"). a-d) show the pristine samples, e-h) those after annealing.

The surface morphology of the pristine, sprayed samples and the corresponding annealed samples is shown in Fig. 5.1. Clearly, the distribution of Au NPs varies across these samples. Specifically, it can be observed that Au NPs directly spray-coated onto silicon wafers lead to a relatively high quantity of aggregates (Fig. 5.1a). In contrast, CNF/Au and CNF/Au/GO samples exhibit a morphology where the Au NPs are homogeneously and densely distributed on the surface of the CNF films (Fig. 5.1b,c). The nano-porous network of CNF could favor a uniform Au NP assembly by sterically inhibiting Au NP agglomeration in the CNF/Au sample.

This suggests that the CNF thin film can serve as a 3D scaffold, enabling a more homogeneous distribution of Au NPs. In the case of the annealed samples, (Fig. 5.1f,g,h), the annealed Au NP sample forms more elongated agglomerates, and the CNF/Au sample undergoes significant morphological changes with Au NPs sintering and forming larger localized aggregates, with sizes ranging from tens to hundreds of nanometers. For the annealed CNF/Au/GO sample, the agglomeration pattern of Au NPs mirrors that of the annealed CNF/Au samples, exhibiting comparable sizes and distributions of Au NPs. The Au NPs sinter and aggregate into localized larger nanoparticles, creating more hotspots in the nanogap, which is beneficial for improving the SERS signal. Additionally, in the sample with the sprayed mixture ("Mixture") and the corresponding annealed samples, there are no such larger localized aggregates, see Fig. 5.1d,h. We relate this to a good interaction between CNF and GO resulting in a more uniform distribution of Au NPs, leading to smaller sizes and distances between particles.

To investigate the SERS performances of our hybrid substrates, Rhodamine 6G (R6G) and Crystal Violet (CV) are chosen as probe molecules. As shown in Fig. 5.2a,b, the main peaks of the vibration modes are in good agreement with the characteristic SERS signals of the pure R6G. It is worth noting that the CNF-based samples exhibit higher SERS intensity than the pure Au sample. For the pristine samples, the CNF/Au/GO sample induces a maximum SERS signal. Notably, after the annealing process, the intensities in the annealed sample are much stronger than the corresponding Au, CNF/Au, CNF/Au/GO, and Mixture samples. Similar results are observed when using CV as the analyte (Fig. 5.2 c,d). Among the annealed samples, the highest SERS sensitivities are received on the aCNF/Au/GO sample, which follows the identical trend: aCNF/Au/GO >aCNF/Au >aMixture >aAu.

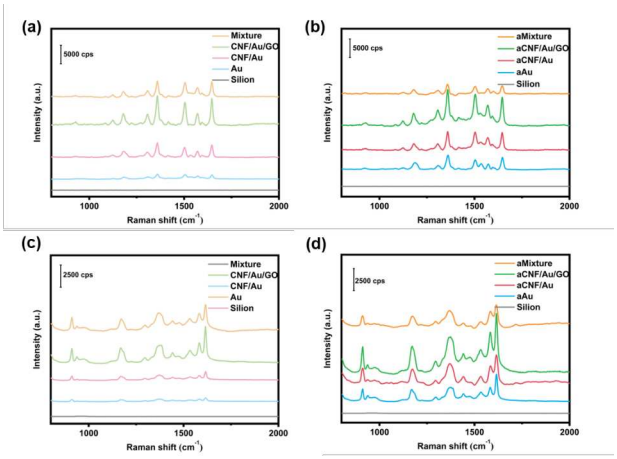

Figure 5.2:
SERS spectra of R6G on various SERS substrates (a) before annealing, (b) after annealing. SERS spectra of CV on various SERS substrates (c) before annealing, (d) after annealing.

In the future, grazing incidence small-angle X-ray scattering (GISAXS) will be used to investigate the structural evolution of Au NPs on or within the CNF layer, confirming the production of more hotspots during the annealing process.

[1] P. Si, N. Razmi, O. Solanki, C. Pandey, R. Gupta , B. Malhotra, M. Willander, A. Zerda, *Nanoscale Adv.* **3**, 2679-2698 (2021)

[2] Q. Chen, M. Betker, C. Harder, C. J. Brett, M. Schwartzkopf, N. M. Ulrich, M. E. Toimil-Molares, C. Trautmann, L. D. Söderberg, C.L. Weindl, V. Körstgens, P. Müller-Buschbaum, M. Ma, S. V. Roth, *Adv. Funct. Mater.* **32**, 2108556 (2022)

5.2 Mesoporous zinc titanate films fabricated via adjusting the ratio of TTIP and ZAD precursors

Y. Li, P. Müllerr-Buschbaum

Metal oxide films with designable morphologies and specific functions are widely fabricated based on the solution method. The solution contains specific precursors and a polymer template which can be burned out after calcination or plasma treatment. After oxidation, the fabricated metal oxide shows designed structures, for example, titania dioxide and zinc oxide. In contrast to pure titania dioxide and zinc oxide, zinc titanate comprising $ZnTiO_3$,[1] Zn_2TiO_4,[2] and $Zn_2Ti_3O_8$,[3] has demonstrated advantages.[4-5] In this work, the hybrid films before oxidation are fabricated based on the solutions consisting of PS-*b*-PEO as a template and two precursors (TTIP and ZAD) dissolving DMF and HCl. Then, the hybrid films are calcined to move the polymer template and obtain the mesoporous zinc titanate films. Since the burn-out temperature of the polymers also depends on the molecular weight of the polymers. If the molecular weight of the polymers is very large, then the temperature needs a higher temperature. Thus, it is very helpful to know the lowest burn-out temperature of the polymer template for a green environment. In Fig. 5.3, the grey curve shows the thermalgravity analysis (TGA) measurement of PS-*b*-PEO powder, and the red curve is the derivation result of the measurement for a better visibility. Based on the two obvious peaks of the red curve, we obtain that the decomposition temperatures of the PS block and PEO block in this template are 347 ^{o}C and 448 ^{o}C, respectively. In addition, the temperature when the polymer can be totally burned out is 486 ^{o}C. Moreover, the instrument utilized for calcination is a general tube furnace in laboratory with natural air. Thus, to guarantee the template can be totally removed, the metal oxide films are produced at 600 ^{o}C.

In the present work, four hybrid films with four mass ratios of TTIP and ZAD (10:0, 5:5, 3:7,

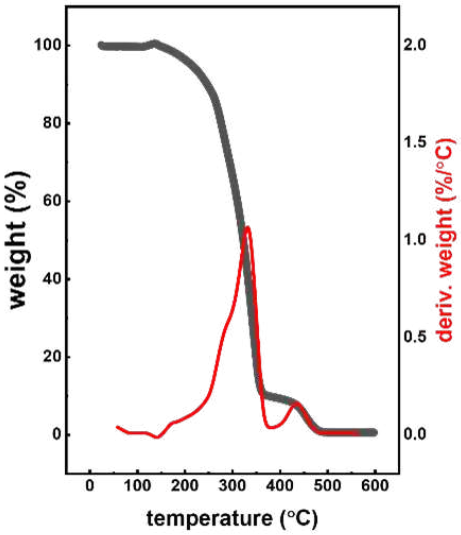

Figure 5.3:
TGA measurements of PS-*b*-PEO powder.

and 0:10) precursors are fabricated. The two of samples contain only TTIP or ZAD and are used as control group to track how the film morphology evolves. After that, the hybrid films are calcined at 600 ^{o}C to obtain mesoporous metal oxide films (Fig. 5.4). Fig. 5.4 shows that with increasing ZAD content, the film morphologies evolve from (a) large wormlike structures, (b) small wormlike and close packed structures, (c) large particles with porous structures, to (d)

desperately wormlike structures. Thus, there are three mesoporous structure films with wormlike structures and a special film in Fig. 5.4(c) when the mass ratio of TTIP to ZAD is 3:7. The large particle sizes are significantly bigger than the polymer template size. Thus, we assume that the large particles can be attributed to the crystals formed out of the metal oxide.

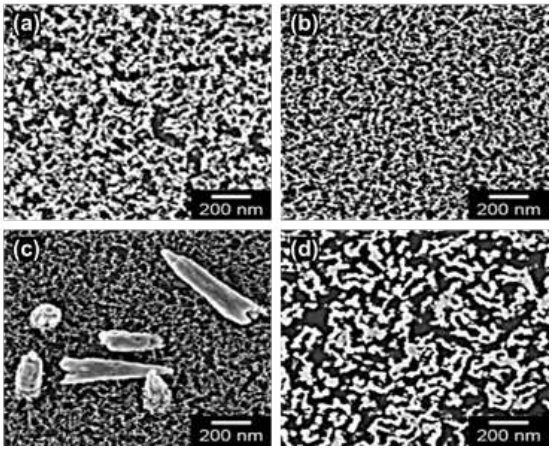

Figure 5.4:
SEM images of the metal oxide film morphology evolution with increasing ZAD content from (a) to (d).

To confirm this assumption, we characterize the four metal oxide films by using grazing incidence X-ray diffraction (GIXD) measurements. As shown in Fig. 5.5, the four curves (a-d) are the samples with increasing ZAD content. The pure TTIP anatase TiO_2 (JCPDS 21-1272) is found in Fig. 5.5 (a). The pure ZAD as expected zincite ZnO (JCPDS 36-1451) is seen in its wurtzite phase in Fig. 5.5(d). With increasing the ZAD contents (from mTTIP:mZAD = 5:5 to mTTIP:mZAD = 3:7), $ZnTiO_3$ (JCPDS 39-0190) and $ZnTiO_x$ are formed shown in Fig. 5.5(b-c), respectively. Compared with the curves of (a, b, d), curve (c) in Fig. 5.5 has a special morphology, which can be probably attributed to crystal type or crystal mixture. Such morphology may have a high potential in the application in photocatalysis and photovoltaic areas. Therefore, the case with special film morphology and crystal type will be investigated in the future.

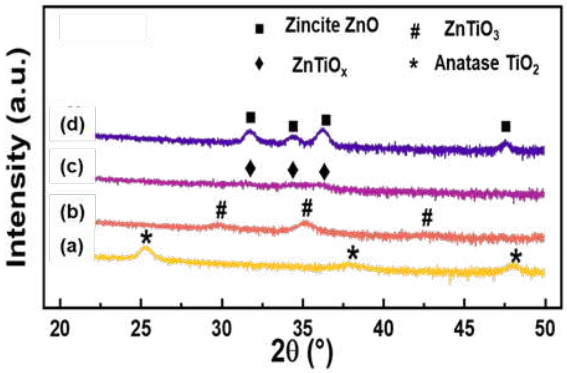

Figure 5.5:
GIXD measurements of calcined films prepared with different precursor ratios. Characteristic peaks of the involved oxides and zinc titanate are labeled.

[1] F. Guo, X. Sun, B. Liu, Z. Yang, J. Wei, D. Xu, *Angew. Chem.* **131**, 18631-18636 (2019).

[2] J. Li, B. Wu, Q. Zhang, H. Wang, Y. Li, *J. Nanosci. Nanotechnol.* **16**, 9568-9574 (2016).

[3] M. Zhao, B. P. Bastakoti, Y. Li, H. Xu, J. Ye, Z. Liu, Y. Yamauchi, *Chem. Commun.* **51**, 14582-14585 (2015).

[4] C. Chuaicham, S. Karthikeyan, J. T. Song, T. Ishihara, B. Ohtani, K. Sasaki, *ACS Appl. Mater. Interfaces* **12**, 9169-9180 (2020).

[5] J. Yu, D. Li, L. Zhu, X. Xu, *J. Alloys Compd.* **681**, 88-95 (2016).

5.3 Emergence of hyperuniformity in 2D mesoporous structure directed by block-copolymer assemblies

G. Pan, P. Müller-Buschbaum

The hyperuniform system represents a recently discovered exotic state of matter that bridges the characteristics of perfect crystals and liquids.[1] Similar to liquids or glasses, hyperuniform systems are statistically isotropic, featuring the absence of conventional long-range translational and orientational order. However, these systems suppress infinite-wavelength density fluctuations, as seen in crystals, showing a subtle, inherent order on the large length scale.[1,2] Hyperuniform states have been identified in a wide range of equilibrium and non-equilibrium physical and biological systems, such as maximally random jammed packings and emulsions.[3-5] Their distinct structural properties lead to unique physical characteristics that are unattainable in either conventional disordered or perfectly crystalline states. While most hyperuniform materials are engineered through top-down approaches, currently, bottom-up fabrication suffers from significant challenges with only a few successful examples.[6]

Here, the fabrication of 2D mesoporous films exhibiting hyperuniformity is proposed (Fig. 5.6). The amphiphilic diblock copolymer polystyrene-b-polyethylene oxide is used as a structure-directing template, which selectively incorporates inorganic precursors. The structure template is removed by oxygen plasma to form mesoporous structures. Importantly, the nanoscale patterning process, based on block copolymer self-assembling, has the potential of multimaterial structuring templated by the block copolymer morphology, thus providing a key for studying the properties of hyperuniform states in different materials (photonic, magnetic, plasmonic ones, etc.).

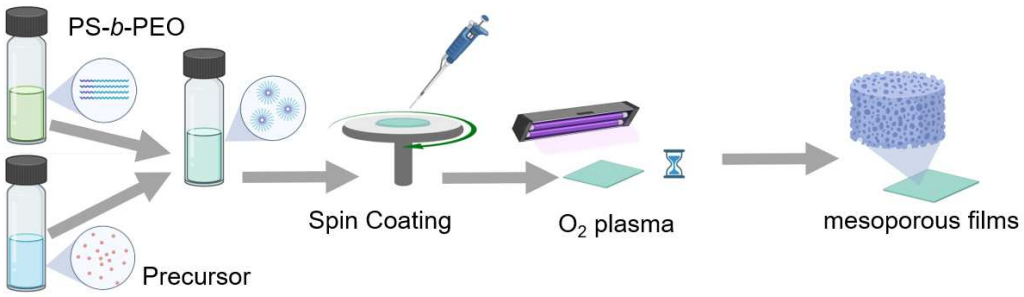

Figure 5.6:
Sketch of mesoporous film fabrication templated by block copolymer self-assembly. Block copolymer micelles can be loaded with various precursors, thus accessing many kinds of materials.

Fig. 5.7a shows the SEM image of the two dimensional mesoporous film, featuring a pore size of around 27 nm. According to the SEM image, there are many small domains of mesopores on the 2D mesoporous film. The 2D Fast Fourier Transform (2D FFT, Fig. 5.7b) shows three concentric diffuse rings, indicating no orientational order but some translational order. A high degree of order in the material system translates into distinct spatial frequencies in the Fourier transform, and thus, well-defined spots can be found in the 2D FFT image. With compartmentalization and translational rotation of individual domains, the spots blur into rings, which is the case here. The power spectral density function (Fig. 5.7c) confirms the translational ordering. However, the bond angle plot (Fig. 5.7d) shows an isotropic angular distribution. The bond angle is calculated

based adjacent pore-pairs and indicates the relative positional information of adjacent two pore-pairs. This contradiction between the orientational disordering and translational ordering is actually from the hyperuniformity of the system. The mesopores have short-range translational correlations but the system suppress density fluctuations of mesopores at long wavelengths, exhibiting hyperuniformity.

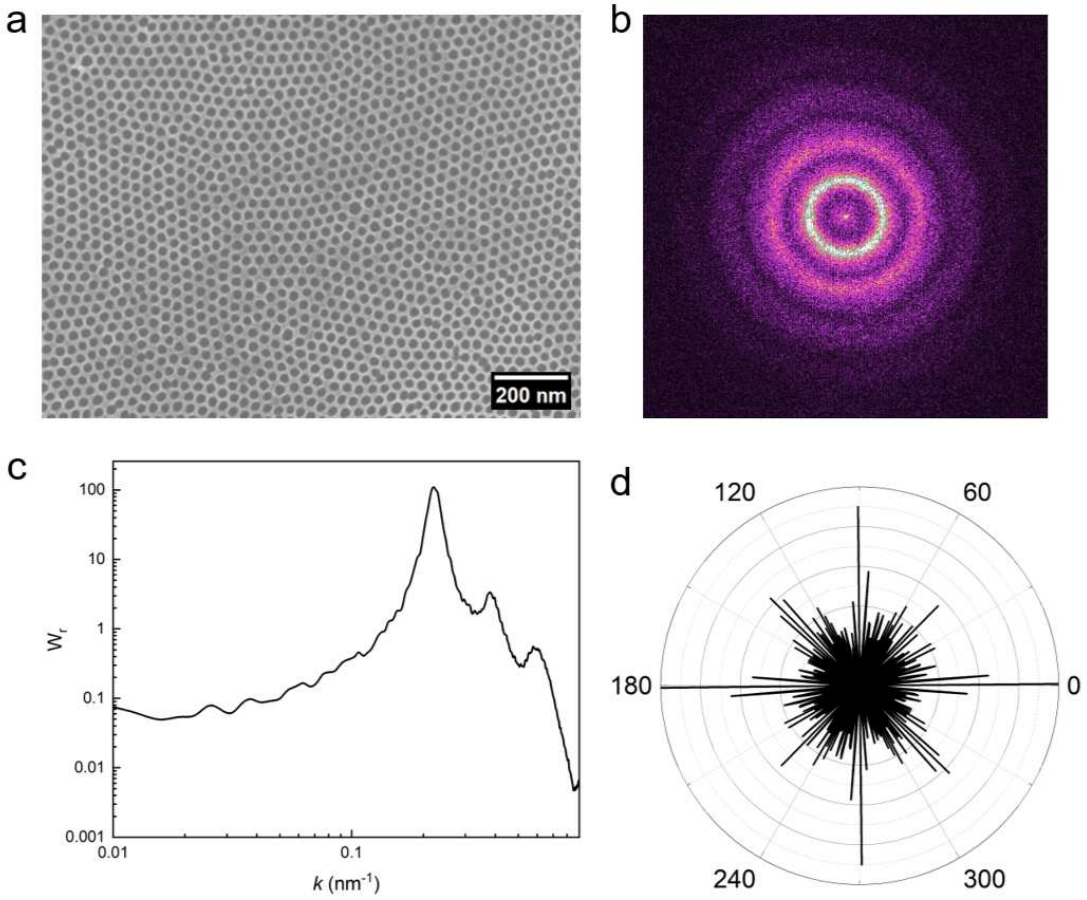

Figure 5.7:
a) SEM image of mesoporous film prepared from block copolymer templated sol-gel synthesis: only short-range topological order is observed. b) The corresponding 2D-FFT pattern. c) Power spectral density function extracted from the SEM image. The peaks in the spectra come from the Fourier transform of the structures, indicating ordered characteristic structures. d) Bond angle plot extracted from the SEM image, indicating isotropic bond angles. The bond angle distribution looks at the angular dependence of the nth neighbor, in this case, the nearest neighbor.

[1] S. Torquato, *Phys. Rep.* **745**, 1-95 (2018)

[2] C. E. Zachary, S. Torquato, *J. Stat. Mech.: Theory Exp.* **12**, P12015 (2009)

[3] R. Kurita1, E. R. Weeks, *Phys. Rev. E* **84**, 030401 (2011)

[4] J. H. Weijs, R. Jeanneret, R. Dreyfus, D. Bartolo, *Phys. Rev. Lett.* **115**, 108301 (2015)

[5] G. Zito1, G. Rusciano, G. Pesce, A. Malafronte, R. D. Girolamo, G. Ausanio, A. Vecchione, A. Sasso, *Phys. Rev. E* **92**, 050601 (2015)

[6] D. Chen, M. A. Klatt, G. H. Fredrickson, *Macromolecules* **57**, 9911-9919 (2024)

6 Materials for energy storage

6.1 Observation of local crystallization in the polymer electrolyte for lithium metal batteries by operando nano-focus WAXS

F. A. C. Apfelbeck, A. Davydok[1], C. Krywka[1], P. Müller-Buschbaum

[1] Helmholtz Zentrum Hereon, Hamburg, Germany

Metallic lithium is a promising candidate as an anode for next-generation batteries due to its low potential of -3.040 V vs. SHE and high theoretical specific capacity of around 3860 mAh/g which is approximately ten times higher compared to graphite (372 mAh/g). However, when operating with liquid, carbonate-based electrolytes, the practical use is still limited due to the uneven lithium deposition that can lead to a rapid decrease in the cell performance. Furthermore, dendritic lithium can cause short circuits as well as thermal runaways. To improve the lifetime of lithium metal cells, several strategies, such as tuning the composition of the liquid electrolyte through additives or surface coatings, are proposed and subject to intense research. Furthermore, switching from liquid to solid electrolytes is generally regarded as a big milestone in the battery community. A particularly unique type of electrolyte are so-called single-ion conducting polymers (SICPs). The idea behind these polymers is that only the lithium ions can move as the anion is attached to the bulky, immobile polymer backbone. In contrast to dual-ion conducting systems, where both anions and cations of the lithium salt are mobile, SICPS are believed to suppress lithium dendrites as they exhibit a theoretical transference number of one.[1] However, the use for practical applications is still under debate as the advantages only come into play at high currents and temperatures.[2] This ambivalence raises the question if single-ion conducting polymer electrolytes indeed restrain lithium dendrites especially at ambient conditions. In other words, is it possible to observe solely the polymer at the interface during the battery operation and hence reveal the potential growth of lithium crystallites?

For this purpose, wide-angle X-ray scattering (WAXS) is an excellent tool for investigating a system regarding its crystalline structure.[3] Moreover, scanning nano-focus (nWAXS) enables locally resolving the crystallinity due to a very small beam size of only a few hundred nanometers in diameter. To investigate the polymer during charging and discharging, a custom built *operando* cell for X-ray transmission experiments, is designed. This cell allows to align the X-ray beam parallel to the material stack. A schematic of the experiment is given in Figure 6.1.

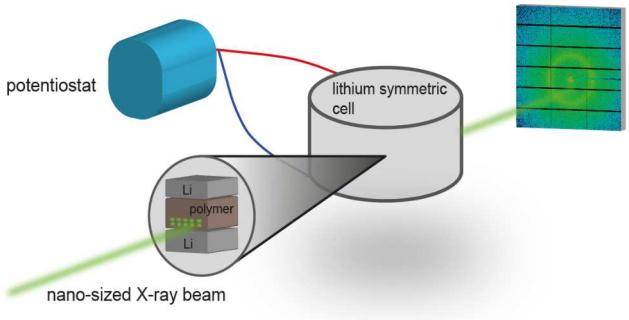

Figure 6.1:
Schematic of the nWAXS experiment.

In this study, the SICP poly((trifluoromethane) sulfonimide lithium styrene) (PSTFSILi) is used. However, due to the high glass-transition temperature, this polymer tends to be brittle when forming free-standing films at room temperature and therefore polymer blending partners are required. For that, poly(vinylidene fluoride-co-hexafluoropropylene) (PVDF-HFP) is utilized. To further enhance the ionic conductivity, the polymer film is swollen in a solution of ethylene carbonate (EC) and propylene carbonate (PC) (1:1 v/v). Grazing incidence wide-angle X-ray

scattering measurements of this gel-type polymer reveal a broad halo in the low q regime. Furthermore, electrochemical cycling of this polymer in a lithium symmetric coin cell configuration exhibits a lifetime of around 330 hours. Next, the custom-built cell was successfully operated at the P03 nanofocus end-station at DESY. The symmetric lithium cell was running for three half-cycles with 30 minutes per half-cycle and stable electrochemical performance at room temperature. The nanosized beam was scanned in a mesh grid pattern during plating and stripping. Fig. 6.2 shows an exemplary radial integration. At $q \approx 1.4$ Å^{-1} the polymer halo can be identified (Fig. 6.2a). Surprisingly, besides the expected polymer halo, also sharp peaks at higher q values (Fig. 6.2b) are visible which are absent in the static GIWAXS measurement. Further sharp peaks are occasionally identified at $q \approx 1.55$ Å^{-1} and $q \approx 2.52$ Å^{-1} (not shown here). This indicates electrochemical reactions at the polymer/lithium metal interface. The intensity of these peaks can be mapped which gives the crystallite kinetics over the three half-cycles.

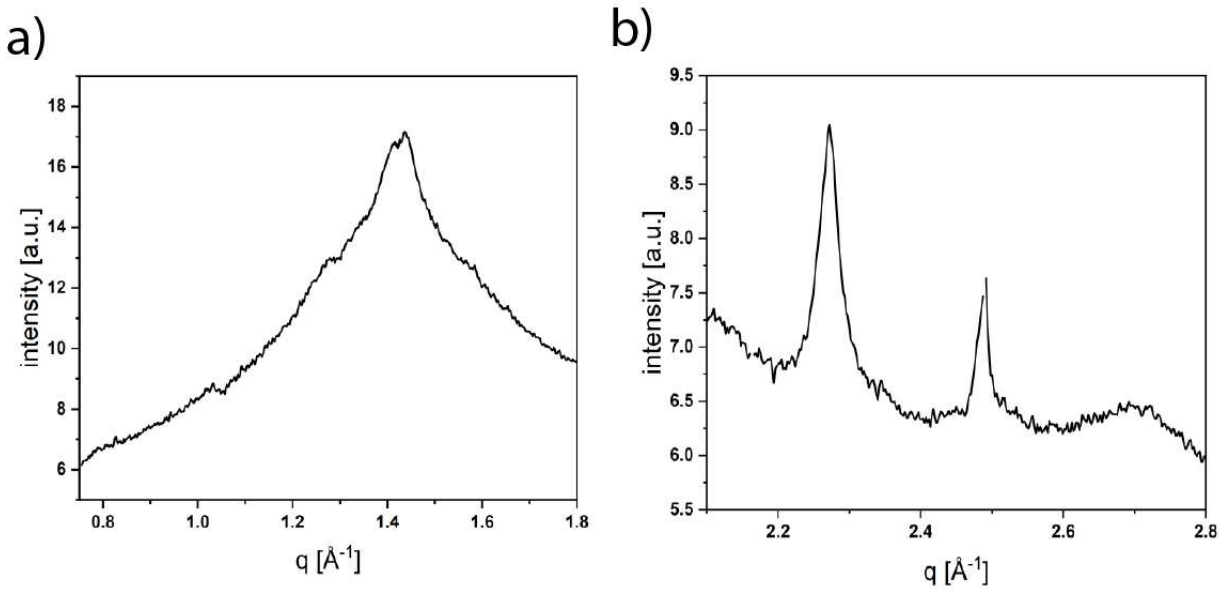

Figure 6.2: Selected radial integration in the low q (a) and high q (b) regime.

In summary, the crystallinity of a single-ion conducting polymer electrolyte was investigated by a pioneering *operando* scanning nWAXS experiment at the DESY P03 nanofocus end-station. For that purpose, a custom built cell was designed that allows for simultaneous electrochemical cycling and X-ray transmission. Surprisingly, the existence of different crystallites in the polymer were proved. Moreover, the kinetics of these crystallites were tracked over time and their origin was ascribed to interfacial reactions.

[1] D. Zhou, D. Shanmukaraj, A. Tkacheva, M. Armand, G. Wang, *Chem* **5**, 2326-2352 (2019)

[2] L. Stolz, S. Hochstädt, S. Röser, M. R. Hansen, M. Winter, J. Kasnatscheew, *ACS Appl. Mater. Interfaces* **14**, 11559–11566 (2022)

[3] J. Gao, C. Wang, D. W. Hang, D. M. Shin, *Chem. Sci.* **12**, 13248 (2021)

[4] N. Li, S. Pratap, S. Pratap, V. Körstgens, S. Vema, L. Song, S. Liang, A. Davydok, C. Krywka, P. Müller-Buschbaum, *Nat. Comm.* **13**, 1525-1530 (2021)

6.2 In-situ WAXS observation of 3D electrodeposition of porous Cu in lithium-metal batteries

L. Cheng, Y. J. Cheng[1], P. Müller-Buschbaum

[1] Hohai University, Changzhou, China

Lithium (Li) metal is the ultimate anode for rechargeable batteries. Its high specific capacity (3860 mAh g^{-1}) and low voltage (-3.04 V vs standard hydrogen electrode) warrant an optimal cell energy density. However, these anodes rely on repeated plating and stripping of Li, which leads to the consumption of the Li inventory and the growth of dendrites that can lead to self-discharge and safety issues. To address these issues and problems related to the volume change of these anodes, a number of different porous conductive scaffolds have been reported to create high surface area electrodes on which Li can be plated reliably. While impressive results have been reported in the literature, current processes typically rely on either expensive or poorly scalable techniques. Herein, we report a scalable fabrication method to create porous Cu anodes using a one-step electrodeposition process. The areal loading, pore structure, and electrode thickness can be tuned by changing the electrodeposition parameters. With in-situ WAXS we study the lithium growth, which can help to explain the mechanisms of dendrite formation. We also provide a feasible method to fabricate the porous Cu cathodes with different electrodeposition solution concentrations.[1-4]

The progress of ”anode-free” lithium-metal batteries, known for their high energy densities, is currently impeded primarily by the insufficient control of lithium nucleation directly on the copper current collector, especially within conventional carbonate electrolytes. However, for the consistent use of anode-free lithium batteries, challenges related to the formation of dead lithium, porous lithium, and lithium dendrites during lithium electrodeposition on copper current collectors must be addressed. Although the electrodeposition of lithium on a copper current collector differs from that on a lithium-metal electrode, the aforementioned problems are essentially the same in both cases. These issues arise from the inability to effectively control the lithium nucleation process, preventing the achievement of 2D homogeneous lithium electrodeposition. Numerous strategies have been proposed to enhance lithium electrodeposition in anode-free cells. Among them, the central chemistry-related approach involves the development of new electrolyte formulations that impact the solvation structure of lithium ions and/or the compositions and morphologies of the solid electrolyte interphase (SEI) layer. Other material-related approaches include i) modifying copper current collectors by synthesizing 3D structures to reduce local current densities and encapsulate electrodeposited lithium, ii) designing artificial SEI layers that are more stable during lithium electrodeposition, and/or iii) coating ”lithiophilic” materials on the copper surface to facilitate lithium nucleation. Improving our understanding of the lithium nucleation process and its intricate interactions with the copper substrate is crucial. The diffusion process described above presents a challenge in achieving a large number of evenly distributed lithium nuclei on the copper surface, resulting in non-uniform electrodeposition. However, it has been demonstrated that the nucleation of lithium on copper significantly improves with an initial chemical prelithiation of the copper surface. This prelithiation saturates the copper surface with lithium, reducing the impact of lithium diffusion through grain boundaries. Consequently, lithium nucleation becomes more homogeneous as seen in Fig. 6.3, particularly when using a specific type of solution. Herein, we use the copper chloride solution. After using direct pulse electrodeposition at 5v for 10 minutes the surface is uniquely covered with copper and the boundaries are clearly illustrated in Fig. 6.3 (a) and (b).

Synchrotron-based nano-focus wide-angle X-ray scattering (nano-WAXS) is a powerful tool to investigate the local crystallinity of the bulk in materials for energy applications. Therefore, we

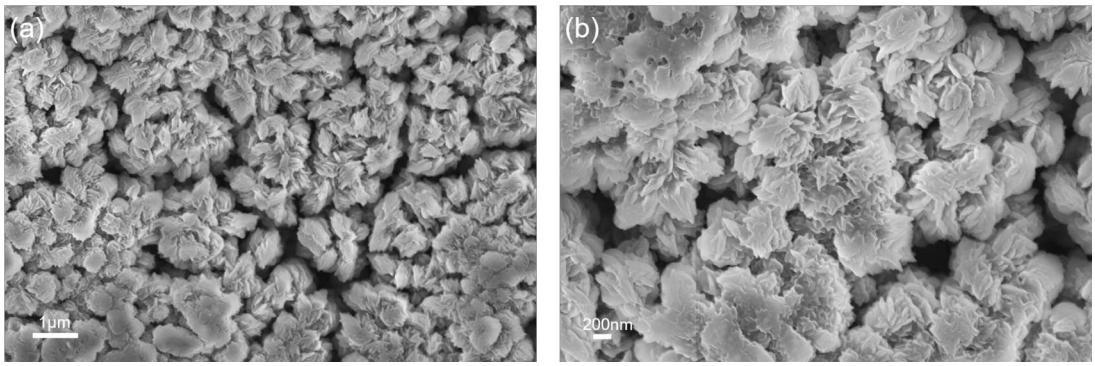

Figure 6.3: SEM images of 3D electrodeposition porous Cu at different scales.

use in-situ nano-WAXS measurements to illustrate the process of Li-Cu dendrite formation, and SEI layer growth during the CV cycling. The nano-WAXS is performed with a set up at DESY, see Fig. 6.4(c). Fig. 6.4 (a)(b) shows the lithium peak signal changing with time evaluation. It also corresponds with the nano-WAXS intensities seen in Fig. 6.4(c), where we can see the peak of lithium growing. The CV cycling is provided in Fig. 6.4(e). The nano-WAXS result clearly reflect the lithium signal growing during its electrochemical reduction and oxidation reaction. Above all, it gives us a better understanding of what happens inside the batteries.

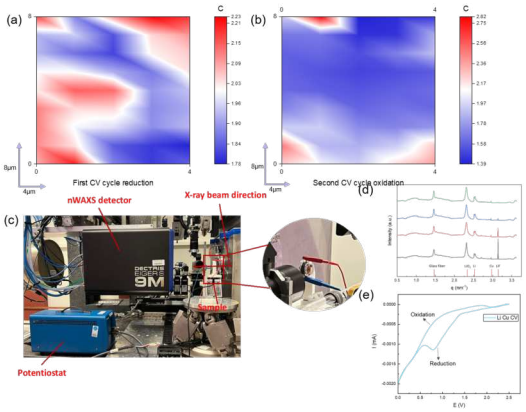

Figure 6.4:
Operando WAXS study of our electrodeposition Cu battery cells.

In summary, the 3D electrodeposition of porous Cu can help to stabilize the electrode via a uniform lithium deposition as seen by SEM and electrochemical performance measurements. The nano-WAXS measurements illustrate the process of lithium dendrite growth during its CV cycling. More tests are needed in the future, such as XPS to understand the decomposition of electrolytes, TEM for copper and lithium nanoscale observation and XRD for copper structural tests. Also, different types of electrodeposition solutions, the conditions such as time, and current of the electrodeposition can be explored.

[1] R. V. Salvatierra, W. Chen, J. M. Tour, *Adv. Energy Sustainability Res.* **2**, 2000110 (2021)

[2] S. Nanda, A. Gupta, A. Manthiram, *Adv. Energy Mater.* **11**, 2000804 (2021)

[3] A. J. Louli, A. Eldesoky, R. Weber, M. Genovese, M. Coon, J. DeGooyer, Z. Deng, R. T. White, J. Lee, T. Rodgers, R. Petibon, S. Hy, S. J. H. Cheng, J. R. Dahn, *Nat. Energy.* **5**, 693 (2020)

[4] C. L. Weindl, C. E. Fajman, Z. Xu, *ACS Appl. Mater. Interfaces* **16**, 2309-2318 (2024)

6.3 Structural characterization of lithium chlorides Li_3MCl_6

F. Falsina, A. Senyshyn[1], P. Müller-Buschbaum

[1] MLZ, Garching, Germany

The demand for batteries with higher power and energy density drives interest in solid-state electrolytes (SSEs), which enable lithium anodes and address electrolyte flammability. Following the development of Li_3YCl_6 [1] and Li_3InCl_6 [2], ternary chlorides like Li_3MCl_6 have gained attention. These can crystallize in monoclinic (*C2/m*), trigonal (*P3m1*), or orthorhombic (*Pnma*) phases [3], with the orthorhombic phase showing much higher conductivity than the trigonal one [4]. Solid-state ball milling is often used for synthesis but results in poor crystallinity, so samples are typically annealed for characterization. This study explores the annealing process and its impact on structure. The samples are synthesized through the following mechanochemical reaction:

$$MCl_3 + LiCl \longrightarrow Li_3MCl_6$$

This is performed in a Fritsch Pulverisette Premium Line ball mill with an air-tight ZrO_2 jar, at $500\,\mathrm{RPM}$ for 5 minutes, followed by 10 minutes of rest, repeated for 99 cycles. After each cycle, the samples are manually reground, and the procedure is repeated three times. Three batches are synthesized for each cation (M = Dy, Ho, Tm, Tl). Structure characterization is initially done on a laboratory XRD to verify synthesis reproducibility. Three measurements per batch are taken, resulting in nine patterns. While crystallinity varies slightly between batches, the variability within the same batch was is similar to that between batches, confirming high reproducibility. Structural characterization of Li_3HoCl_6 during annealing is carried out at the P02.1 beamline at PETRA III, with a photon energy of $60\,\mathrm{keV}$ and a sample-to-detector distance of $1800\,\mathrm{mm}$, using a quarter-ring configuration. Results show that the conductive *Pnma* phase dominates at low temperatures. However, above $250\,^{\circ}\mathrm{C}$, there is a marked increase in the *P3m1* phase, which has only been identified in annealed samples by our group.

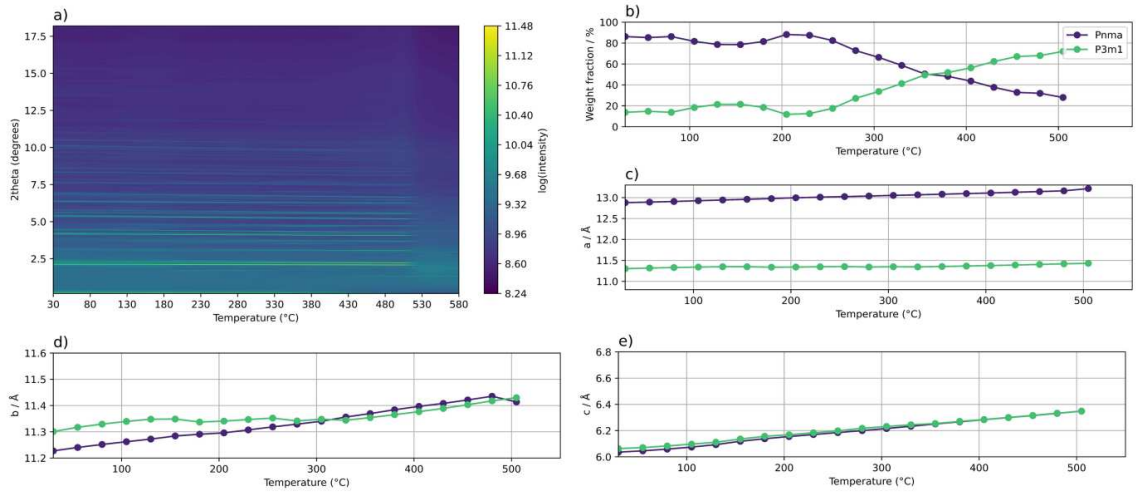

Figure 6.5:
a) Contour Plot obtained in a spinning capillary (0.6 mm) setup, for temperatures comprised between 30 C and 580 C. b) Weight fraction for orthorombic (Pnma) and trigonal (P3m1) phases. c), d) and e): a, b and c lattice parameters, respectively.

A custom cell is designed for future conductivity evaluation of synthesized samples. It allows easy powder filling within a glovebox and remains airtight for measurements outside using

techniques like electrochemical impedance spectroscopy and galvanostatic intermittent titration. The cell can apply up to 100 MPa pressure on the sample with a 30 Nm torque on the shaft. Mechanical simulations performed with Fusion 360 software are shown in Fig. 6.7.

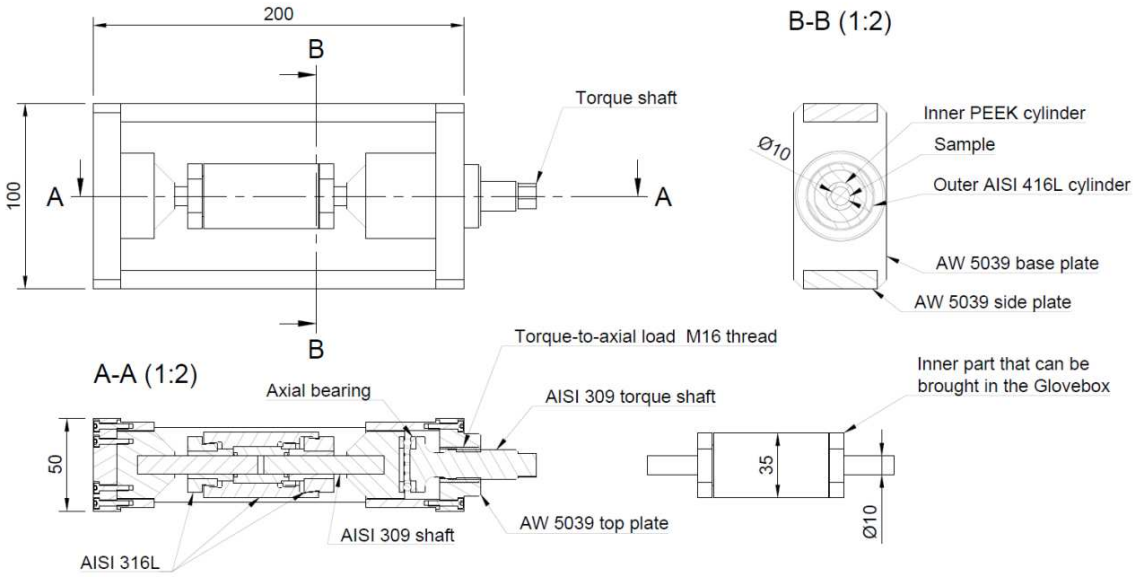

Figure 6.6: Tecnical drawing of the cell.

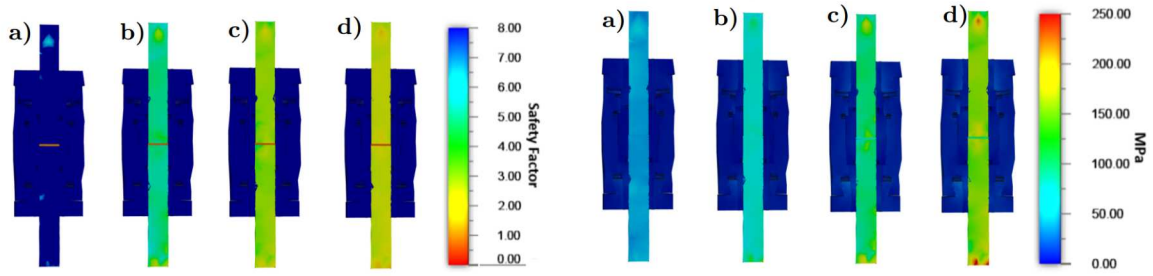

Figure 6.7:
Safety factor (left) and stress (right) for a) 10 Nm, b) 20 Nm c) 30 Nm and d) 40 Nm torque applied to the thread.

[1] T. Asano, A. Sakai, S. Ouchi, M. Sakaida, A. Miyazaki, S. Hasegawa, *Adv. Mater.* **30**, 1803075 (2018)

[2] X. Li, J. Liang, J. Luo, et al. *Energy Environ. Sci.* **12**, 2665 (2019)

[3] X. Li, J. Liang, X. Yang, et al. *Energy Environ. Sci.* **13**, 1429 (2020)

6.4 Impact of silicon additives on the lithiation of graphite in commercial battery anodes during electrochemical cycling

T. Hölderle, D. Petz[1], V. Kochetov[1], A. Kriele[1], V. Baran [2], Z. Hegedüs[2], U. Lienert[2], M. Avdeev[3], P. Müller-Buschbaum, A. Senyshyn[1]

[1] MLZ, Garching, Germany

[2] DESY, Hamburg, Germany

[3] ANSTO, Sydney, Australia

Graphite in the form of negative electrodes can be found nowadays in almost every commercial lithium ion battery (LIB), due to its high structural stability during the electrochemical cycling and its relatively high theoretical specific capacity of 372 mAh/g [1]. However, the growing market demands higher energy densities at lower costs. A promising alternative are silicon-based anodes, which offer significantly higher theoretical specific capacities of 2400 mAh/g compared to graphite [2]. However, during the de-/lithiation process, silicon undergoes a significant volume change of approximately 300%, causing high mechanical stress. This makes it challenging for the practical use in the LIB, due to potential fragmentation of the electrode particles, electrical contact losses and capacity fade of the cell [2]. To address this issue and maintain structural integrity while increasing the cell's specific capacity, composite materials based on graphite with silicon additives have been developed and implemented in today's LIBs. While diffraction techniques can easily map the structural evolution of crystalline graphite during the electrochemical cycle, analyzing silicon's structural changes is more challenging. During the first lithiation, silicon transitions from a crystalline to an amorphous state [3], making it difficult to detect via diffraction techniques.

In the following contribution, we investigate the structural signal of graphite-based anodes with added silicon during the electrochemical cycle in various commercial battery cells. Four different commercial cylindrical battery cells are selected: LG INR21700 50H (short: 50H), Samsung INR21700 40T (short: 40T), LG INR18650 HG2 (short: HG2), and Panasonic NCR18650 B (short: NNP). These cells have varying silicon content in the anodes. Operando neutron powder diffraction measurements are conducted at the ECHIDNA instrument (ANSTO, Sydney) and SPODI instrument (FRM II, Garching) under similar settings, utilizing low cycling currents for high structural resolution. During electrochemical cycling, the signal of graphite lithiation is clearly resolved for all LIBs. In the discharged state, the graphite's 002 reflection is observed at approximately 3.35Å interplanar spacing d. With increasing lithiation, the reflection is moving towards higher d spacing, showing a phase transition first towards a LiC_{12} and later to a LiC_6 phase (Fig. 6.8), forming a biphasic system [4]. However, no specific signal from the silicon is detected. Electrochemical data and differential voltage analysis reveal distinct peaks corresponding to structural transitions in the LIB electrodes. The first three peaks observed in the data mark the different lithiation stages in the low lithiated region of graphite, while the fourth peak G_2 marks the onset of the phase transition to LiC_6 phase. The final observed peak corresponds to a phase transition in the cathode material. The characteristic signals of the differential voltage analysis can be perfectly assigned to the structural changes resolved with diffraction. However, comparing data from different cells revealed variations in the positions of these peaks. For the 50H cell, the first peak appeared at 30% capacity, for 40T/HG2 at 22%, and for NNP already at 13%. Similarly, in the diffraction data, the onset of graphite lithiation is delayed in all cells except for the NNP cell, as indicated by the graphite reflection remaining at the same d-spacing value despite increasing lithiation. This behavior reflects a multi-step lithiation process of the composite electrode. Initially, silicon grains within the electrode are lithiated, followed by the lithiation of the remaining graphite grains. These steps are governed by the different standard potentials (V vs. Li+/Li) of the components: silicon, which has a higher standard potential of

0.4 V, is lithiated before graphite, which has a standard potential of 0.1 V. The extent of the delay in graphite lithiation depends on the silicon content in the electrode. To confirm this hypothesis, we perform energy-dispersive X-ray spectroscopy (EDX) to quantify silicon content in the selected commercial LIBs. The measurements reveal the highest silicon content in the 50H cell (10.5%w/w), intermediate amounts in the 40T/HG2 cells (4.6–4.7%w/w), and no detectable silicon in the NNP cell. These findings align well with the observations in the structural and electrochemical data. In conclusion, while silicon remains in an amorphous state, its integration within graphite-based anodes can be effectively characterized by the delayed lithiation of graphite, as revealed by diffraction techniques and electrochemical analysis.

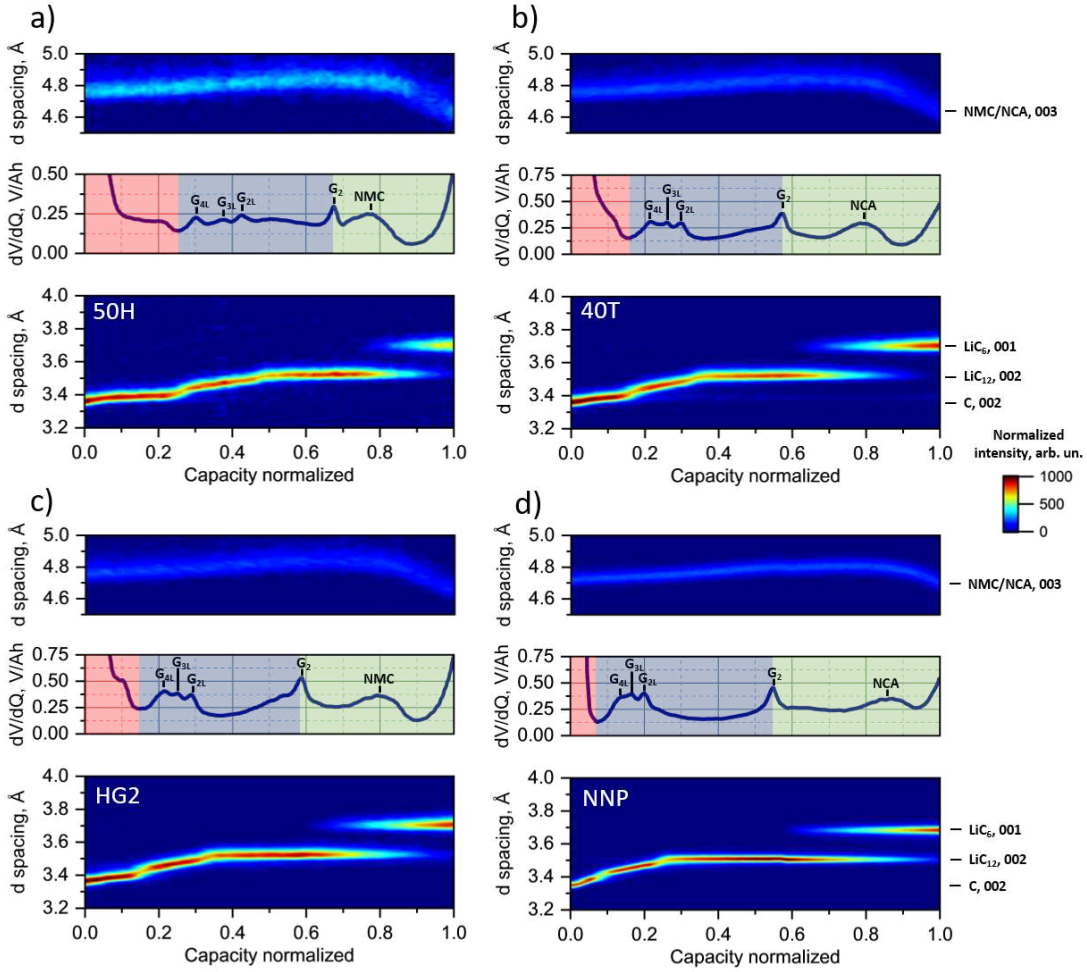

Figure 6.8:
Powder diffraction data combined with differential voltage analysis for a) 50H, b) 40T, c) HG2, and d) NNP cell, revealing the evolution of reflection intensities, with an electrochemical response of anode and cathode. The background color shows the silicon lithiation and onset (red), the lithiation in the solid solution regime (blue), and the biphasic regime (green).

[1] B. Scrosati, J. Garche, *J. Power Sources* **195**, 2419-2430 (2010)

[2] M. N. Obrovac, L. Christensen, D. B. Le, J. R. Dahn, *J. Electrochem. Soc.* **154**, A849 (2007)

[3] P. Limthongkul, Y. I. Jang, N. J. Dudney, Y. M. Chiang, *Acta Materialia* **51**, 1103-1113 (2003)

[4] C. Didier, W. K. Pang, Z. J. Guo, S. Schmid, V. K. Peterson, *Chem. Mater.* **32**, 2518-2531 (2020)

6.5 Unveiling the Li/electrolyte interface behavior for dendrite-free lithium batteries by operando nano-focus WAXS

Y. Liang, A. Davydok[1], C. Krywka[1], P. Müller-Buschbaum

[1] HZH, Hamburg, Germany

The pursuit of interfacial stable lithium metal batteries (LMBs) has been a longstanding challenge in the field, particularly since metallic lithium replaces graphite as an anode material. Replacing the hazardous organic liquid electrolyte with a solid electrolyte is a crucial step for enhancing safety and expanding the potential applications of LMBs. The low-cost poly(ethylene oxide) (PEO) composite electrolyte stands out as the promising candidate due to its high flexibility, strong Li+ solubility, and excellent processability [1].Introducing low molecular weight plasticizers is an effective strategy to improve the conductivity of PEO electrolyte. The plasticizers not only enhance thermal stability and reduce PEO crystallinity, but they also significantly improve ion conductivity [2]. Furthermore, they contribute to the formation of a stable Li/electrolyte interface composed of LiF, Li_3N, and organic components, which helps to suppress lithium dendrite penetration and improves the overall battery performance.

In this work, an interfacial-stable PEO composite electrolyte is fabricated with the addition of succinonitrile (SN) for all-solid-state LMBs. With the incorporation of SN, the modified electrolyte demonstrates a high ion conductivity of 2.69 × 10^{-4} S cm^{-1} and Li+ transfer number of 0.57, attributed to the reduced PEO crystallinity of 10.09 %. This results in the stable Li plating/stripping at 0.1 mA cm^{-2} over 1000 h and an increased critical current density of 0.7 mA cm^{-2}, exhibiting a superior compatibility with metallic lithium. Furthermore, we observe the lithium dendrite growth and the SEI layer formation during the first cycle by operando nanofocus wide-angle X-ray scattering (nWAXS), as shown in Fig.6.9. Li symmetric cells with an contact area of 0.35 cm^2 are cycled at the current density of 0.05 mA cm^{-2}. The X-ray beam is focused on the Li/electrolyte interface area of 2 μm × 8 μm (4 × 16 frames) to locally resolve structural changes.

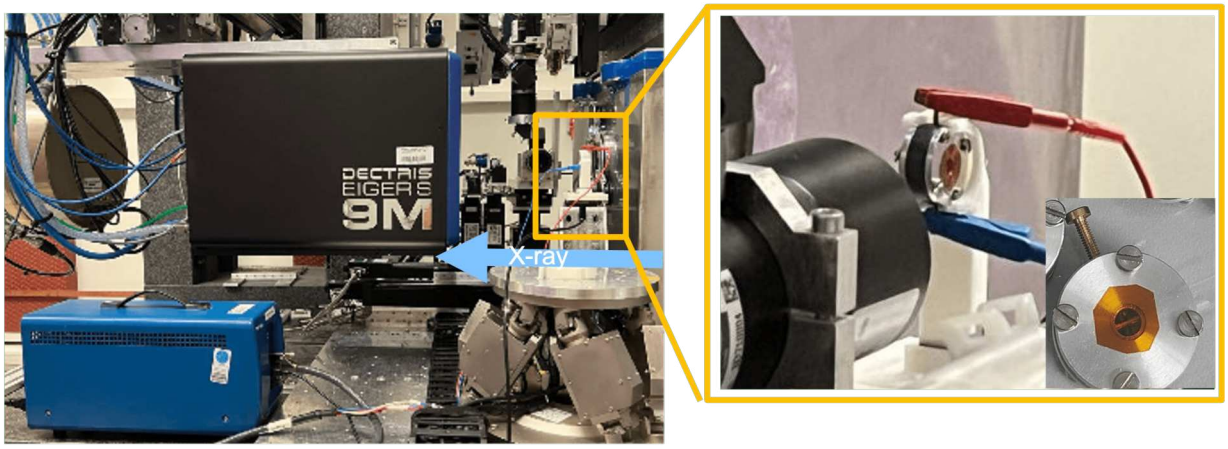

Figure 6.9:
Photo of the operando set-up used at the nanofocus endstation of the beamline P03 to perform nWAXS measurements.

Fig.6.10 shows the temporal q maps for the prominent Li (110) peak over two charge/discharge cycles of Li/PEO-10SN/Li and Li/PEO-0SN/Li cells, respectively, revealing the lithium dendrites formation process. In Fig.6.10a, no visible mossy Li growth is observed along the (110)

direction after repeated Li plating and stripping, indicating that dendrites do not form at the Li/PEO-10SN interface. This stable interface in lithium metal batteries guarantees cycling stability, mitigating dendrite growth and promoting uniform lithium deposition. In contrast, in the reference sample (Fig.6.10b), large metallic nano Li crystals grow from the metallic lithium side, then distribute along the vertical direction (q_y from 2 to 7.5 μm) with respect to the X-ray beam, and finally reach the electrolyte phase during the first half-cycle. This leads to the micro-short circuit within the cells. In the following cycles, the Li (110) remains visible, especially during the second charge and discharge cycles, indicating a continuous growth of the nano lithium crystals at the interface, which ultimately results in cell failure. Additionally, nWAXS reveals the SEI formation mechanism. The main SEI components, LiF and Li_3N, begin to form from the electrolyte side around halfway through the first charging cycle and continuously extend to the lithium metal side at the end of the first discharging cycle. This process creates a uniform and stable Li/electrolyte interface layer that effectively suppresses the lithium dendrite growth, promoting Li+ diffusion and uniform Li+ plating/stripping.

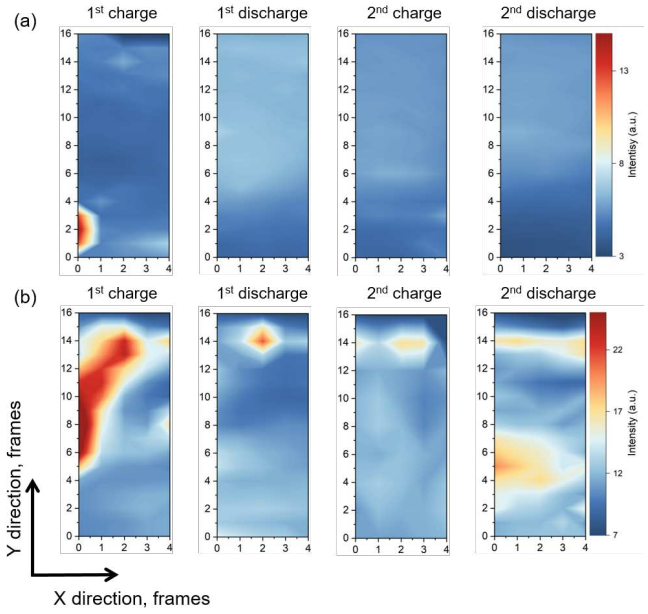

Figure 6.10:
Temporal 2D q maps of Li (110) peak in the scanned area during two cycles of (a) Li/PEO-10SN electrolyte interface and (b) Li/PEO-0SN electrolyte interface.

In summary, we fabricate a succinonitrile-enhanced PEO composite electrolyte that effectively improves the conductivity and compatibility toward metallic lithium, and use operando nWAXS for real-time monitoring of the lithium dendrites growth and SEI formation. The addition of SN reduces crystallinity and promotes the molecule intercalations, which enhanced the ion conductivity. The modified composite electrolyte demonstrates a superior stability against metallic lithium, creates a uniform and stable Li/electrolyte interface layer that effectively suppresses the lithium dendrite growth, promoting Li+ diffusion and uniform Li+ plating/stripping. Thus, our findings validate that the use of simple additives as effective strategy for improving electrochemical performance in all-solid-state LMBs. Furthermore, the insights gained from operando nWAXS measurements will facilitate a deeper understanding of dendrite growth and SEI formation across various battery types, allowing for optimization of interface behavior and electrochemical properties in future research.

[1] K. Qin, K. Holguin, M. Mohammadiroudbari, J. Huang, E. Y. S. Kim, R. Hall, C. Luo, *Adv. Funct. Mater.* **31**, 2009694 (2021)

[2] X. Su, X. Xu, Z. Ji, J. Wu, F. Ma, L. Fan, *Electrochem. Energy Rev.* **7**, 2 (2024)

6.6 Anode-free lithium-metal batteries with polymer-coated electrodes for future battery applications

P. T. Papadaki, F. A. C. Apfelbeck, P. Müller-Buschbaum

Lithium-ion batteries (LIBs) have seen significant improvements in terms of energy density over the past few years, currently reaching specific energies of up to 250 Wh/kg. However, graphite anodes are reaching their upper limit soon. To satisfy future energy demands, the use of lithium metal anodes, with a much higher theoretical capacity compared to graphite, is required. Nevertheless, the commercialization of lithium-metal batteries (LMBs) is hindered by various challenges related to the high reactivity of lithium. Challenges such as the formation of an unstable solid-electrolyte interface (SEI), dendrite growth, and low Coulombic efficiency lead to safety risks and reduced battery lifetimes. To address these issues, various strategies have been explored, including solid polymer electrolytes (SPEs). Another promising approach is the coating of the electrodes with thin protective polymer films. More specifically, thin polymer films on the Li-electrode are able to promote uniform lithium-ion deposition and prevent the aforementioned degradation mechanisms. Numerous polymers, such as PEO, PDMS, and PVDF-HFP, have been tested as coatings for lithium-ion batteries [1], [2].

In this work, the single ion conducting polymer poly(trifluoromethane)sulfonimide lithium methacrylate (PMTFSILi) is chosen to be mixed with poly(ethylene)oxide PEO in different weight ratios, in order to reduce the crystallinity of PEO and at the same time promote the conductivity of Li-ions. The copper surface is modified by the aforementioned polymer mixture to improve the lithium deposition and promote the formation of a uniform lithium layer on the copper surface. Accordingly, the influence of the polymer composition on the plating/stripping mechanism is examined via electrochemical impedance spectroscopy (EIS), cyclic voltammetry, and voltage profile measurements.

The polymer solution preparation involves dissolving the desired amounts of PEO and PMTFSILi in DI water. The concentration of the solution remains constant at 2 mg/mL, because of the high viscosity of PEO when it is mixed with water. Commercial copper foils cleaned with an acid bath are used. The polymer solution is drop-cast onto the clean Cu foils and left to dry for 24 hours under ambient conditions. Finally, Li-Cu half-cells are assembled in an Argon glovebox. The preparation and coating processes of the prepared solutions on cleaned Cu foils are depicted schematically in Fig. 6.11 (a) and (b).

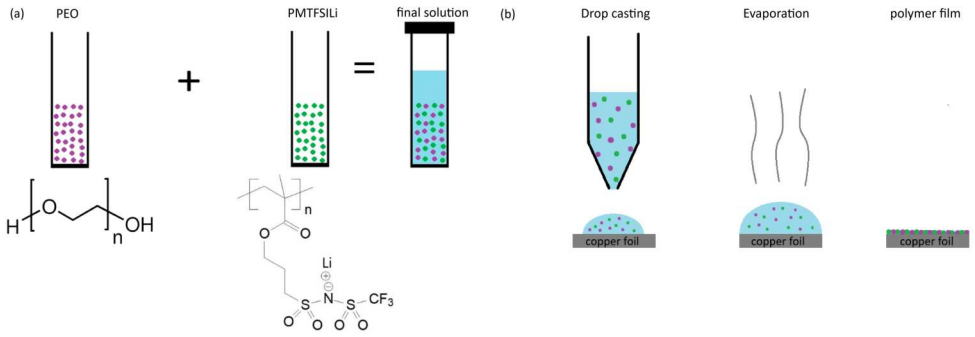

Figure 6.11:
(a) Preparation of PEO-PMTFSILi solution in DI water, and b) drop-casting of polymer mixture on Cu foils

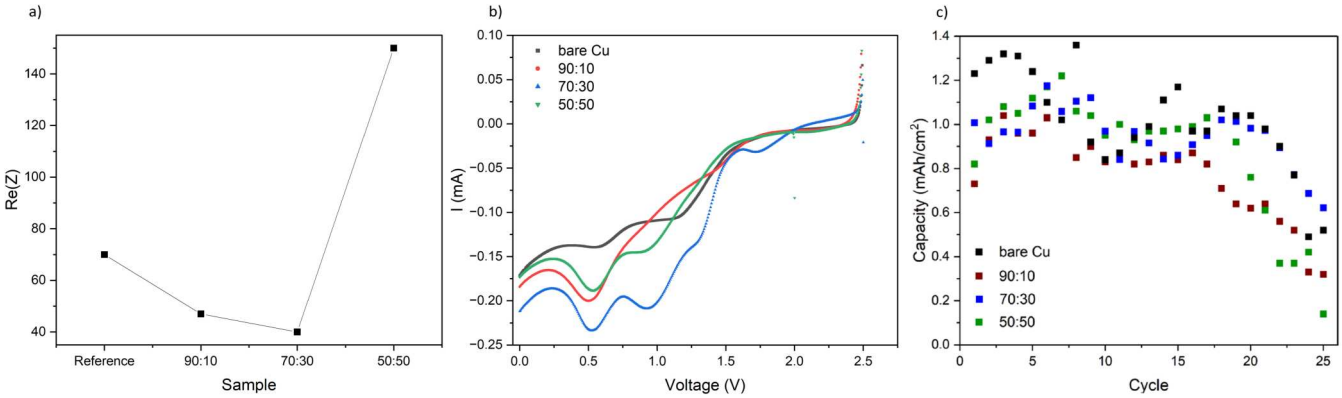

Figure 6.12:
a) Impedance trend with increasing PMTFSILi content in Li-Cu cells. (b) CV comparison of different samples for the first cycle. (c) Capacity retention of modified and unmodified Li-Cu cells.

Fig. 6.12 shows the acquired results from EIS, cyclic voltammetry, and cycling measurements conducted on modified and unmodified Li-Cu cells. From the impedance measurements in Fig.6.12 (a), it becomes evident that there is a trend in the interfacial resistance depending on the content of the SIC polymer. The optimal resistance is recorded for the 70:30 ratio, in agreement with previous studies [3]. It implies decreased charge transfer resistance which, in turn, suggests an improved conductivity. A comparison of the capacity retention of Li-Cu cells with bare and modified Cu electrodes for 25 cycles is shown in Fig.6.12 (b). In general, all samples exhibit similar behavior marked by strong fluctuations of the capacity overtime. Furthermore, 90:10 and 50:50 samples show a strongly decreasing capacity after the 18th cycle. However, the 70:30 sample demonstrates similar capacity values with the bare Cu between the 17th and 23rd cycles and achieves higher capacities during the last two cycles of the measurement. This result provides an indication of improved plating-stripping processes for the 70:30 sample, compared to the other coatings tested in this study. Finally, a comparison of cyclic voltammetry curves for different samples is shown in Fig. 6.12 (c). The first peak occurring at approximately 1.15 V for the bare Cu and 0.9 V for the modified Cu foils is associated to the reduction of lithium nitrate ($LiNO_3$) [4], which was used as an additive in the LiTFSI, DME/DOL (1:1) electrolyte. The reduction of $LiNO_3$ appears to be a onetime process, since it does not repeat in subsequent cycles. The second peak at 0.55 V is related to electrolyte consumption and is present for all samples and for all subsequent cycles of the experiment. The continuous electrolyte consumption is probably connected to the inability of $LiNO_3$ to form a robust SEI alone. It is worth mentioning that 70:30 ratio demonstrates the most intense reduction and electrolyte consumption peaks during the first cycle which suggests better lithium mobility within the cell.

[1] J. Lopez, A. Pei, J. Young Oh, G.-J. N. Wang, Y. Cui, Z. Bao, *JACS* **140**, 11735-11744 (2018)

[2] Z. Huang, S. Choudhury, N. Paul, J. H. Thienenkamp, P. Lennartz, H. Gong, P. Müller- Buschbaum, G. Brunklaus, R. Gilles, Z. Bao, *Adv. Energy Mater.* **12**, 2103187 (2021)

[3] J. L. Olmedo-Martinez, L. Porcarelli, A. Alegria, D. Mecerreyes, A. J. Müller, *Macromolecules* **53**, 4442-4453 (2020)

[4] Y. Lin, J. Chen, H. Zhang, J. Wang, *J. Energy Chem.* **80**, 207-214 (2023)

6.7 Current tab influence on performance of 26650-type LFP lithium-ion batteries

D. Petz, M. J. Mühlbauer[1,2], V. Baran[1,3], J. Rebelo Kornmeier[1], A. Schökel[3], T. Pirling[4], P. Müller-Buschbaum, A. Senyshyn[1]

[1] MLZ, Garching, Germany

[2] IAM/KIT, Karlsruhe, Germany

[3] DESY, Hamburg, Germany

[4] ILL, Grenoble, France

The rapid growth of the electric mobility sector has brought the development of lithium-ion batteries into focus. Among the commonly used layered cathode materials such as LCO, NMC, NCA, the olivine structured lithium iron phosphate (LFP) offers the safest chemistry, leading to a growing share of LFP batteries in the global battery market. In addition, LFP has exceptional cycle rate capabilities that permit high peak charge/discharge currents, making them suitable for high-performance applications, i.e. rapid acceleration and effective recovery of kinetic energy during braking.

Two high-performance lithium-ion batteries of 26650-type with $LiFePO_4||C$ cell chemistry are characterized noninvasively using electrochemical and diffraction-based methods. Their discharge and charge behavior are investigated using incremental capacity analysis and differential voltage analysis normalized to the state of charge. A non-destructive characterization based on synchrotron radiation diffraction in X-ray diffraction computed tomography reveals the lithiation state of cathode and anode materials in the fully charged state under operando conditions, as shown in Fig. 6.13.

The local lithium content in the positive and negative electrodes of the cells under investigation (x in Li_xC_6 and y in Li_yFePO_4) is determined non-destructively by XRD-CT. The investigations are carried out on fresh cells in the fully charged state, and the in-plane lithium distribution is determined at half height. The lithium concentrations obtained are shown in false colors in Fig. 6.13a for the anodes and Fig. 6.13b for the cathodes.

A similar degree of lithiation of the anode is observed: The plane-averaged lithium content in the graphite anode x in Li_xC_6 is determined to be x=0.91(5) and x=0.91(8) in cell 1 and cell 2, respectively characterized by different degrees of lithium distribution. For example, in cell 1, the Li distribution in the plane of lithium content along the graphite anode strip was relatively uniform, comparable to cell #34 from ref. [1]. Cell 2 clearly shows residues of current tabs in its lithium distribution profile and exhibits notable deviations from the mean values at the positions of the current tabs. Ring-shaped features with systematically lower lithiation are observed at the position of the current tabs, towards the center pin and cell casing (similar to the findings in ref. [1]). Evidence of a heterogeneous lithium distribution is also present in the distribution histograms of both cells, with a sharp peak observed in the data from cell 1 (corresponding to a uniform lithium distribution). In contrast, this peak is sufficiently smeared in cell 2, indicating a more heterogeneous lithiation of the anode.

The average lithium content y in the plane of the Li_yFePO_4 cathode is determined for fully charged cell 1 and cell 2 to be y=0.09(8) and y=0.03(9), respectively. The observed lithium distributions in the anode and cathode are complementary, i.e., in areas with lower lithium concentration, the lithium content in the cathode is higher, and vice versa. In contrast to the anode, in cell 1 the lithiation of the cathode displays a weak gradient along the electrode stripe from the cell center to the cell casing. It systematically shows higher lithium concentrations in the cathode area closer to the outer edge. In cell 2, the position of the current tabs at the anode (which have a systematically lower lithiation state) is characterized by the higher lithium contents on the cathode side.

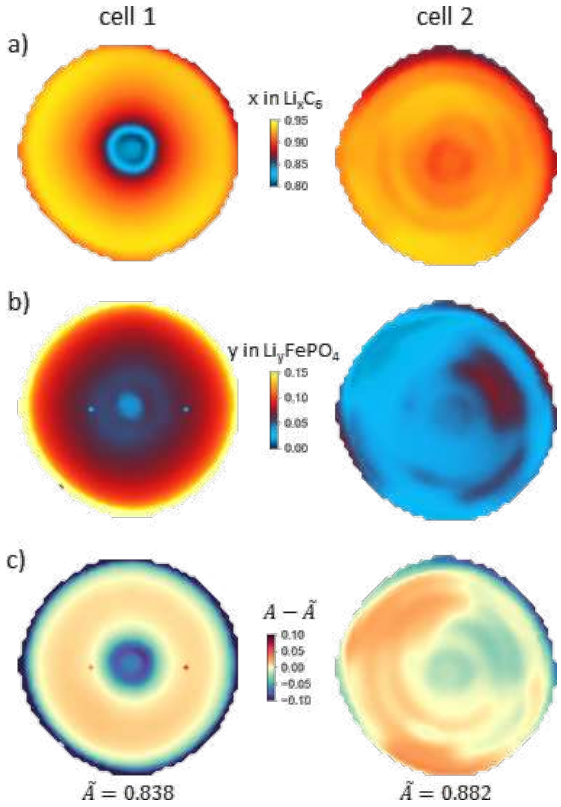

Figure 6.13:
In-plane lithiation of battery electrodes in 26650 cells (at half-height): a) x in Li_xC_6 in the graphite anode, b) y in the Li_yFePO_4 cathode for cell 1 (left) and cell 2 (right), and c) in-plane distribution of electrode "utilization" A-Ã

Based on the observed differences between x and y in cells 1 and 2, one can introduce an "exchange" or "activity" map A, defined as A=x-y, which reflects the local "utilization" of the electrode materials, i.e., the degree to which their potential capacity is utilized. The mean in-plane electrode "utilization" is determined for cells 1 and 2 as A=0.83(8) and A=0.88(2), respectively, showing that cell 2 is potentially more "stressed" during cycling (compared to cell 1). In such a way, quantified electrode stress levels can be directly compared/associated with cell lifetime. To assess the spatial information, the deviation of A from its median is plotted in Fig. 6.13c for both cells. The recorded distributions show that the "exchange" parameter A is homogeneously distributed across the mid-plane of cell 1. In contrast, cell 2 exhibits more significant deviations with systematically lower activities occurring at each current tab location. Positions with higher activities A exhibit the highest accommodated stress during cell cycling, leading to faster material degradation and, correspondingly, faster aging. Based on those mentioned above, it can be concluded that despite the initially higher capacity of cell 2, the extended local "cell usage" would lead to faster degradation of cell 2 compared to cell 1.
The obtained findings can help characterize larger-size Li-ion batteries, which provide higher energy and power densities. A homogeneous usage of the electrode materials can further help increase energy and power densities as well as increase cell safety, i.e., by suppressing dendrite formation.

[1] D. Petz, M.J. Mühlbauer, A. Schökel, K. Achterhold, F. Pfeiffer, T. Pirling , M. Hofmann, A. Senyshyn, *Batteries Supercaps* **4**, 327 (2021)

6.8 Complementary neutron and X-ray measurements on the lithiation mechanism of LiAl electrodes

T. A. Pham, R. Gilles[1], P. Müller-Buschbaum

[1] MLZ, Garching, Germany

Metal alloys, such as LiAl, are gaining more interest as anode materials for lithium-ion batteries because they exhibit a high theoretical capacity while being inexpensive. Aluminum has an almost three times higher specific capacity with $993\,\mathrm{mAh/g}$ in relation to the commonly used graphite anode.[1] During lithiation, aluminum begins to form a solid solution with lithium, the so called α-LiAl phase. Once the solubility limit is reached upon lithiation, the α-LiAl undergoes a phase transition to the β-LiAl phase.[2]
Al electrodes are electrochemically lithiated to different states of charge (SoC) in coin cells with Li metal as a counter electrode with a current rate of C/40. In this study, the 25% lithiation degree is compared to the 50% lithiation degree. Here, 100% lithiation is defined as the pure β-LiAl phase. X-ray diffraction (XRD) measurements are conducted on the disassembled electrodes with the goal of understanding the lithiation mechanism and to determine the fractions of α-and β-LiAl phases (see Fig. 6.14). The quantitative phase analysis yields that 25% lithiated samples show a higher amount of α-LiAl. Simultaneously, the amount of β-LiAl in the samples increases with higher lithiation degrees as expected. Additionally, LiOH can be identified, which is more prominent for the 50% lithiated samples and results from the reaction of Li with the moisture in ambient air.

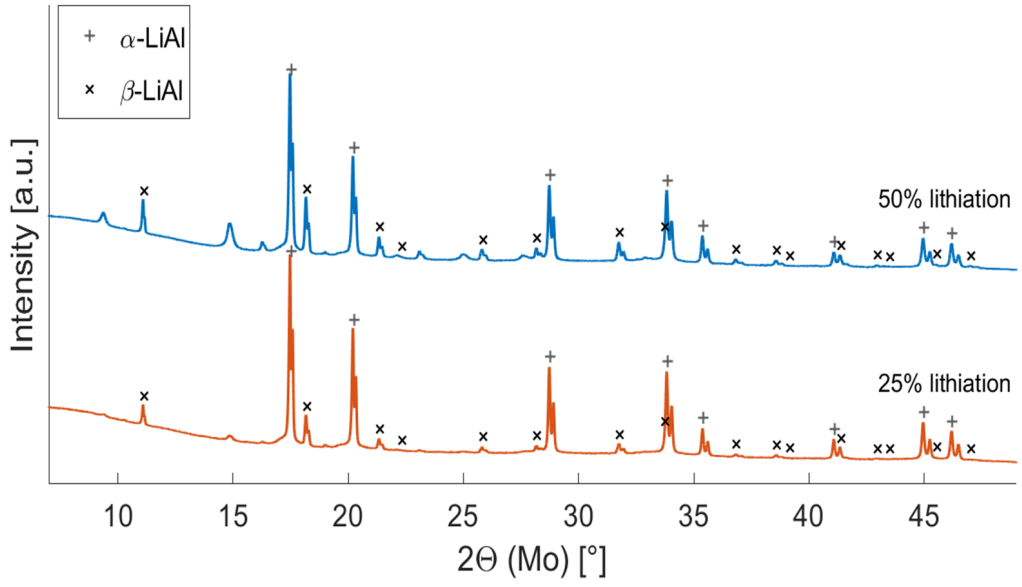

Figure 6.14:
a) XRD patterns for different lithiation degrees (25% and 50%). α-LiAl, β-LiAl and LiOH were identified as phases in the samples. The peaks that are not assigned to LiAl belong to LiOH. The XRD measurements were performed in transmission mode with Mo radiation.

Additional neutron depth profile measurements are performed in NPI CAS Rez at the CANAM infrastructure to determine the Li distribution throughout the lithiated samples. 25% and 50% lithiated samples are compared to an unlithiated pristine Al sample (see Fig. 6.15a). It shows that even with 25% lithiation, the Li already reaches the back of the electrode and confirms the assumption for the Rietveld analysis, that pristine Al is no longer present.

For the 50% sample, the concentration shows a shoulder from 2 µm to 5 µm with a higher slope before this slope declines again (see Fig. 6.15), suggesting the formation of β-LiAl regimes. From 5 µm onwards, the concentration decreases at a slower rate, which is close to the 25% sample. However, the concentration does not reach the value of the 25% lithiation sample in the bulk of the foil and always remains at a higher level throughout the entire thickness. For the 25% lithiated sample, the elevated Li concentration decrease from the surface towards the bulk indicates these β-LiAl regimes. Since the concentration inside the bulk is relatively constant, it can be assumed that it mainly consists of the α-LiAl phase. Furthermore, it is visible that the concentration does not reach zero at any point, which confirms that the electrode is lithiated throughout the whole thickness. For the 50% lithiated sample, the β-LiAl regimes grow further into the bulk, which is visible at elevated concentrations. On both sides of the electrodes, surface peaks could be identified that either result from the formation of a solid-electrolyte interphase, LiOH from the reaction of Li with water or the formation of Li-Al-O glass.

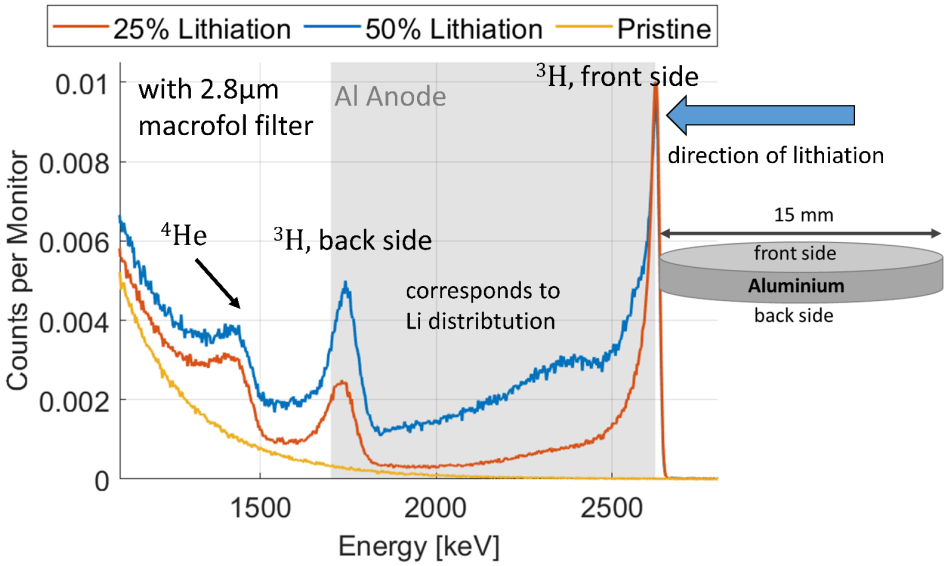

Figure 6.15:
a) NDP spectra for 0%, 25% and 50% lithiation. Li atoms get activated by the neutrons and emit ^{3}H and ^{4}He particles. The detected counts correspond to the Li concentration inside the sample. The energy of the detected ^{3}H and ^{4}He particles give insight into the depth position of the reaction.

[1] H. Wang, H, Tan, X. Luo, H. Wang, T. Ma, M. Lv, X. Song, S. Jin, X. Chang, X. Li, *J. Mater. Chem. A* **8**, 25649-25662 (2020)

[2] D. X. Liu, A. C. Co, *J. Am. Chem. Soc.* **181** (1), 231-238 (2015)

[3] L. Wells, T. A. Pham, G. G. Eshetu, S. Seidlmayer, G. Ceccio, A. Canavo, J. Vacik, A. Mikitisin, P. Müller-Buschbaum, R. Gilles, E. Figgemeier, *ChemElectroChem* **11** e202400322 (2024)

6.9 Understanding of sodium diffusion pathways in NASICON solid-state electrolytes

I. Pivarníková[1], R. Gilles[1], P. Müller-Buschbaum

[1] MLZ, Garching, Germany

Sodium-ion batteries (SIBs) have been extensively studied in the recent decade as a promising alternative to lithium-ion batteries (LIBs), primarily due to sodium's lower cost and greater natural abundance [1]. While many research studies have focused on SIBs utilizing liquid electrolytes, growing safety concerns have driven increasing interest in all-solid-state batteries (ASSBs). Solid electrolytes offer several key advantages, including non-flammability, non-toxicity, non-volatility, and enhanced thermal stability. Furthermore, replacing liquid electrolytes with solid-state electrolytes could enable the use of high-voltage cathode materials and Li/Na metal anodes, enabling the way for next-generation high-energy-density ASSBs. The main challenge lies in identifying a solid electrolyte with high ionic conductivity ($> 10^{-3}$ S cm^{-1}), a wide electrochemical stability window, and low production costs.

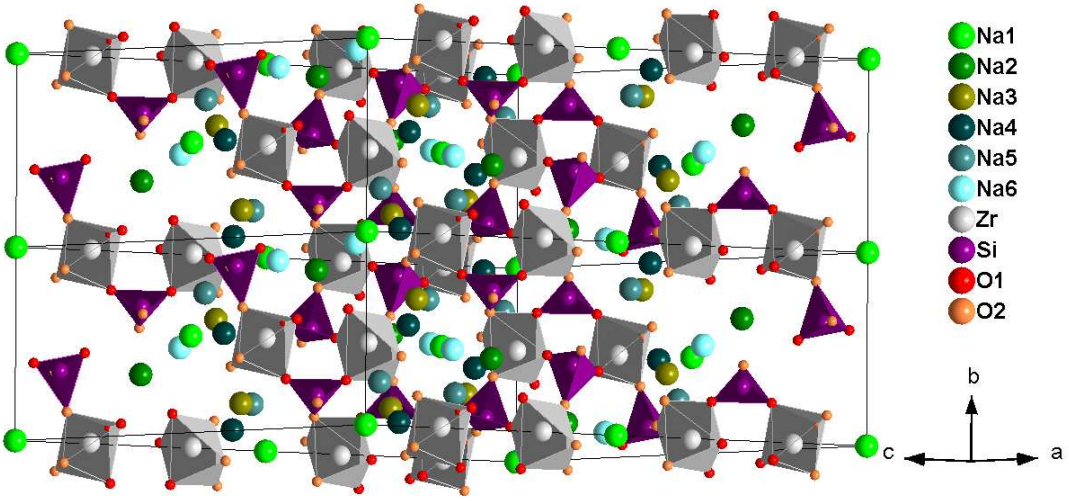

Figure 6.16:
NASICON structure: $Na_{1+x}Zr_2Si_xP_{3-x}O_{12}$ ($0 \leq x \leq 3$) consisting of corner-sharing ZrO_6 octahedra and PO_4/SiO_4 tetrahedra and mobile Na positions: monoclinic $C2/c\, f^{12}e^2a$ structure model. Visualized with Endeavour software [2]. Adapted from [3].

NASICON (sodium superionic conductor)-based ceramics are among the most promising solid-state electrolytes for all-solid-state batteries [4]. Their exceptional ionic conductivity is generally attributed to variations in Na^+ concentration, where an optimal balance between occupied and vacant sodium sites is needed. The maximum sodium occupancy per unit cell is 4. The presence of Na vacancies is crucial to allow Na^+ diffusion within the structure. However, the sodium ion diffusion mechanism remains not completely understood, as discrepancies persist between reported average structure models, local structures, and the number and positions of sodium sites.

To bridge this gap, this study investigates the diffusion mechanism and structural evolution governing Na^+ transport in $Na_{1+x}Zr_2Si_xP_{3-x}O_{12}$ ($0 \leq x \leq 3$) using multimethod study including quasielastic neutron scattering (QENS) and powder X-ray diffraction (XRD). Structural changes associated with the monoclinic $C2/c$ to rhombohedral $R\bar{3}c$ phase transition and their

impact on sodium ion diffusion are here examined over the temperature range of 298 K to 640 K.

The final monoclinic $C2/c\ f^{12}e^2a$ structure from Rietveld-refined XRD data with six available Na sites, where Na can migrate is shown in Fig. 6.16. Analysis of the QENS data reveals that Na^+ migration in this NASICON material corresponds to the Chudley-Elliott jump diffusion model, demonstrating two distinct Na^+ diffusive motions on two different time and length scales. In this model, Na^+ migrates between crystallographic sites by a series of successive jumps. The combination and direct comparison of results from both methods reveals the sodium diffusion pathways: local and long-range diffusion processes.

In Fig. 6.17, the Na-Na interatomic distances extracted from XRD refinements as a function of measured temperature are shown. They are compared with QENS-derived jump diffusion distances and show the shortest Na-Na distance through which local, long-range chain diffusion and, afterward, long-range cross-chain Na^+ diffusion occur. The localized short-range faster motion describes local in-cage diffusion concentrated around the Na1 site and is dominant under ≈ 400 K. Above 400 K, the local diffusion is still present. However, two separate long-range diffusion processes start to take place. Such a systematic study offers significant insights into the family of NASICON ceramic solid-state materials, which aims to improve its application for next-generation of ASSBs.

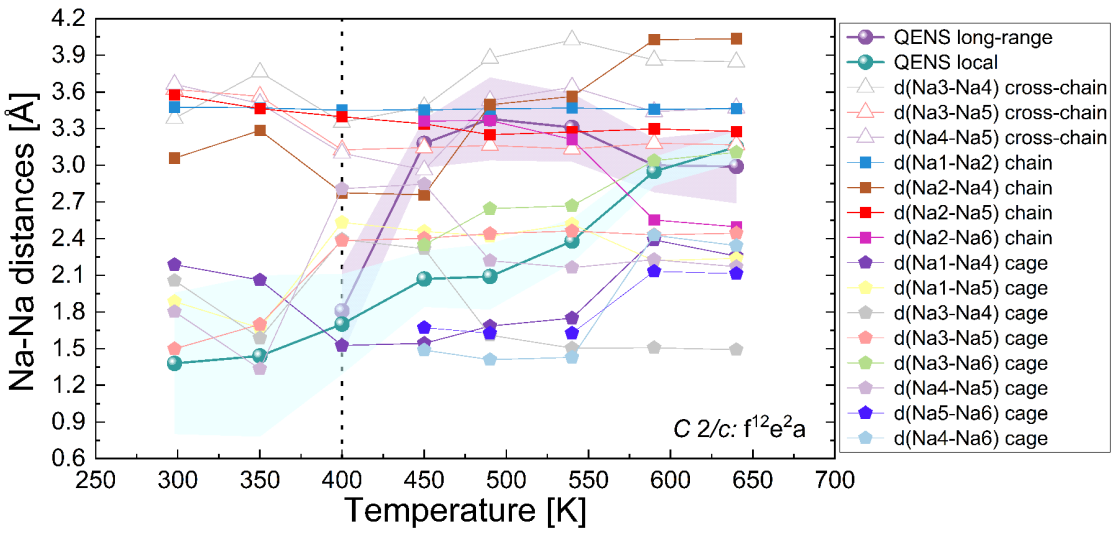

Figure 6.17:
Comparison of all relevant XRD Na-Na distances for the monoclinic $C2/c\ f^{12}e^2a$ model with QENS. The purple and blue areas mark the upper/lower error limits for QENS-derived jump distances. The dashed line indicates a change in diffusion mechanism at ≈ 400 K. Solid lines are guides to the eye. Adapted from [3].

[1] K. Chayambuka, G. Mulder, D. L. Danilov, P. H. L. Notten, *Adv. Energy. Mater.* **10**, 2001310 (2020)

[2] H. Putz and K. Brandenburg, *Endeavour - Structure Solution from Powder Diffraction*, https://www.crystalimpact.de/endeavour, (accessed 08/10/2024)

[3] I. Pivarníková, S. Seidlmayer, M. Finsterbusch, G. Dück, N. Jalarvo, P. Müller-Buschbaum, R. Gilles, *submitted* (2025)

[4] M. Guin and F. Tietz, *J. Power Sources* **273**, 1056-1064 (2015)

6.10 Analysis of $LiCoO_2$ surface components after cycling in the electrode with PIM-1 additives

R. Qi, X. Liu[1, 3], Y. Xia[1], Y-J. Cheng[1, 2], P. Müller-Buschbaum

[1] NIMTE, Ningbo, China
[2] HHU, Changzhou, China
[3] SHU, Shanghai, China

$LiCoO_2$ (LCO) maintains a clear competitive edge over other cathode materials, owing to its straightforward synthesis, high compact density, impressive initial Coulombic efficiency, outstanding cycling stability, and high voltage plateau. However, it often comes hand in hand with significant capacity decay and performance degradation when raising the cut-off voltage. When the cut-off voltage reaches 4.5 V, LCO may undergo harmful phase transitions (from the O3 phase to the H1-3 metastable phase) and structure collapse, resulting in a gradual voltage fading and a capacity deterioration.[1] Moreover, the cathode-electrolyte interphase (CEI) layer is unstable. Co^{4+} ions tend to dissolve in the electrolyte under high voltage, which accelerates the decomposition of the electrolyte and leads to undesired interfacial side reactions. This decreases the electrochemical kinetics and increases the capacity decay.[2] Therefore, it still remains a challenge to achieve a practical LCO based battery working at 4.5 V with stable cycling. Herein, we propose an additive to prepare the electrode, which uses a tiny amount of multifunctional polymer of intrinsic microporosity (PIM-1) to stabilize LCO at 4.5 V without any other binder. PIM-1 is a kind of microporous organic polymer which relies on its own rigidity and nonplanar distorted structure of the molecules to form micropores. In this work, we demonstrate that multiple issues occurring for LCO at a high voltage can be addressed by introducing PIM-1 as a multifunctional cathode additive to replace the PVDF binder during the process of electrode fabrication. PIM-1 can inhibit the destruction of the LCO lattice to a certain extent under the high-voltage condition with a tiny amount (0.5%) of addition. Moreover, PIM-1 molecules play a crucial role in forming the stable, inorganic rich CEI layer. Consequently, this work focuses on analyzing the component changes of LCO electrodes before and after cycling.

The content and composition of the CEI film are analyzed by XPS, as shown in Fig. 6.18. Fig. 6.18a shows the elemental content of the CEI on the surface of the electrodes before and after cycling. After cycling, the content of F and Li in the CEI on the surface of the LCO/PIM-1 electrode significantly increases, whereas the surface F and Li elemental content of the LCO/PVDF electrode changes minimally. Additionally, there is a slight increase in the P content on the surface of LCO/PIM-1. The valence states of each element on the surface are determined through curve fits of the N 1s, C 1s, O 1s, P 2p, and F 1s spectral peaks. In Fig. 6.18b and c, the changes of the valence state of the N before and after cycling in the LCO/PIM-1 and LCO/PVDF electrodes are displayed respectively. For LCO/PVDF electrodes, there is almost no N element in the CEI before and after cycling. However, for LCO/PIM-1 electrodes, the C≡N peak before cycling originates from -CN in PIM-1, and after cycling, it exhibits the presence of inorganic N-O peaks and N-Li peaks in the CEI. Fig. 6.18d and e illustrate the valence states of C and O on the electrode surfaces after cycling. It can be observed that LCO/PIM-1 exhibits weaker peak intensities of C-O and C=O bonds than LCO/PVDF (Fig. 6.18d), implying the less byproducts of carbonate solvents decomposition. These findings indicate that compared to the LCO/PVDF electrode, the CEI on the LCO/PIM-1 electrode contains fewer organic compounds and generates inorganic compounds with P-O bonds. [3] Additionally, to investigate the formation process of inorganic compounds in the CEI during cycling, ex-situ XPS is used to determine the changes of the valence states of P and F elements on the cathode surface before cycling, after 1 cycle, 10 cycles,

50 cycles, and 100 cycles, as shown in Fig. 6.18f-i. In Fig. 6.18f-g, the LCO/PVDF electrode surface exhibits a significant formation of F-P-O bonds and a smaller amount of P-O bonds as the number of cycles increases, whereas the opposite trend is observed in the LCO/PIM-1 electrode. Considering the analysis of F in Fig. 6.18h i, it becomes evident that a substantial amount of LiF is formed gradually on the surface of the LCO/PIM-1 electrode. The fit results indicate that the addition of PIM-1 promotes the formation of LiF and LixPFyOz compounds in the CEI on the cathode surface. The enhanced formation of inorganic LiF species at the surface of the LCO electrode surface helps to stabilize the CEI layer and thus to improve the cyclic stability. Moreover, compared to the organic-rich components, inorganic-rich components possess a higher ionic conductivity and better electrochemical stability, which further accelerates the electrochemical kinetics within the CEI layer and at the interface, leading to improving the rate performance in the LCO/PIM-1||Li batteries.

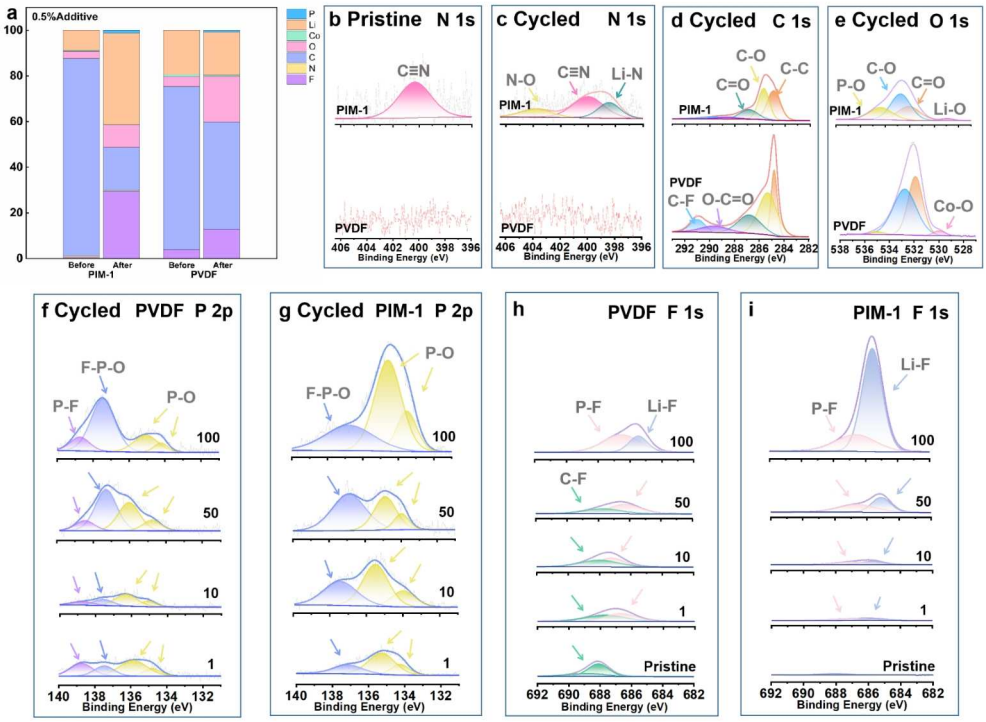

Figure 6.18:
a) Quantitative analysis of the elementary compositions at the surface of the LCO/PIM-1 and LCO/PVDF electrodes before and after 100 cycles; N 1s XPS spectra of the LCO/PIM-1 electrodes and LCO/PVDF electrodes before b) and after c) 100 cycles; d) C 1s and e) O 1s XPS spectra of the LCO/PIM-1 electrodes and LCO/PVDF electrodes after 100 cycles; and P 1s (LCO/PVDF (f) and LCO/PIM-1 (g)) and F 1s (LCO/PVDF (h) and LCO/PIM-1 (i)) XPS spectra before and after different cycles.

[1] Y. Huang, Y. Zhu, H. Fu, M. Ou, C. Hu, S. Yu, Z. Hu, C. T. Chen, G. Jiang, H. Gu, H. Lin, W. Luo, Y. Huang, *Angew. Chem. Int. Ed.* **60 (9)**, 4682-4688 (2021)

[2] M. S. Kim, Z. Zhang, P. E. Rudnicki, Z. Yu, J. Wang, H. Wang, S. T. Oyakhire, Y. Chen, S. C. Kim, W. Zhang, D. T. Boyle, X. Kong, R. Xu, Z. Huang, W. Huang, S. F. Bent, L. W. Wang, J. Qin, Z. Bao, Y. Cui, *Nat. Mater.* **21 (4)**, 445-454 (2022)

[3] W. M. Seong, K. Yoon, M. H. Lee, S.-K. Jung, K. Kang, *Nano Letters* **19 (1)**, 29-37 (2019)

6.11 Multi-localized-high-concentration lithium-ion electrolytes improve the interface of electrode/electrolyte

W. Guo, T. Zheng, P. Müller-Buschbaum

Conventional carbonate-based electrolytes have been extensively utilized in lithium-ion batteries for over three decades. However, only a limited number of these electrolytes exhibits sufficient stability under the more demanding conditions required with a Li metal anode. Precise control over the solvation structure can mitigate the adverse effects caused by certain solvent molecules. Consequently, several alternative and innovative electrolyte systems have been reported, including high-concentration electrolytes (HCE)[1] and weakly solvating electrolytes (WSE)[2]. In this project, we propose a novel concept of multi-localized-high-concentration electrolytes (MLHCE) using lithium dual-salt to construct a unique solvation structure that forms a solid electrolyte interface (SEI) layer. Various electrochemical measurements are done and SEM techniques are used to investigate the influence of different solvation structures on lithium deposition and SEI layer formation in order to enhance the long-term performance and high-rate capability of lithium metal batteries.

Four electrolytes are tested in Li/Al and Li/Cu cells. Among these four electrolytes, DFN is the electrolyte that is used in the MLHCE system. In Li/Al cell, linear sweep voltammetry is measured while in Li/Cu cell, the results of cyclic voltammetry are obtained. As shown in Fig. 6.19. In Fig. 6.19a, it can be seen that HCE has the earliest onset potential, around 3.8V. While LCE starts rising at a potential slightly above 4.0 V. Then, DN and DFN have onset potentials very close to 4.2 V. The HCE system initiates the reaction at the lowest potential, indicating that it might be the most reactive or least stable among the tested conditions. In contrast, DN and DFN have the highest onset potentials, suggesting greater stability or resistance to decomposition. Besides, DN and DFN systems show the highest stability, with their currents remaining low until around 4.2 V, indicating that these systems are more resistant to electrochemical reactions until higher potentials are reached. HCE exhibits less stability as they start reacting at lower potentials.This LSV analysis suggests that HCE is a more reactive system that initiates electrochemical processes at lower potentials, which might be beneficial for certain applications but could also lead to stability issues. On the other hand, DN and DFN are more stable, with higher onset potentials, making them more suitable for applications requiring high-voltage stability.

The CV curves also demonstrate the excellent electrochemical behavior of DFN. When the scan rate is in 5mV/s (Fig. 6.19b), the CV curves at this scan rate show broad, indistinct redox peaks. The oxidation and reduction processes are not well-defined, especially for LCE and HCE, suggesting minimal redox activity or diffusion-limited behavior. The DFN electrolyte shows slightly higher current responses, indicating better redox activity. However, when the scan rate rises to 10mV/s (Fig. 6.19c), more pronounced oxidation and reduction peaks are observed for DN and DFN electrolytes around 0.4 V. DFN, in particular, shows the most significant redox peaks, indicating efficient oxidation and reduction reactions due to better electrode/electrolyte interactions. The higher current response of DFN also suggests better electrochemical activity and potentially higher ionic conductivity. This behavior is more prominent in the 10 mv/s graph. In conclusion, increasing the scan rate from 5 mV/s to 10 mV/s amplifies the peak currents, particularly for DN and DFN, indicating that these systems have faster electron transfer kinetics. DFN stands out as having the most significant response to the increased scan rate, highlighting its potential for high-performance applications.

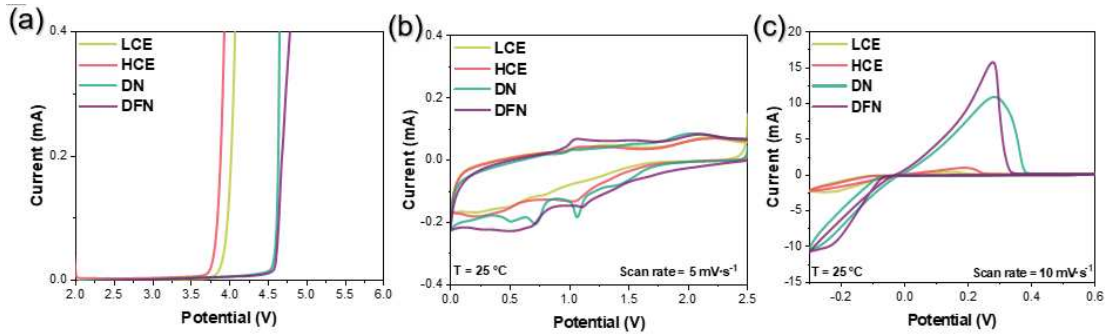

Figure 6.19:
Electrochemical testing results for four electrolytes a) Linear Sweep Voltammetry, b) Cyclic Voltammetry with rate in 5mV/s and C) Cyclic Voltammetry with rate in 10 mV/s.

In SEM measurements, lithium deposition on copper electrodes of batteries with four electrolytes are observed with the magnification of 1k. The morphology of the deposits caused by these four electrolytes varies and the detailed results and analyses are shown below. For the LCE electrolyte(Fig.6.20a), SEM shows that the surface appears rough with a large number of irregular, needle-like structures, indicative of lithium dendrite formation. The dendrites are densely packed and distributed unevenly across the surface. For the HCE(Fig.6.20b), the surface morphology is similar to that of LCE, with a dense network of lithium dendrites. However, the dendrites seem slightly less pronounced and more clumped together, indicating a marginally better performance in terms of reducing dendrite formation compared to LCE. In the DN electrolyte(Fig. 6.20c), the surface shows a more uniform deposition with fewer dendrites compared to LCE and HCE. The dendrites present are shorter and less densely packed, indicating a reduction in dendrite formation. Lastly, in the DFN electrolyte(Fig. 6.20d), the surface appears the most uniform and smooth among all the electrolytes. Dendrite formation is minimal, with the surface largely free from the needle-like structures seen in the other electrolytes. The SEM images reveal a clear trend in the effectiveness of the electrolytes in preventing lithium dendrite formation.

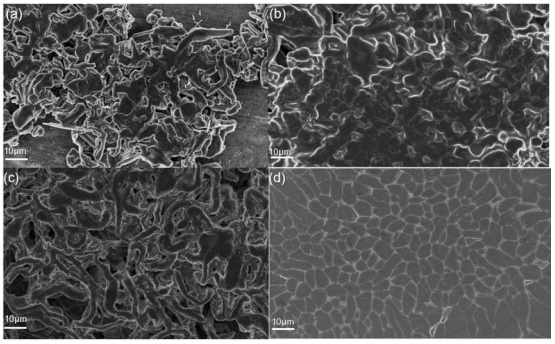

Figure 6.20:
SEM results of four electrolytes a) LCE, b) HCE, C) DN and d) DFN.

In summary, DFN exhibits the best performance, with minimal dendrite formation, leading to a smooth and uniform electrode surface. This surface morphology analysis aligns well with the CV results, where DFN showed the highest current responses and the most distinct redox peaks, indicating superior electrochemical activity and stability.

[1] Yamada Y, Furukawa K, Sodeyama K, Kikuchi K, Yaegashi M, Tateyama Y, Yamada A, *JACS* **136**, 24654781 (2014)

[2] Wang Z, Zhang B, *Energy Materials and Devices* **1**, 9370003 (2023)

6.12 Temperature-resolved crystal structure of ethylene carbonate

L. Westphal, V. Kochetov[1], V. Baran[2], M. Avdeev[3,4], P. Müller-Buschbaum, A. Senyshyn[1]

[1] MLZ, Garching, Germany
[2] DESY, Hamburg, Germany
[3] ANSTO, Sydney, Australia
[4] University of Sydney, Sydney, Australia

Lithium-ion batteries (LIBs) have been widely used as power sources for portable electronics and are of interest for electric vehicles and network applications (large-scale electricity storage). While there have been significant changes from the initial design of the LIBs, the main solvents constituting the liquid electrolyte, responsible for the charge transfer between the electrodes, remained mostly unchanged [1]. An important class of solvents used in liquid electrolytes are linear and cyclic carbonates because of the combination of properties in a mixture with two or more solvents with a lithium salt and additives [1]. Ethylene carbonate (EC), with its high dielectric constant [1] and ability to provide the protective SEI layer, is present in almost all commercial batteries, mixed with other solvents due to its high melting point, being solid at room temperature [2]. In the presented project, the long- and short-range order of EC is studied. EC crystallizes in the monoclinic space group $C2/c$, and the model proposed by Matias *et al.* is used as a starting point for Rietveld refinement [3]. The analyzed datasets present the temperature-dependent evolution of the unit cell from 3 K up to 310 K measured by neutron and synchrotron powder diffraction. The neutron data was collected at the high-resolution powder diffractometers SPODI, FRM II (Munich, Germany) at room temperature and temperature-dependent from 3 K up to 300 K at Echidna, ANSTO (Sydney, Australia). Additionally, synchrotron measurements from 100 K to 310 K were performed at the powder diffraction beamline P02.1, DESY (Hamburg, Germany). The structural model obtained from the simultaneous refinement of powder diffraction data taken at all three instruments at room temperature is displayed in Fig. 6.21a). During temperature dependent powder diffraction measurements upon heating, a pronounced temperature dependence of lattice dimensions was observed. The behavior of the cell parameters upon heating, obtained from Rietveld refinement of the temperature-dependent data, is presented in Fig. 6.21b).

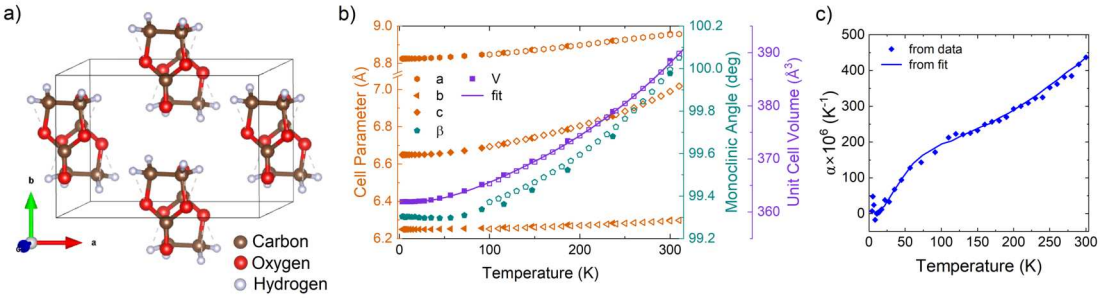

Figure 6.21:
a) Structural model of the unit cell of Ethylene Carbonate at room temperature from simultaneous Rietveld refinement of neutron and synchrotron powder diffraction data at Echidna (ANSTO), SPODI (FRM II) and P02.1 (DESY). b) Evolution of the cell parameters a, b, and c, the monoclinic angle β, and the unit cell volume upon heating from neutron (solid symbols) and synchrotron (open symbols) data, with a fit to the volume according to the Mie-Grüneisen equation of state. c) Thermal expansion of EC as calculated from refined unit cell volume (symbols) and from the Mie-Grüneisen fit (line).

The thermal expansion of the volume can be parametrized in the framework of a Debye model for the internal energy [4]. The internal energy of the crystal is split into two separate contributions, coming from the molecules and the whole lattice. Assuming the Grüneisen parameter γ and the bulk modulus K to be temperature independent, the thermal evolution of the unit cell volume can be described within the first order Grüneisen approximation as follows

$$V(T) = V_0 + 9\frac{\gamma}{K}k_\mathrm{B}T\left[N_1\left(\frac{T}{\theta_{\mathrm{D},1}}\right)^3\int_0^{\frac{\theta_{\mathrm{D},1}}{T}}\frac{x^3\mathrm{d}x}{\mathrm{e}^x-1} + N_2\left(\frac{T}{\theta_{\mathrm{D},2}}\right)^3\int_0^{\frac{\theta_{\mathrm{D},2}}{T}}\frac{x^3\mathrm{d}x}{\mathrm{e}^x-1}\right]$$

with the number of atoms per unit cell split into both Debye terms N_1 and N_2, and $\theta_{\mathrm{D},1}$ and $\theta_{\mathrm{D},2}$ being the Debye temperatures. The best fit is obtained with the Debye temperatures being $\theta_{\mathrm{D},1} = 201(10)\,\mathrm{K}$ and $\theta_{\mathrm{D},2} = 2063(60)\,\mathrm{K}$. From the evolution of the volume of the unit cell, the volumetric thermal expansion was calculated and is presented in Fig. 6.21c). The anomalous behavior displayed by an additional increase of the thermal expansion coefficient after reaching an initial plateau supports the idea of a second Debye temperature.
Additionally, the short-range order in EC was investigated by Pair Distribution Function (PDF) analysis. Fig. 6.22a) shows PDFs obtained from measurements at P02.1 and the Swiss-Norwegian Beamline BM31, ESRF (Grenoble, France) at room temperature together with respective fits to the unit cell. The unit cell parameters and fractional atomic coordinates resulting from the fits align with the unit cell refined from powder diffraction. At P02.1, measurements were also performed on molten EC after heating the sample over the melting point as seen in Fig. 6.22b). Looking at a larger r range, the long-range order can clearly be seen in the PDF of solid EC. After melting, no order can be seen above a distance of 3.4 Å, showing the loss of long-range order while the molecular geometry is preserved.

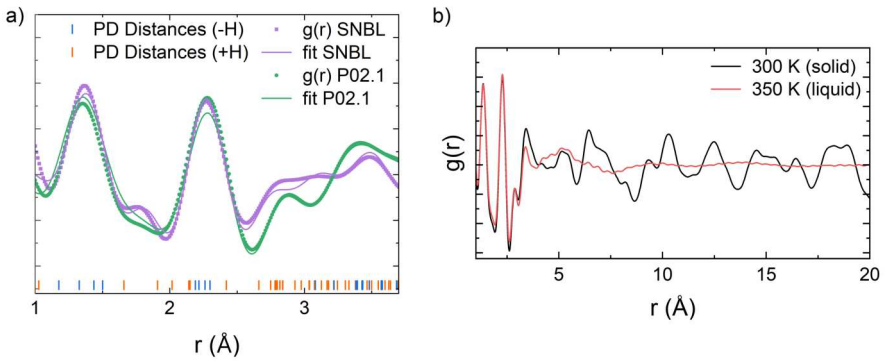

Figure 6.22:
a) Pair distribution functions of EC at 300 K obtained at BM31 (purple symbols) and P02.1 (green) with corresponding fits to the unit cell structure. For comparison, the blue and orange bars at the bottom indicate atomic distances from powder diffraction, excluding and including hydrogen. b) Comparison of pair distribution functions obtained at P02.1 before and after melting, showing the loss of long-range order at r > 3.4 Å.

[1] B. Flamme, G. Rodriguez-Garcia, M. Weil, M. Haddad, P. Phansavath, V. Ratovelomanana-Vidal A. Chagnes, *Green Chem.* **19**, 1828-1849 (2017)

[2] J.-M. Tarascon, M. Armand, *Nature* **414**, 359-367 (2001)

[3] P. M. Matias, G. A. Jeffrey, L. M. Wingert, J. R. Ruble, *J. Mol. Struct. THEOCHEM* **184**, 247-260 (1989)

[4] L. Vočadlo, K. S. Knight, G. D. Price, I. G. Wood, *Phys. Chem. Miner.* **29**, 132-139 (2002)

6.13 A small amount of sodium difluoro(oxalate)borate additive induces anion-derived interphases for sodium-ion batteries

L. Xia, P. Müller-Buschbaum

In sodium-ion batteries (SIBs), the properties of the electrode-electrolyte interphases (EEIs) influence the battery performance [1, 2]. In this work, we propose the utilization of a very small amount of 0.5% sodium difluoro(oxalate)borate (NaDFOB) additive to manipulate the structure of the electric double layer (EDL) on the electrode/electrolyte interface to construct anion-derived EEIs. By preferentially adsorbing at the inner Helmholtz plane (IHP) of both electrode surfaces, $DFOB^-$ induces the formation of anion-derived, NaF-dominated, and inorganic-rich EEIs. Consequently, Na half-cells and Na full-cells can achieve an excellent cycling ability.

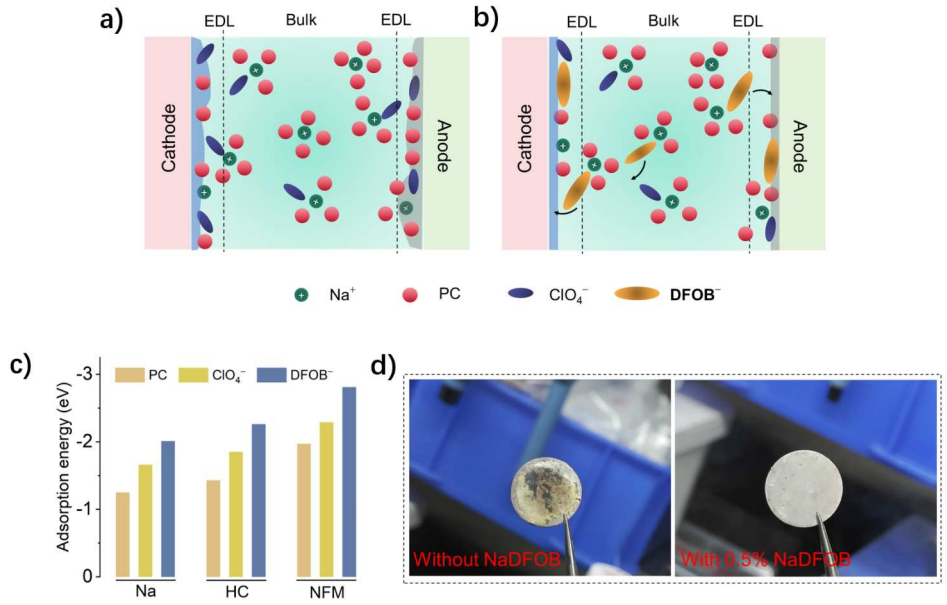

Figure 6.23:
Schematic illustration of a) traditional EDLs leading to continuous decomposition and inducing the formation of solvent-derived EEIs and b) $DFOB^-$-induced EDLs facilitating the formation of anion-derived inorganic-dominated EEIs. c) Adsorption energy (E_{ads}) for PC solvent molecules, ClO_4^- ions, and $DFOB^-$ ions on Na metal, HC anode and NFM cathode, respectively. d) Photographs of the Na metal stored in the electrolytes with and without NaDFOB after 10 days at room temperature.

Herein, a small amount additive of 0.5% NaDFOB is introduced into 1 mol L^{-1} $NaClO_4$/propylene carbonate (PC) electrolyte to construct a robust inorganic-rich EEIs (Fig. 6.23). In contrast, a traditional EDL promotes the continuous decomposition of the electrolyte due to a large number of free solvents, leading to the formation of a solvent-derived and thick interphase during the cycling process (Fig. 6.23). We summarize the adsorption energies of for PC solvent molecules, ClO_4^- ions, and $DFOB^-$ ions on Na metal, Mn-based layered oxides ($Na_xNi_{0.25}Fe_{0.25}Mn_{0.5}O_2$, NFM) cathode, and hard carbon (HC) anode, respectively. As seen, on all electrode surfaces, the adsorption energy decreases in the order of $DFOB^-$, ClO_4^-, PC, indicating that $DFOB^-$ anions are the dominating ions in the IHP, thereby actively participating in the formation of $DFOB^-$ anion-derived EEIs on both two electrodes. Then we put fresh Na foils in two different electrolytes and let them stand for 10 days at 25°C. As depicted in Fig. 6.23,

the color of the electrolyte without NaDFOB turns from colorless to yellow, with the Na foil displaying significant changes. In contrast, the electrolyte containing NaDFOB retains its original color, and the surface of the Na foil appears gray-white. Further verification reveals that the incorporation of $DFOB^-$ into the electrolyte facilitates the formation of a stable interphase layer through $DFOB^-$ preferential adsorption-decomposition.

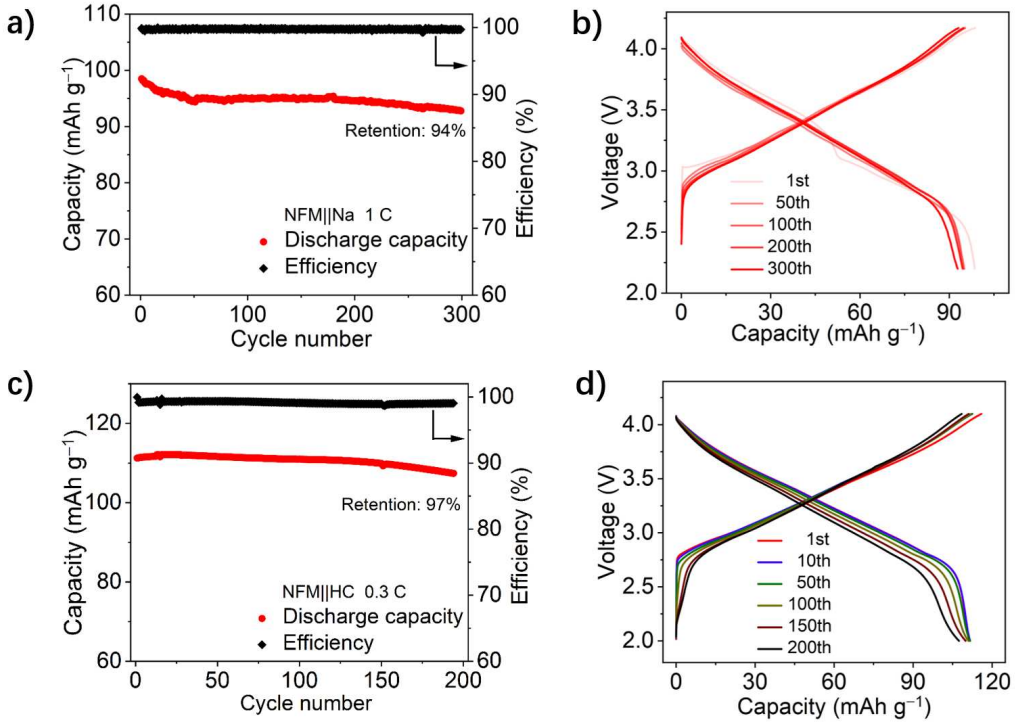

Figure 6.24:
a) Long-cycling stability b) and charge-discharge curves of NFM cathode in the NaDFOB containing electrolyte at 1.0 C. The cycling performance c) and the corresponding charge-discharge curves d) of the NFM-HC full-cell at 0.3 C.

We evaluate the long-term cycling stability of the NFM cells without/with the 0.5% NaDFOB electrolytes at 1 C, as displayed in Fig. 6.24. After 300 cycles, the capacity fades from 98.5 mAh g^{-1} to 92.8 mAh g^{-1}, which corresponds to capacity retention of 94.2% and an average CE of 99.7%. Fig. 6.24 shows the nearly overlapping charge-discharge curves for different cycles, which further confirm an excellent cycling performance of the NFM electrode in the NaDFOB electrolyte. Then, we measure the viability of the NaDFOB-containing electrolyte for the NFM-HC full cell 0.3 C. For the NFM-HC full cell, the reversible capacity of the full cell fades from 111.3 to 107.4 mAh g^{-1} after 200 cycles, with a capacity retention of 97%, and the average CE remains 99%, demonstrating an excellent cycling stability. The results suggest that the proposed trace amount of the NaDFOB-additive possess a significant advantage in enabling excellent cycling stability for the batteries.

[1] Q. Qiu, T. Zheng, L. Huang, T. Xu, L. Pan, W. Sun, H. Tian, W. Zhang, Q. Yu, Y. Liang, Y. Yan, J. Yuan, P. Müller-Buschbaum, L. Xia *Energy Stor. Mater.* **73**, 103858 (2024)

[2] L. Huang, Q. Qiu, M. Yang, H. Li, J. Zhu, W. Zhang, S. Wang, L. Xia, P. Müller-Buschbaum, *ACS Appl. Mater. Interfaces* **16**, 46392-46400 (2024)

6.14 Stabilizing $LiNi_{0.5}Co_{0.2}Mn_{0.3}O_2$ at 4.6 V and boosting its capacity via ultra-thin Al_2O_3 layers

Z. Xu, X. Fan[1], Y. Xia[1], Y. Cheng[1], P. Müller-Buschbaum
[1] NIMTE, Ningbo, China

As a core technology of electric vehicles (EVs), lithium-ion batteries with high energy density, safety and long cycling life, are being intensively developed, driven by the growing demand applications of the EVs. Ni-rich layered cathode materials ($LiNi_xCo_yMn_zO_2$, x+y+z=1) have garnered significant attention from both academia and industry due to their high theoretical capacity and elevated working voltage. Increasing the working voltage of the $LiNi_{0.5}Co_{0.2}Mn_{0.3}O_2$ (NCM523) cathode to 4.6 V can further enhance its specific capacity as well as energy density, and improving the utilization of lithium ions within the NCM523, thus solidifying its advantages over other cathode materials. However, this higher voltage (e.g. 4.6 V) compromises its cycling stability, making it less suitable for real-world applications. At high voltages, on the one hand, excessive decomposition of carbonate electrolyte solvents and the formation of an overly thick cathode-electrolyte interface (CEI) layer are promoted, On the other hand, the lattice oxygen in the NCM lattice is continuously lost, resulting in structural collapse and irreversible phase transitions.

Constructing a stable CEI layer is an effective strategy to achieve good electrochemical kinetics by inhibiting oxidative decomposition of the carbonate- based electrolyte. To achieve this goal,we present a method to modify the cathode electrode containing the Ni-rich layered materials (Herein: NCM523). By applying an ultra-thin Al_2O_3 layer measuring 0.4 nm in thickness, the enhanced cathode electrolyte interphase (CEI) layer significantly improves the structural stability of NCM523, particularly at high oxidation potential (4.6 V).

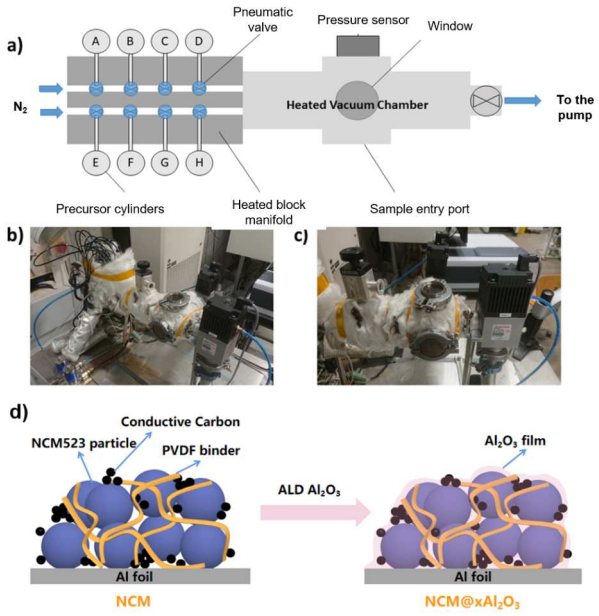

Figure 6.25:
a) Schematic top-view representation of the ALD set-up, b) picture of the overall system, c) glass wool covered vacuum chamber, d) schematic diagram of the formation process of NCM523@xAl_2O_3 electrode.

As showed in Fig 6.25a-c, the pristine NCM523 electrodes are placed in the reaction chamber. Pre-pumping and heating of the chamber and block manifold until reaching <0.04 mbar, 130

°C and 50 °C, respectively. Trimethyl aluminum (TMA, 98 %, Strem) and hydrogen peroxide (H_2O_2, 30 wt% in water, Sigma Aldrich) are used as Al and O precursors, respectively. All precursors are loaded in stainless steel cylinders. TMA and H_2O_2 precursors are heated at 30 °C, then the N_2 flow rate is adjusted to 20 mL min^{-1}, yielding a background pressure of 0.17-0.20 mbar. Then, the ALD Al_2O_3 reaction cycle is decoupled in the following steps: (1) 10 s of pumping time, (2) 0.1 s TMA pulse, (3) purging the chamber with the pure nitrogen flow for 15 s, which is enough to attain the background pressure and remove by-products, (4) 0.5 s H_2O_2 pulse, (5) purging the chamber with the pure nitrogen flow for 15 s, which is enough to attain the background pressure and remove by-products. This sequence constitutes an ALD cycle. The samples are denoted as NCM523@xAl_2O_3, where x is the number of ALD cycles. Schematic diagram of the formation process of NCM523@xAl_2O_3 electrode is shown in Fig. 6.25d.

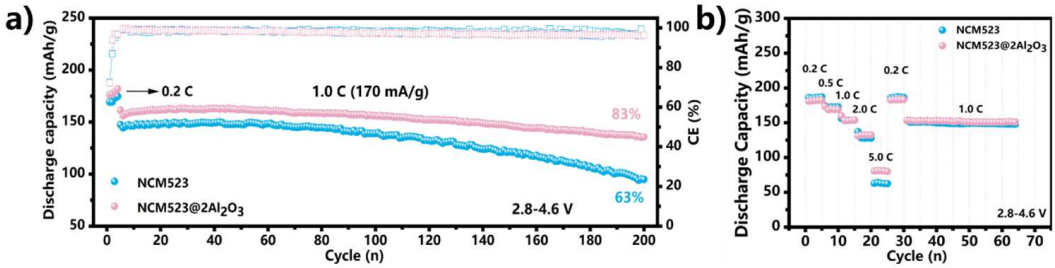

Figure 6.26:
Cycling performance (a) and rate performance (b) of NCM523||Li and NCM523@2Al_2O_3||Li half-cells at 2.8-4.6 V.

Cyclic stability is an important factor in improving the driving range of electric vehicles. Fig. 6.26a shows the performance of NCM523||Li and NCM523@2Al_2O_3||Li half-cells at a rate of 1 C (1 C = 170 mA g^{-1}) for 200 cycles between 2.8 V and 4.6 V. The initial NCM523 electrode shows a discharge specific capacity of 150 mAh g^{-1} at 1 C, and the discharge specific capacity of 95 mAh g^{-1} after 200 cycles (capacity retention 63%). In contrast, the NCM523@2Al_2O_3 electrode exhibits a discharge specific capacity of 163 mAh g^{-1}, which still maintains at 136 mAh g^{-1} after 200 cycles (capacity retention 83%). It is observed that the NCM523@2Al_2O_3 electrode has a higher reversible capacity and capacity retention than the pristine NCM523. The results indicate that the Al_2O_3 coating through 2 cycles of ALD deposition helps to alleviate the capacity fading of NCM523 at 4.6 V, and the ultra-thin The Al_2O_3 layer does not sacrifice the capacity of NCM523 cathode. The impact of the ALD coating on the rate performance of the NCM523 cathode between 2.8 V and 4.6 V is investigated (Fig. 6.26b) with the current densities increased sequentially from 0.2 C, 0.5 C, 1 C, 2 C to 5 C, and then returned to 0.2 C and 1 C (1 C = 170 mA g^{-1}). Since the diffusion rate of cathode lithium-ions is lower at higher current densities, the discharge capacity decreases with increasing current density. The capacities of NCM523 and NCM523@2Al_2O_3 electrodes at rates of 0.2 C, 0.5 C, 1 C, 2 C, 5 C, 0.2 C and 1 C are 204 (187), 187 (182), 173 (170), 153 (153), 137 (131), 63 (81), 186 (183) and 153 (154) mAh g^{-1}, respectively. However, a clear difference is found at 5 C rate, where the NCM523@2Al_2O_3 electrode exhibits a higher capacity (23% improvement) than the pristine NCM523 electrode, and again returns to a small current (0.2 C and 1 C), the NCM523@2Al_2O_3 electrode shows better recovery properties. The results show that only 2 cycles of ALD Al_2O_3 is sufficient to improve the cycling and rate performance of the single crystal NCM523 cathode at 4.6 V.

6.15 Operando study on structure-activity relationship between electrolyte components and electrochemical performance for all-solid-state lithium battery

Y. Yan, L. Liu[1], A. Davydok[2], C. Krywka[2], R. A. Fischer[1], P. Müller-Buschbaum

[1] TUM, Chemistry department, Garching, Germany
[2] HZH, Hamburg, Germany

All-solid-state lithium-ion batteries (ASSLIBs) are the most promising power sources for high-safety and high-energy-density energy storage devices. However, the practical application of ASSLBs has been hindered by poor interfacial stability and inferior ionic conductivity. [1] Poly(ethylene oxide) (PEO)-based composite electrolytes play a crucial role in determining the overall electrochemical performance of solid-state batteries because of their superior interfacial compatibility, high ionic conductivity, and outstanding solubility against lithium salts. Herein, layered-double-hydroxide (LDH) reinforced PEO composite polymer electrolytes (CPEs) are designed, which deliver a wide electrochemical window, excellent electrochemical performance, and good interfacial stability. Moreover, the structure-activity relationship between the component structure of the electrolyte and the electrochemical performance is elucidated by operando nanofocus wide-angle X-ray scattering (nWAXS). [2]

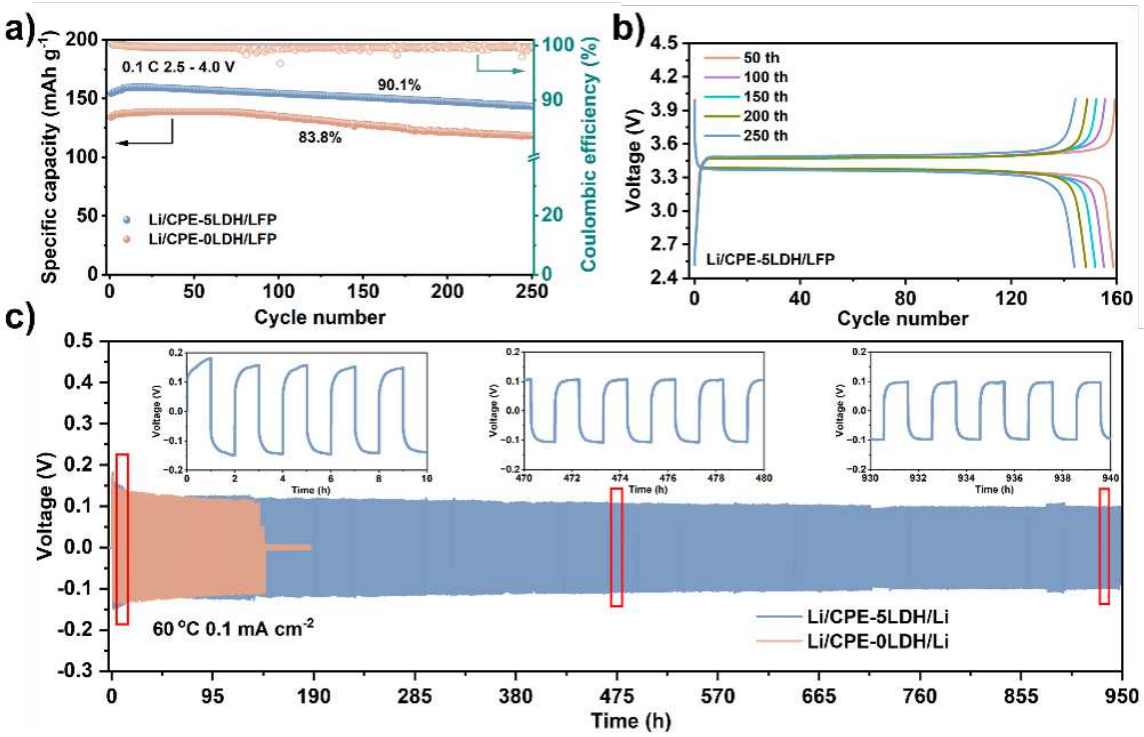

Figure 6.27:
a) Cyclic performance of Li/CPEs/$LiFePO_4$ coin cells at 0.1 C. b) The corresponding charge-discharge curves of Li/CPE-5LDH/$LiFePO_4$ coin cell at 0.1 C. c) Galvanostatic cycling curves of Li/CPEs/Li symmetric cells at a current density of 0.1 mA cm^{-2} at 60 °C.

The full-cell performance of different CPEs is studied to verify their practicality. The long-term cycle performance test of Li/CPEs/LFP cell (Fig. 6.27a) is conducted at 60 °C. The Li/CPE-0LDH/$LiFePO_4$ cell exhibits a low capacity retention rate of only 83.8%. In contrast, the Li/CPE-5LDH/$LiFePO_4$ cell exhibits excellent cycling stability, with a high capacity retention of 90.1% at 0.1 C over 250 cycles. The corresponding charge-discharge curves of

Li/CPE-5LDH/$LiFePO_4$ cells show perfect trends and low polarization(Fig. 6.27b). Stability against lithium metal is also a crucial factor for ASSLIBs. The galvanostatic cycling curves of Li/CPEs/Li are measured with a current density of 0.1 mA cm^{-2} at 60 °C(Fig. 6.27c). The Li symmetric cell with CPE-5LDH shows ultra-long cycling stability, which works over 900 h. However, the cell with CPE-0LDH only works for 150 h. These results indicate that the CPE-5LDH effectively inhibits the growth of lithium dendrites and prevents dendrites from piercing the electrolyte, thereby enhancing the stability of electrochemical performance.

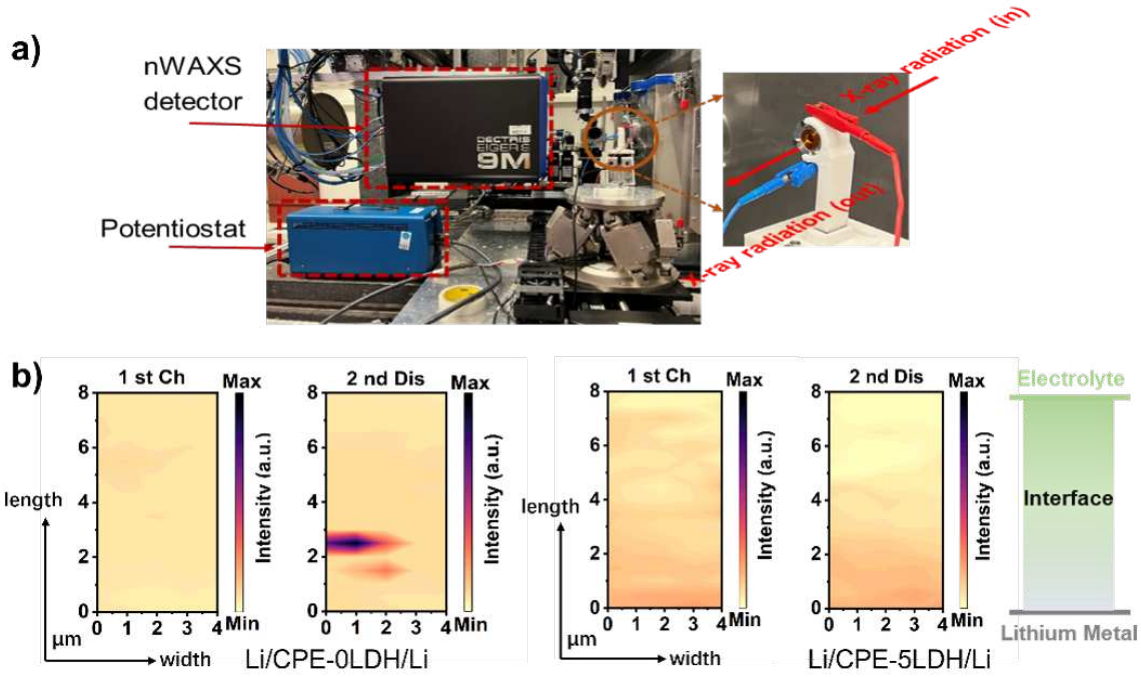

Figure 6.28:
a) Operando setup for nWAXS measurements at DESY P03 beamline. b) 2D maps of Li (110) peak intensities in the scanned area (4 μm × 8 μm) around the Li/electrolyte interface during the first charge/discharge cycles.

The operand nWAXS(Fig. 6.28a) studies are carried out at the P03 beamline at DESY. As shown in Fig. 6.28b, the maps for the prominent Li (110) peak intensities illustrate the lithium dendrites formation process during the first charge/discharge cycles of Li/CPE-0LDH/Li and Li/CPE-5LDH/Li cells, respectively. For Li/CPE-0LDH/Li cells, a significant localized lithium signal is observed along the (110) crystal plane during lithium plating and stripping processes, indicating the formation of high-intensity lithium dendrites at the Li/CPE-0LDH interface. The presence of the lithium dendrite directly pierces the solid electrolyte and causes a short circuit in the battery. In contrast, for Li/CPE-5LDH cells, no localized high-intensity lithium signals are detected along the (110) crystal plane. The lithium distribution is uniform and weak, suggesting that adding LDH mitigates lithium dendrite growth and promotes a uniform lithium deposition. Such a stable interface is beneficial to improve cycle stability, thereby enhancing the overall electrochemical performance of lithium metal batteries.

[1] J. Fu, Z. Li, X. Zhou, X. Guo, *Mater. Adv.* **3**, 3809 (2022)

[2] Cy M. Jeffries, J. Ilavsky, A. Martel, S. Hinrichs, A. Meyer, J. S. Pedersen, A. V. Sokolova, D. I. Svergun, *Nat. Rev. Methods. Primers* **1**, 70 (2021)

6.16 Polymer of intrinsic microporosity as the silicon-based anode electrode additive

M. Yang, Y. Cheng[1,2], P. Müller-Buschbaum

[1] NIMTE, Ningbo, China
[2] HHU, Changzhou, China

Silicon-based anodes are promising alternatives due to their high theoretical specific capacity and low voltage platform to traditional graphite anodes for high-energy-density lithium-ion batteries (LIBs). However, their performance is significantly hindered by silicon's substantial volume expansion during cycling, which often leads to electrode degradation. [1,2] Therefore, it is crucial to design a robust electrode structure and establish a stable solid electrolyte interface (SEI) to address these challenges. Herein, an intrinsic microporosity polymer PIM-COOH is prepared, compatible with the polyacrylic acid (PAA) binder as a silicon-based anode additive. The microporous structure of the PIM-COOH molecule can effectively improve the transport of lithium ions and improve the electrochemical kinetics. As a result, good lithium-ion transport and mechanical integrity are maintained, resulting in improved long-term stability and high-rate performance.

By introducing intrinsic microporosity polymer PIM-COOH as an electrode additive in the silicon-based anode electrode, only 0.1% of the total solid mass of the electrode can have a significant effect. Fig. 6.29 a,c) shows the cycling performance of the electrodes (SiC-PIM-COOH) and without (SiC-ST) adding PIM-COOH. After 400 cycles, the electrodes with and without PIM-COOH maintain 75 % and 32 % capacity, respectively.

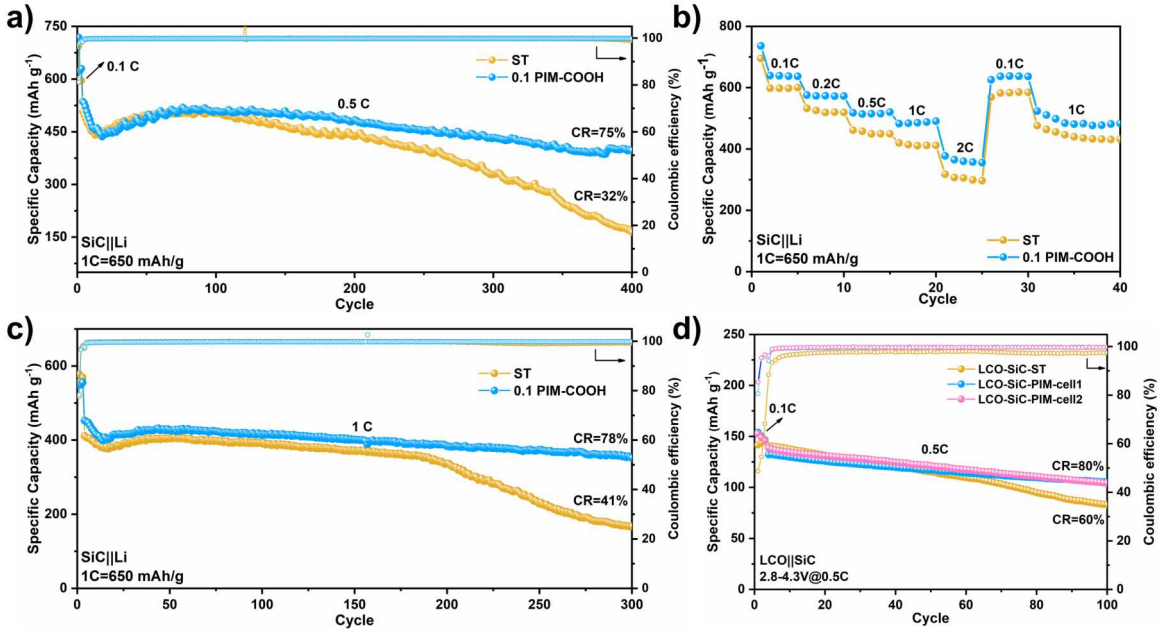

Figure 6.29:
Cycling performance a), c) and rate capacity b) of the Li/SiC cells with and without adding the PIM-COOH. d) Cycling performance of the LCO/SiC full-cells between 2.8 V and 4.3 V at 0.5 C.

Fig. 6.29 b) compares the capacities of the SiC-PIM-COOH and SiC-ST electrodes at different current densities.An enhanced rate performance is found in the case of the SiC-PIM-COOH electrode as evidenced by the higher capacities at the current densities from 0.1 C to 2 C. Such

a finding implies that the SiC-PIM-COOH electrode bears a good structure and electrochemical stability to survive a large rate test. To further verify the feasibility of the SiC-PIM-COOH electrode for use in LIBs, a full cell is assembled with commercial $LiCoO_2$ (LCO) as the cathode and the SiC as the anode as shown in Fig. 6.29 d), The LCO/SiC-PIM-COOH full cell exhibits better cycling performance compared with the LCO/SiC-ST full cell. After 100 cycles, the electrodes with SiC-PIM-COOH and SiC-ST maintain a capacity retention of 80% and 60%, respectively. It indicates that the beneficial roles played by the SiC-PIM-COOH electrode in the half-cell are also effective in the full-cells, leading to improved electrochemical performance.

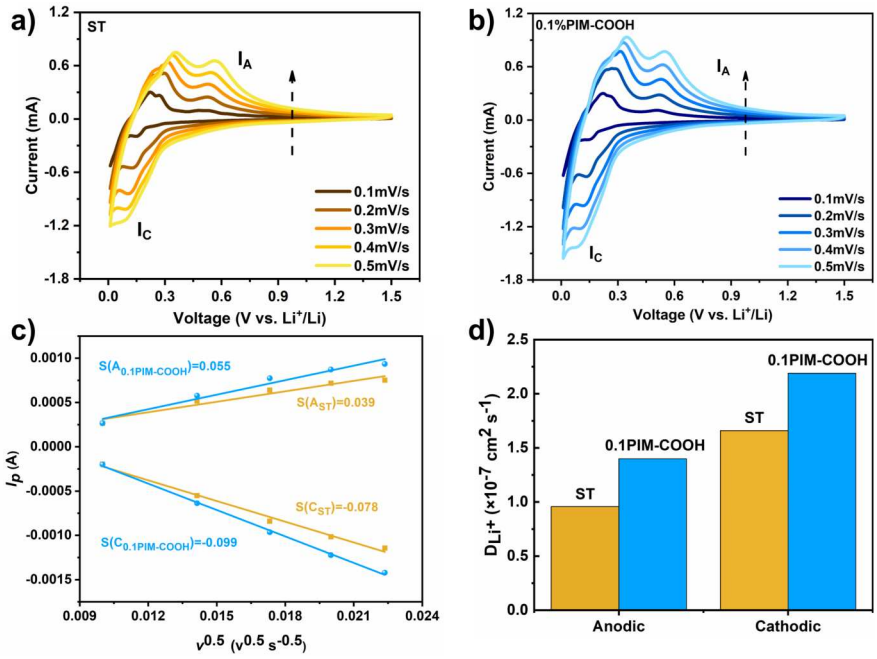

Figure 6.30:
Li-ion diffusion coefficients of the SiC electrode. CV curves of the SiC-ST a) and SiC-PIM-COOH b) electrodes at different potential scanning rates in the range of 0.1 mV/s - 0.5 mV/s. The relationship between peak current and the square root of the potential scanning rates c). Comparison of the calculated D_{Li^+} d).

Ionic conductivity analysis is performed to better understand the origin of the improved electrochemical performance of the SiC-PIM-COOH electrode. Fig. 6.30 a,b) show the CV curves of the SiC-PIM-COOH and SiC-ST electrodes at different scanning rates from 0.1 mV/s to 0.5 mV/s, respectively. Under different scanning rates, the cathodic and anodic peak current exhibits a linear relationship with the square rates, which can be used to characterize the Li-ion diffusion coefficients. The SiC-PIM-COOH electrode has a higher lithium ion transport rate than the SiC-ST electrode as shown in Fig. 6.30 c,d). It can be seen that the addition of a self-porous PIM-COOH additive to the electrode is beneficial to improving the electrochemical kinetics.
In conclusion, PIM-COOH is well-compatible with PAA and promotes the rapid transport of lithium ions due to the presence of a porous structure. The affinity between the electrode and the electrolyte is enhanced by the microporous nature of the PIM-COOH additive. As a result, good lithium-ion transport and mechanical integrity are maintained, leading to improved long-term stability and rate performance.

[1] X. Zuo, J. Zhu, P. Müller-Buschbaum,Y. Cheng, *Nano Energy.* **31**, 113-143 (2017)

[2] M. Yang, P. Chen, J. Li, R. Qi, Y. Huang, P. Müller-Buschbaum, Y. Cheng, K. Guo, Y. Xia, *J. Mater. Chem. A.* **11**, 6205-6216 (2023)

6.17 Fabrication and application of PEO-based electrolytes for Li-S batteries

C. Yuan, L. Zhang[1], P. Müller-Buschbaum

[1] Soochow University, Suzhou, China

Lithium–sulfur (Li–S) batteries have emerged as highly promising next-generation energy storage systems due to their exceptional theoretical specific capacity of 1675 $mAhg^{-1}$ and energy density of 2600 $WhKg^{-1}$. In addition, the natural abundance, low cost and environmental friendliness of sulfur further enhance its appeal, presenting advantages in both sustainability and economic feasibility. Despite these benefits, issues such as the "shuttle effect" and intrinsic low conductivity of sulfur hinder the widespread application of Li-S batteries. [1] These challenges require innovative advancements in material design and electrolyte optimization.

Electrolyte selection is important in determining the overall performance of Li-S batteries. Conventional liquid electrolytes, composed of organic solvents and lithium salts, provide high ionic conductivity but face significant instability issues. The dissolution and shuttling of lithium polysulfides in liquid electrolytes result in capacity fading and safety concerns, limiting their effectiveness. In contrast, polyethylene oxide (PEO)-based solid polymer electrolytes introduce a fundamentally different ionic conduction mechanism, offering notable advantages. Liquid electrolytes primarily conduct ions through the movement of solvated lithium ions in the liquid phase. Although this allows for high ionic conductivity, it also facilitates the dissolution and migration of polysulfides, as shown in Fig. 6.31. This phenomenon exacerbates the shuttle effect, decreasing the efficiency and lifespan of the battery. PEO-based electrolytes, on the other hand, transport lithium ions through the segmental motion of polymer chains, as illustrated in Fig. 6.31. This unique mechanism significantly restricts polysulfide mobility, suppressing their dissolution and shuttling. As a result, PEO-based electrolytes offer the enhanced cycling stability. Additionally, the chemical and electrochemical stability of PEO against lithium metal reduces the risk of dendrite formation, ensuring improved battery safety.[2]

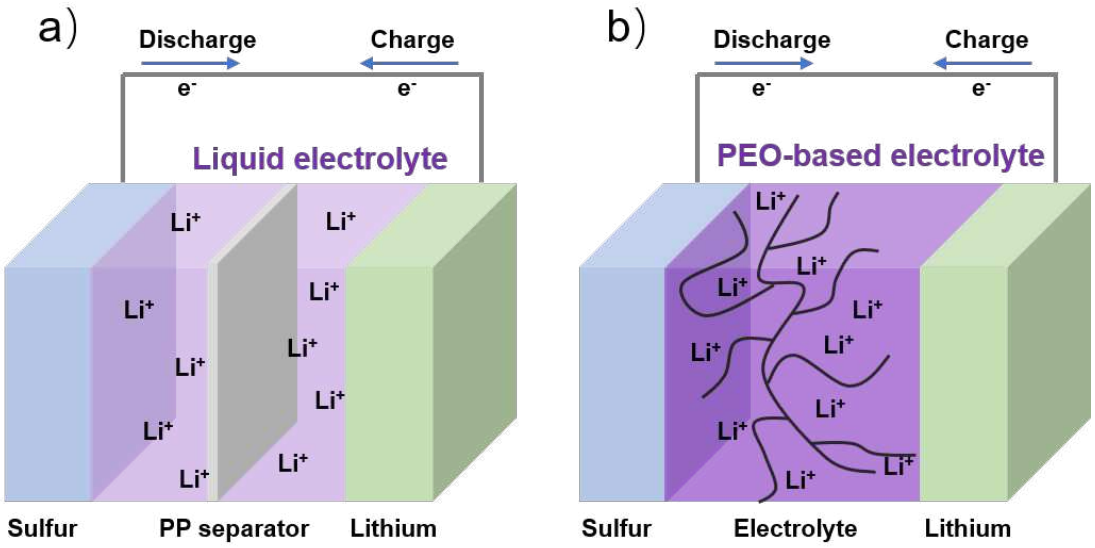

Figure 6.31:
Schematic diagram of Li-S batteries using (a) liquid electrolyte and (b) PEO-based polymer electrolyte.

Although PEO-based electrolytes exhibit relatively low ionic conductivity at room temperature, their thermal stability and compatibility with lithium metal make them an ideal candidate for next-generation Li–S batteries. These electrolytes are typically prepared using the following procedure. Initially, PEO and lithium bis(trifluoromethanesulfonyl)imide (LiTFSI) are dissolved in acetonitrile (ACN) solvent in a predetermined ratio. Once the materials are fully dissolved, aluminum oxide (Al_2O_3) is added, and the solution is stirred thoroughly to achieve a uniform polymer-salt mixture. This mixture is then cast onto a polytetrafluoroethylene (PTFE) mold and allowed to solidify. Upon solidification, the self-supporting polymer film is peeled off, resulting in the formation of a PEO-based solid polymer electrolyte.[3]

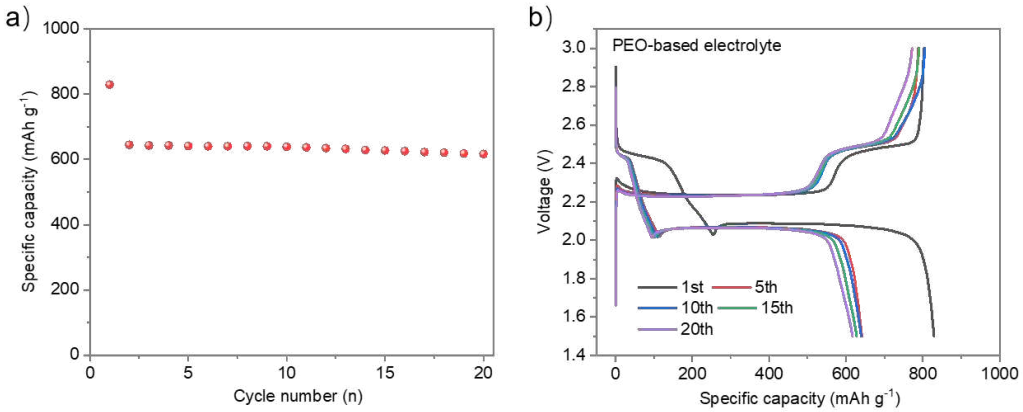

Figure 6.32:
Schematic diagram of Li-S batteries using (a) liquid electrolyte and (b) PEO-based electrolyte.

To validate the stability of PEO-based electrolytes, Li-S batteries incorporating a sulfur cathode, PEO-based electrolyte, and lithium anode are assembled. As displayed in Fig. 6.32, these cells deliver an initial discharge-specific capacity of 830 $mAhg^{-1}$, indicating the smooth facilitation of Li-ion transport by the PEO-based electrolyte. Furthermore, the discharge/charge curves in Fig. 6.32 demonstrates two distinct voltage platforms corresponding to the multi-step conversion of sulfur species. The higher voltage platform signifies the liquid-liquid transition from long-chain to short-chain polysulfides, while the lower voltage platform represents the liquid-solid transition from short-chain polysulfides to lithium sulfide. Even after 20 cycles, the cell maintains a substantial capacity of 617 $mAhg^{-1}$, showcasing the excellent electrochemical stability and efficiency of the PEO-based electrolyte within the voltage window of Li–S batteries.

In summary, PEO-based electrolytes offer a transformative approach to addressing the limitations of liquid electrolytes in Li–S batteries. By combining superior chemical stability, enhanced safety, and the ability to suppress polysulfide dissolution, PEO-based electrolytes significantly improve battery performance.

[1] P. Zeng, H. Zou, C. Cheng, L. Wang, C. Yuan, G. Liu, J. Mao, T. S. Chan, Q. Wang, L. Zhang, *Adv. Funct. Mater.* **33**, 202214770 (2023)

[2] X. Chen, C. Zhao, K. Yang, S. Sun, J. Bi, N. Zhu, Q. Cai, J. Wang, W. Yan, *Energy Environ. Mater.* **6**, 12483 (2023)

[3] R. Fang, H. Xu, B. Xu, X. Li, Y. Li, J. B. Goodenough, *Adv. Funct. Mater.* **31**, 2001812 (2021)

6.18 Insight into the cyclability of LiF-coated $LiNi_{0.9}Co_{0.05}Mn_{0.05}O_2$ cathodes in sulfide-based all-solid-state batteries

Z. Zhang[1,2], W. Zhao[2], T. Brezesinski[2]

[1] MLZ, Garching, Germany

[2] BELLA, Karlsruhe, Germany

LiF has been proven to be an effective cathode coating material in liquid lithium-ion battery systems due to its high chemical stability, high ionic conductivity, and low electronic conductivity[1]. However, its application in all-solid-state lithium battery systems has not been extensively studied. In this research, the impact of LiF coatings on the $LiNi_{0.9}Co_{0.05}Mn_{0.05}O_2$ (NCM90) cathodes in sulfide-based all-solid-state batteries was investigated. The primary objective was to explore whether LiF coatings could enhance the stability of cathodes and improve battery performance by mitigating degradation in sulfide electrolytes.$LiNi_{0.9}Co_{0.05}Mn_{0.05}O_2$ cathodes were synthesized and coated with LiF using two different methods: a solid-state mixing method and a liquid-phase mixing method. A range of characterization techniques, including X-ray diffraction (XRD), scanning electron microscopy (SEM), and charge-discharge cycling tests, were employed to evaluate the structural integrity and electrochemical behavior of the cathodes. Charge-discharge cycling tests were conducted to assess capacity retention, and impedance spectroscopy was employed to examine degradation mechanisms over multiple cycles.

The surface morphology of LiF@NCM90 prepared by two different methods is shown in Figure 6.33. SEM analysis revealed that the solid-phase method resulted in agglomerated and uneven LiF coatings. In contrast, the liquid-phase method produced a more uniform distribution of LiF with consistent coating thickness. This uniformity is crucial for maintaining the integrity and performance of the cathode material in the battery.

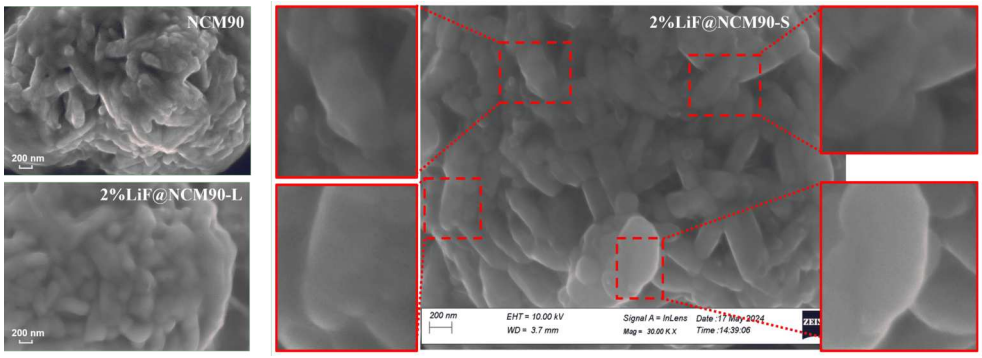

Figure 6.33:
High-magnification SEM images of pristine NCM90, LiF@NCM90-L, and LiF@NCM90-S. Red boxes mark uneven, thicker areas of LiF.

According to the cycling performance of the LiF-coated NCM90 cathodes synthesized by liquid-phase mixing method, 1%LiF@NCM90 exhibited a remarkable enhancement in capacity retention (Figure 6.34, maintaining approximately 92% of their initial capacity after 200 charge-discharge cycles, compared to just 75% for the uncoated cathodes under the same conditions. Additionally, LiF-coated NCM90 exhibited narrower and higher reversible redox peaks with smaller polarization compared to pristine CAM (Figure 6.35), indicating faster charge transfer kinetics, and corresponding a improved electrochemical performance. [2] The H2→H3 transition causes an abrupt lattice volume change, leading to mechanical stress, which can induce

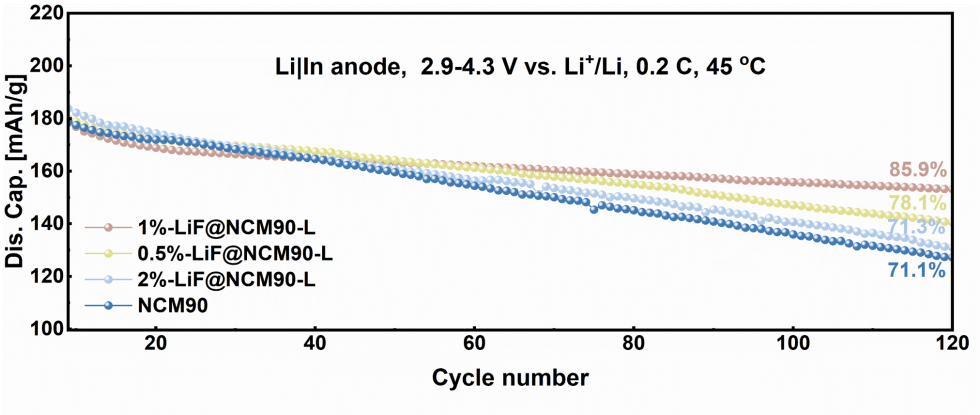

Figure 6.34:
Long-term cycling performance of the pristine NCM90 and LiF@NCM90 cathodes prepared using liquid-mixing method in ASSLB cells.

microcracks or contact loss between particles and the solid electrolyte (SE), is significantly mitigated in the LiF-coated samples.
The intensity of the H2 to H3 peaks decreases less in the 1% and 0.5% LiF-coated samples, suggesting better structural protection. This improvement is likely due to the uniform LiF coating, which helps maintain the integrity of the electrode structure over cycling.

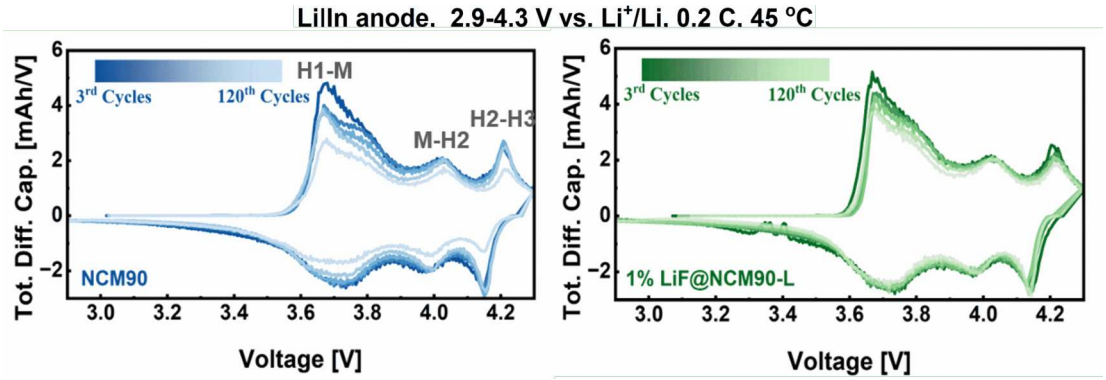

Figure 6.35:
dQ/dV curves from the 3rd to the 120th cycle of ASSLB cells using pristine NCM90, and 1%LiF@NCM90-L.

In conclusion, the study demonstrates that LiF-coated $LiNi_{0.9}Co_{0.05}Mn_{0.05}O_2$ cathodes synthesized by liquid-phase method exhibit superior cycling stability and performance, with significant improvements in capacity retention. These findings offer important insights for the development of more stable and efficient all-solid-state battery technologies. Future research will focus on exploring alternative coatings and surface modifications to further enhance cathode stability, as well as examining the interactions between cathodes and electrolytes under various operational conditions.

[1] X. Xiong, Z. Xunhui, X. Yin, H. Guo, X. Li, *Mater. Lett.* **110**, 4-9 (2013)

[2] H.-J. Noh, S. Youn, C. S. Yoon, Y.-K. Sun, *J. Power Sources* **233**, 121-130 (2013)

6.19 Exploration of binding energies in solvents with varying dielectric constants

Q. Zeng, T. Zheng, P. Müller-Buschbaum

The interaction between lithium ions and solvents plays a crucial role in determining the performance and stability of lithium metal batteries (LMBs). Recent advances have highlighted the importance of weakly solvating electrolytes, which can reduce the number of free solvent molecules and promote the formation of a stable solid electrolyte interface (SEI), thereby improving ion transport efficiency and battery life. [1-2] By studying the kinetics, one can gain a deeper understanding of how the electrolyte system promotes the stability and high ionic conductivity of LMBs. [3-4] These findings are important for designing advanced electrolytes specifically designed to improve battery efficiency, balance strong ion-solvent interactions and optimal ion transport.
Density Functional Theory (DFT) calculations are used to calculate the binding energy of lithium ions with various solvents and the effects of dielectric constants on solvent-lithium ion interactions. Certain solvents, including glymes such as diglyme (G2), triglyme (G3), tetraglyme (G4), and pentaglyme (G5), as well as crown ethers like 15-crown-5 (15c5) and 18-crown-6 (18c6), are selected due to their high solubility for lithium salts and compatibility with lithium metal anodes. The binding energy is calculated as the total energy difference between the solvated system and its isolated components, offering a direct measure of ion-solvent interaction strength. The results highlight the relationship between solvent structure and binding energy, providing insights into their interaction mechanisms.

a)

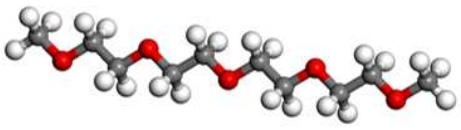

b)

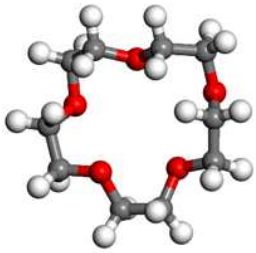

c)

Solvent	E_{total} (Ha)	E_{Li+} (Ha)	$E_{solvent}$ (Ha)	E_{abs} (eV)
Li - DME	-315.974372	-7.257093	-308.608612	-2.957046
Li - G2	-469.721602	-7.257093	-462.321445	-3.893057
Li - G3	-623.461607	-7.257093	-616.034293	-4.632053
Li - G4	-777.189677	-7.257093	-769.747234	-5.043744
Li - G5	-930.912799	-7.257093	-923.460236	-5.319129
Li - 15c5	-776.001871	-7.257093	-768.561144	-4.997048
Li - 18c6	-929.720678	-7.257093	-922.273809	-5.164184

Figure 6.36:
a) Chain-like solvent (G4); b) Crown-like solvent (15c5); c) Table showing binding energies and components for comparing lithium-ion binding in different solvents.

From a structural perspective shown in Fig. 6.36, crown solvents are more advantageous than catenary solvents because they have well-defined ring geometries that provide a stable and selective coordination environment for lithium ions. At the same time, the crown structure can effectively wrap lithium ions and reduce direct contact with the surrounding solvent. This helps stabilize the lithium ions and may help make the solid electrolyte interface (SEI) in lithium batteries more uniform. While in terms of binding energy shown in the data table in Fig. 6.36, in longer chain solvents (e.g., G4 and G5), adding more oxygen atoms can significantly enhance the binding strength with lithium ions. This finding suggests that while the crown solvents excel in structural stability and selectivity, the chain solvents can achieve stronger interactions by increasing the number of coordination sites. The choice between the two depends on the specific requirements of the electrolyte system, balancing bonding strength and structural advantages.

As shown in Fig. 6.37, different solvent binding energies obtained under different dielectric

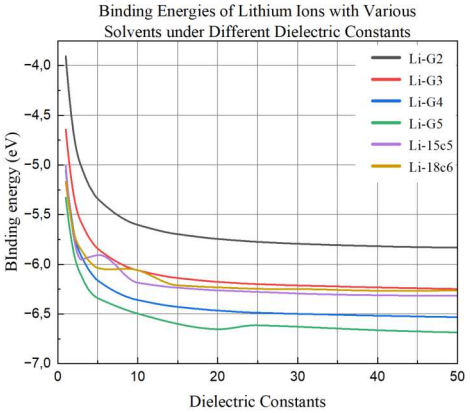

Figure 6.37:
Binding energies of lithium ions with various solvents as a function of dielectric constants (1.01–50). The plot compares chain-like solvents (G2, G3, G4, G5) and crown-like solvents (15c5, 18c6).

constants are fitted. For each solvent, an increase in the dielectric constant leads to stronger binding energies, a phenomenon that is particularly pronounced in the lower dielectric constant range (1.01 to 10). Chain solvents show a more pronounced increase in binding energy with increasing dielectric constant. In contrast, crown solvents show relatively little dependence on the dielectric constant. This behavior is due to their rigid ring structure, which forms a predefined coordination environment around the lithium ion. This structure is less adaptable to changes in the dielectric medium, making the binding energy of crown ether solvents less sensitive to changes in the external environment. However, this rigidity provides an advantage by ensuring consistent and selective coordination of lithium ions, making crown ethers particularly suitable for applications that require stable and predictable solvation behavior.

In summary, both solvent type and dielectric environment play a key role in determining the binding energy of lithium ions. Crown ethers are ideal candidates for weakly solvating electrolytes due to their consistent binding energy and stable coordination geometry, which is essential for the formation of a stable solid electrolyte interface (SEI). On the other hand, glyme has greater flexibility and adaptability, making it suitable for applications with tunable binding energy. By leveraging the advantages of each solvent type, advanced electrolyte systems can be designed to meet the different requirements of lithium metal batteries.

[1] R. Murugan, V. Thangadurai, W. Weppner, *Angew. Chem. Int. Ed.* **46**, 7778–7781 (2007).

[2] J. Lu, Y. J. Lee, X. Luo, K. C. Lau, M. Asadi, *Nature* **529**, 377–382 (2016).

[3] M. Asadi, K. Kim, C. Liu, A. V. Addepalli, P. Abbasi, *Science* **353**, 467–470 (2016).

[4] S. Zhang, T. Xue, J. Li, W. Sun, J. Chen, *Int. J. Mol. Sci.* **25**, 13268 (2024).

6.20 Advanced polymer-based solid-state electrolytes for high-performance lithium metal batteries

J. Zhai, Y. Yan, P. Müller-Buschbaum

Lithium metal, the lightest metallic material, offers ultra-high theoretical capacity and the lowest electrode potential, enabling high energy density [1]. These properties make it suitable for electronics, EVs, and portable devices [2]. However, safety concerns arise due to SEI layer breakage, excessive electrolyte consumption, and dendrite growth, leading to capacity loss and electrode instability [3]. Solid-state polymer electrolytes mitigate these risks by eliminating flammable solvents and offering flexibility and cost-effectiveness, but suffer from low ionic conductivity. Incorporating fillers like PIM-1 enhances ion transport, promotes salt dissociation, and improves mechanical stability.

Coin cell batteries are assembled using a PIM-1 modified polymer electrolyte membrane, with LFP as the cathode and lithium metal as the anode. The polymer electrolyte serves as both the electrolyte and separator. As shown in Fig. 6.38, the prepared PEO-PIM composite solid electrolyte is a uniform bright yellow translucent membrane without obvious powder agglomerates. Before assembly, the coin cell components are pretreated to remove impurities. In a glove box, the battery is assembled in the order: negative shell, spring, spacer, lithium sheet, PIM-1 membrane, LFP cathode, and positive shell. The assembly process is shown in Fig. 6.38, and the battery is sealed using an automatic crimping machine.

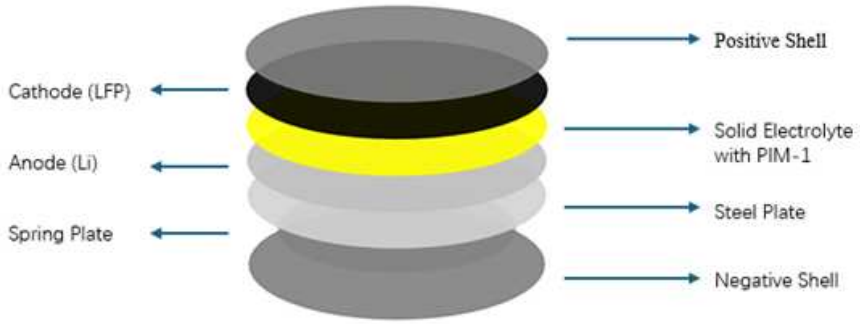

Figure 6.38:
Schematic representation of the modified PIM-1-based solid-state electrolyte architecture for enhanced lithium metal battery performance.

The electrochemical performance of the coin cell is investigated. The LSV results in Fig. 6.39 show the electrochemical stability of PEO+LiTFSI and PEO+LiTFSI+PIM-1 systems. PEO+LiTFSI decomposes at around 3.8 V, indicating a limited stability. In contrast, PIM-1 increases the onset to about 4.75 V, expanding the stability window by suppressing high-voltage decomposition.
The wider stability window of PEO+LiTFSI+PIM-1 enhances the compatibility with high-voltage cathodes, making it a promising electrolyte for lithium metal batteries. This improvement is due to strong interactions between PIM-1 and LiTFSI anions, delaying decomposition and expanding the voltage range.

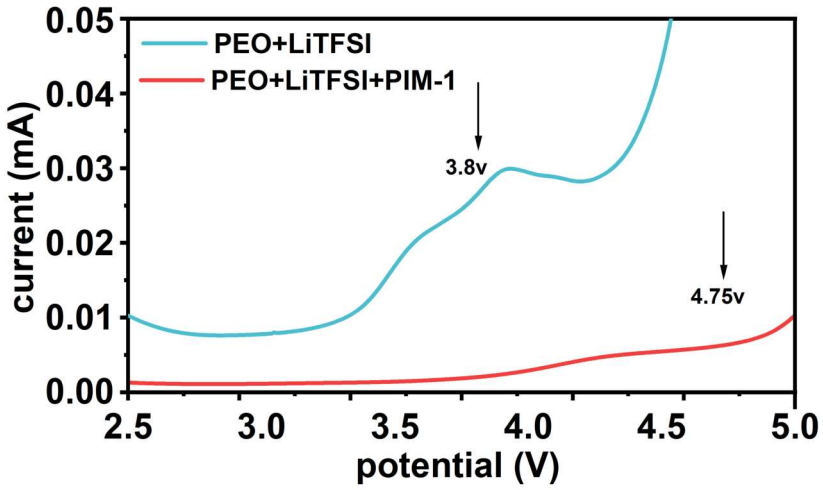

Figure 6.39:
Linear sweep voltammetry (LSV) analysis of the electrochemical stability for PEO+LiTFSI and PEO+LiTFSI+PIM-1 at 60°C.

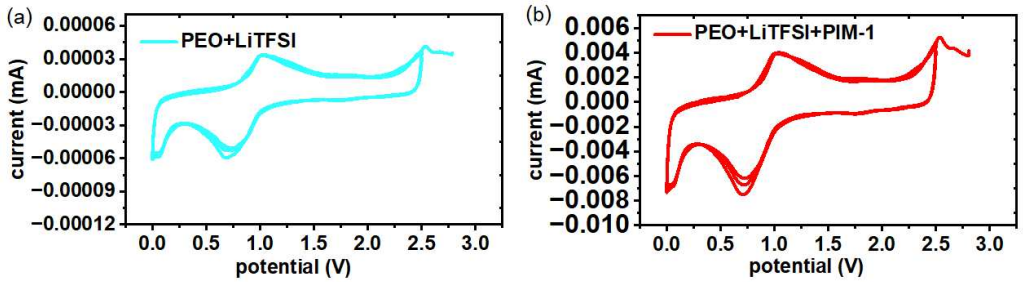

Figure 6.40:
Cyclic voltammetry measurements measured for PEO-LiTFSI- PIM-1 recorded between 2.5 and 0 V and then back to 2.5V, conducted at 60°C.

The cyclic voltammetry (CV) curves in Fig. 6.40 (a) and (b) show the electrochemical behavior of PEO+LiTFSI and PEO+LiTFSI+PIM-1 systems. In Fig. 6.40 (a), the peak separation (ΔE) of PEO+ LiTFSI between the anodic and cathodic peaks is 0.336 V, indicating a moderate polarization and a slower ion transport due to its limited ionic conductivity. In Fig. 6.40 (b), PEO+LiTFSI+PIM-1 exhibits a smaller ΔE of 0.32 V, suggesting improved ionic conductivity and faster charge transfer. This enhancement is attributed to PIM-1's strong interaction with LiTFSI anions and increased ion mobility. The reduced ΔE demonstrates PIM-1's positive effect on the electrochemical performance of the PEO-based electrolyte, enhancing its efficiency for lithium metal batteries.

[1] D. Lin, Y. Liu, Z. Liang, H.-W. Lee, J. Sun, H. Wang, K. Yan, J. Xie, Y. Cui, *Nat. Nanotechnol.* **11**, 626–632 (2016).

[2] J. Liu, L. Dong, D. Chen, Y. Han, Y. Liang, M. Yang, J. Han, C. Yang, W. He, *Small Methods* **4**, 1900753 (2020).

[3] K. Xu, *Chem. Rev.* **104**, 4303–4418 (2004).

6.21 Anchoring and competition: weakly solvated structure of glymes enhance stability in lithium metal batteries operating under extreme conditions

T. Zheng, Y-J. Cheng[1], P. Müller-Buschbaum

[1] NIMTE, Ningbo, China

The widely known issues that cause lithium metal batteries (LMBs) to decrease in capacity primarily arise from unstable and fragile solid electrolyte interfaces (SEIs). These issues exacerbate irreversible lithium loss and ultimately reduce the battery cycle life, potentially leading to short circuits and thermal runaway. Recent research has demonstrated that innovative systems such as high-concentration electrolytes (HCEs), localized-high-concentration electrolytes (LHCEs), and weakly solvating electrolytes (WSEs) exhibit exceptional Coulombic efficiencies. These benefits are attributed to reduced free solvent molecules coupled with increased ion clusters like contact ion pairs (CIPs) and aggregates (AGGs), resulting in a SEI enriched with inorganic components. However, HCE and LHCE approaches are often prohibitively expensive for commercial applications. Concurrently, weakly solvating solvents with limited capacity for solvation exhibit an insufficient dissolution efficacy for certain lithium salts characterized by high donor numbers in WSEs, as well as a restricted temperature range.[1-2] Therefore, developing new electrolytes that are cost-effective while maintaining compatibility with various lithium salts represents a crucial strategy for advancing applications in LMBs.

To address these challenges, ether-based solvents like diglyme (G2) are initially selected as the base solvent due to their advantageous low viscosity properties and high solubility for lithium salts, including $LiNO_3$. These solvents effectively dissolve various lithium salts, demonstrating excellent compatibility with lithium metal anodes. Additionally, Li bis(fluorosulfonyl)imide (LiFSI) is chosen as the primary salt owing to its high ionic conductivity and capacity to provide effective F sources for the SEI, rendering it an optimal choice. Additionally, $LiNO_3$ functions as a multifunctional additive that not only undergoes decomposition to generate products like Li_3N, thereby facilitating the formation of a more stable SEI but also exhibiting robust interactions with Li ions. Thus, it can serve as an "anchor" to stabilize specific regions of the solvated structure (Fig. 6.41). Finally, fluoroethylene carbonate (FEC) functions as a co-solvent that complements the ether solvents and demonstrates notable differences in the solubility of LiFSI and $LiNO_3$: While FEC effectively dissolves LiFSI, its solubility for $LiNO_3$ is comparatively low. Therefore, it can be regarded as a pseudo-diluent for $LiNO_3$ to mediate the solvation structure.

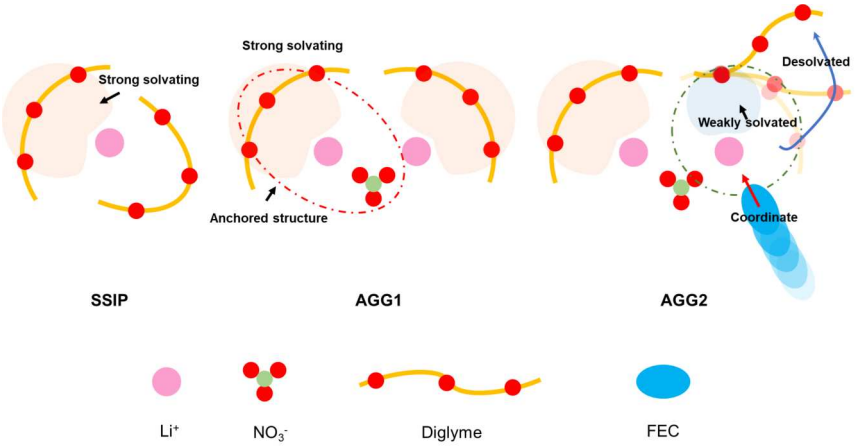

Figure 6.41: Evolution of competitive mediation to convert from strong solvating to weakly solvating.

Fig. 6.42 shows that Li deposition kinetics are further investigated in Li/Cu and Li/Li cells. The DFN electrolyte exhibits a remarkable Li plating/stripping CE of 99.20%, surpassing the values obtained in LCE (90%) and HCE (97.91%). Fig.6.42b shows the impedance of Li/Li symmetric cells before working. HCE demonstrates the highest interfacial impedance, which is ascribed to the overly high lithium salt concentration resulting in an excessively high electrolyte viscosity. Upon the addition of $LiNO_3$, the impedance of DN decreases significantly compared with that of LCE; while DFN possesses the smallest interfacial impedance, which is also by the previous kinetic tests and MD simulation results. Moreover, the DFN electrolyte exhibits outstanding compatibility and exceptional stability in Li/Li symmetric cells and reliability during calendar aging. (Fig. 6.42c) The overpotential of cells with LCE exhibits a significant increase after 500 hours, primarily attributed to the pronounced decomposition of electrolytes and accumulation of the SEI layer. When the concentration increases, the cell exhibits a cycling life of 1400 h. Additionally, adding $LiNO_3$ also improves the cycling life due to the inorganic products decomposed by $LiNO_3$. In contrast, the DFN electrolytes can support that the cells work more than 3000 h with a very low polarization due to the high Li ion transference number and small interfacial impedance.

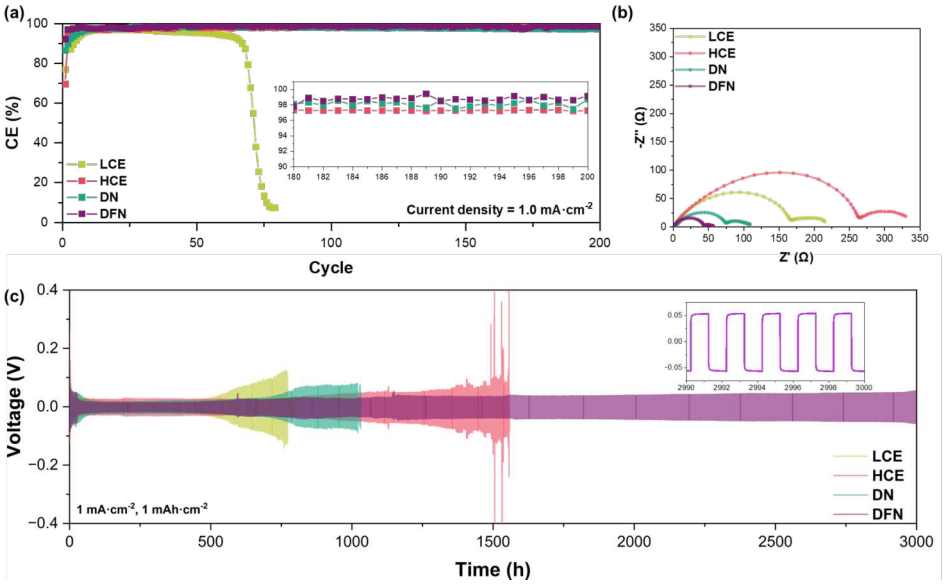

Figure 6.42:
(a) Long-term cycling of Li/Cu half cells. (b) Nyquist plots of electrochemical impedance spectra for Li/Li symmetric cells after 8 hours rest. (c) Long-term cycling of Li/Li symmetric cells.

In summary, in this formulation, the C-O-C bonds of glymes are competitively substituted by other anions and solvents to achieve single-site oxygen coordination, thereby facilitating a weaker solvation effect. The designed electrolyte significantly enhances the stability of lithium metal batteries at high temperatures by promoting the formation of a denser, more inorganic SEI film and reducing impedance, which improves electrochemical compatibility.

[1] Yan C, Cheng X-B, Tian Y, *Adv. Mater.* **30**, 1707629 (2018)

[2] Zheng T, Xiong J, Zhu B, Shi X, Cheng Y-J, Zhao H, Xia Y, *J. Mater. Chem. A* **9**, 9307-9318 (2021)

7 Real-time characterizations

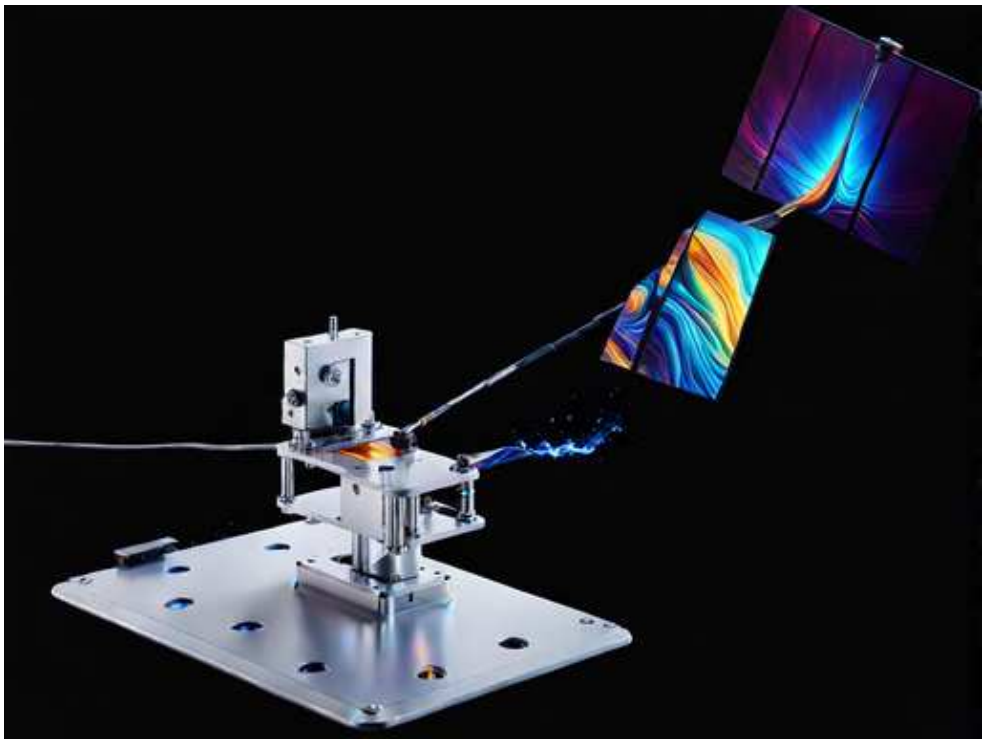

7.1 Investigating Au Deposition with HiPIMS and DcMS on PS, P4VP and PSS

Y. Bulut[1],B. Sochor[1], K. A. Reck[2],B. Schummer[3], A. Meinhardt[4,5], J. Drewes[2], S. Liang, T. Guan, A. Jeromin[4,5], A. Stierle[4,5], T. F. Keller[4,5], T. Strunskus[2], F. Fraupel[2], P. Müler-Buschbaum, S. V. Roth[1,6]

[1] DESY, Hamburg, Germany
[2] CAU, Kiel, Germany
[3] IIS, Fürth, Germany
[4] CXNS, Hamburg, Germany
[5] UHH, Hamburg, Germany
[6] KTH, Stockholm, Sweden

Thin metal films are crucial for applications in organic electronics, catalysis, and sensors. Gold (Au), due to its inertness and high scattering length density (SLD), is a model system for studying metal-polymer interactions. While direct current magnetron sputtering (dcMS) is a well-established technique, it requires preprocessing steps like plasma treatment to improve adhesion, which can be detrimental to polymer substrates. High-power impulse magnetron sputtering (HiPIMS), an emerging alternative, offers improved adhesion and more uniform deposition without additional surface treatments. However, the in situ growth behavior of HiPIMS-deposited metal films remains underexplored. This study aims to fill this gap by investigating and comparing the in situ formation of Au layers on different polymer substrates under dcMS and HiPIMS conditions.

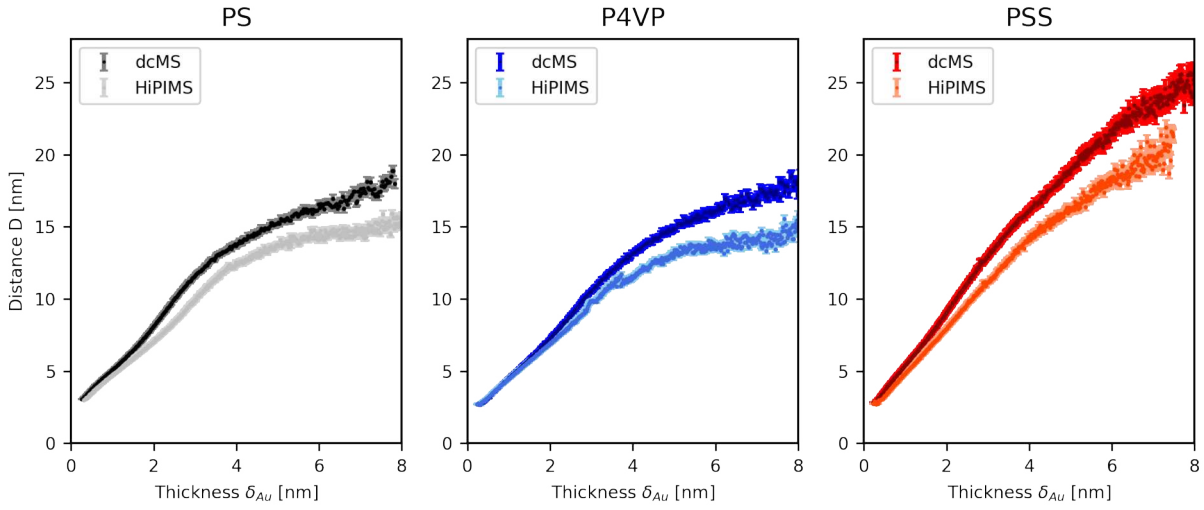

Figure 7.1: In situ evolution of the distance of Au islands forming on PS, P4VP, and PSS.[1]

A frequently used technique to obtain polymer thin films in the nanometer thickness regime is spin-coating. The polymer thin films of Polystyrene (PS), and poly-4-vinylpyridine (P4VP), and polystyrene sulfonic acid (PSS) were prepared by a spin casting procedure on pre-cleaned Si substrates. The in-situ GISAXS/GIWAXS investigations were performed with a custom-made mobile deposition chamber developed by the group from CAU Kiel [2] and upgraded with a unipolar HiPIMS source. This deposition chamber was mounted at the beamline P03, PETRA III, DESY, Hamburg. For the in-situ experiments, a PILATUS 2M detector (Dectris, Switzerland) with a pixel size of 172x172 µm^2 was used as GISAXS detector, and a custom-shaped LAMBDA 9M detector (Xspectrum, Germany) with a pixel size of 55 µm in simultaneous GIWAXS geometry. The experiments were performed using an incident angle of α_i = 0.4° and an X-ray

wavelength of 1.05 Å. The sample-to-detector distance (SDD) was set to SDD = 3230 ± 2 mm. For quantitative analysis, horizontal line cuts were done at the Yoneda peak of PS, P4VP and PSS to obtain the average lateral size and morphology of the clusters on the polymer surface, which is shown in Fig. 7.1.
Fig. 7.1 shows the in situ distance evolution of Au sputtering on PS, P4VP, and PSS. The Au growth follows the Volmer-Weber growth mode consisting of four well-known stages being classified as nucleation, diffusion-mediated coalescence, lateral growth vertical growth.[2] Herein, the distance is tracked, showing that upon further deposition the size of the distance increases.[2] The Au growth is tracked until a deposited thickness of δ_{Au} = 8 nm. During the distance evolution it can be observed that the Au growth under HiPIMS condition results in smaller average distances compared to dcMS.[2] This behavior can be observed throughout every of the studied polymer templates. In addition, FESEM images are capture at a thickness of δ_{Au} = 4 nm, which is shown in Fig. 7.2. The surface coverage of the Au layer is extracted under dcMS sputter condition being Au:PS$_{dcMS}$ = 76 ± 1 %, Au:P4VP$_{dcMS}$ = 77 ± 1 % and Au:PSS$_{dcMS}$ = 84 ± 1 %.[2] For HiPIMS deposited Au, the surface coverage is Au:PS$_{HiPIMS}$ = 93 ± 1 %, Au:P4VP$_{HiPIMS}$ = 93 ± 1 % and Au:PSS$_{HiPIMS}$ = 96 ± 1 %. This finding shows that under HiPIMS condition a smaller average distance is achieved during the deposition and the surface coverage is increased up to 10 % at δ_{Au} = 4 nm.[2]

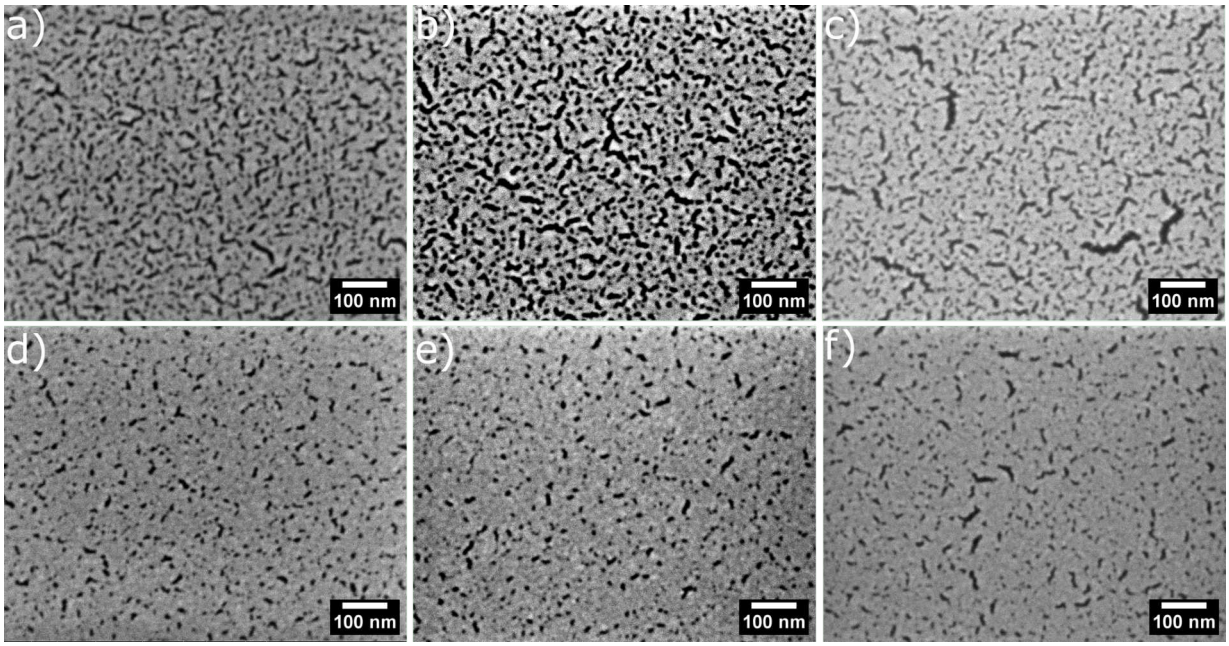

Figure 7.2:
FESEM images of Au-coated (a,d) Au:PS, (b,e) Au:P4VP and (c,f) Au:PSS with (a-c) dcMS and (d-f) HiPIMS with a deposited Au thickness of δ_{Au} = 4nm.[2]

[1] M. Gensch, M. Schwartzkopf, W. Ohm, C. J. Brett, P. Pandit, S. Koyiloth Vayalil, L. Bießmann, L. P. Kreuzer, J. Drewes, O. Polonskyi, T. Strunskus, F. Faupel, A. Stierle, P. Müller-Buschbaum, and S. V. Roth, *ACS Appl. Mater. Interfaces*, **11**, 29419 (2019)

[2] Y. Bulut, B. Sochor, K. A. Reck, B. Schummer, A. Meinhard, J. Drewes, S. Liang, T. Guan, A. Jeromin, A. Stierle, T. F. Keller, T. Strunskus, F. Faupel, A. Stierle, P. Müller-Buschbaum, and S. V. Roth, *Langmuir*, **11**, 22591 (2024)

7.2 Kinetics of structure and interface formation induced by photo-polymerization for submicron additive manufacturing

S. Chen, R. A. T. M. van Benthem[1], J. F. G. A. Jansen[2], M. K. G. Johansson[3], P. Müller-Buschbaum, S. V. Roth[3,4]

[1] TU/e, Eindhoven, the Netherlands
[2] Covestro, Geleen, the Netherlands
[3] KTH, Stockholm, Sweden
[4] DESY, Hamburg, Germany

Photo-induced polymerization of (meth)acrylate-based films is a widely used industrial technique due to its excellent spatial resolution combined with low energy consumption and high cure speed. Additive manufacturing, also known as 3D printing [1], is widely used in mechanical and optical properties applications [2,3]: fiber optic coatings, optical adhesives, and micro-lenses. In 3D printing, excellent structural control, as well as inter-layer uniformity, are key to fabricating high-resolution parts [3]. Although the photopolymerization is widely used, the fundamental understanding of the physical structure induced by photopolymerization and interface formation during the transition from solid-liquid to solid-solid interfaces in multilayer films are more of missing pieces. In the current study, we select three solvents suitable for polyurethane dimethacrylate (ethanol, n-butyl acetate, and toluene) and combine them with grazing incidence small angle X-ray scattering (GISAXS) to investigate the effect of solvents on the formation of photocured monolayer nanostructures and the interfaces formation mechanisms of multilayer films.

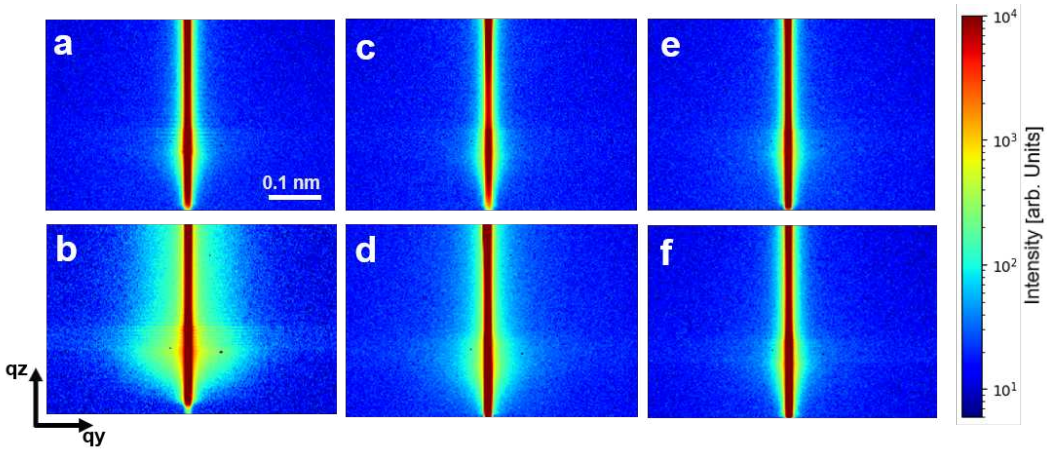

Figure 7.3:
2D GISAXS pattern before and after UV-curing of monolayer resin films: a, b show the films before and after curing with n-butyl acetate as solvent, respectively. c, d show the films before and after curing with ethanol as solvent, respectively. e, f show the films before and after curing with toluene as solvent, respectively.

The uncured liquid resin films assembled from different solvents (Fig. 7.3a,c,e) have different structural information, but all of them show disorder overall. After UV-curing, the three films (Fig. 7.3b,d,f) showed distinct and different structural transformations. The pre-assembly of resin molecular chains in domains by different solvents directly contributes to the growth of nanostructured domains during photopolymerization process and ultimately leads to the formation of heterogeneous nanostructures in the cross-linked state. A detailed model-based analysis using the effective interface approximation allows to detail the influence of the solvents on nanostructure formation during cross-linking. The liquid resin pre-assembled from n-butyl

acetate has the smallest domains, and the main structural domains formed after photopolymerization have a radius of 22.6 nm $\pm$ 2 nm. The liquid resins preassembled from toluene have relatively large size and the structural transformation induced by photopolymerization has low heterogeneity.

The solvent swelling effects on the polymer molecular chains reorganizes the photopolymerization-induced nanostructures, which is an intermediate step that cannot be neglected in the preparation of multilayer films. We find that the swelling effect of n-butyl acetate and ethanol on the polymer films mainly causes the larger nanostructured domains (radius $>$ 100 nm) to increase in size. The large-scale reorganization of nanostructures leads to the relaxation of the nanostructured network induced by photopolymerization resulting in the release of shrinkage stresses and alters the film surface (Fig. 7.4a). The resulting structural changes in the surface interact with the subsequently deposited resin to form new structures and buried interfaces.

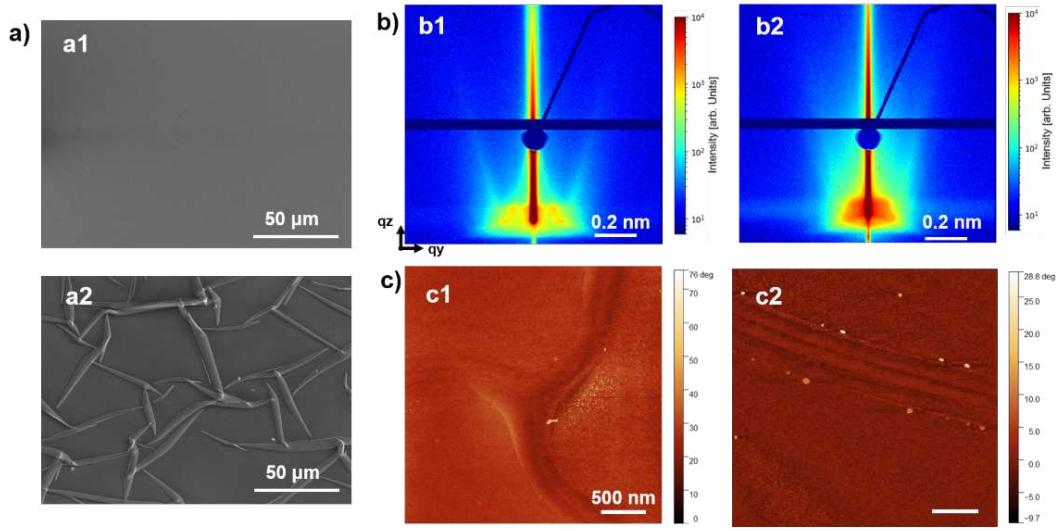

Figure 7.4:
GISAXS data and surface morphology of swollen monolayer and bilayer films with oblique form factors. a) SEM images of the cross-linked monolayers. a1, a2 present the morphology of cross-linked monolayers before and after wetting with n-butyl acetate. b) 2D GISAXS pattern. b1, b2 show the bilayer films with n-butyl acetate and toluene as solvent, respectively. c) AFM phase images. c1, c2 show the morphology of the bilayer films with n-butyl acetate and toluene as solvent, respectively.

The facetted morphology (Fig. 7.4b) is formed by the subsequent assembly of the liquid resin and the solvent with substrate film surface. This is apparent via the inclined streaks. These facetted nanostructures formed have different morphologies (Fig. 7.4c) due to nanostructure growth heterogeneity and swelling effects induced by different solvents. Currently, we extracted typical length scales of the nanostructures of n-butyl acetate and toluene-based bilayer films with cylindrical and spherical form factors, respectively. The structural information will be subsequently refined by simulating facetted nanostructures by standard GISAXS modelling software.

[1] J. Chen, X. Liu, Y. Tian, W. Zhu, C. Yan, Y. Shi, L. B. Kong, H. J. Qi, K. Zhou, *Adv. Mater.* **34**, 2102877 (2022)

[2] T. Gissibl, S. Thiele, A. Herkommer, H. Giessen, *Nat. Commun.* **7**, 11763 (2016)

[3] X. Zeng, J. Plain, S. Jradi, C. Darraud, F. Louradour, R. Bachelot, P. Royer, *Opt. Express* **19**, 4805-4814 (2011)

7.3 Ternary hybrid thin films containing mixed magnetic nanoparticles investigatzed investigated by in situ GISAXS

C. R. Everett, A. Lak[1], M. Opel[2], F. Hartmann[3], M. Bitsch[3], M. Gallei[3], M. Schwartzkopf[4], P. Müller-Buschbaum

[1] TU Braunschweig, Braunschweig, Germany

[2] Bayerische Akademie der Wissenschaften, Garching, Germany

[3] Saarland University, Saarbrücken, Germany

[4] DESY, Hamburg, Germany

Ternary hybrid films consisting of a diblock copolymer (DBC) and two types of nanoparticles (NPs) are interesting nanocomposites because of the synergistic combination of the properties of the relevant constituents and expand the functionality of traditional binary DBC/NP systems. DBCs are polymers composed of two chemically distinct blocks, and in the case of amphiphilic block copolymers, these materials undergo microphase separation when deposited out of solution as thin films, and it is possible to achieve nanostructured thin films with spherical, cylindrical, gyroid, or lamellar domains. [1] The morphology of the final thin film can be manipulated and controlled by tuning the volume ratio of the two blocks or by changing the segregation strength of the copolymer, which is dependent on the block-block interaction parameter (χ) and the number of repeating units (N). In addition to morphology tuning, tuning of the domain sizes is possible by varying the molecular weight of the polymer, with an increase in molecular weight corresponding to an increase in domain size. The tunability of DBC thin films makes them attractive for use as scaffolds and templates for inorganic materials such as NPs. [2] NPs demonstrate unique size-dependent properties, and in the case of magnetic NPs, NP size can influence the resulting magnetic properties of the material. Furthermore, through the combination of two different types of magnetic NPs, specific tuning of the magnetic behavior of a nanocomposite can be realized.

In this work, we focus on the synthesis of ternary DBC/NP thin films containing two different types of NPs (DBC/NP1/NP2). Polystyrene-*block*-poly(methyl methacrylate) (PS-*b*-PMMA), nickel NPs (Ni) coated with short PMMA-like ligands, and cobalt ferrite NPs ($CoFe_2O_4$) coated in oleic acid ligands were chosen for the investigated system. The NPs were coated in ligands to control the localization of the NPs into a specific polymer domain. This is typically accomplished by decorating the NPs with ligands that are chemically similar to one block, thus driving the localization of the nanoparticles to that block [3]. Thin films with varying NP concentrations were are printed from the solution in a one-step slot-die coating process. The morphology evolution of the hybrid magnetic thin films is monitored with grazing-incidence small-angle X-ray scattering (GISAXS) during the drying process.

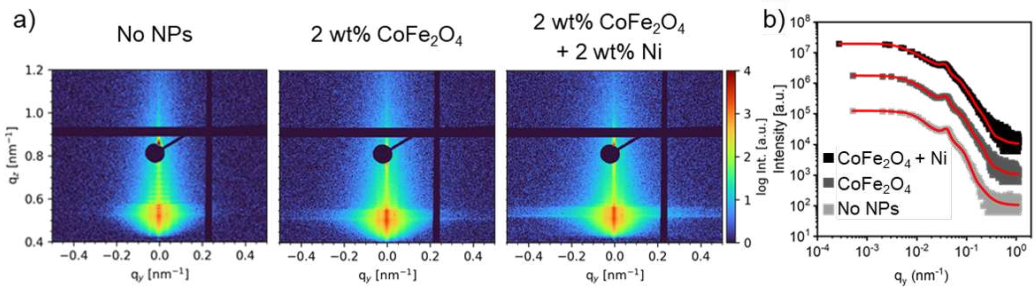

Figure 7.5: a) GISAXS images of as-printed, dry films. b) Fitted line cuts taken from the Yoneda region of the thin films.

The 2D GISAXS images data of the dry films after the printing process for the investigated DBC/NP systems are shown in Figure Fig. 7.5a: no NPs, 2 wt% $CoFe_2O_4$, and 2 wt% Ni with 2 wt% $CoFe_2O_4$. Furthermore, fitted line cuts taken from the Yoneda region of the thin films are shown in Figure Fig. 7.5b. From the 2D GISAXS data, it is possible to extract information about the polymer template, including the size of the polymer domains and the spacing between the domains. As NPs are added to the films, changes in the GISAXS patterns are observed, particularly seen through the appearance of scattering intensity at large q_y values, corresponding to the presence of individual NPs and NP aggregates. From the fitted lines cuts in Figure Fig. 7.5b, the incorporation of the NPs into the DBC template is confirmed for both the binary film and the ternary film as the structural information of the polymer shows no significant changes.

The functionality and magnetic properties of the binary and ternary films are investigated using a superconducting quantum interference device (SQUID) magnetometer. Figure Fig. 7.6 shows the temperature-dependent behavior of the saturation magnetization, M_s, remanence, M_r, and coercivity, H_c, for the ternary and binary films. Due to the presence of more NPs in the ternary system, M_s is higher for the ternary film than for the binary film. Furthermore, M_r and H_c are enhanced when compared to the binary film but still demonstrate the expected temperature-dependent behavior and decrease as the temperature is increased. The successful fabrication of ternary hybrid films containing two types of magnetic NPs highlights the potential for the tuning of the magnetic properties of such films, making them attractive for application in magnetic sensing or magnetic storage applications.

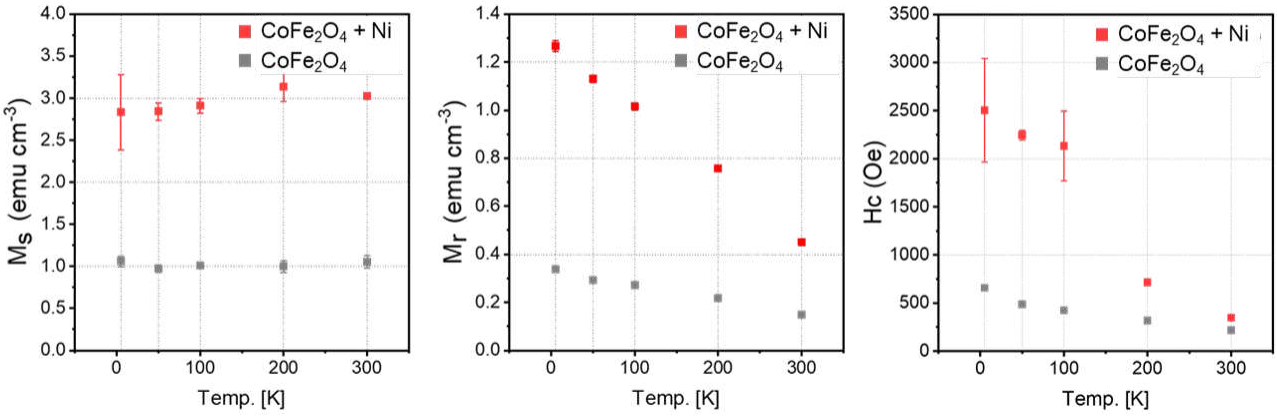

Figure 7.6: Saturation magnetization (M_s), remanence (M_r), and coercivity (H_c) of the binary hybrid film containing only $CoFe_2O_4$ NPs and ternary hybrid film containing both $CoFe_2O_4$ NPs and Ni NPs measured at five different temperatures. The ternary film shows enhanced magnetic properties as compared to the binary hybrid film.

[1] H. Hu, M. Gopinadhan, C. O. Osuji, *Soft Matter* **10**, 3867-3889 (2014)

[2] W. Cao, S. Xia, X. Jiang, M. Appold, M. Opel, M. Plank, R. Schaffrinna, L. P. Kreuzer, S. Yin, M. Gallei, M. Schwartzkopf, S. V. Roth, P. Müller-Buschbaum, *ACS Appl. Mater. Interfaces* **12**, 7557-7564 (2020)

[3] B. J. Kim, J. Bang, C. J. Hawker, J. J. Chiu, D. J. Pine, S. G. Jang, S. Yang, E. J. Kramer, *Langmuir* **23**, 12693-12703 (2007)

7.4 Influence of humidity-induced morphology changes of beta-lactoglobulin templated titania hybrid thin films on the Seebeck coefficient

L. F. Huber, S. Bernstorff[1], P. Müller-Buschbaum

[1] Elettra, Trieste, Italy

Fossil fuels still comprise the majority of electricity production around the world. [1] With typical energy conversion efficiencies between 30% and 50 % for state-of-the-art heat engines, most of the primary energy is lost to waste heat. [2] This represents tremendous potential for energy generation using the thermoelectric effect. The Seebeck effect enables the conversion of low-grade waste heat into usable electrical power. Nanostructuring has the potential to significantly improve the thermoelectric figure of merit ZT. Nanostructured titania can be achieved using biotemplating. In this work, we focus on the use of solution-based production and meniscus-guided slot-die coating [3] to emphasize scalability and mass production. Additionally, we substitute currently used toxic and scarce metal-based thermoelectric materials with abundant and environmentally friendly biohybrid materials. For this, we have chosen β-lactoglobulin (BLG) as the templating material to nanostructure titania thin films. Carbon black nanoparticles are also added to improve the electrical conductivity. BLG, a whey protein from cow and sheep milk, stands out due to its water solubility, non-toxicity, and pH-dependent structural changes. [4] However, the presence of BLG in these hybrid films introduces sensitivity to ambient humidity, as water molecules can be adsorbed by the films, causing the BLG components to swell. This swelling alters the morphology, leading to degradation of the hybrid films, which is potentially detrimental to their functionality in the aforementioned applications. Therefore, understanding and preventing this degradation is crucial.

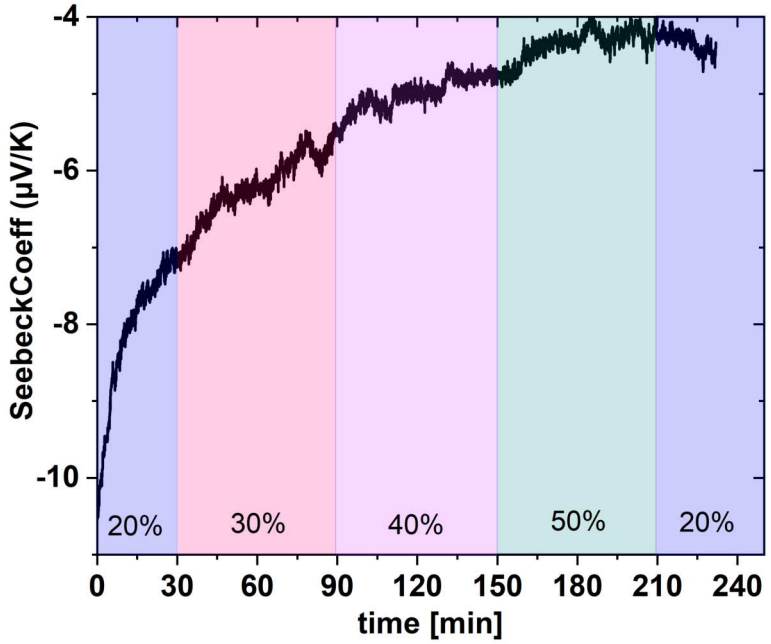

Figure 7.7:
Evolution of the Seebeck coefficient during 4 hour operando measurement at different relative humidity values.

To investigate the mesoscale structural changes induced by humidity, X-ray scattering techniques such as grazing incidence small angle X-ray scattering (GISAXS) can be used. Operando GISAXS experiments are performed at the Austrian SAXS beamline at ELETTRA synchrotron. Simultaneously, the Seebeck coefficient is measured to compare the structural changes during operation, with changes in the thermoelectric performance. A strong reduction in the Seebeck coefficient can be observed even at low levels of relative humidity (Fig. 7.7). Reducing the relative humidity from 50 % to 20 % does not lead to a significant recovery in the Seebeck coefficient. The total reduction of the Seebeck coefficient of almost 60 % coincides with morphological changes seen in Fig. 7.8. Here, structural changes can also be observed at 20% relative humidity. However, even higher levels of relative humidity seem not to influence the thin film morphology further. A reference measurement of the Seebeck coefficient at 10 % relative humidity shows no significant change. Therefore, the structural changes induced by the increased humidity cause a decrease of the Seebeck coefficient.

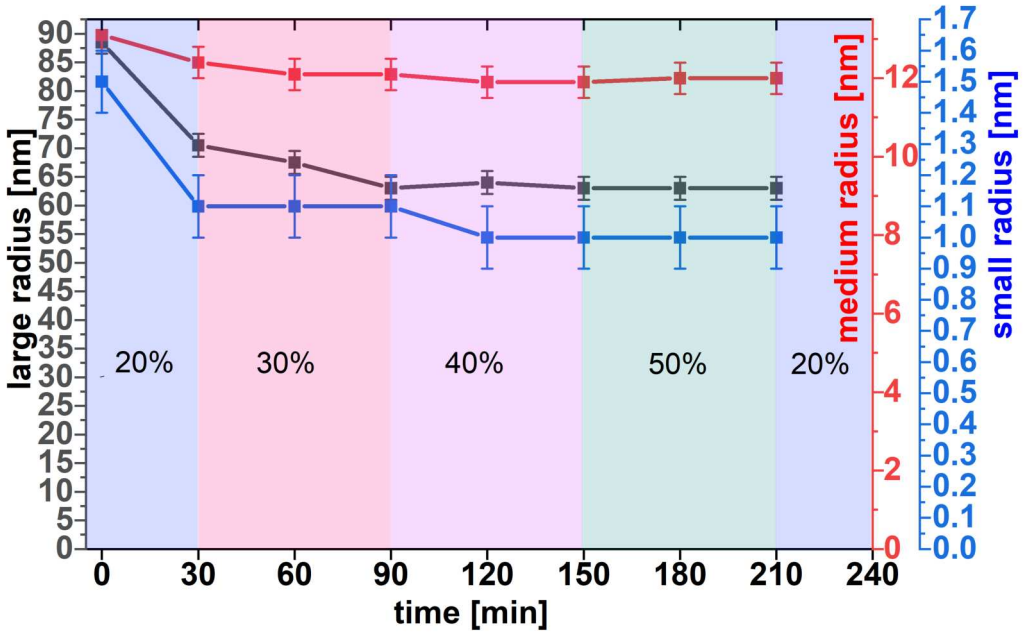

Figure 7.8:
Modelling results for in operando GISAXS measurements at different relative humidity levels.

[1] bp, *Statistical Review of World Energy* 1-68 (2020)

[2] C. Forman, I. K. Muritala, R. Pardemann, B. Meyer, *Renewable Sustainable Energy Rev.* **57**, 1568-1579 (2016)

[3] M. A. Reus, T. Baier, C. G. Lindenmeir,A. F. Weinzierl,A. Buyan-Arivjikh, S. A. Wegener, D. P. Kosbahn,L. K. Reb,J. Rubeck,M. Schwartzkopf,S. V. Roth,P. Müller-Buschbaum, *Rev. Sci. Instrum.* **95**, (2024)

[4] J. Adamcik, R. Mezzenga, *Macromolecules* **45**, 1137–1150 (2012)

7.5 Tracking degradation of non-fullerene organic solar cells under dynamic environmental conditions

L. Li, P. Müller-Buschbaum

Over the past few years, advancements in non-fullerene materials and fabrication techniques have significantly contributed to the improvement of the single organic solar cell (OSC) performance, pushing their power conversion efficiency (PCE) up to 20%. Moreover, compared to conventional silicon-based photovoltaics, OSCs exhibit notable benefits, including flexibility and solution processability. However, limited device stability remains the primary obstacle preventing their widespread adoption. The degradation of OSCs arises from multiple factors. Some originate from chemical processes, such as reactions with oxygen and moisture, while others result from physical changes, like morphology alterations caused by operating temperature fluctuations. Some remarkable studies are focusing on the specific process of device degradation. For instance, operando X-ray scattering studies have been conducted to investigate device performance under different environmental conditions, leading to many unique discoveries [1]. However, in real-world environments, environmental parameters are not applied in a constant manner but rather fluctuate dynamically in cycles. For example, temperature and humidity change periodically with sunrise and sunset, following the cyclic variation of light intensity. In extreme conditions, such as in deserts, these fluctuations can be quite substantial. This raises an important question: In a changing environment, does the degradation process of the device continuously accumulate, or does it undergo a cyclic recovery?

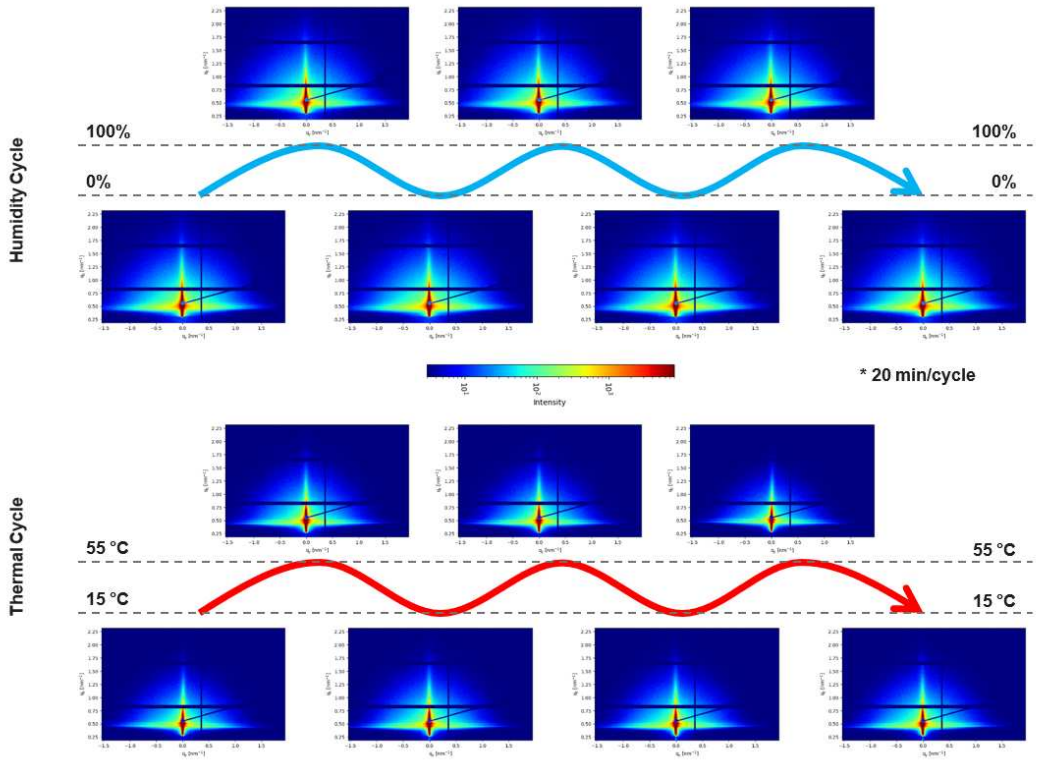

Figure 7.9:
2D GISAXS data at different stages of humidity cycling (0% – 100%) and temperature cycling (15°C – 55°C).

In this study, we prepare active layers (non-fullerene acceptor:BTP-4F, donor polymer: D18) commonly used in organic solar cells and conducted in situ X-ray scattering measurements in

a specialized setup capable of controlling environmental variations. We select three adjustable variables: temperature, humidity, and illumination. Under real-world conditions, according to meteorological records, these three factors are coupled: as sunlight intensity increases, temperature gradually rises while humidity decreases; conversely, when sunlight diminishes, temperature drops, and humidity increases. To investigate the individual effects of each factor on device degradation, we varied only one parameter at a time during the experiments. The humidity is cycled between 0% and 100%, while the temperature changes between 15°C and 55°C.

Fig. 7.9 displays 2D GISAXS data at different stages of the temperature and humidity cycling. During the transition from 0% to 100% humidity, changes of the intensity near the Yoneda region can be observed. By performing a 1D line cut near this region and conducting preliminary fits, it can be determined that the intensity at larger q values decreases, while the intensity at relatively smaller q values increases to some extent. This suggests a structural evolution in the thin film, where smaller structures transform into larger ones. By comparing the 2D GISAXS data and extracted 1D line cuts of the thin films at different stages but with the same humidity, it is observed that their intensity and peak positions do not differ significantly. To some extent, this indicates that during the humidity cycling process, the thin film structure also undergoes a cyclic variation. Similarly, a comparable pattern is observed in the experiments involving temperature cycling.

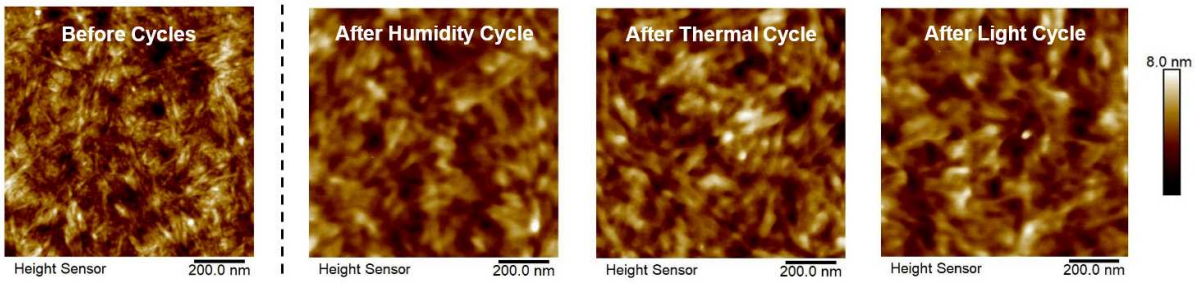

Figure 7.10:
AFM topography images show the height difference before and after environmental cycle operations.

As we can see in Fig. 7.10, the AFM characterization of the active layers before and after environmental cycling shows noticeable differences. After cycling, the surface structures appear slightly larger compared to before (from a few nanometers to over ten nanometers.), indicating that the active layer has undergone a certain degree of degradation. This result is consistent with the structural size changes observed in the GISAXS analysis, showing that surface and inner structures change in a similar fashion. However, surface characterization of intermediate stages is still ongoing.

In summary, we perform in situ GISAXS characterization and AFM measurements on the active layer of organic solar cells under environmental cycling conditions. The experimental results suggest that the degradation of the active layer is unlikely to progress linearly but instead follows a dynamic process influenced by the repeated changes in environmental conditions. In the future, we will investigate the relationship between the specific device performance and the cycling process while also working to improve the fits of the GISAXS data.

[1] X. Jiang, A. J. Gillett, Z. Tianle, S. Xin, J. E. Heger, S. Kun, L. V. Spanier, R. Guo, S. Liang, S. Bernstorff, P. Müller-Buschbaum, *Energy Environ. Sci.* **16**, 5970-5981 (2023)

7.6 Thermal cycling of printed organic solar cells

C. G. Lindenmeir, S. Bernstroff[1], P. Müller-Buschbaum

[1] Elettra, Triste, Italy

Organic solar cells (OSCs) have received a lot of attention in recent years because of their non-toxicity, high absorbance, quick energy payback times, and high efficiencies achieved in just a few years of research. Furthermore, OSCs are especially interesting due to their simple solution-based production process, which enables thin and flexible solar cells. Especially slot-die printing is a very promising fabrication approach because it is fast, causes low waste, and is easily up-scalable [1], making OSCs even more viable for future applications like being used in space. Space application is particularly promising for OSCs since they are lightweight, thin, and have a far higher power-to-weight ratio than commercially available gallium arsenide solar cells [2]. This lowers the cost of a rocket launch drastically. OSCs have already proven to work in space for a short period of time [3]. However, the harsh circumstances found in space, including high vacuum, radiation, and extremely high temperatures, are expected to cause the OSCs to degrade quickly. Thus, in this study, we examine how printed OSCs are affected by extreme temperature variations ranging from 0 to 120 °C. Using operando grazing incidence small-angle X-ray scattering (GISAXS), we investigate their degradation process.
In the first part of this work, we look at the temperature influence on OSCs. Therefore, we track the power conversion efficiency (PCE), the fill factor (FF), the short circuit current (I_{SC}), and the open circuit voltage (V_{OC}) during cycling the temperature sinusoidally from 0 to 120 °C with increasing amplitude. With increasing temperature also the PCE, the FF, and the I_{SC} are rising, which can be seen in Fig. 7.11 a), b) and d) respectively. On the other hand, the V_{OC} is decreasing with higher temperatures, which can be seen in Fig. 7.11 c).

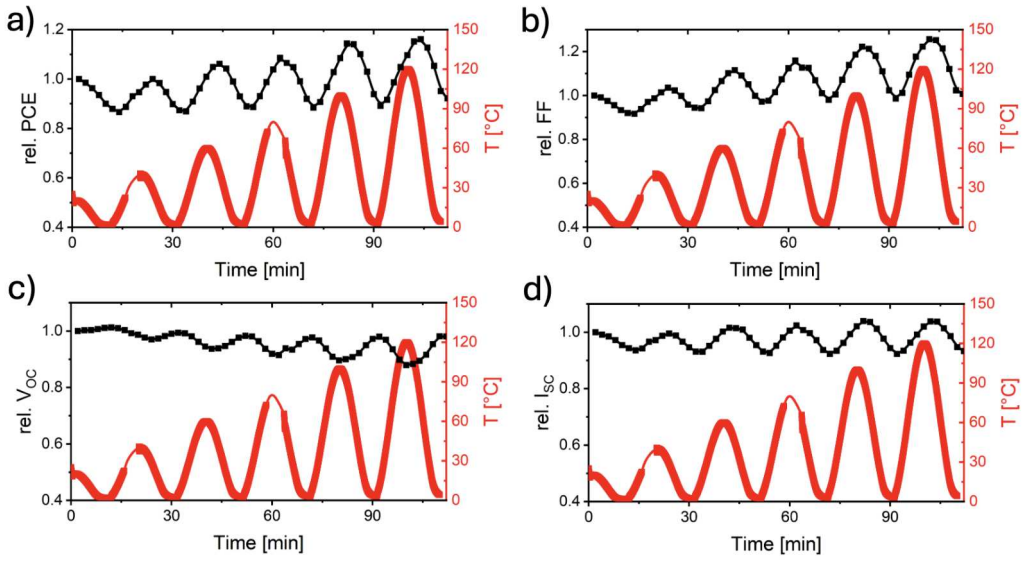

Figure 7.11:
Electronic properties of an organic solar cell during thermal cycling: a) PCS, b) FF, in c) V_{OC}, and d) I_{SC}. The temperature curve is plotted in red.

To gain a better understanding of the influence of temperature cycling on the organic active layer, operando grazing incidence small-angle X-ray scattering (GISAXS) is performed to gain information about structure changes in the film during operation and temperature cycling. GISAXS data are always taken at the extrema of the temperature curve, and the horizontal line

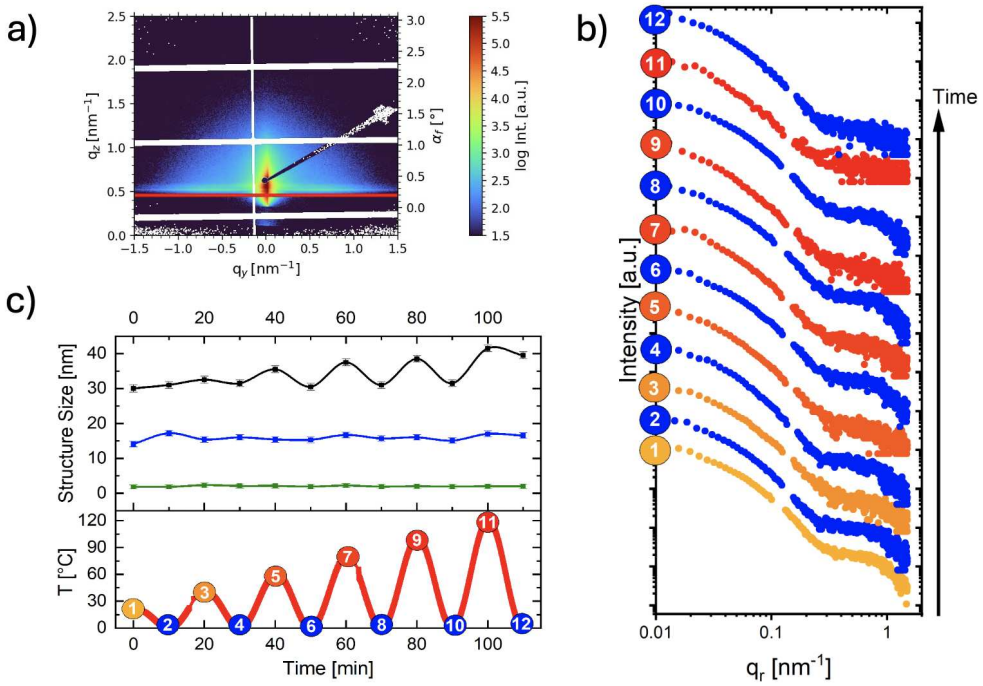

Figure 7.12:
a) 2D GISAXS data of an OSC with the red line indicating the position of the horizontal line cut at the critical angle. b) Horizontal line cuts during the thermal cycling process shifted along the y axis. The blue curves are measured at 0°C while the orange/red curves are measured at the increasing temperature amplitude maximum from 20 to 120 °C. c) Size changes of the three structures inside the active layer as determined from the fits of the horizontal line cuts.

cuts are taken at the critical angle (shown in Fig. 7.12 a)) and fitted with three independent cylindrical structures to track the size changes over the whole temperature cycle. The horizontal line cuts are shown in Fig. 7.12 b). The blue curves represent the measurements always taken at 0 °C and the orange/red curves represent the measurements taken at the increasing temperature amplitude maximum from 20 to 120 °C. When looking at the horizontal line cuts taken always at 0°C, no pronounced changes are visible except after heating up to 120°C. When looking at the change in structure sizes in Fig. 7.12 c) gained by the fit of the horizontal line cuts, one can see that the small and medium size structures (marked in green and blue) are not changing, while the largest structure (marked black) is shifting towards larger structures when increasing the temperature. The film morphology overall is stable over the temperature cycle and we see reversible changes in the structure happening up to 100 °C, which changes into irreversible morphology transformations after heating to 120 °C.
The results show that PCE, FF, and I_{SC} increase with temperature, while V_{OC} decreases during the thermal cycling of an OSC. In situ GISAXS measurements reveal that the film morphology remains stable, with reversible structural changes up to 100°C. However, irreversible changes occur after 120°C, particularly in the largest structures.

[1] S. Razza, S. Castro-Hermosa, A. Di Carlo, T. M. Brown, *APL Mater.* **4**, 091508 (2016)

[2] S. Xiong, K. Fukuda, S. Lee, K. Nakano, X. Dong, T. Yokota, K. Tajima, Y. Zhou, T. Someya, *Adv. Sci.* **9**, 2105288 (2022)

[3] L. K. Reb, M. Böhmer, B. Predeschly, S. Grott, C. L. Weindl, G. I. Ivandekic, R. Guo, C. Dreißigacker, R. Gernhäuser, A. Meyer, P. Müller-Buschbaum, *Joule* **4**, 1880-1892 (2020)

7.7 In-situ observation of quasi-2D wide-bandgap perovskites under light and rapid thermal cycling

K. Sun, M. Schwarztkopf[1], P. Müller-Buschbaum
[1] DESY, Hamburg, Germany

To further boost the power conversion efficiency of perovskites solar cells (PSCs), tandem solar cells are applied by integrating wide-bandgap perovskites ($\approx$ 1.7 eV) with other mature narrow-bandgap solar cells, e.g., c-Si and CIGS. However, three-dimensional wide-bandgap perovskites with mixed halides suffer from phase separation under light and heat conditions, limiting their solar cells performance and operational stability. Previous studies suggested that reduced dimensionality (n) can effectively suppress ion migration and therefore phase segregation [1]. Reduced-dimensional perovskites (RDPs) can be categorized into two representative classes: Ruddlesden-Popper (RP) ($A'_2A_{n-1}B_nX_{3n+1}$) and Dion-Jacobson (DJ) ($RA_{n-1}B_nX_{3n+1}$), where the inorganic slabs separated by bulky organic spacers (A', monovalent organic spacers; R, divalent organic spacers), and n refers to the number of inorganic layer sheets. In addition, it is suggested that the organic spacers dictate the ion migration in mixed-halide RDPs. Nevertheless, a study of comparing different categories of RDPs with higher dimensionality (n $>$1) under light thermal cycling is still missing.

Herein, we monitor the wide-bandgap RP ($BA_2MA_3Pb_4(I_{0.6}Br_{0.4})_{13}$) and DJ ($(PDMA)MA_3Pb_4(I_{0.6}Br_{0.4})_{13}$) perovskites under light illumination and rapid thermal cycling by in-situ grazing-incidence wide-angle X-ray scattering (GIWAXS), where BA and PDMA refer to butylammonium and 1,4-phenylenedimethanammonium, respectively. We find that the wide-bandgap RP perovskites undergo phase separation after 3 thermal cycles, with the out-of-plane direction being more affected. In contrast, DJ perovskites are more stable against thermal cycling comparing to that of RP perovskites. Understanding the behaviors of wide-bandgap RP and DJ RDPs under extreme conditions provide new insights for designing new perovskite top cells in tandem applications and enhancing their stability.

RDPs are prepared via a one-step spin-coating deposition method on ITO or glass substrates. It is often the case that a mixture of different n-phases is easily formed in RDPs during film growth. Fig.7.13a shows the PL spectra of RP and DJ perovskite excited from the glass side, demonstrating the presence of lower n-phase (n = 2, $\approx$ 520 nm) in both RP and DJ perovskite. Synchrotron-based GIWAXS is utilized to monitor the structure change of RDPs under light illumination and thermal cycling. To accelerate the degradation, we apply rapid heating and cooling rate with one full cycle of 15 min (Fig.7.14). We observe the scattering peak oscillation of RP and DJ RDPs, corresponding to the temperature-induced lattice expansion and shrinkage. Notably, an additional sample-to-detector (SDD) correction by calibrating the ITO peak is applied to rule out instrumental effect. In addition, the intensity of PbI_2 ($\approx 0.9\mathring{A}^{-1}$) of RP RDPs is largely enhanced at 18 min, whereas the PbI_2 peak of DJ RDPs is relatively stable under thermal cycling, demonstrating the stability of DJ RDPs against light and temperature variations. There is a reversible phase separation ($\approx 1.0\mathring{A}^{-1}$) of RP RDPs (Fig.7.14a, bottom) after three thermal cycles (≈ 50 min) at the maximum temperature, while this phenomenon is absent in DJ RDPs. Taken together, this indicates that DJ RDPs are more stable compared to RP RDPs under light illumination and thermal cycling.
In summary, we investigate the thermal stability of representative RP and DJ perovskites using in-situ GIWAXS measurements. Our results demonstrate that DJ perovskites are more stable and do not undergo phase separation under thermal cycling. Thus, our work paves the way for utilizing reduced-dimensional perovskites under extreme conditions.

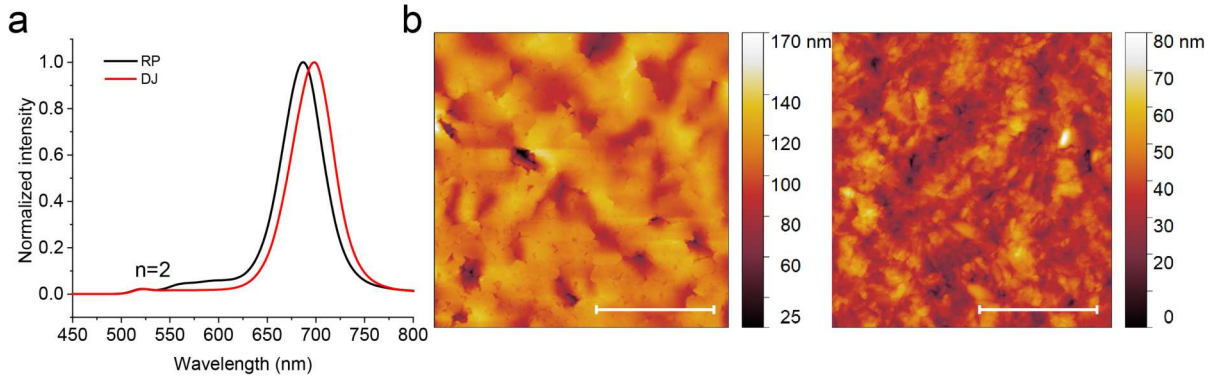

Figure 7.13:
a) Photoluminescence spectra of wide-bandgap RP and DJ films on glass, excited from the glass side. b) AFM images of RP (left) and DJ (right), where the scale bar is 2 μm.

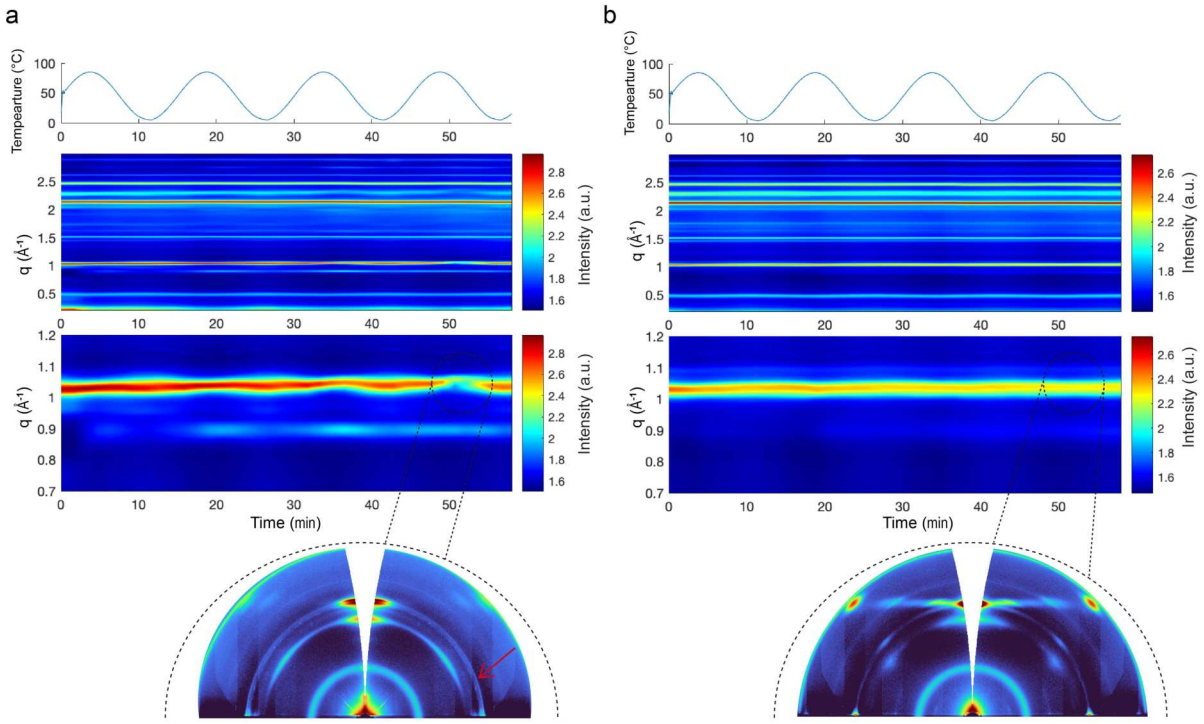

Figure 7.14:
Time evolution of GIWAXS data plotted as radically integrated line profiles of 2D GIWAXS data during thermal cycling (5°C to 85°C, 15 min/cycle), where the temperature evolution is shown in the figure. a) RP film on ITO and b) DJ film on ITO substrates. The enlarged time-resolved GIWAXS of RP and DJ is placed underneath, with the 2D reshaped GIWAXS data of both RP and DJ is given, showing the peak splitting of RP (red arrow) under thermal cycling.

[1] T. L. Leung, Z. Ren, A. A. Syed, J. Popović, *ACS. Energy. Lett.* **7**, 3500-3508 (2022)

7.8 Morphological evolution of organic film formation during spray deposition

S. Xiong, P. Müller-Buschbaum, S. V. Roth[1,2]

[1] DESY, Hamburg, Germany
[2] KTH, Stockholm, Sweden

Organic solar cells (OSCs) have received broad interest owing to low-cost, flexibility, semitransparent, non-toxicity, and being ideal for roll-to-roll large-scale processing ability. Significant advances have been made in the field of OSCs including high-performance active layer materials, electrodes, interlayers, and novel device structures. Solution processability allows for material diversification and, thus, for developing sustainable, low-cost manufacturing technologies to optimize the solution-to-film process [1]. The film formation process of organic thin films involves kinetic and thermodynamic non-equilibrium processes assisting the fixation of molecules from disordered to ordered structures. Ultrasonic spray deposition (USD) is a scalable large-area deposition technique that leads to smoother and more homogenous films than airbrush spray deposition. USD offers several benefits compared to spin-coating, such as superior scalability for large-area applications, reduced material wastage, and improved substrate compatibility. This technique enables a uniform deposition on uneven surfaces and can be more cost-efficient, presenting an alternative for large-scale and economical production of organic photovoltaic devices [2].
Owing to the exploitation of simple and efficient solution-treated OSCs, poly(3,4-ethylenedioxythiophene):polystyrene sulfonate (PEDOT:PSS) is considered as one of the standard hole transport layers. It can be dispersed in water or organic solvents [3]. In this study, we use USD to develop sprayed OSCs. In detail, the nanoscale morphology and structural transition of PEDOT:PSS film formation under varying spray conditions are investigated. We aim to demonstrate the principles of rational modulation on the morphology of PEDOT:PSS to achieve high-efficiency sprayed OSCs.

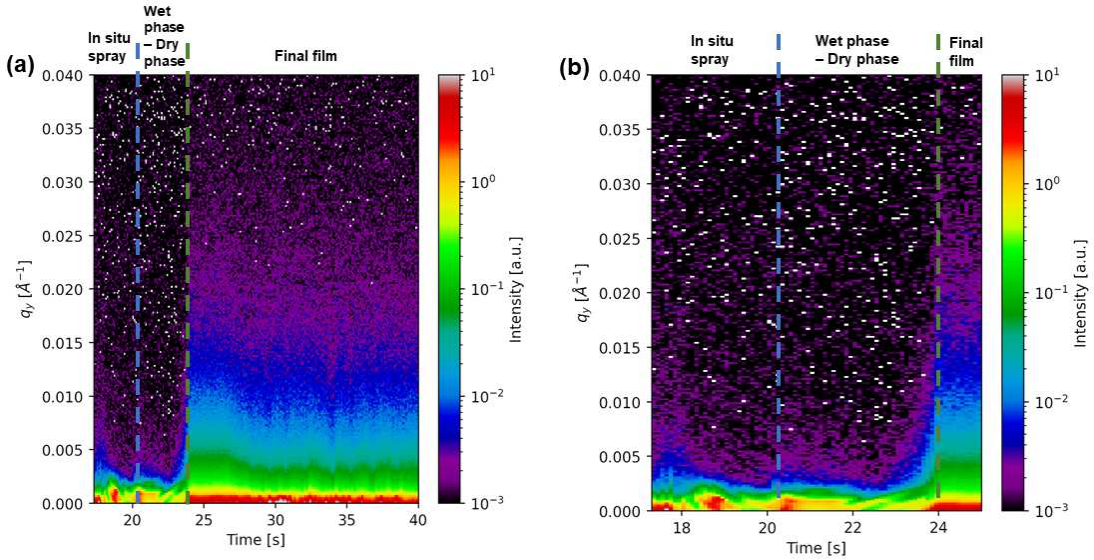

Figure 7.15:
(a) Mapping of horizontal line cuts from the 2D GISAXS data showing the spray deposition and (b) zoom in into the in-situ and drying processes.

For the structural evolution during the non-equilibrium state of the film formation, in-situ grazing-incidence small-angle X-ray scattering (GISAXS) is used to monitor the spray process of PEDOT:PSS in real-time. Fig. 7.15(a) shows the mapping of horizontal line cuts from the 2D GISAXS data of the complete spray deposition process, including the drying phase. The process can effectively be divided into three distinct stages. The first stage, known as the spray solution

period, involves the atomization of the solution and the deposition onto the substrate, lasting for around 2.5-3.5 s. The second stage is the transition from a wet to a dry film, during which the PEDOT:PSS chains begin to self-assemble and progressively pack into a partially ordered structure as the solvent evaporates, with a duration of around 2.8-3.1 s. The third stage is the final formation of the film with the complete evaporation of the solvent, where PEDOT:PSS chains and molecules are fixed in a well-ordered arrangement. Additionally, a zoom into the first 6.7 seconds of the same process is shown in Fig. 7.15(b). In this regime, the phase before the in-situ spray phase (blue) and the wet phase to the dry phase can be clearly distinguished.

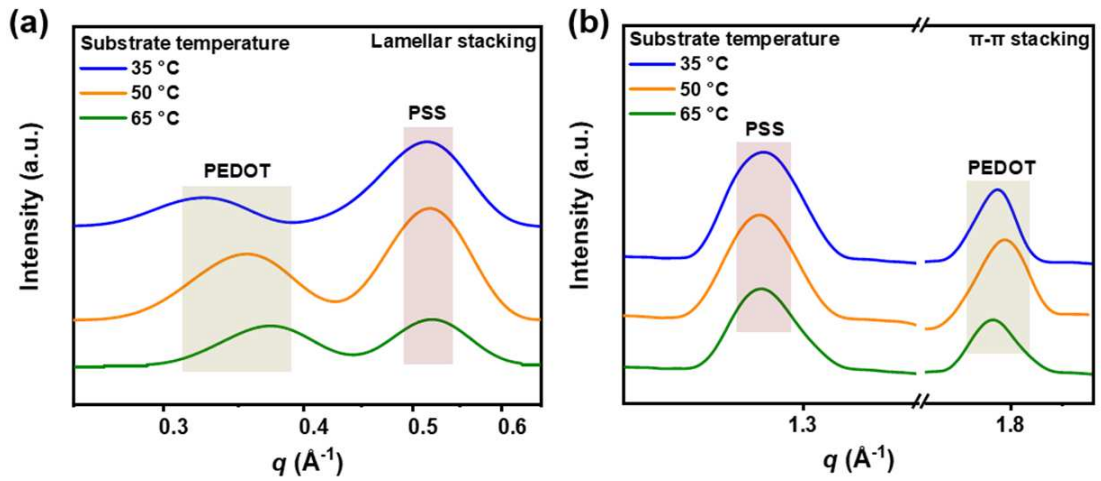

Figure 7.16:
Line cuts of 2D GIWAXS data for (a) lamellar stacking and (b) π-π stacking of sprayed PEDOT:PSS films at different substrate temperatures.

To investigate the surface morphology and crystallinity of the final films, atomic force microscopy (AFM) and grazing-incidence wide-angle X-ray scattering (GIWAXS) are conducted. Here, different substrate temperatures are used upon spray deposition of PEDOT:PSS. All the films are relatively uniform with fewer aggregations, and the roughness of the films gradually enhances with the increase in the deposition substrate temperature, indicating a temperature-induced aggregation of PEDOT:PSS. For GIWAXS data analysis, two angular regions are chosen in order to analyze the lamellar stacking and π-π stacking of PEDOT and PSS (Fig. 7.16). With increasing substrate temperature, USD-prepared PEDOT:PSS films show a first enhanced and then decreased lamellar stacking (change in intensity) and π-π stacking of PEDOT and PSS, suggesting the temperature-induced molecular conformation transition of PEDOT:PSS. At a medium substrate temperature, the USD-prepared PEDOT:PSS films exhibit the highest lamellar and π-π stacking diffraction intensity, along with the most compact π-π stacking of PEDOT, indicating the highest structural order.
In summary, we optimize the film formation of PEDOT:PSS for the USD process. The favorable phase separation and highest structural order occurred for depositing PEDOT:PSS at the medium substrate temperature, which indicates the temperature-dependent properties of the sprayed PEDOT:PSS films. This provides an effective guideline for the realization of large-area production of organic photovoltaic devices by elucidating the structure-processing-function relationship.

[1] Z. Wang, K. Gao, Y. Kan, M. Zhang, C. Qiu, L. Zhu, Z. Zhao, X. Peng, W. Feng, Z. Qian, X. Gu, A. K.-Y. Jen, B. Tang, Y. Cao, Y. Zhang, F. Liu, *Nat. Commun.* **12**, 332 (2021)

[2] J. Cheng, R. Hu, X. Meng, Y. Li, X. Yan, X. Yang, Xi. Liao, L. Li, Q. Pei, K. Chong, *Sol. RRL* **2**, 1800064 (2018)

[3] Y. Tong, B. Xu, F. Ye, *Adv. Funct. Mater.* **34**, 2310865 (2024)

8 Development of instrumentation and software

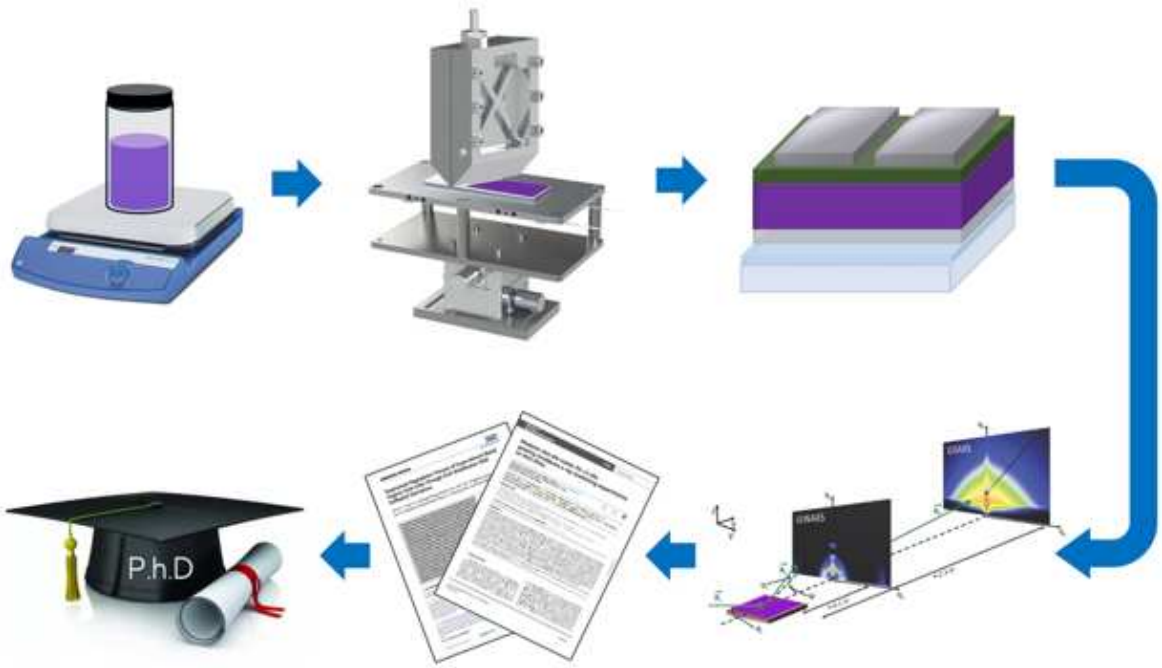

8.1 Machine learning-supported analysis of time-resolved 2D GISAXS data reveals the film formation of nanostructured titania during spray deposition

J. E. Heger, S. Dan[1], Y. Zhai[1], S. V. Roth[1,2], P. Müller-Buschbaum

[1] DESY, Hamburg, Germany
[2] KTH, Stockholm, Sweden

Nanostructured titania has a wide range of applications in energy materials, such as next-generation photovoltaics, batteries, and the photocatalytic hydrogen generation. An important aspect of titania applications in energy materials is the achievement of a tailored nanostructure by means of wet-chemistry synthesis, which enables the material to be solution processible and meets economical interests, such as large-scale deposition during spray or slot-die coating in ambient conditions. Such wet-chemistry approaches are typically based on block copolymer directed templating of the nanostructure but are also increasingly based on more sustainable, aqueous biopolymer solutions. [1]

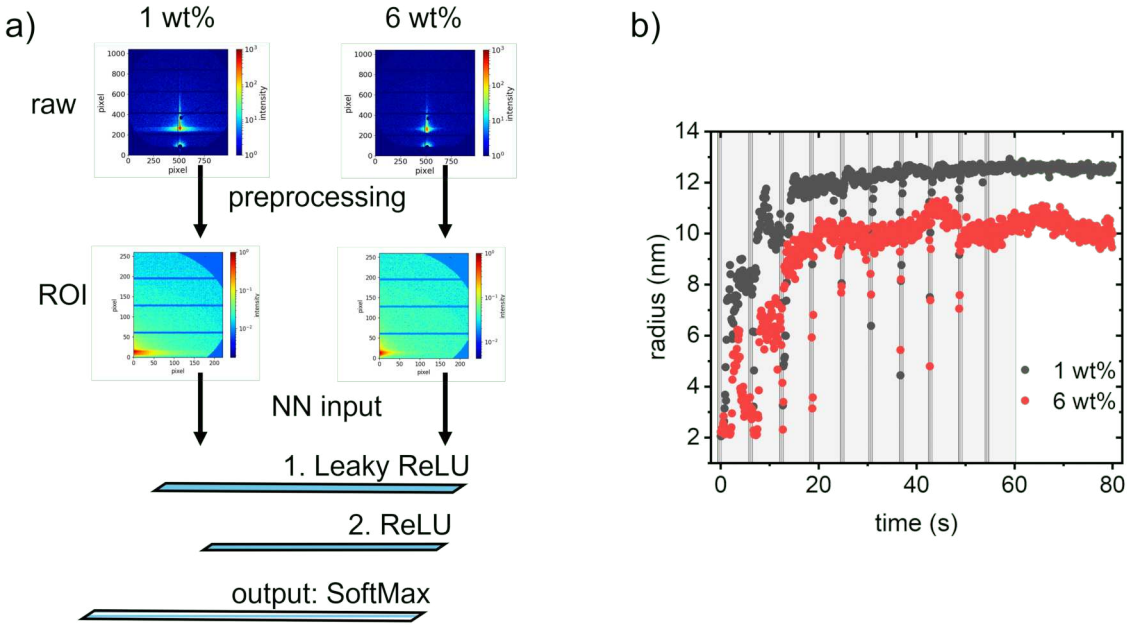

Figure 8.1:
a) Flow diagram of 2D GISAXS analysis by the neural network. b) Domain growth for the 1 wt% and 6 wt% samples as predicted by the neural network recognizes the distinct growth behavior and individual spray pulses.

To understand the influence of the template on the nanostructure of titania and thus being able to control the performance of titania in applications, time-resolved characterization of film formation using grazing-incidence small-angle X-ray scattering (GISAXS) is indispensable. GISAXS provides a representative picture of the sample structure and not only benefits the understanding of nanostructured titania but also other cutting-edge topics in material science. These include the development of highly efficient organic or perovskite photovoltaics, where nanoscale morphology plays a crucial role in optimizing light absorption and charge transport. Furthermore, GISAXS gives insights into the design of functional coatings for biological or medical applications, such as biocompatible surfaces for implants and antimicrobial films. The high brilliance at the synchrotron facility enables researchers to track the fast kinetics of structure formation with high temporal resolution. A typical exposure period of 10 Hz and above makes it possible to capture rapid transformations during film formation based

on solvent evaporation, crystallization, and phase separation. Consequently, a large amount of complex data is obtained, that typically requires expert knowledge for a correct interpretation and time-consuming analysis. The required expertise, however, limits the wide range of possible GISAXS studies in the nanoscience community and slows down further development and innovative research. Given this challenge, an increasing focus is put on machine-learning supported analysis of such data. [2-4] The software framework VIPR (Versatile Inverse Problem Software Framework) aims to lower barriers for a wide range of scientists working in the field of nanoscience to apply time-resolved characterization by in-situ GISAXS to their science cases and efficiently use experimental time at large scale facilities. [5]
In this context, we demonstrate the potential of a neural network that was trained on synthetic 2D GISAXS data to analyze experimental, time-resolved 2D GISAXS data on the fly, thus bringing immediate feedback to the user at the synchrotron. This approach aims to ensures an efficient use of cost expensive beamtime and at the same time checks if the validity of the experimental data is given. Here, the in-situ 2D GISAXS data was acquired during the spray deposition of biotemplated titania films. Based on the amount of biotemplate (1 wt% and 6 wt%), two different weight ratios of biotemplate and titania precursor were installed, which is known to tailor the nanostructure of the overall composite. The experiment is based on layer-by-layer deposition by pulsed spray coating, where a 0.1 s spray pulse was performed every 6 s for 10 times, followed by 20 s of drying time. Hence, the experiment lasted in total 80 s, and with an exposure period of 10 Hz, a total number of 800 2D GISAXS data frames per sample were acquired. The experimental raw data is preprocessed by cropping the data down to a certain region of interest followed by masking of hot pixels and intensity normalization (Fig. 8.1a). After this preprocessing, the data is fed to the neural network, which was trained on synthetic data of simulated hemispherical form factors with a constant Gaussian size distribution. The neural network is a multilayer dense model implemented using TensorFlow Keras and consists of two dense layers. The first dense layer has 1024 nodes with a Leaky ReLU activation function (α = 0.03), followed by a second dense layer with 504 nodes and a standard ReLu activation function. The output layer consists of 270 units, producing a probability distribution from which the predicted weighted average radius of the mean structure size is obtained by SoftMax. The results are presented in Fig. 8.1b. For a total of 800 data points per sample, the neural network predicts a sigmoidal domain growth on different time scales, resulting in an overall larger domain radius of about 12.5 nm for the 1 wt% sample compared to about 10 nm for the 6 wt% sample. Furthermore, the neural network recognizes characteristic features of spray deposition, such as the individual spray pulses, which are leading to a drop in size due to the altered surface conditions. This prediction is of crucial importance to understand the film formation and to verify a successful spray deposition experiment. Furthermore, the neural network trained on synthetic data shows flexibility in analyzing different kinds of experimental data, which is promising for a straightforward application to a wide range of time-resolved 2D GISAXS data sets.

[1] J. E. Heger, W. Chen, S. Yin, N. Li, V. Körstgens, C. Brett, W. Ohm, S. V. Roth, P. Müller-Buschbaum, *Adv. Funct. Mater.* **32**, 2113080 (2022)

[2] A. Hinderhofer, A. Greco, V. Starostin, V. Munteanu, L. Pithan, A. Gerlach, F. Schreiber, *J. Appl. Cryst.* **56**, 3 (2023)

[3] L. Pithan, V. Starostin, D. Marecek, L. Petersdorf, C. Völter, V. Munteanu, M. Jankowski, O. Konovalov, A. Gerlach, A. Hinderhofer, B. Murphy, S. Kowarik, and F. Schreiber, *J. Synchrotron Rad.* **30**, 1064 (2023)

[4] Z. He, J. Lütgert, M. G. Stevenson, B. Heuser, D. Ranjan, C. Qu, D. Kraus, *High Power Laser Sci. Eng.* **12**, e46 (2024)

[5] https://vipr-project.de/en/home

8.2 Space VALIdation of Improved Novel solar cells (SVAL*IN) – progressing the development of thin film solar cells in space

L. V. Spanier, C. Dreißigacker[1], P. Müller-Buschbaum

[1] DLR, Köln, Germany

The demand for lightweight and efficient energy harvesting technologies for space applications has driven significant advances in thin-film solar cells. These devices, characterized by their low mass, flexibility, and tunable optoelectronic properties, are particularly suited for space missions where minimizing payload weight and maximizing energy efficiency are critical. Organic solar cells, perovskite solar cells, and tandem configurations of these technologies represent promising solutions for next-generation space power systems. Their ability to be fabricated using scalable printing techniques further enhances their potential for deployment in large-area, low-cost applications, such as satellite arrays, planetary rovers, and lightweight orbital systems.

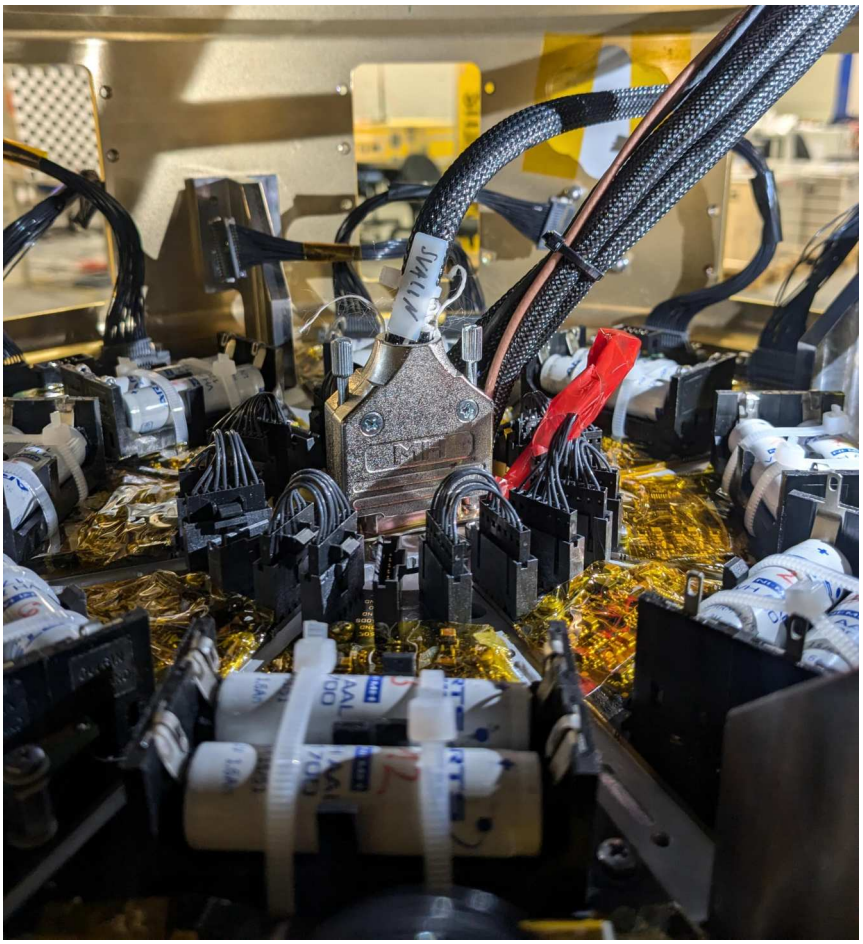

Figure 8.2:
Photo of the inside of the SVAL*IN payload installed on the suborbital rocket. The solar cells are later mounted radially outwards within the open windows.

Building on previous experiments [1-2], a follow-up project focuses on testing high-efficiency ternary organic solar cells, printed organic solar cells, and perovskite solar cells in two configurations (n-i-p and p-i-n). The experiment is designed to explore the performance of these solar cells under extended suborbital conditions, providing valuable insights in preparation for future tandem-cell experiments (Fig. 8.2). The flight, launched from Esrange Space Center in Sweden, reached an apogee of 308 km, enabling a prolonged experiment phase under near-space conditions. The payload was equipped with aerodynamically optimized experiment

modules that minimized the accumulation of soot from the rocket's ablative heat shield during ascent, ensuring the solar cells remained clean and unobstructed (Fig. 8.3). Additionally, newly integrated spectrometers allowed for real-time monitoring of changes in the solar cells' absorption behavior, providing unprecedented insight into their optoelectronic stability under near-space conditions.

Post-flight characterization will focus on grazing-incidence small-angle X-ray scattering (GISAXS) and grazing-incidence wide-angle X-ray scattering (GIWAXS) to investigate morphological changes in the thin films. These measurements will provide detailed insights into structural modifications at the nanoscale, including potential phase segregation, crystallinity alterations, and interface stability. Understanding these changes is critical for optimizing the material compositions and device architectures of thin-film solar cells for prolonged space missions.

Figure 8.3:
Photo of the fully integrated payload. The SVAL*IN experiment is located towards the bottom of the payload at the height of the letter "U".

This experiment represents a significant step forward in the development of advanced thin-film solar cells for space applications. By integrating real-time spectroscopic monitoring and a comprehensive study on the resistance of various solar cell architectures against environmental effects in space, the project has laid the foundation for future tandem-cell experiments and long-duration orbital tests. Such efforts are vital for realizing lightweight, high-performance solar power systems capable of sustaining the energy demands of next-generation space exploration.

[1] L.K. Reb, M. Böhmer, B. Predeschly, S. Grott, C.L. Weindl, G.I. Ivandekic, R. Guo, C. Dreißigacker, R. Gernhäuser, A. Meyer, and P. Müller-Buschbaum, *Joule* **4**, 1880 (2020).

[2] L.K. Reb, M. Böhmer, B. Predeschly, L.V. Spanier, C. Dreißigacker, A. Meyer, and P. Müller-Buschbaum, *Solar RRL* **6**, 2270112 (2022).

9 Teaching and outreach

9.1 Lectures, seminars and lab courses

Lectures, seminars and lab courses Spring Term 2024

- Prof. Christine Papadakis, PhD
  Angewandte Physik: Polymerphysik 2
- Prof. Christine Papadakis, PhD
  Materialwissenschaften
- Prof. Dr. Peter Müller-Buschbaum, Prof. Dr. Christian Große
  Mess- und Sensortechnologie
- Prof. Dr. Peter Müller-Buschbaum,
  Nanostructured Soft Materials 2
- Prof. Dr. Winfried Petry
  Physik mit Neutronen 2
- Prof. Dr. Peter Müller-Buschbaum, Prof. Christine Papadakis, PhD
  Bachelor-Seminar: Funktionelle weiche Materialien
- Prof. Dr. Peter Müller-Buschbaum
  Seminar: Current Problems in Organic Photovoltaics
- Prof. Dr. Bastian Märkisch, Prof. Dr. Peter Müller-Buschbaum,
  Dr. Christoph Morkel, Prof. C. Pfleiderer
  Seminar: Neutronen in Forschung und Industrie
- Prof. Dr. Peter Müller-Buschbaum, Prof. Christine Papadakis, PhD
  Seminar: Polymers
- Prof. Dr. Peter Müller-Buschbaum, Prof. Christine Papadakis, PhD
  ProSeminar: Structure and Dynamics of Condensed Matter

Autumn Term 2024/25

- Prof. Christine Papadakis, PhD
  Angewandte Physik: Polymerphysik 1
- Prof. Dr. Peter Müller-Buschbaum
  Nanostructured Soft Materials 1
- Prof. Dr. Winfried Petry
  Physics with Neutrons 1
- Prof. Dr. Peter Müller-Buschbaum
  Seminar: Current Problems in Organic Photovoltaics
- Prof. Dr. Peter Müller-Buschbaum, Prof. Christine Papadakis, PhD
  Seminar: Polymers
- Prof. Dr. Peter Müller-Buschbaum, Prof. Christine Papadakis, PhD
  ProSeminar: Structure and Dynamics of Condensed Matter

Lab Courses 2024 (Fortgeschrittenenpraktika)

- *Atomic Force Microscopy*
- *Characterization of Polymers with Differential Scanning Calorimetry*

9.2 Conferences and public outreach

Heinz Maier-Leibnitz Zentrum (MLZ)
Machine Learning Conference for X-Ray and Neutron-Based Experiments
Bürgerhaus Garching, April 8 – 10, 2024

P. Müller-Buschbaum
Lehrerfortbildung Nanotechnologien und Zukunftsmaterialien
46. Edgar-Lüscher-Seminar
Zwiesel, April 12 – 14, 2024

46. Edgar-Lüscher-Seminar am Gymnasium Zwiesel
Thema: **Nanotechnologie und Zukunftsmaterialien**

Freitag, 12. April bis Sonntag, 14. April 2024

Schirmherr: **Prof. Dr. Thomas Hofmann, Präsident der TU München**

Veranstalter: **Der Ministerialbeauftragte für die Gymnasien in Niederbayern, Ltd. OStD Peter Brendel**

Wissenschaftliche Leitung: **Prof. Dr. Peter Müller-Buschbaum und Prof. Dr. Winfried Petry, TU München**

Org. am Gymnasium Zwiesel: **OStD Martin Huber, StR Stephan Loibl und OStR Claus Starke**

Freitag, 12. April 2024

10:00-12:00 *Experimente zu Nanotechnologie und Zukunftsmaterialien für und mit Schülern* –
Dr. Silke Staehler-Schöpf, Max Planck Institut für Quantenooptik MPG
Dr. Andreas Kratzer, TUM School of Education, Leiter TUM Science Lab

14.45-15.15 Begrüßung

15.15-16.30 *Anwendung von DNA Origami,* Elisabeth Erber, (LMU, Faculty of Physics)

16.30-17.15 Diskussion und Kaffeepause

17.15-18.30 *Katalyse mit in-situ Elektronenmikroskopie,* Prof. Marc Willinger, (LS für Elektronenmikroskopie, TUM NAT School)

18.30-18.45 Diskussion

Samstag, 13. April 2024

09.00-10.15 *Werkstoffcharakterisierung auf der Nanoskala,* Dr. Michael Hofmann (Forschungs-Neutronenquelle Heinz Maier Leibnitz, TUM FRM II)

10.15-11.00 Diskussion und Kaffeepause

11.00-12.15 *Topologische Materialien,* Prof: Dr. Christian Pfleiderer (LS für Topologie korrelierter Systeme, TUM NAT School)

12.15-12.30 Diskussion

14.30-15.45 *Neue Solarzellen basierend auf Perowskiten,* Dr. Claudiu Mortan (Institut für Photovoltaik, Universität Stuttgart)

15.45-16.30 Diskussion und Kaffeepause

16.30-17.45 *Quantentechnologien für Sensoren und Aktuatoren,* Prof. Dr. Jonathan Finley (LS für Halbleiter Strukturen und -Quantensysteme, TUM WSI & NAT School)

17.45-18.00 Diskussion

Sonntag, 14. April 2024

09.00-10.15 *Nachhaltige Materialien,* Prof. Dr. Stephan Roth (DESY, Hamburg und Royal Institute of Technology, Sweden)

10.15-11.00 Diskussion und Kaffeepause

11:00-12:15 *Graphen*, Prof. Dr. Paul Seifert (Institute of Physics, Universität der Bundeswehr München)

12.15-13.00 Diskussion
Thema für 47. Edgar-Lüscher-Seminar

P. Müller-Buschbaum, C. M. Papadakis

Summer School of the Chair of Functional Materials and Soft Matter Group

TUM Science and Study Center Raitenhaslach, July 16 – 19, 2024

Summer School of the Chair for Functional Materials and Soft Matter Group
TUM Akademiezentrum Raitenhaslach
July 16 - 19, 2024

	Tuesday, July 16, 2024	**Wednesday, July 17, 2024** *Shuttle bus departing at 8:30 am*	**Thursday, July 18, 2024** *Bus departing at 8:30 am*	**Friday, July 19, 2024** *Shuttle bus departing at 8:30 am*
09:00 - **10:30**	Journey from Garching (Meet at 9:45 am for departure at 10 am)	SAXS/SANS GISAXS	Excursion to Königssee	Master talks AI for text writing
10:30-11:00		Coffee break		Coffee break
11:00 - **12:15**	Social Media	GIWAXS XRR/NR		Presentation Discussion groups
13:00	Lunch	Lunch		Lunch
14:00 - **15:30**	UV-Vis FT-IR	3 discussion groups: SAXS, GISAXS, GIWAXS		Journey to Garching
15:30-16:00	Coffee break	Coffee break		
16:00 - **18:00**	DLS Calibration	Beamtime Good scientific practice		
18:00-20:00	Dinner	Dinner	19:30 - 20:30 Dinner	
20:00 - **21:30**	4 discussion groups: UV-Vis, FTIR, DLS, Calibration	3 discussion groups: XRR/NR, Beamtime, Good scientific practice	20:30: AI for data analysis	

P. Müller-Buschbaum, Akademie für Lehrerfortbildung Dillingen
Lehrerfortbildung Astrophysik
Edgar-Lüscher Lectures Dillingen, September 18 – 20, 2024

EDGAR–LÜSCHER–LECTURES DILLINGEN/DONAU 2024
Thema: Astrophysik und Kosmologie
Datum: Mittwoch, 18. September bis Freitag, 20. September 2024
Tagungsort: Akademie für Lehrerfortbildung Dillingen
Veranstalter: Akademie für Lehrerfortbildung Dillingen und TU München
wissenschaftliche Leitung: Prof. Dr. Peter Müller-Buschbaum,
Technische Universität München.

Programm

Mittwoch, 18. 09. 2024
15:00 – 15:30 Begrüßung
OStR Beate Landherr / Prof. Dr. Peter Müller-Buschbaum (TUM, Physik)

15:30 – 17:00 Kosmische Kartographie, Informationsfeldtheorie, & künstliche Intelligenz
PD Dr. Torsten Enßlin (Max-Planck-Institut für Astrophysik, Garching)

18:30 – 20:00 Das James Webb Space Telescope – Neue Rekorde in der Astronomie
Dr. Eva Schinnerer (Max-Planck-Institut für Astronomie, Heidelberg)

Donnerstag, 19. 09. 2024
8:30 – 10:00 Dunkle Materie
PD Dr. Mathias Garny (Physik-Department, Technical University of Munich)

10:00 – 10.30 Kaffeepause

10:30 – 12:00 Galaxiencluster
Dr. Sebastian Bocquet (Department of Physics at Ludwigs-Maximilians University, Munich)

15:30 – 17:00 Asteroiden-Astrophysik: ein aktueller Blick in die Forschung
Dr. Thomas G. Müller (Max-Planck-Institut für extraterrestrische Physik, Garching)

18:30 – 20:00 Gravitationswellen
Dr. Gudrun Wanner (MPI für Gravitationsphysik, Hannover)

Freitag, 20. 09. 2024
8:30 – 10:00 Suche nach extraterrestrischen Planeten und extraterrestrischem Leben
Dr. Ruth Titz-Weider (DLR Berlin)

10:00 – 10.30 Kaffeepause

10:30 – 12:00 Planetenentstehung
Prof. Dr. Til Birnstiel (Department of Physics at Ludwigs-Maximilians University, Munich)

Ab 12:00 Lehrgangsabschluss
Prof. Dr. Peter Müller-Buschbaum / OStR Beate Landherr

TUM, Zhejiang Sci-tech University, China
Sino-German Workshop Exploration of Structure and Morphology in Polymers by Advanced Scattering Techniques (ExpAdvScaTech)
Hangzhou, China, October 13 – 18, 2024

9.3 Service to the community

Prof. Dr. Peter Müller-Buschbaum:

- Since 01/2024 Deputy Editor of the journal „ACS Applied Materials and Interfaces“ of American Chemical Society (ACS)
- Since 11/2023 Supervising Professor ”Electronic Lab” of TUM School of Natural Sciences
- Since 05/2023 Member of TUM Sustainability Board
- Since 10/2021 Head of Network of Renewable Energies (NRG) by the Munich Institute of Integrated Materials, Energy and Process Engineering (MEP) at TUM
- Since 10/2021 Core Member of Integrated Research Institute (IRI), Munich Institute of Integrated Materials, Energy and Process Engineering (MEP) at TUM
- Since 1/2019 Council Member of Excellence Cluster ”ORIGINS”
- Since 3/2015 Member of ”Advanced Light Source (ALS) Review Panel”
- Since 6/2014 Member of Stanford Synchrotron Radiation Lightsource (SSRL) Review Panel
- Since 3/2012 Head of KeyLab ”TUM.Solar” of the Bavarian Research Project ”Solar Technologies Go Hybrid” (SolTech) at TUM
- Since 2011 German representative at the European Polymer Federation (EPF) for Polymer Physics
- Since 02/2010 Spokesman of the Energy Section of TUM Physics Department
- Since 02/2010 Member of TUM.Energy
- Since 2010 German Representative at the European Synchrotron User Organization (ESUO)
- Since 2008 Chairman of ”DESY Photon Science User Committee” at the Synchrotron Radiation Laboratory DESY in Hamburg

Prof. Christine M. Papadakis, PhD:

- Member of Beamtime Allocation Panel C08, ESRF
- Vice women's representative of the Physics Department at TU München

Prof. Dr. Winfried Petry:

- TUM Emeritus of Excellence
- From June to December 2024: Member of the Expert Commission of the Bavarian Government "Kernfuson und neuartige Kerntechnologien"
- Member of the Project Advisory Committee der European Spallation Source (ESS), Lund, Sweden
- Supervising professor and member of the "Kuratoriums der Bayerischen Elite Akademie (BEA)"
- Member of the Scientific Advisory Committee der Naturwissenschaten der Karl Fransen Universität und der Technischen Universität Graz (NAWI Graz)
- Member of the Steering Committee of Institute Laue Langevin (ILL), Grenoble, France

10 Publications, talks, posters, and funding

10.1 Publications

- S. Alam, H. Aldosary, C. E. Petoukhoff, X. Yiang, T. Váry, W. Althobaiti, M. Alqurashi, H. Tang, J. I. Khan, V. Nádaždy, P. Müller-Buschbaum, G. C. Welch, F. Laquai
  Thermally-induced degradation in PM6:Y6-based bulk heterojunction organic solar cells
  Adv. Funct. Mater. **34**, 2308076 (2024)

- S. Alam, C. E. Petoukhoff, J. P. Jurado, H. Aldosary, X. Jiang, T. Váry, H. Al Nasser, A. Dahman, W. Althobaiti, S. P. Gonzalez Lopez, W. Alsufyani, P. Müller-Buschbaum, V. Nádaždy, H. Hoppe, F. Laquai
  Influence of thermal annealing on microstructure, energetic landscape and device performance of P3HT: PCBM-based organic solar cells
  J. Phys. Energy **6**, 025013 (2024)

- J. Allwang, S. Da Vela, A. Chroni, D. Selianitis, A. Papagiannopoulos, C. M. Papadakis
  Aggregation behavior and inner structure of nanoparticles from trypsin and chondroitin sulfate in a wide pH range – implications for the design of biocompatible nanocarriers
  ACS Appl. Nano Mater. **7**, 18318-18328 (2024)

- P. A. Alvarez Herrera, G. P. Meledam, B.-J. Niebuur, Y. Taji, L. Chiappisi, C. Henschel, A. Laschewsky, A. Schulte, C. M. Papadakis
  Effect of pressure on the micellar structure of PMMA-b-PNIPAM diblock copolymers in aqueous solution
  Macromolecules **57**, 10263-10274 (2024)

- F. A. C. Apfelbeck, J. E. Heger, T. Zheng, T. Guan, M. Schwartzkopf, S. V. Roth, P. Müller-Buschbaum
  Influence of the polymer binder composition on the charge transfer resistance, morphology, and crystallinity of $LiFePO_4$ electrodes revealed by electrochemical impedance spectroscopy and grazing incidence small- and wide-angle X-ray scattering
  Small Sci. **4**, 2400154 (2024)

- D. E. Apostolides, G. Michael, C. S. Patrickios, B. Notredame, Y. Zhang, J.-F. Gohy, S. Prévost, M. Gradzielski, F. A. Jung, C. M. Papadakis
  Dynamic covalent amphiphilic polymer conetworks based on end-linked Pluronic F108: preparation, characterization, and evaluation as matrices for gel polymer electrolytes
  ACS Appl. Mater. Interfaces **16**, 23813-23825 (2024)

- Y. Bao, M. Li, H. Jin, X. Wang, J. Zeng, Y. Feng, W. Hui, D. Wang, L. Gu, J. Zhang, Y. Hua, X. Wang, B. Xu, W. Chen, Z. Wu, P. Müller-Buschbaum, L. Song
  Directional charge carrier management enabled by orderly arranged perovskite heterodomain with defined size for self-powered photodetectors
  Adv. Funct. Mater. **34**, 2404697 (2024)

- J.-L. Barrat, C. M. Papadakis, C. Tsitsilianis *et al.*
  Soft matter roadmap
  J. Phys. Mater. **7**, 012501 (2024)

- M. Betker, T. Erichlandwehr, B. Sochor, E. Erbes, A. Kurmanbay, Y. Alon, Y. Li, I. Fernandez-Cuesta, P. Müller-Buschbaum, S. A. Techert, L. D. S öderberg, S. V. Roth
Micrometer-thin nanocellulose foils for 3D organic electronics
Adv. Funct. Mater. **34**, 2403952 (2024)

- K. Buducan, B. Baumeister, T. Chemnitz, B. Stepnik, R. Macian-Juan, W. Petry
A European manufacturing line for monolithic U–Mo bare foil production
Nuclear Engineering and Design **422**, 113137 (2024)

- Y. Bulut, B. Sochor, K. A. Reck, B. Schummer, A. Meinhardt, J. Drewes, S. Liang, T. Guan, A. Jeromin, A. Stierle, T. F. Keller, T. Strunskus, F. Faupel, P. Müller-Buschbaum, S. V. Roth
Investigating gold deposition with HiPIMS and dcMS on polystyrene, poly-4-vinylpyridine and polystyrene sulfonic acid
Langmuir **40**, 22591-22601 (2024)

- M. Chen, N. Hu, W. Wang, L. Lei, H. Fan, P. Müller-Buschbaum, Q. Zhong
Enhanced hydrogen evolution in porous and hybrid g-C_3N_4/Pt-PVDF electrospun membranes via piezoelectricity from water flow energy
Adv. Funct. Mater. **34**, 2402477 (2024)

- Q. Chen, T. Künniger, Q. Song, K. Zhang, A. Chumakov, Y. Bulut, C. Harder, P. Müller-Buschbaum, S. V. Roth, A. Braun
Hygro-dynamic and conductive actuator that restructures and heals by water
Adv. Funct. Mater. **34**, 2402924 (2024)

- S. Chen, C. Harder, I. Ribca, B. Sochor, E. Erbes, Y. Bulut, L. Pluntke, A. Meinhardt, B. Schummer, M. Oberthür, T. F. Keller, L. D. S öderberg, S. A. Techert, A. Stierle, P. Müller-Buschbaum, M. K. G. Johansson, J. Navarro, S. V. Roth
Sprayed water-based lignin colloidal nanoparticle-cellulose nanofibril hybrid films with UV-blocking ability
Nanoscale Adv. **6**, 5031-5041 (2024)

- Y. Chen, H. Qi, K. Wang, Z. Kang, G. Pan, C. R. Everett, P. Müller-Buschbaum, Y. Tong, H. Wang
Multifunctional buried interface modification enables efficient tin perovskite solar cells
Small Methods **8**, 2300029 (2024)

- N. Ding, N. Hu, J. Zhang, H. Xu, L. Meng, X. Cai, P. Müller-Buschbaum, D. Qi, Q. Zhong
Reversible and photochromic peony-shaped hairpin prepared from electrospun hybrid nanofibers for visualized solar UV radiation detector
ACS Appl. Nano Mater. **7**, 8140-8150 (2024)

- H. Duan, S. Li, J. Zhao, H. Yang, H. Tang, D. Qi, Z. Huang, X. Xu, L. Shi, P. Müller-Buschbaum, Q. Zhong
Microstructure evolution of reactive polyurethane films during in situ polyaddition and film-formation processes
Macromol. Rapid Com. **45**, 2400284 (2024)

- C. R. Everett, X. Jiang, M. A. Reus, H. Zhong, M. Bitsch, M. Plank, M. Gallei, M. Opel, M. Schwartzkopf, S. V. Roth, P. Müller-Buschbaum
Printed thin magnetic films via ternary hybrid diblock copolymer films containing magnetic iron oxide and nickel nanoparticles
ACS Appl. Mater. Interfaces **16**, 71060-71069 (2024)

- N. Glück, N. S. Hill, M. Giza, E. Hutter, I. Grill, J. Schlipf, U. Bach, P. Müller-Buschbaum, A. Hartschuh, T. Bein, T. Savenije, P. Docampo
The balancing act between high electronic and low ionic transport influenced by perovskite grain boundaries
J. Mater. Chem. A **12**, 11635-11643 (2024)

- T. Guan, S. Liang, Y. Kang, E. Pensa, D. Li, W. Liang, Z. Liang, Y. Bulut, K. Reck, T. Xiao, R. Guo, J. Drewes, T. Strunskus, M. Schwartzkopf, F. Faupel, S. V. Roth, E. Cortés, L. Jiang, P. Müller-Buschbaum
High-power impulse magnetron sputter deposition of Ag on self-assembled Au nanoparticle arrays at low-temperature dewetting conditions
ACS Appl. Mater. Interfaces **16**, 40286-40296 (2024)

- R. Guo, Q. Xiong, A. Ulatowski, S. Li, Z. Ding, T. Xiao, S. Liang, J. E. Heger, T. Guan, X. Jiang, K. Sun, L. K. Reb, M. A. Reus, A. Chumakov, M. Schwartzkopf, M. Yuan, Y. Hou, S. V. Roth, L. M. Herz, P. Gao, P. Müller-Buschbaum
Trace water in lead iodide affecting perovskite crystal nucleation limits the performance of perovskite solar cells
Adv. Mater. **23**, 2310237 (2024)

- X. Guo, Z. Jia, S. Liu, R. Guo, F. Jiang, Y. Shi, Z. Dong, R. Luo, Y.-D. Wang, Z. Shi, J. Li, J. Chen, L. K. Lee, P. Müller-Buschbaum, D. S. Ginger, D. J. Paterson, Y. Hou
Stabilizing efficient wide-bandgap perovskite in perovskite-organic tandem solar cells
Joule **8**, 2554-2569 (2024)

- C. Harder, M. Betker, A. E. Alexakis, Y. Bulut, B. Sochor, L. D. Söderberg, E. Malmström, P. Müller-Buschbaum, S. V. Roth
Poly(sobrerol methacrylate) colloidal inks sprayed onto cellulose nanofibril thin films for anticounterfeiting applications
ACS Appl. Nano Mater. **7**, 10840-10851 (2024)

- T. Hölderle, M. Monchak, V. Baran, A. Kriele, M. J. Mühlbauer, V. Dyadkin, A. Rabenauer, A. Schökel, H. Ehrenberg, P. Müller-Buschbaum, A. Senyshyn
Thermal structural behavior of electrochemically lithiated graphite (Li_xC_6) anodes in Li-ion batteries
Batteries & Supercaps **7**, e202300499 (2024)

- N. Hu, D. Gao, F. Song, C. Yang, J. Zhang, P. Müller-Buschbaum, Q. Zhong
Effect of embedded g-C_3N_4 nanosheets on hydration and thermal response behavior of cross-linked thermo-responsive copolymer films
Langmuir **40**, 14663-14673 (2024)

- L. Huang, Q. Qiu, M. Yang, H. Li, J. Zhu, W. Zhang, S. Wang, L. Xia, P. Müller-Buschbaum
Achieving the inhibition of aluminum corrosion by dual-salt electrolytes for sodium-ion batteries
ACS Appl. Mater. Interfaces **16**, 46392-46400 (2024)

- T.-Y. Huang, A. P. Le Brun, B. Sochor, C.-M. Wu, Y. Bulut, P. Müller-Buschbaum, S. V. Roth, Y.-L. Yang
Nanometer-thick ITIC bulk heterojunction films as non-fullerene acceptors in organic solar cells
ACS Appl. Nano Mater. **7**, 17588-17595 (2024)

- Y. Huang, W. Zhou, H. Zhong, W. Chen, G. Yu, W. Zhang, S. Wang, Y. Sui, X. Yang, Y. Zhuang, J. Tang, L. Cao, P. Müller-Buschbaum, A. Aierken, P. Han, Z. Tang
  Triethylsilane introduced precursor engineering towards efficient and stable perovskite solar cells
  Mater. Today Adv. **21**, 100449 (2024)

- Q. Ji, W. Chen, X. Chen, X. Wang, Q. Dong, S. Yin, Y. Shen, P. Müller-Buschbaum, Y.-J. Cheng, Y. Xia
  Synergistic effect of dual phases to improve lithium storage properties of Nb_2O_5
  ACS Appl. Mater. Interf. **16**, 7232-7242 (2024)

- X. Jiang, J. Zeng, K. Sun, Z. Li, Z. Xu, G. Pan, R. Guo, S. Liang, Y. Bulut, B. Sochor, M. Schwartzkopf, K. A. Reck, T. Strunskus, F. Faupel, S. V. Roth, B. Xu, P. Müller-Buschbaum
  Sputter-deposited TiO_x thin film as a buried interface modification layer for efficient and stable perovskite solar cells
  Nano Energy **132**, 110360 (2024)

- Z. Kang, Y. Tong, K. Wang, Y. Chen, P. Yan, G. Pan, P. Müller-Buschbaum, L. Zhang, Y. Yang, J. Wu, H. Xie, S. Liu, H. Wang
  Tailoring low-dimensional phases for improved performance of 2D-3D tin perovskite solar cells
  ACS Materials Lett. **6**, 1-9 (2024)

- Z. Kang, K. Wang, L. Zhang, Y. Yang, J. Wu, Y. Tong, P. Yan, Y. Chen, H. Qi, K. Sun, P. Müller-Buschbaum, X. Zhang, J. Shang, H. Wang
  Homogenizing the low-dimensional phases for stable 2D-3D tin perovskite solar cells
  Small **20**, 2402028 (2024)

- C.-H. Ko, P. Wastian, D. Schanzenbach, P. Müller-Buschbaum, A. Laschewsky, C. M. Papadakis
  Dynamic behavior of poly(N-isopropylmethacrylamide) in neat water and in water/methanol mixtures
  Langmuir **40**, 15150-15160 (2024)

- Y. Kong, S. Wang, Y. Li, G. Pan, Y. Bulut, S. Zhang, G. Chai, Z. Wu, H. Qin, W. Fan, Q. Liu, Z. Wei, H. Y. Woo, P. Müller-Buschbaum, S. V. Roth, Q. Zhang, W. Ma
  Donor–acceptor copolymer with a linear backbone induced ordered and robust doping morphology for efficient and stable organic electrochemical devices
  ACS Appl. Mater. Interfaces **16**, 33885-33896 (2024)

- L. P. Kreuzer, F. Yang, Z. Evenson, D. Holland-Moritz, A. Bernasconi, T. Hansen, M. Blankenburg, A. Meyer, W. Petry
  Dynamical and structural properties of undercooled Cu-Ti melts investigated with neutron and X-ray diffraction
  Phys. Rev. B **109**, 174108 (2024)

- D. Lei, W. Shang, L. Cheng, Poonam, W. Kaiser, P. Banerjee, S. Tu, O. Henrotte, J. Zhang, A. Gagliardi, J. Jinschek, E. Cortés, P. Müller-Buschbaum, A. S. Bandarenka, M. Z. Hussain, R. A. Fischer
  Ion-transport kinetics and interface stability augmentation of zinc anodes based on fluorinated covalent organic framework thin films
  Adv. Energy Mater. **14**, 2403030 (2024)

- J. Li, C. Jin, R. Jiang, J. Su, T. Tian, C. Yin, J. Meng, Z. Kou, S. Bai, P. Müller-Buschbaum, F. Huang, L. Mai, Y.-B. Cheng, T. Bu
Homogeneous coverage of the low-dimensional perovskite passivation layer for formamidinium–caesium perovskite solar modules
Nat. Energy **9**, 1540-1550 (2024)

- M. Li, Y. Bao, W. Hui, K. Sun, L. Gu, X. Kang, D. Wang, B. Wang, H. Deng, R. Guo, Z. Li, X. Jiang, P. Müller-Buschbaum, L. Song, W. Huang
In situ surface reconstruction towards planar heterojunction for efficient and stable $FAPbI_3$ quantum dot solar cells
Adv. Mater. **36**, 2309890 (2024)

- Y. Li, N. Li, C. Harder, S. Yin, Y. Bulut, A. Vagias, P. M. Schneider, W. Chen, S. V. Roth, A. S. Bandarenka, P. Müller-Buschbaum
Factors shaping the morphology in sol-gel derived mesoporous zinc titanate films: unveiling the role of precursor competition and concentration
Adv. Mater. Interfaces **11**, 2400215 (2024)

- Y. Li, N. Li, S. Tu, Y. Alon, Z. Li, M. Betker, D. Sun, A. Kurmanbay, W. Chen, S. Liang, S. Shi, S. V. Roth, P. Müller-Buschbaum
Drop-cast hybrid poly(styrene)-b-poly(ethylene oxide) metal salt films: solvent evaporation and crystallinity-dependent evolution of film morphology
Small **20**, 2406279 (2024)

- Z. Li, Y. Li, J. Zhang, R. Guo, K. Sun, X. Jiang, P. Wang, S. Tu, M. Schwartzkopf, Z. Li, C.-Q. Ma, P. Müller-Buschbaum
Suppressed degradation process of green-solvent based organic solar cells through ZnO modification with sulfhydryl derivatives
Adv. Energy Mater. **15**, 2402920 (2024)

- S. Liang, T. Guan, S. Yin, S. Tu, R. Guo, Y. Bulut, K. A. Reck, J. Drewes, W. Chen, T. Strunskus, M. Schwartzkopf, F. Faupel, S. V. Roth, Y.-J. Cheng, P. Müller-Buschbaum
In situ studies revealing the effect of Au surfactant on the formation of ultra-thin Ag layers using high-power impulse magnetron sputter deposition
Nanoscale Horiz. **9**, 2273-2285 (2024)

- Y. Liang, T. Zheng, K. Sun, Z. Xu, T. Guan, F. A. C. Apfelbeck, P. Ding, I. D. Sharp, Y. Cheng, M. Schwartzkopf, S. V. Roth, P. Müller-Buschbaum
Operando study insights into lithiation/delithiation processes in a poly(ethylene oxide) electrolyte of all-solid-state lithium batteries by grazing incidence X-ray scattering
ACS Appl. Mater. Interfaces **16**, 33307-33315 (2024)

- K. Liu, P. Zhang, P. Müller-Buschbaum, Q. Zhong
Enhanced UV protection in silk fibroin based electrospun fabrics realized via orientation induced high efficiency of azobenzene isomerization
Int. J. Biol. Macromol. **268**, 131638 (2024)

- S. Liu, Y. Lu, C. Yu, J. Li, R. Luo, R. Guo, H. Liang, X. Jia, X. Guo, Y.-D. Wang, Q. Zhou, X. Wang, S. Yang, M. Sui, P. Müller-Buschbaum, Y. Hou
Triple-junction solar cells with cyanate in ultrawide bandgap perovskites
Nature **628**, 306-312 (2024)

- I. López-Fernández, D. Valli, C.-Y. Wang, S. Samanta, T. Okamoto, Y.-T. Huang, K. Sun, Y. Liu, V. S. Chirvony, A. Patra, J. Zito, L. De Trizio, D. Gaur, H.-T. Sun, Z. Xia, X. Li, H. Zeng, I. Mora-Ser ó, N. Pradhan, J. P. Mart ínez-Pastor, P. Müller-Buschbaum, V. Biju, T. Debnath, M. Saliba, E. Debroye, R. L. Z. Hoye, I. Infante, L. Manna, L. Polavarapu
Lead-free halide perovskite materials and optoelectronic devices: progress and prospective
Adv. Funct. Mater. **34**, 2307896 (2024)

- R. Ma, X. Jiang, T. A. Dela Peña, W. Gao, J. Wu, M. Li, S. V. Roth, P. Müller-Buschbaum, G. Li
Insulator polymer matrix construction on all-small-molecule photoactive blend towards extrapolated 15000 hour T80 stable devices
Adv. Mater. **36**, 2405005 (2024)

- B.-J. Niebuur, V. Pipich, M.-S. Appavou, D. Mullapudi, A. Nieth, E. Rende, A. Schulte, C. M. Papadakis
PNIPAM mesoglobules in dependence on pressure
Langmuir **40**, 22314-22323 (2024)

- R. A. Pacalaj, Y. Dong, I. Ramirez, R. C. I. MacKenzie, S. M. Hosseini, E. Bittrich, J. E. Heger, P. Kaienburg, S. Mukherjee, J. Wu, M. Riede, H. Ade, P. Müller-Buschbaum, M. Pfeiffer, J. R. Durrant
From generation to collection – impact of deposition temperature on charge carrier dynamics of high-performance vacuum-processed organic solar cells
Energy Environ. Sci. **17**, 9215-9232 (2024)

- C. M. Papadakis, B.-J. Niebuur, A. Schulte
Thermoresponsive polymers under pressure with a focus on poly(N-isopropylacrylamide) (PNIPAM)
Langmuir **40**, 1-20 (2024)

- C. Peng, S. Liang, Y. Yu, L. Cao, C. Yang, X. Liu, K. Guo, P. Müller-Buschbaum, Y.-J. Cheng, C. Wang
A chronicle of titanium niobium oxide materials for high-performance lithium-ion batteries: from laboratory to industry
Carbon Neutralization **3**, 1036-1091 (2024)

- W. Petry
Kernenergie - eine Option für die Zukunft!
Berichte des Internationalen Begegnungszentrums der Wissenschaft, Jahresbericht des Internationalen Begegnungszentrums (IBZ) München e. V. p. 22 – 27(2024)

- D. Petz, V. Baran, J. Park, A. Sch ökel, A. Kriele, J. Rebelo-Kornmeier, C. Paulmann, M. Koch, T. Nilges, P. Müller-Buschbaum, A. Senyshyn
Heterogeneity of lithium distribution in the graphite anode of 21700-type cylindrical Li-ion cells during degradation
Batteries **10**, 68 (2024)

- V. Pipich, T. Starc, R. Kasher W. Petry Y. Oren, D. Schwahn
The porous system of a reverse osmosis membrane – operando studies with small-angle neutron scattering
Chem. Eng. J. **495**, 153304 (2024)

- I. Pivarníková, M. Flügel, N. Paul, A. Cannavo, G. Ceccio, J. Vacíkm, P. Müller-Buschbaum, M. Wohlfahrt-Mehrens, R. Gilles, T. Waldmann
Observation of preferential sputtering of Si/graphite anodes from Li-ion cells by GD-OES and its validation by neutron depth profiling
J. Power Sources **594**, 233972 (2024)

- R. Qi, M. Yang, T. Zheng, X. Liu, Y. Xia, Y.-J. Cheng, P. Müller-Buschbaum
Multifunctional umbrella: In situ interface film forming on the high-voltage $LiCoO_2$ cathode by a tiny amount of nanoporous polymer additives for high-energy-density Li-ion batteries
Small **20**, 2310287 (2024)

- Q. Qiu, T. Zheng, L. Huang, T. Xu, L. Pan, W. Sun, H. Tian, W. Zhang, Q. Yu, Y. Liang, Y. Yan, J. Yuan, P. Müller-Buschbaum, L. Xia
A small amount of sodium difluoro(oxalate)borate additive induces anion-derived interphases for sodium-ion batteries
Energy Storage Mater. **73**, 103858 (2024)

- K. A. Reck, Y. Bulut, Z. Xu, S. Liang, T. Strunskus, B. Sochor, H. Gerdes, R. Bandorf, P. Müller-Buschbaum, S. V. Roth, A. Vahl, F. Faupel
Early-stage silver growth during sputter deposition on SiO_2 and polystyrene – comparison of biased DC magnetron sputtering, high-power impulse magnetron sputtering (HiPIMS) and bipolar HiPIMS
Appl. Surf. Sci. **666**, 160392 (2024)

- J. Reitenbach, P. Wang, L. F. Huber, S. A. Wegener, R. Cubitt, D. Schanzenbach, A. Laschewsky, C. M. Papadakis, P. Müller-Buschbaum
Salt-mediated tuning of the cononsolvency response behavior of PNIPMAM thin films
Macromolecules **57**, 10635-10647 (2024)

- M. A. Reus, T. Baier, C. G. Lindenmeir, A. F. Weinzierl, A. Buyan-Arivjikh, S. A. Wegener, D. P. Kosbahn, L. K. Reb, J. Rubeck, M. Schwartzkopf, S. V. Roth, P. Müller-Buschbaum
Modular slot-die coater for in situ grazing-incidence X-ray scattering experiments on thin films
Rev. Sci. Instrum. **95**, 043907 (2024)

- M. A. Reus, A. Krifa, Q. A. Akkerman, A. Biewald, Z. Xu, D. P. Kosbahn, C. L. Weindl, J. Feldmann, A. Hartschuh, P. Müller-Buschbaum
Layer-by-layer printed metal hybrid (Cs:FA)PbI_3 perovskite nanocrystal solar cells
Adv. Opt. Mater. **12**, 2301008 (2024)

- M. A. Reus, L. K. Reb, D. P. Kosbahn, S. V. Roth, P. Müller-Buschbaum
INSIGHT: In situ heuristic tool for the efficient reduction of grazing-incidence X-ray scattering data
J. Appl. Cryst. **57**, 509-528 (2024)

- S. Saifi, X. Xiao, S. Cheng, H. Guo, J. Zhang, P. Müller-Buschbaum, G. Zhou, X. Xu, H.-M. Cheng
An ultraflexible energy harvesting-storage system for wearable applications
Nat. Commun. **15**, 6546 (2024)

- D. Sandner, K. Sun, A. Stadlbauer, M. W. Heindl, Q. Y. Tan, M. Nuber, C. Soci, R. Kienberger, P. Müller-Buschbaum, F. Deschler, H. Iglev
Hole localization in bulk and 2D lead halide perovskites studied by time-resolved infrared spectroscopy
J. Amer. Chem. Soc. **146**, 19852-19862 (2024)

- R. Saymung, R. Potai, C. M. Papadakis, N. Traiphol, R. Traiphol
Acid-responsive polydiacetylene-Na^+ assemblies with unique red-to-blue color transition
Heliyon **10**, e27572 (2024)

- R. Schönecker, P. Bianchini, F. Thomas, W. Petry, C. Reiter
TAILLEFER - A tool for sensitivity analysis and uncertainty propagation studies for steady-state thermal-hydraulic simulations of involute fuel element research reactors
Nuclear Science Engineering (2024)

- A. Shahzad, F. Yang, J. Steven, C. Neiss, A. Panchenko, K. Goetz, C. Vogel, M. Weisser, J. P. Embs, W. Petry, W. Lohstroh, A. G örling, I. Goychuk, T. Unruh
Atomic diffusion in liquid gallium and gallium-nickel alloys probed by quasielastic neutron scattering and molecular dynamic simulations
J. Phys: Condens. Matter **36**, 175403 (2024)

- G. Shen, X. Li, Y. Zou, H. Dong, D. Zhu, Y. Jiang, X. R. Ng, F. Lin, P. Müller-Buschbaum, C. Mu
High-performance and large-area inverted perovskite solar cells based on NiO_x films enabled with a novel microstructure-control technology
Energy Environ. Mater. **7**, e12504 (2024)

- Z. Shi, R. Guo, R. Luo, X. Wang, J. Ma, J. Feng, X. Niu, E. Alvianto, Z. Jia, X. Guo, H. Liang, J. Chen, Z. Li, K. Sun, X. Jiang, Y. Wu, P. Müller-Buschbaum, W. Hu, Y. Hou
"T-shaped" carbazole alkylammonium cation passivation in perovskite solar cells
ACS Energy Lett. **9**, 419-427 (2024)

- B. Sochor, S. Schraad, L. F. Huber, A. Hexemer, T. Laarmann, S. K. Vayalil, P. Müller-Buschbaum, S. V. Roth
Effect of layer thickness on the thermoelectric properties of fully sprayed poly(3-hexylthiophene-2,5-diyl) thin films doped with chloroauric acid
J. Coat. Technol. Res. **21**, 1945-1954 (2024)

- T. Soto-Montero, S. Kralj, R. Azmi, M. A. Reus, J. S. Solomon, D. M. Cunha, W. Soltanpoor, D. S. Utomo, E. Ugur, B. Vishal, M. Ledinsky, P. Müller-Buschbaum, F. Babbe, D. K. Lee, C. M. Sutter-Fella, E. Aydin, S. De Wolf, M. Morales-Masis
Single-source pulsed laser-deposited perovskite solar cells with enhanced performance via bulk and 2D passivation
Joule **8**, 3412-3425 (2024)

- R. Steinbrecher, P. Zhang, C. M. Papadakis, P. Müller-Buschbaum, A. Taubert, A. Laschewsky
Boosting the photo-switchability of double-responsive water-soluble polymers by incorporating arylazopyrazole dyes
Chem. Commun. **60**, 1747-1750 (2024)

- K. Sun, R. Guo, S. Liu, D. Guo, X. Jiang, L. F. Huber, Y. Liang, M. A. Reus, Z. Li, T. Guan, J. Zhou, M. Schwartzkopf, S. D. Stranks, F. Deschler, P. Müller-Buschbaum
Deciphering structure and charge carrier behavior in reduced-dimensional perovskites
Adv. Funct. Mater. **34**, 2411153 (2024)

- T. Tian, S. Tu, A. Xu, S. Yin, A. L. Oechsle, T. Xiao, A. Vagias, J. Eichhorn, J. Suo, Z. Yang, S. Bernstorff, P. Müller-Buschbaum
Unraveling the morphology-function correlation of mesoporous ZnO films upon water exposure
Adv. Funct. Mater. **34**, 2311793 (2024)

- S. Tu, T. Tian, T. Xiao, X. Yao, S. Shen, Y. Wu, Y. Liu, Z. Bing, K. Huang, A. Knoll, S. Yin, S. Liang, J. E. Heger, G. Pan, M. Schwartzkopf, S. V. Roth, P. Müller-Buschbaum
Humidity stable thermoelectric hybrid materials toward a self-powered triple sensing system
Nat. Photonics **18**, 586-594 (2024)

- S. Tu, T. Tian, J. Zhang, S. Liang, G. Pan, X. Ma, L. Liu, R. A. Fischer, P. Müller-Buschbaum
Electrostatic tailoring of freestanding polymeric films for multifunctional thermoelectrics, hydrogels, and actuators
ACS Nano **18**, 34829-34841 (2024)

- A. Vagias, T. Manouras, A. Buchner, P. Gutfreund, L. Porcar, M. Jacques, L. Chiappisi, D. P. Kosbahn, M. Wolf, L. Guasco, R. Dahint, M. Vamvakaki, Peter Müller-Buschbaum:
Grazing-incidence small-angle neutron scattering at high pressure HP-GISANS: a soft matter feasibility study on grafted brush films
J. Appl. Cryst. **57**, 1978-1983 (2024)

- T. Waldmann, C. Hogrefe, M. Flügel, I. Pivarníková, C. Weisenberger, E. Delz, M. Bolsinger, L. Boveleth, N. Paul, M. Kasper, M. Feinauer, R. Sch äfer, K. Bischof, T. Danner, V. Knoblauch, P. Müller-Buschbaum, R. Gilles, A. Latz, M. H ölzle, M. Wohlfahrt-Mehrens
Efficient workflows for detecting Li depositions in lithium-ion batteries
J. Electrochem. Soc. **171**, 070526 (2024)

- X. Wang, J. Li, R. Guo, X. Yin, R. Luo, D. Guo, K. Ji, L. Dai, H. Liang, X. Jia, J. Chen, Z. Jia, Z. Shi, S. Liu, Y. Wang, Q. Zhou, T. Wang, G. Pan, P. Müller-Buschbaum, S. D. Stranks, Y. Hou
Regulating phase homogeneity by self-assembled molecules for enhanced efficiency and stability of inverted perovskite solar cells
Nat. Photonics **18**, 1269-1275 (2024)

- X. Wang, Z. Song, H. Tang, Y. Li, H. Zhong, J. Wu, W. Wang, S. Chen, W. Zhang, F. Fang, J. Hao, D. Wu, P. Müller-Buschbaum, L. Cao, Z. Tang, J. Tang, L. Zhang, K. Wang, W. Chen
Synergic surface modifications of PbS quantum dots by sodium acetate in solid-state ligand exchange towards shortwave infrared photodetectors
ACS Appl. Mater. Interfaces **16**, 44164-44173 (2024)

- W. Wei, C. Zhang, Z. Chen, W. Chen, G. Ran, G. Pan, W. Zhang, P. Müller-Buschbaum, Z. Bo, C. Yang, Z. Luo
Precise methylation yields acceptor with hydrogen-bonding network for high-efficiency and thermally stable polymer solar cells
Angew. Chem. Int. Ed. **63**, e202315625 (2024)

- C. L. Weindl, C. E. Fajman, Z. Xu, T. Zheng, G. E M öhl, N. Chaulagain, K. Shankar, R. Gilles, T. F. F ässler, P. Müller-Buschbaum
Dendritic copper current collectors as capacity boosting material for polymer-templated Si/Ge/C anodes in Li-ion batteries
ACS Appl. Mater. Interf. **16**, 2309-2318 (2024)

- L. Wells, T. A. Pham, G. G. Eshetu, S. Seidlmayer, G. Ceccio, A. Cannavo, J. Vacík, A. Mikitisin, P. Müller-Buschbaum, R. Gilles, E. Figgemeier
Unraveling the role and impact of alumina on the nucleation and reversibility of ß-LiAl in aluminum anode based lithium-ion batteries
ChemElectroChem **11**, e202400322 (2024)

- Q. Wu, Z. Xu, Y. Yu, M. Peng, J. Gao, L. Nie, Y.-J. Cheng, P. Müller-Buschbaum, Y. Xia
Surface coating of NCM523 cathode electrodes by the difunctional block copolymer/lithium salts composites
Langmuir **40**, 14863-14871 (2024)

- T. Xiao, Z. Bing, Y. Wu, W. Chen, Z. Zhou, F. Fang, S. Liang, R. Guo, S. Tu, G. Pan, T. Guan, K. Wang, X. W. Sun, K. Huang, A. Knoll, Z. L. Wang, P. Müller-Buschbaum
A multi-dimensional tactile perception system based on triboelectric sensors: towards intelligent sorting without seeing
Nano Energy **123**, 109389 (2024)

- T. Xiao, S. Tu, T. Tian, W. Chen, W. Cao, S. Liang, R. Guo, L. Liu, Y. Li, T. Guan, H. Liu, K. Wang, M. Schwartzkopf, R. A. Fischer, S. V. Roth, P. Müller-Buschbaum
Autonomous self-healing hybrid energy harvester based on the combination of triboelectric nanogenerator and quantum dot solar cell
Nano Energy **125**, 109555 (2024)

- J. Xu, J. Zhang, L. Zhao, H. Xu, X. Cai, P. Müller-Buschbaum, Q. Zhong
Hybrid waterborne polyurethane/graphitic carbon nitride nanosheet films for self-cleaning and anti-bacterial applications
ACS Appl. Nano Mater. **7**, 28841-28850 (2024)

- T. Xu, T. Zheng, Z. Ru, J. Song, M. Gu, Y. Yue, Y. Xiao, S. Amzil, J. Gao, P. Müller-Buschbaum, K. Wang, H. Zhao, Y.-J. Cheng, Y. Xia
Ether-based electrolyte for high-temperature and high-voltage lithium metal batteries
Adv. Funct. Mater. **34**, 2313319 (2024)

- J. Ye, A. Ren, L. Dai, T. Baikie, R. Guo, D. Pal, S. Gorgon, J. E. Heger, J. Huang, Y. Sun, R. Arul, G. Grimaldi, K. Zhang, J. Shamsi, Y.-T. Huang, H. Wang, J. Wu, A. F. Koenderink, L. Torrente Murciano, M. Schwartzkopf, S. V. Roth, P. Müller-Buschbaum, J. J. Baumberg, S. D. Stranks, N. C. Greenham, L. Polavarapu, W. Zhang, A. Rao, R. L. Z. Hoye
Direct linearly-polarised electroluminescence from perovskite nanoplatelet superlattices
Adv. Funct. Mater. **34**, 2316088 (2024)

- F. Ye, T. Tian, J. Su, R. Jiang, J. Li, C. Jin, J. Tong, S. Bai, F. Huang, P. Müller-Buschbaum, Y. B. Cheng, T. Bu
Tailoring low-dimensional perovskites passivation for efficient two-step-processed $FAPbI_3$ solar cells and modules
Adv. Energy Mater. **14**, 2302775 (2024)

- W. Yimkaew, J. Allwang, C. M. Papadakis, R. Traiphol, N. Traiphol
Colorimetric detection of anionic surfactant using polydiacetylene/zinc (II)/zinc oxide nanocomposites with unique yellow-to-red color transition
J. King Saud Univ. Sci. 103557. **36**, (2024)

- J. Yu, M. Chen, N. Hu, W. Wang, L. Lei, H. Fan, P. Müller-Buschbaum, Q. Zhong
Long-lasting hydrogen evolution and efficient dew harvest realized via electrospinning polyvinylidene fluoride membrane on hybrid hydrogels
Small Sci. **4**, 2400046 (2024)

- Q. Yu, W. Sun, S. Wang, Q. Qiu, W. Zhang, H. Tian, L. Xia, P. Müller-Buschbaum
Smart electrolytes for lithium batteries with reversible thermal protection at high temperatures
Batteries & Supercaps **7**, e202400339 (2024)

- J. Zhang, Z. Li, X. Jiang, L. Xie, G. Pan, A. Buyan-Arivjikh, T. Baier, S. Tu, L. Li, M. Schwartzkopf, S. Koyiloth Vayalil, S.V. Roth, Z. Ge, P. Müller-Buschbaum
Revealing the effect of solvent additive selectivity on morphology and formation kinetics in printed non-fullerene organic solar cells at ambient conditions
Adv. Energy Mater. 2404724 (2024)

- S. Zhang, T. Tian, J. Li, Z. Su, C. Jin, J. Su, W. Li, Y. Yuan, J. Tong, Y. Peng, S. Bai, P. Müller-Buschbaum, F. Huang, Y.-B. Cheng, T. Bu
Surface passivation with tailoring organic potassium salt for efficient $FAPbI_3$ perovskite solar cells and modules
Adv. Funct. Mater. **34**, 2401945 (2024)

- T. Zheng, T. Xu, J. Xiong, W. Xie, M. Wu, Y. Yu, Z. Xu, Y. Liang, C. Liao, X. Dong, Y. Xia, Y.-J. Cheng, Y. Xia, P. Müller-Buschbaum:
Multipoint anionic bridge: asymmetric solvation structure improves the stability of lithium-ion batteries
Adv. Sci. **11**, 2410329 (2024)

- H. Zhu, Q. Wang, W. Chen, K. Sun, H. Zhong, T. Ye, Z. Wang, W. Zhang, P. Müller-Buschbaum, X. W. Sun, D. Wu, K. Wang *Chiral perovskite-QD composites with high circularly polarized luminescence performance achieved through additive-solvent engineering*
J. Chem. Phys. **160**, 234703 (2024)

- Z. Zhu, D. Qi, Z. Z. Yang, Y. Wang, P. Müller-Buschbaum, Q. Zhong
Nanogels containing gold nanoparticles on cotton fabrics for comfort control via localized surface plasmon resonance
ACS Appl. Nano Mater. **7**, 1222-1232 (2024)

- Y. Zou, X. Bai, S. Kahmann, L. Dai, S. Yuan, S. Yin, J. E. Heger, M. Schwartzkopf, S. V. Roth, C.-C. Chen, J. Zhang, S. D. Stranks, R. H. Friend, P. Müller-Buschbaum
A practical approach towards highly reproducible and high-quality perovskite films based on an aging treatment
Adv. Mater. **36**, 2307024 (2024)

- Y. Zou, J. Eichhorn, J. Zhang, F. A. C. Apfelbeck, S. Yin, L. Wolz, C.-C. Chen, I. D. Sharp, P. Müller-Buschbaum
Microstrain and crystal orientation variation within naked triple-cation mixed halide perovskites under heat, UV, and visible light exposure
ACS Energy Lett. **9**, 388-399 (2024)

- Y. Zou, Q. Song, J. Zhou, S. Yin, Y. Li, F. A. C. Apfelbeck, T. Zheng, M.-K. Fung, C. Mu, P. Müller-Buschbaum
  Ammonium sulfate to modulate crystallization for high-performance rigid and flexible perovskite solar cells
  Small **20**, 2401456 (2024)

10.2 Talks

- P. A. Alvarez Herrera, F. Zheng, P. Zhang, J. Reitenbach, H. Amenitsch, P. Müller-Buschbaum, C. Henschel, A. Laschewsky, A. Schulte, C. M. Papadakis
  Effect of pressure on the micellar structure of PMMA-b-PNIPAM in a water/methanol mixture
  DPG Spring Meeting of the Condensed Matter Section 2024, Berlin, 17 – 22 March

- F. A. C. Apfelbeck, G. E. Wittmann, L. Cheng, Y. Liang, Y. Yan, A. Davydok, C. Krywka, P. Müller-Buschbaum
  Operando observation of local lithium-based crystallites inside the polymer electrolyte in lithium metal batteries by nanofocus WAXS
  MLZ Conference 2024: Neutrons for Energy Storage, Fürstenried, 4 – 7 June 2024

- F. A. C. Apfelbeck, G. E. Wittmann, L. Cheng, Y. Liang, Y. Yan, A. Davydok, C. Krywka, P. Müller-Buschbaum
  Operando observation of lithium dendrite growth in polymer-based batteries by nanofocus WAXS
  DPG Spring Meeting of the Condensed Matter Section 2024, Berlin, 17 – 22 March 2024

- F. A. C. Apfelbeck, G. E. Wittmann, L. Cheng, Y. Liang, Y. Yan, A. Davydok, C. Krywka, P. Müller-Buschbaum
  Operando observation of the polymer electrolyte in lithium metal batteries by nanofocus WAXS
  23th SAXS/WAXS/GISAXS satellite workshop of DESY Users' Meeting, Hamburg, 22 – 24 January 2024

- A. Buyan-Arivjikh, T. Baier, J. Zhang, Y. Li, G. Pan, Z. Xu, M. Schwartzkopf, S. V. Roth, S. Vayalil, P. Müller-Buschbaum
  Effect of Perovskite Nanocrystal Nucleation Seeds on Microstructure and Crystallization Pathways in Organic-Inorganic Halide Perovskite Thin Films
  DPG Spring Meeting of the Condensed Matter Section 2024, Berlin, 17 – 22 March 2024

- A. Buyan-Arivjikh, J. Fricker, Y. Li, G. Pan, M. Schwartzkopf, S. V. Roth, S. Vayalil, P. Müller-Buschbaum
  Perovskite Nanocrystal Nucleation Seeds for Improved Microstructure and Faster Crystallization in Organic-Inorganic Halide Perovskite Thin Films
  MLZ User Meeting 2024, Munich, 05 - 06 December 2024

- C. R. Everett, G. Pan, M. A. Reus, D. P. Kosbahn, A. Lak, F. Hartmann, M. Bitsch, M. Gallei, M. Opel, M. Schwartzkopf, P. Müller-Buschbaum
  Tracking the morphology evolution of functional magnetic hybrid diblock copolymer-nanoparticle thin films by in situ GISAXS
  DPG Spring Meeting of the Condensed Matter Section 2024, Berlin, 17 – 22 March 2024

- J. E. Heger, S. V. Roth, P. Müller-Buschbaum
  Training of neural networks for the analysis of grazing-incidence X-ray scattering data
  23th SAXS/WAXS/GISAXS satellite workshop of DESY Users' Meeting, Hamburg, 22 – 24 January 2024

- J. E. Heger, W. Chen, H. Zhong, T. Xiao, C. Harder, F. A. C. Apfelbeck, A. F. Weinzierl, R. Boldt, L. Schraa, E. Euchler, A. K. Sambale, K. Schneider, M. Schwartzkopf, S. V. Roth, P. Müller-Buschbaum
  Strain-induced deformation of quantum dot superlattices in thin films on flexible substrates revealed by in-situ GISAXS
  DPG Spring Meeting of the Condensed Matter Section 2024, Berlin, 17 – 22 March 2024

- J. E. Heger
  Revealing the nanostructure of biopolymer-tailored hybrid films with grazing-incidence scattering
  Sino-German Workshop "ExpAdvScaTech", Hangzhou, China, 13 – 18 October 2024

- J. E. Heger, S. Dan, Y. Zhai, S. V. Roth, P. Müller-Buschbaum
  Structure formation in functional films based on sustainable biohybrid composites revealed by machine-learning-supported grazing-incidence X-ray scattering
  XIX edition of the International Small-Angle Scattering Conference (SAS2024), Taipeh, Taiwan, 3 – 8 November 2024

- J. E. Heger
  Update on machine learning-supported analysis of time-resolved 2D GISAXS data
  VIPR Annual Meeting, Tutzing, 09 – 10 December 2024

- L. F. Huber, P. Müller-Buschbaum
  Tailoring morphologies of protein-templated titania nanostructures
  DPG Spring Meeting of the Condensed Matter Section 2024, Berlin, 17 – 22 March 2024

- D. P. Kosbahn, M. A. Reus, L. K. Reb, A. Krifa, Q. A. Akkerman, A. Biewald, M. Schwartzkopf, A. Chumakov, J. Feldmann, A. Hartschuh, S. V. Roth, P. Müller-Buschbaum
  Structure and morphology investigations on printed perovskite quantum dot films
  DPG Spring Meeting of the Condensed Matter Section 2024, Berlin, 17 – 22 March 2024

- Z. Li, P. Müller-Buschbaum
  In-situ GIWAXS and GISAXS Observation of Suppressed Degradation Process of Green-Solvent based Organic Solar Cells through ZnO Modification with –SH Derivatives
  DPG Spring Meeting of the Condensed Matter Section 2024, Berlin, 17 – 22 March 2024

- Y. Liang, T. Zheng, K. Sun, Z. Xu, T. Guan, F. A. C. Apfelbeck, P. Ding, I. D. Sharp, Y. Cheng, M. Schwartzkopf, S. V. Roth, P. Müller-Buschbaum
  Real-Time Monitoring of Electrochemical Reactions in All-Solid-State Lithium Batteries By Simultaneous Grazing-Incidence Small-Angle/Wide-Angle X-Ray Scattering
  DPG Spring Meeting of the Condensed Matter Section 2024, Berlin, 17 – 22 March 2024

- C. G. Lindenmeir, M. A. Reus, S. A. Wegener, C. R. Everett, J. E. Heger, S. Bernstroff, P. Müller-Buschbaum
  Printing of Organic Solar Cells
  ATUMS: Annual Meeting, Venice, 17 – 19 June 2024

- C. G. Lindenmeir, M. A. Reus, S. A. Wegener, C. R. Everett, J. E. Heger, S. Bernstroff, P. Müller-Buschbaum
  Degradation of Printed Organic Solar Cells at Extreme Temperatures
  2024 MRS Fall Meeting & Exhibit, Boston, 1 – 6 December 2024

- P. Müller-Buschbaum
  Report of the Users Committee (DPS-UC) - report 2023
  DESY Users' Meeting, Hamburg, 22 – 24 January 2024

- P. Müller-Buschbaum
  Multimodal in-situ probe studies during printing of hybrid films
  23th SAXS/WAXS/GISAXS satellite workshop of DESY Users' Meeting, Hamburg, 22 – 24 January 2024

- P. Müller-Buschbaum
  In-situ studies on hybrid thin film formation with advanced grazing incidence methods
  European XFEL Users' Meeting - Workshop" in Schenefeld, 22 – 24 January 2024

- P. Müller-Buschbaum
  A basic introduction to GISANS
  TUM Physics Department in Garching, 1 February 2024

- P. Müller-Buschbaum
  In Situ and Operando Scattering Studies on Perovskite Solar Cells
  ACS Spring Meeting 2024, New Orleans, USA, 17 – 21 March 2024

- P. Müller-Buschbaum
  Machine Learning Conference for X-Ray and Neutron-Based Experiments - welcome
  Machine Learning Conference for X-Ray and Neutron-Based Experiments 2024, Garching, 8 – 10 April 2024

- P. Müller-Buschbaum
  Multimodal in-situ probe studies during printing of active layers for solar cells
  Sino-German Workshop on Printable Photovoltaics in Wuhan, China, 18 April 2024

- P. Müller-Buschbaum
  Structure control during in-situ printing of donor-acceptor blend films
  MRS Spring Meeting 2024, Seattle, USA, 22 – 26 April 2024

- P. Müller-Buschbaum
  In Situ and Operando Scattering Studies on Quantum Dot-based Devices
  ECS Spring Meeting 2024, San Francisco, USA, 26 – 30 May 2024

- P. Müller-Buschbaum
  MLZ Conference Neutrons for Energy Storage - welcome
  MLZ Conference 2024: Neutrons for Energy Storage, Fürstenried, 4 – 7 June 2024

- P. Müller-Buschbaum
  Multimodal in-situ probe studies during printing of perovskite solar cells
  ACS Fall Meeting 2024, Denver, USA, 18 – 22 August 2024

- P. Müller-Buschbaum
  Switching kinetics of thin thermo-responsive polymer films
  Workshop "Self-organizing Polymers", Potsdam, 26 – 27 September 2024

- P. Müller-Buschbaum
  Exploration of Structure and Morphology in Polymers by Advanced Scattering Techniques
  Sino-German Workshop "ExpAdvScaTech", Hangzhou, China, 13 – 18 October 2024

- P. Müller-Buschbaum
  Grazing incidence neutron scattering: challenges and possibilities
  Sino-German Workshop "ExpAdvScaTech", Hangzhou, China, 13 – 18 October 2024

- P. Müller-Buschbaum
  Multimodal in-situ probe studies during printing of perovskite solar cells
  Sino-German Workshop on Printable Photovoltaics Nuremberg, 28 – 30 October 2024

- P. Müller-Buschbaum
  In Situ and Operando Grazing-Incidence Scattering Studies on Organic-Inorganic Functional Thin Films for Solar Cells
  XIX edition of the International Small-Angle Scattering Conference (SAS2024), Taipeh, Taiwan, 3 – 8 November 2024

- P. Müller-Buschbaum
  Advanced in situ scattering studies during thin film deposition via printing, spin coating, spray coating and sputter deposition
  MRS Fall Meeting 2024, Boston USA, 1 – 6 December 2024

- C. M. Papadakis
  Hydrogels from triblock copolymers with pH- and temperature responsive blocks
  TU Bergakademie Freiberg, 24 January 2024

- C.-H. Ko, P. Wastian, D. Schanzenbach, A. Laschewsky, P. Müller-Buschbaum, C. M. Papadakis
  Dynamic behavior of poly(N-isopropylmethacrylamide) in water/methanol mixtures
  DPG Spring Meeting of the Condensed Matter Section 2024, Berlin, 17 – 22 March

- C. M. Papadakis
  Thermoresponsive block copolymers – what can scattering methods tell us?
  Workshop "Self-organizing polymers", Fraunhofer IAP, Potsdam-Golm, 27 September, 2024

- D. Petz, P. Müller-Buschbaum, A. Senyshyn
  Aging driven composition and distribution of electrochemical lithiated graphite anodes in Li-ion batteries
  5. Lüscher-Wassermann Seminar 2024 , Klosters, 03 – 09 February 2024

- D. Petz, A. Senyshyn, V.Kochetov, M. Mühlbauer, P. Müller-Buschbaum
  Diffraction tomography studies of lithium distribution in 18650-type Li-ion cells
  ACS Spring 2024, New Orleans, 23 – 27 March 2024

- D. Petz, P. Müller-Buschbaum, A. Senyshyn
  Aging-related changes in the Lithium Distribution of 18650-type Li-ion batteries
  MLZ Conference 2024: Neutrons for Energy Storage, Fürstenried, 4 – 7 June 2024

- D. Petz, J. Rebelo Kornmeier, P. Müller-Buschbaum, A. Senyshyn
  Operando investigation of the electrolyte uptake of the electrodes in 18650-type Li-ion batteries
  MLZ User Meeting 2024, Munich, 05 – 06 December 2024

- I. Pivarníková, M. Flügel, N. Paul, A. Cannavo, G. Ceccio, J. Vacík, P. Müller-Buschbaum, M. Wohlfahrt-Mehrens, T. Waldmann, R.Gilles
  Investigation of Li depth profiles in Si/graphite anodes from Li-ion battery cells via NDP and GD-OES
  DPG Spring Meeting of the Condensed Matter Section 2024, Berlin, 17 – 22 March 2024

- I. Pivarníková, M. Flügel, N. Paul, A. Cannavo, G. Ceccio, J. Vacík, P. Müller-Buschbaum, M. Wohlfahrt-Mehrens, T. Waldmann, R.Gilles
  Neutron depth profiling and GDOES as tools for characterization of Li plating in Si/graphite anodes from Li ion battery cells
  MLZ Conference 2024: Neutrons for Energy Storage, Fürstenried, 4 – 7 June 2024

- R. Qi, M. Yang, T. Zheng, X. Liu, Y. Xia, Y-J. Cheng, P. Müller-Buschbaum
  In-situ interface film forming on the high-voltage $LiCoO_2$ cathode by a tiny amount of nanoporous polymer additives
  MLZ User Meeting 2024, Munich, 05 – 06 December 2024

- J. Reitenbach, P. Wang, L. F. Huber, S. A. Wegener, R. Cubitt, D. Schanzenbach, A. Laschewsky, C. M. Papadakis, P. Müller-Buschbaum
  Investigation of the Solvent Uptake of Salt-containing PNIPMAM Thin Films
  DPG Spring Meeting of the Condensed Matter Section 2024, Berlin, 17 – 22 March 2024

- J. Reitenbach
  Influence of Salt Addition on the Responsiveness of PNIPMAM Thin Films Towards Solvent Vapor Atmospheres
  Sino-German Workshop "ExpAdvScaTech", Hangzhou, China, 13 – 18 October 2024

- K. Sun, R. Guo, S. Liu, D. Guo, X. Jiang, L. F. Huber, Y. Liang, M. A. Reus, Z. Li, T. Guan, Ju. Zhou, M. Schwartzkopf, S. D. Stranks, F. Deschler, P. Müller-Buschbaum
  Deciphering the Interplay of Structure and Charge Carrier Dynamics in Reduced-Dimensional Perovskites
  245th ECS Meeting, San Francisco, 26 – 30 May 2024

- K. Sun, R. Guo, S. Liu, D. Guo, X. Jiang, L. F. Huber, Y. Liang, M. A. Reus, Z. Li, T. Guan, Ju. Zhou, M. Schwartzkopf, S. D. Stranks, F. Deschler, P. Müller-Buschbaum
  Deciphering the Interplay of Structure and Charge Carrier Dynamics in Reduced-Dimensional Perovskites
  DPG Spring Meeting of the Condensed Matter Section 2024, Berlin, 17 – 22 March 2024

- S. A. Wegener, A. Buyan-Arivjikh, Z. Li, K. Sun, X. Jiang, M. Schwarzkopf, P. Müller-Buschbaum
  Impact of Space Like Temperature Conditions on Metal Halide Perovskite Solar Cells
  MRS Fall Meeting and Exhibit 2024, Bosten, 01 – 06 December 2024

- L. Westphal, V. Kochetov, V. Baran, M. Avdeev, F. Porcher, P. Müller-Buschbaum, A. Senyshyn
  Temperature-resolved Crystal Structure of Ethylene Carbonate
  MLZ User Meeting 2024, Munich, 05 – 06 December 2024

- Z. Xu, G. Pan, T. Zheng, M. Peng, Y. Xia, Y. Cheng, P. Müller-Buschbaum
  Upgrading Carbonate Electrolytes for Lithium Metal Batteries by Synergetic Additives
  DPG Spring Meeting of the Condensed Matter Section 2024, Berlin, 17 – 22 March 2024

- Z. Xu, G. Pan, T. Zheng, M. Peng, Y. Xia, Y. Cheng, P. Müller-Buschbaum
  Upgrading Carbonate Electrolytes for Lithium Metal Batteries by Synergetic Additives
  ATUMS Annual Conference, Venice, 17 – 19 June 2024

- J. Zhang, P. Müller-Buschbaum
  In situ and operando GIWAXS/GISAXS for organic electronics
  Tsinghua University, Shenzhen, 7 – 19 September 2024

- F. Zheng, P. A. Alvarez Herrera, J. Kohlbrecher, A. Constantinou, T. K. Georgiou, C. M. Papadakis
  Injectable hydrogels from thermoresponsive tri- and tetrablock terpolymers: A structural analysis
  The 38th Conference of the European Colloid and Interface Society (ECIS), Copenhagen, 01 – 06 September 2024

- F. Zheng, P. A. Alvarez Herrera, J. Kohlbrecher, A. Constantinou, T. K. Georgiou, C. M. Papadakis
  Injectable hydrogels from thermoresponsive triblock terpolymers: Structural investigation using small-angle neutron scattering
  Sino-German Workshop "ExpAdvScaTech", Hangzhou, China, 13 – 18 October 2024

- F. Zheng, D. Kosbahn, W. Xu, P. Zhang, L. Wang, C. Jeffries, T.K. Georgiou, C. M. Papadakis
  Self-assembly of thermo- and pH-responsive amphiphilic multiblock terpolymers
  MLZ User Meeting 2024, Munich, 05 – 06 December 2024

- H. Zhong, J. G. Ebel, X. Wang, F. Allegretti, I. Piquero-Zulaica, W. Chen, P. Müller-Buschbaum
  Structure Modulation of Interdot Matrix in PbS Colloidal Quantum Dot solids
  DPG Spring Meeting of the Condensed Matter Section 2024, Berlin, 17 – 22 March 2024

10.3 Posters

- F. A. C. Apfelbeck, Y. Liang, Y. Yan, T. Guan, A. Chumakov, P. Müller-Buschbaum
  Monitoring the polymer electrolyte for lithium metal batteries by in situ GIWAXS
  DESY Users' Meeting, Hamburg, 22 – 24 January 2024

- T. Baier, G. Pan, A. Buyan-Arivjikh, J. Zhang, Y. Li, M. Schwartzkopf, S. Koyiloth, P. Müller-Buschbaum
  Fabrication and Characterisation of Formamidinium Lead Iodide Perovskite Nanocrystal Layers
  DPG Spring Meeting of the Condensed Matter Section 2024, Berlin, 17 – 22 March 2024

- T. Baier, G. Pan, A. Buyan-Arivjikh, J. Zhang, P. Müller-Buschbaum
  In Situ GIWAXS of Slot-Die Coated Perovskite Quantum Dot Thin-Films
  Machine Learning Conference for X-Ray and Neutron-Based Experiments 2024, Garching, 8 – 10 April 2024

- T. Baier, H. Zhong, A. Buyan-Arivjikh, J. Zhang, X. Jiang, A. Chumakov, S. Koyiloth, P. Müller-Buschbaum
  Influence of Temperature and Light on the Structure of Lead Halide Perovskite Nanocrystals
  13th SolTech Conference 2024, Nürnberg, 25 – 27 September 2024

- A. Buyan-Arivjikh, J. Fricker, G. Pan, J. Zhang, Z. Xu, T. Baier, Y. Li, M. Schwartzkopf, S. K. Vayalil, S. V. Roth, P. Müller-Buschbaum
  Perovskite Nanocrystal Nucleation Seeds for Improved Microstructure and Faster Crystallization in Organic-Inorganic Halide Perovskite Thin Films
  CeNS-e-conversion workshop at Venice International University 2024, San Servolo, Italy, 23 – 26 September 2024

- M. Chatterjee, H. Zhong, P. Müller-Buschbaum
  Printing n-type PbS quantum dot ink for solar cells
  DPG Spring Meeting of the Condensed Matter Section 2024, Berlin, 17 – 22 March 2024

- S. Chen, Y. Zhai, J. Zhou, J. Zhang, G. Pan, L. Li, C. Everett, S. K. Vayalil, R. A. T. M. van Benthem, J. F. G. A. Jansen, M. Johansson, P. Müller-Buschbaum, S. V. Roth
  Kinetics of nanostructure and interface evolution induced by photopolymerization for sub-micron additive manufacturing
  MLZ User Meeting 2024, Munich, 05 – 06 December 2024

- S. Chen, C. Harder, I. Ribca, Y. Bulut, P. Müller-Buschbaum, M. Johansson, J. Navarro, S. V. Roth
  Water-based lignin colloidal particle and cellulose nanofibrils hybrid films with UV-block ability by spray deposition
  DPG Spring Meeting of the Condensed Matter Section 2024, Berlin, 17 – 22 March 2024

- L. Cheng, T. Zheng, Z. Xu, P. Müller-Buschbaum
  3D Electrodeposition of Porous Cu for long-cycling Lithium- Metal Batteries
  MLZ User Meeting 2024, Munich, 05 – 06 December 2024

- L. Cheng, T. Zheng, Z. Xu, P. Müller-Buschbaum
  3D Electrodeposition of Porous Cu for long-cycling Lithium- Metal Batteries
  DPG Spring Meeting of the Condensed Matter Section 2024, Berlin, 17 – 22 March 2024

- X. Ci, X. Jiang, G. Pan, J. Zhang, Z. Li, K. Sun and P. Müller-Buschbaum
  Facet-dependent photovoltaic efficiency and stability variations in mixed Sn-Pb perovskite solar cells
  DPG Spring Meeting of the Condensed Matter Section 2024, Berlin, 17 – 22 March 2024

- X. Ci, X. Jiang, G. Pan, J. Zhang, Z. Li, K. Sun and P. Müller-Buschbaum
  Facet-dependent photovoltaic efficiency and stability variations in mixed Sn-Pb perovskite solar cells
  SolTech Conference 2024, Nuremberg, 25 – 27 September 2024

- X. Ci, X. Jiang, G. Pan, J. Zhang, Z. Li, K. Sun and P. Müller-Buschbaum
  Facet-dependent photovoltaic efficiency and stability variations in mixed Sn-Pb perovskite solar cells
  MLZ User Meeting 2024, Munich, 05 – 06 December 2024

- J. Darsow, L. V. Spanier, C. Gscheidle, U. Walter, C. Everett, P. Müller-Buschbaum
  Organic solar cells for space application: Investigation of the nanostructure and degradation effects due to mechanical stress
  DPG Spring Meeting of the Condensed Matter Section 2024, Berlin, 17 – 22 March 2024

- M. Garg, Y. Liang, P. Müller-Buschbaum
  Development of biocompatible polymer-electrolyte batteries for use in implantable medical devices
  DPG Spring Meeting of the Condensed Matter Section 2024, Berlin, 17 – 22 March 2024

- T. Garg, Y. Liang, P. Müller-Buschbaum
  Study of PEO-LLZTO composite electrolyte in all-solid state lithium ion battery
  DPG Spring Meeting of the Condensed Matter Section 2024, Berlin, 17 – 22 March 2024

- Y. Guo, C. Harder, G. Pan, S. Tu, Y. Bulut, G. Nemeth, F. Borondics, B. Sochor, S. Vayalil, D. Söderberg, P. Müller-Buschbaum, S. V. Roth
  Biopolymer-Templated Deposition of Hierarchical 3D-Structured Graphene Oxide/Gold Nanoparticle Hybrids for Surface-Enhanced Raman Scattering
  MLZ User Meeting 2024, Munich, 05 – 06 December 2024

- Y. Guo, C. Harder, G. Pan, S. Tu, Y. Bulut, B. Sochor, S. Vayalil, D. Söderberg, P. Müller-Buschbaum, S. V. Roth
  Biopolymer-Templated Deposition of Hierarchical 3D-Structured Graphene Oxide/Gold Nanoparticle Hybrids for Surface-Enhanced Raman Scattering
  DPG Spring Meeting of the Chemical and Polymer Physics Section 2024, Berlin, 17 – 22 March 2024

- J. E. Heger, S. V. Roth, P. Müller-Buschbaum
  Training of neural networks for the analysis of grazing-incidence X-ray scattering data
  DESY Users' Meeting, Hamburg, 22 – 24 January 2024

- J. E. Heger, S. V. Roth, P. Müller-Buschbaum
  Training of neural networks for the analysis of grazing-incidence X-ray scattering data
  Machine Learning Conference for X-Ray and Neutron-Based Experiments 2024, Garching, 8 – 10 April 2024

- J. E. Heger, S. Dan, Y. Zhai, S. V. Roth, P. Müller-Buschbaum
  Machine learning-supported analysis of time-resolved 2D GISAXS data
  VIPR Annual Meeting, Tutzing, 09 – 10 December 2024

- T. Hölderle, P. Müller-Buschbaum, A. Senyshyn
  Thermal and structural stability of lithiated graphite anodes
  Batterieforum Deutschland, Berlin, 21 – 23 January 2024

- T. Hölderle, P. Müller-Buschbaum, A. Senyshyn
  How do lithiated anodes decompose with temperature?
  5. Lüscher-Wassermann Seminar 2024, Klosters, 03 – 09 February 2024

- T. Hölderle, M. Monchak, V. Baran, A. Kriele, M. J. Mühlbauer, V. Dyadkin, A. Schökel, H. Ehrenberg, P. Müller-Buschbaum, A. Senyshyn
  Thermal and structural stability of electrochemical lithiated graphite battery anodes
  ACS Spring 2024, New Orleans, USA, 17 – 21 March 2024

- T. Hölderle, P. Müller-Buschbaum, A. Senyshyn
  Understanding Li/Ni disorder effects in NCA-type battery cathodes
  MLZ Conference 2024: Neutrons for Energy Storage, Munich, 04 – 07 June 2024

- T. Hölderle, P. Müller-Buschbaum, A. Senyshyn
  Structural analysis of cation mixing in NCA-type battery cathodes
  MLZ User Meeting 2024, Munich, 05 – 06 December 2024

- Z. Jin, X. Jiang, P. Müller-Buschbaum
  Tuning the band gap of double perovskite by anion exchange
  DPG Spring Meeting of the Condensed Matter Section 2024, Berlin, 17 – 22 March, 2024

- Z. Jin, X. Jiang, P. Müller-Buschbaum
  Tuning the band gap of double perovskite by anion exchange
  Machine Learning Conference for X-Ray and Neutron-Based Experiments 2024, Garching, 8 – 10 April 2024

- Z. Jin, X. Jiang, P. Müller-Buschbaum
  Gas quenching under ambient condition for efficient and stable perovskite solar cells with surface passivation
  MLZ User Meeting 2024, Munich, 05 – 06 December, 2024

- X. Jiang, Z. Xu, Y. Bulut, S. V. Roth, P. Müller-Buschbaum
  Sputter-Deposited TiO_x Thin Film as a Buried Interface Modification Layer for Efficient and Stable Perovskite Solar Cells
  DPG Spring Meeting of the Condensed Matter Section 2024, Berlin, 17 – 22 March 2024

- X. Jiang, Z. Xu, Y. Bulut, S. V. Roth, P. Müller-Buschbaum
  Sputter-Deposited TiO_x Thin Film as a Buried Interface Modification Layer for Efficient and Stable Perovskite Solar Cells
  The 13th SolTech Conference 2024, Nuremberg, 25 – 27 September 2024

- X. Jiang, Z. Xu, Y. Bulut, S. V. Roth, P. Müller-Buschbaum
  Sputter-Deposited TiO_x Thin Film as a Buried Interface Modification Layer for Efficient and Stable Perovskite Solar Cells
  MLZ User Meeting 2024, Munich, 05 – 06 December 2024

- D. P. Kosbahn, M. P. Le Dû, J. Reitenbach, L. V. Spanier, R. Steinbrecher, A. Laschewsky, R. Cubitt, C. M. Papadakis, P. Müller-Buschbaum
  Influence of Azobenzene Moieties on the Swelling Behavior of Poly(Dimethylacrylamide) Films in Water Vapor under UV-Irradiation
  MLZ User Meeting 2024, Munich, 05 – 06 December 2024

- D. P. Kosbahn, M. P. Le Dû, J. Reitenbach, L. V. Spanier, R. Steinbrecher, A. Laschewsky, R. Cubitt, T. Saerbeck, C. M. Papadakis, P. Müller-Buschbaum
  Photoswitchable Molecules: Impact on Swelling in Thermoresponsive Polymer Films under UV Irradiation
  DPG Spring Meeting of the Condensed Matter Section 2024, Berlin, 17 – 22 March 2024

- Y. Li, N. Li, S. Yin, C. Harder, Y. Bulut, A. Vagias, S. V. Roth, P. Müller-Buschbaum
  Mesoporous hybrid films obtained via sol-gel route for photovoltaic application
  DPG Spring Meeting of the Condensed Matter Section 2024, Berlin, 17 – 22 March 2024

- Y. Li, N. Li, S. Yin, A. Vagias, C. Harder, Y. Bulut, S. V. Roth, P. Müller-Buschbaum
  Probing series morphologies of mesoporous zinc titanate oxide films for machine learning
  Machine Learning Conference for X-Ray and Neutron-Based Experiments 2024, Garching, 8 – 10 April 2024

- Z. Li, S. Vagin, J. Zhang, K. Sun, X. Jiang, R. Guo, M. Schwartzkopf, B. Rieger, P. Müller-Buschbaum
  Operando GIWAXS Observation of Green-solvent Based PBDB-TF-T1: BTP-4F-12 Organic Solar Cells with EH-P as Solid Additive
  TUM Sustainability Day, Garching, 12 June 2024

- Z. Li, S. Vagin, J. Zhang, K. Sun, X. Jiang, R. Guo, M. Schwartzkopf, B. Rieger, P. Müller-Buschbaum
  Suppressed Degradation Process of PBDB-TF-T1:BTP-4F-12 based Organic Solar Cells with Solid Additive Atums Green
  Soltech Conference 2024, Nuremberg, 25 – 27 September 2024

- Z. Li, S. Vagin, J. Zhang, K. Sun, X. Jiang, R. Guo, M. Schwartzkopf, B. Rieger, P. Müller-Buschbaum
  Suppressed Degradation Process of PBDB-TF-T1:BTP-4F-12 based Organic Solar Cells with Solid Additive Atums Green
  MLZ User Meeting 2024, Munich, 05 – 06 December 2024

- Y. Liang, T. Zheng, K. Sun, Z. Xu, T. Guan, F. A. C. Apfelbeck, P. Ding, I. D. Sharp, Y. Cheng, M. Schwartzkopf, S. V. Roth, P. Müller-Buschbaum
  Real-Time Monitoring of Electrochemical Reactions in All-Solid-State Lithium Batteries By Simultaneous Grazing-Incidence Small-Angle/Wide-Angle X-Ray Scattering
  245th Electrochemical Society Meeting 2024, San Francisco, 26 – 30 May 2024

- C. G. Lindenmeir, M. A. Reus, A. Buyan-Arivjikh, S. A. Wegener, C. R. Everett, J. E. Heger, S. Bernstroff, P. Müller-Buschbaum
  Optimization of Slot-Die Printed Organic Solar Cells
  DPG Spring Meeting of the Condensed Matter Section 2024, Berlin, 17 – 22 March 2024

- L. Li, L. Spanier, Z. Jin, L. Huber, G. Pan, P. Müller-Buschbaum
  Tracking degradation of non-fullerene organic solar cells under dynamic environmental conditions
  MLZ User Meeting 2024, Munich, 05 – 06 December 2024

- L. Li, P. Müller-Buschbaum
  Layer-by-layer Deposited Non-fullerene Organic Solar Cells
  DPG Spring Meeting of the Condensed Matter Section 2024, Berlin, 17 – 22 March 2024

- G. Pan, T. Zheng, S. Liang, A. Buyan-Arivjikh, C. Ehgartner, N. Hüsing, M. Schwartzkopf, S.V. Roth,
  P. Müller-Buschbaum
  Time-dependent morphology evolution of templated mesoporous titanium films
  DPG Spring Meeting of the Condensed Matter Section 2024, Berlin, 17 – 22 March 2024

- G. Pan, A. Buyan-Arivjikh, J. Zhang, Z. Xu, M. Schwartzkopf, S.V. Roth,
  P. Müller-Buschbaum
  Kinetics of block copolymer micelles close packing revealed by in situ GISAXS
  Machine Learning Conference for X-Ray and Neutron-Based Experiments 2024, Garching, 8 – 10 April 2024

- G. Pan, A. Buyan-Arivjikh, J. Zhang, Z. Xu, M. Schwartzkopf, S.V. Roth, P. Müller-Buschbaum
  Unveiling the Kinetics of Block Copolymer Micelles Close Packing by In Situ GISAXS
  MLZ User Meeting 2024, 05 – 06 December 2024

- D. Petz, P. Müller-Buschbaum, A. Senyshyn
  Degradation-induced spatial heterogeneity of lithium distribution in the graphite anode of 21700-Li-ion cells
  Batterieforum 2024, Berlin, 24 – 26 January 2024

- D. Petz, P. Müller-Buschbaum, A. Senyshyn
  Lithium Distribution in 18650-type Li-ion batteries over its lifetime
  MLZ Conference 2024: Neutrons for Energy Storage, Fürstenried, 4 – 7 June 2024

- D. Petz, J. Rebelo Kornmeier, P. Müller-Buschbaum, A. Senyshyn
  Heterogeneity of Lithium Distribution in the Graphite Anode of 21700-Type Cylindrical Li-Ion Cells during Degradation
  MLZ User Meeting 2024, Munich, 05 – 06 December 2024

- T. A. Pham, S. Seidlmayer, I. Pivarnikova, S. Friedrich, A. Sommer, C. Didier, V. Peterson, P. Müller-Buschbaum, R. Gilles
  Investigating the ageing of multi-layer 5 Ah pouch cells with $LiNi_{0.8}Co_{0.15}Al_{0.05}O_2$ cathodes and silicon anodes
  MLZ User Meeting 2024, Munich, 05 – 06 December 2024

- T. A. Pham, S. Seidlmayer, I. Pivarnikova, S. Friedrich, A. Sommer, C. Didier, A. Jossen, R. Daub, V. Peterson, P. Müller-Buschbaum, R. Gilles
  Operando neutron diffraction experiments in order to investigate the lithiation and ageing mechanism of industrial scale multi-layer 5 Ah pouch cells
  DPG Spring Meeting of the Condensed Matter Section 2024, Berlin, 17 – 22 March 2024

- I. Pivarníková, S. Seidlmayer, M. Finsterbusch, G. Dück, N. Jalarvo, P. Müller-Buschbaum, R. Gilles
  Sodium diffusion mechanism in Zr-, Sc- and Al/Y- substituted NASICON solid electrolytes studied by X-ray and neutron scattering
  MLZ Conference 2024: Neutrons for Energy Storage, Fürstenried, 4 – 7 June 2024

- R. Qi, M. Yang, T. Zheng, Y-J Cheng, P. Müller-Buschbaum
  Multifunctional Umbrella: In-Situ Interface Film Forming on the High-Voltage $LiCoO_2$ Cathode by a Tiny Amount of Nanoporous Polymer Additives for High-Energy-Density Li-Ion Batteries
  MLZ Conference 2024: Neutrons for Energy Storage, Fürstenried, 4 – 7 June 2024

- R. Qi, M. Yang, T. Zheng, Y-J Cheng, P. Müller-Buschbaum
  Multifunctional Umbrella: In-Situ Interface Film Forming on the High-Voltage $LiCoO_2$ Cathode by a Tiny Amount of Nanoporous Polymer Additives for High-Energy-Density Li-Ion Batteries
  DPG Spring Meeting of the Condensed Matter Section 2024, Berlin, 17 – 22 March 2024

- Faryal Talib, Huaying Zhong,, P. Müller-Buschbaum
  P-type PbS CQD ink for slot-die coating of solar cells
  DPG Spring Meeting of the Condensed Matter Section 2024, Berlin, 17 – 22 March 2024

- S. A. Wegener, A. Buyan-Arivjikh, G. Pan, C. R. Everett, P. Müller-Buschbaum
  Setup for in Operando X-ray Scattering of Thin Film Solar Cells under Dynamic Temperature Variation
  DPG Spring Meeting of the Condensed Matter Section 2024, Berlin, 17 – 22 March 2024

- L. Westphal, V. Baran, M. Avdeev, F. Porcher, P. Müller-Buschbaum, A. Senyshyn
  Temperature dependent crystal structure of Ethylene Carbonate
  DPG Spring Meeting of the Condensed Matter Section 2024, Berlin, 17 – 22 March 2024

- L. Westphal, V. Baran, M. Avdeev, F. Porcher, P. Müller-Buschbaum, A. Senyshyn
  Temperature dependent crystal structure of Ethylene Carbonate
  MLZ Conference 2024: Neutrons for Energy Storage, Fürstenried, 4 – 7 June 2024

- L. Westphal, V. Kochetov, V. Baran, M. Avdeev, F. Porcher, P. Müller-Buschbaum, A. Senyshyn
  Temperature-resolved Crystal Structure of Ethylene Carbonate
  MLZ User Meeting 2024, Munich, 05 – 06 December 2024

- S. Xiong, C. Harder, B. Sochor, P. Müller-Buschbaum, S. V. Roth
  Evolution of morphology and optical properties of thin films probed in situ during spraying
  DESY Users' Meeting, Hamburg, 22 – 24 January 2024

- S. Xiong, B. Sochor, C. Harder, P. Müller-Buschbaum, S. V. Roth
  In-situ tracking the evolution of morphology and optical properties of thin films during spraying and annealing for organic solar cells
  DPG Spring Meeting of the Condensed Matter Section 2024, Berlin, 17 – 22 March 2024

- S. Xiong, P. Müller-Buschbaum, S. V. Roth
  Machine Learning (ML)-Assisted Fabrication and Scattering data for Solar Cells
  Machine Learning Conference for X-Ray and Neutron-Based Experiments 2024, Garching, 8 – 10 April 2024

- Z. Xu, G. Pan, X. Jiang, S. Liang, Y. Bulut, B. Sochor, K. Reck, T. Strunskus, F. Faupel, Y. Xia, Y. Cheng, S. V. Roth, P. Müller-Buschbaum
  A solid-state electrolyte interface layer-amphiphilic polymer/metal composite nanoarray for lithium metal battery
  Machine Learning Conference for X-Ray and Neutron-Based Experiments 2024, Garching, 8 – 10 April 2024

- Z. Xu, P. Müller-Buschbaum
  Constructing ultra-stable (solid electrolyte interphase) SEI and CEI (cathode electrolyte interphase) layers for high energy density lithium metal batteries
  MLZ Conference 2024: Neutrons for Energy Storage, Fürstenried, 4 – 7 June 2024

- W. Xu, L. Fietzke, R. A. Gumerov, F. Zheng, P. Zhang, D. Soloviov, I. I. Potemkin, R. Jordan, C. M. Papadakis
  Conformation of Star-like molecular brushes with amphiphilic diblock copolymer side arms
  DPG Spring Meeting of the Condensed Matter Section 2024, Berlin, 17 – 22 March 2024

- W. Xu, S.-F. Saravanou, F. Kounelaki, C. Tsitsilianis, C. M. Papadakis
  Crosslinking mechanisms of alginate-based graft copolymer with thermoresponsive side arms
  The 5th International Conference on Bio-based Polymers and Composites 2024, Budapest, 1 – 5 September 2024

- W. Xu, S.-F. Saravanou, F. Kounelaki, C. Tsitsilianis, C. M. Papadakis
  Crosslinking mechanisms of alginate-based graft copolymer with thermoresponsive side arms
  MLZ User Meeting 2024, Munich, 5 – 6 December 2024

- Y. Yan, Y. Liang, F. A. C. Apfelbeck, G. Pan, P. Müller-Buschbaum
  Operando study on structure-activity relationship between electrolyte components and electrochemical performance for all-solid-state lithium-ion batteries
  MLZ Conference 2024: Neutrons for Energy Storage, Fürstenried, 4 – 7 June 2024

- Y. Yan, Y. Liang, F. A. C. Apfelbeck, G. Pan, P. Müller-Buschbaum
  Operando study on structure-activity relationship between electrolyte components and electrochemical performance for all-solid-state lithium-ion batteries
  DPG Spring Meeting of the Condensed Matter Section 2024, Berlin, 17 – 22 March 2024

- M. Yang, Y. Xia, Y. Cheng, P. Müller-Buschbaum
  Poly (acrylic acid) Locally Enriched in Slurry Enhances Electrochemical Performance of the SiOx Lithium-Ion Battery Anode
  MLZ User Meeting 2024, Munich, 05 – 06 December 2024

- J. Zhang, P. Müller-Buschbaum
  Revealing the effect of solvent additive selectivity on formation kinetics in printed active layers for organic solar cells
  MLZ User Meeting 2024, Munich, 05 – 06 December 2024

- J. Zhang, P. Müller-Buschbaum
  Revealing the effect of solvent additive selectivity on formation kinetics in printed active layers for organic solar cells
  Joint CeNS/e-conversion Workshop, Venice, 22 – 26 September 2024

- J. Zhang, P. Müller-Buschbaum
  Revealing the effect of solvent additive selectivity on formation kinetics in printed active layers for organic solar cells
  Machine Learning Conference for X-Ray and Neutron-Based Experiments 2024, Garching, 8 – 10 April 2024

- J. Zhang, P. Müller-Buschbaum
  Revealing the effect of solvent additive selectivity on formation kinetics in printed active layers for organic solar cells
  DPG Spring Meeting of the Condensed Matter Section 2024, Berlin, 17 – 22 March 2024

- P. Zhang, R. Steinbrecher, A. Laschewsky, D. Soloviov, P. Müller-Buschbaum, C. M. Papadakis
  Phase behavior of thermo- and photoresponsive diblock copolymers for non-invasive schizophrenic switching
  DPG Spring Meeting of the Condensed Matter Section 2024, Berlin, 17 – 22 March 2024

- Z. Zhang, W. Zhao, T. Brezesinski
  Insight into the Cyclability of LiF-Coated $LiNi_{0.9}Co_{0.05}Mn_{0.05}O_2$ Cathodes in Sulfide-Based All-Solid-State Batteries
  MLZ User Meeting 2024, Munich, 05 – 06 December 2024

- F. Zheng, P. A. Alvarez Herrera, J. Kohlbrecher, A. Constantinou, T. K. Georgiou, C. M. Papadakis
  A structural analysis: Injectable hydrogels from thermoresponsive tri- and tetrablock terpolymers
  DESY Users Meeting 2024, Hamburg, 20 – 24 January 2024

- F. Zheng, P. A. Alvarez Herrera, J. Kohlbrecher, A. Constantinou, T. K. Georgiou, C. M. Papadakis
  Injectable hydrogels from thermoresponsive tri- and tetra- block terpolymers investigated using scattering methods
  DPG Spring Meeting of the Condensed Matter Section 2024, Berlin, 17 – 22 March 2024

- T. Zheng, Y. Cheng, P. Müller-Buschbaum
  High-concentration Lithium-ion Electrolyte Overcomes the Challenges of High-temperature Lithium Batteries
  DPG Spring Meeting of the Condensed Matter Section 2024, Berlin, 17 – 22 March 2024

- H. Zhong, W. Chen, M. A. Scheel, L. Spanier, C. R. Everett, X. Jiang, S. Yin, M. S. Hörtel, J. Zhang, B. B. O. Seibertz, M. Schwartzkopf, S. V. Roth, P. Müller-Buschbaum
  In-situ study of IZO growth for the application of PbS Quantum Dot Solar Cells
  Machine Learning Conference for X-Ray and Neutron-Based Experiments 2024, Garching, 8 – 10 April 2024

10.4 Invited Talks at the Institute of Functional Materials and Soft Matter Physics Group

- Francesco Falsina, Fraunhofer Institute for Applied Polymer Research IAP
  Acetate based electrolytes: modelling and applications
  17 January 2024

- Ziyan Zhang, Karlsruhe Institute of Technology (KIT)
  Insight into the Cyclability of LiF-Coated $LiNi_{0.9}Co_{0.05}Mn_{0.05}O_2$ Cathodes in Sulfide-Based All-Solid-State Batteries
  4 September 2024

- Prof. Lakshminarayana Polavarapu, Universidade de Vigo, Spain
  Colloidal Lead Halide Perovskite Nanocrystals: Surface Defects vs. Emission Properties
  1 October 2024

10.5 Funding

Deutsche Forschungsgemeinschaft:

- *NSF-DFG MISSION: In-situ- und Operando-Untersuchungen von weichen Materialien an vergrabenen Grenzflächen*
  Grant Number: MU 1487/44-1
  Project Leader: Prof. Dr. Peter Müller-Buschbaum

- *Oberflächenmodifikation von Lithium-Batterie-Anoden mit multifunktionalen Block-Copolymeren*
  Grant Number: MU 1487/38-1
  Project Leader: Prof. Dr. Peter Müller-Buschbaum

- *In-Situ Untersuchungen von Keimbildungs- und Wachstumsprozessen*
  Grant Number: MU 1487/39-1
  Project Leader: Prof. Dr. Peter Müller-Buschbaum

- Teilprojekt *Inorganic-organic hybrid photovoltaic solar cells using novel hybrid materials* im GRK 2022: University of Alberta / Technische Universität München Internationale Graduiertenschule für Funktionelle Hybridmaterialien (ATUMS) der DFG IRTG-2022
  Project Leader: Prof. Dr. Peter Müller-Buschbaum

- *Amphiphile Selbstorganisation komplett nicht-invasiv orthogonal schaltbarer Blockcopolymere*
  Grant Number: MU 1487/42-1, Project Leader: Prof. Dr. Peter Müller-Buschbaum
  Grant Number: PA 771/31-1, Project Leader: Prof. Christine M. Papadakis, PhD

- *Einstellbare Morphologien in dünnen Filmen aus geladenen Multiblockpolymeren*
  Grant Number: PA 771/30-1
  Project Leader: Prof. Christine M. Papadakis, PhD

- *Molekulare Bürsten mit amphiphilen thermoresponsiven Seitenketten - von der Synthese über Lösungen zu selbtassemblierten Gelen*
  Grant Number: PA 771/27-1, Project Leader: Prof. Christine M. Papadakis, PhD

Bundesministerium für Bildung und Forschung:

- *VIPR: Vielseitiges Software Framework zur Lösung inverser Probleme Teilprojekt: 5*
  Project Leader: Prof. Dr. Peter Müller-Buschbaum

Bundesministerium für Wirtschaft und Klimaschutz/ DLR:

- *Erprobung und Untersuchung neuartiger Solarzelltechnologien im Weltraum*
  Project Leader: Prof. Dr. Peter Müller-Buschbaum

Bayerisches Staatsministerium für Wissenschaft und Kunst:

- Im Rahmen des Munich Institute of Integrated Materials, Energy and Process Engineering (MEP):
  Solar Technologies Go Hybrid (SolTech) - Forschungsnetzwerk TUM.solar
  Project Leader: Prof. Dr. Peter Müller-Buschbaum

- Im Rahmen des Munich Institute of Integrated Materials, Energy and Process Engineering (MEP)/ Netzwerk Regenerative Enegien:
  Aufbau eines interdisziplinären Netzwerks aus Lehrstühlen der Technischen Universität München und anderen Forschungseinrichtungen zur Förderung der Forschungsaktivitäten im Bereich der regenerativen Energien
  Project Leader: Prof. Dr. Peter Müller-Buschbaum

Others:

- Im Rahmen des Exzellenzclusters e-conversion:

  e-conversion
  Principal Investigator: Prof. Dr. Peter Müller-Buschbaum

  Impact of morphology on the polaron dynamics in polymer: nonfullerene blends for photovoltaic applications
  Principal Investigators: Prof. Dr. Peter Müller-Buschbaum, Prof. Dr. Reinhard Kienberger

  Defect and energy level tuning of printed hybrid perovskite films for photovoltaic applications
  Principal Investigators: Prof. Dr. Peter Müller-Buschbaum, Dr. Johanna Eichhorn

11 The Chair

11.1 Staff

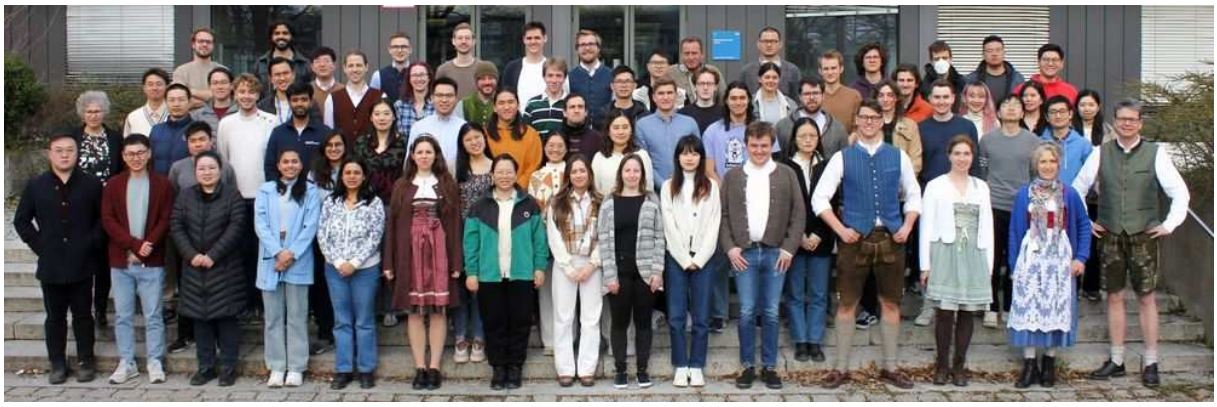

Chair:

Prof. Dr. Peter Müller-Buschbaum

Professor:

Prof. Christine M. Papadakis, PhD

Professor Emeritus:

Prof. Dr. Winfried Petry

Visiting Professor:

Prof. Lan Xia, PhD

Postdocs:

Dr. Julian Eliah Heger

Fellows:

Dr. Michael Leitner
Dr. Wiebke Lohstroh
Dr. Jürgen Neuhaus
Dr. Neelima Paul
Dr. Apostolos Vagias

PhD Students:

Pablo Andres Alvarez Herrera
Fabian Alexander Christian Apfelbeck
Thomas Baier
Daniel Bonete-Wiese
Yusuf Bulut
Altantulga Buyan-Arivjikh
Shouzheng Chen
Lyuyang Cheng
Christopher Reck Everett
Francesco Falsina
Tianfu Guan
Yingjian Guo
Constantin Harder
Guangjiu Pan
Tobias Hölderle
Linus Huber
Xiongzhuo Jiang
Zhaonan Jin
David Kosbahn
Morgan Le Dû
Lixing Li
Yanan Li
Zerui Li
Suzhe Liang
Yuxin Liang
Christoph Gernot Lindenmeir
Anna Oberbauer
Anna Lena Oechsle
Wenqi Xu
Dominik Petz
Thien An Pham
Ivana Pivarnikova
Ruoxuan Qi
Julija Reitenbach
Manuel Andree Reus
Ronja Schoenecker
Simon Schraad
Ali Semerci
Lukas Viktor Spanier
Kun Sun
Ting Tian
Suo Tu
Peixi Wang
Simon Wegener
Christian Ludwig Weindl
Lea Westphal
Tianxiao Xiao
Shuxian Xiong
Zhuijun Xu
Yingying Yan
Ming Yang
Jinsheng Zhang
Peiran Zhang
Ziyan Zhang
Feifei Zheng
Tianle Zheng
Huaying Zhong

Master Students:

Tarek Azzouni
Tim Bohnen
Mrinalini Chatterjee
Liansong Chu
Jan Darsow
Eric Fuchs
Kin Long Fong
Friederike Ganster
Mayank Garg
Tannu Garg
Kyriaki Nektaria Gavriilidou
Yujia Gu
Wenzhe Guo
Lukas Kühnemann
Yifeng Liu
Petar Lovric
Lorenzo Nastasi
Paraskevi Papadaki
Antariksh Parichha
Antonio Prior Fernández Amat
Ni Lar Win Pyae
Martin Seiter
Xinwei Tian
Hagen Tockhorn
Faryal Talib
Manuel Trigueros Galdón
Anthony Myron Vizcaino Rojas
Daniel Wenczel
Ruodong Yang
Qihan Zeng
Ivonne Andrea Zitzmann

Bachelor Students:

Julian Bischof
Ilie S. Cernev
Samuel Daxwanger
Jascha Fricker
Natalie Gedrich
Theresa Gillitzer
Alexander Hinke
Tim Höppner
Florentin Hundsrucker
Aleksandar Iliev
Felix Kerscher
Nils Künne
Dominik Krizanac
Isabela López González
Adrian Margieh
Xaver Meyer
Alexander Morlang
Lorenz Pech
Magdalena Pfaller
Niklas Reinecke
Victor Reisenauer
Nikolaus Sefalidis
Antonio Torres
Samuel Weingartner
Laurin Wieczorek
Stefan Wiedemann
Dominik Wiedenmann
Tianrui Xu
Leart Zuka

Students Assistants:

Jascha Fricker
Leire Arrue Medina

Technical/Administrative Staff:

Reinhold Funer
Andreas Huber
Josef Kaplonski
Sanja Ulrich
Marion Waletzki

11.2 Guests

- Prof Xiaomin Xu, Tsinghua University, Shenzhen, China
  16 January 2024
- Prof. Dr. André Laschewsky, Universität Potsdam
  26 June 2024
- Prof. Dr. Ezzeldin Sobhi Metwalli Ali, German University in Cairo - GUC, Egypt
  22 – 31 July 2024
- Prof. Dr. Quan Niu, South China University of Technology, Guangzhou, China
  21 August – 6 September 2024
- John Garcia, M.Sc., University of Alberta, Canada
  28 August – 31 October 2024
- Dr. Lakshminarayana Polavarapu, Uniersity of Vigo, Spain
  1 September – 30 November 2024
- Dr. Deepika Gaur, University of Vigo, Spain
  16 September – 16 December 2024

11.3 Graduations

- **Accomplished PhD Theses**

  Tianfu Guan
  Unraveling Hybrid Plasmonic Nanostructures Using Advanced Scattering Technique

  Julian Eliah Heger
  Formation and deformation of functional (Bio)hybrid films revealed by advanced scattering methods

  Yanan Li
  Mesoporous structures of hybrid films based on PS-b-PEO template with TTIP and ZAD

  Suzhe Liang
  Formation Fundamentals and Applications of Ultra-Thin Metal Layers

  Anna Lena Oechsle
  Advancement of PEDOT:PSS as thermoelectric material and the investigation of environmental influences on its performance

  Ting Tian
  Diblock copolymer-directed coassembly toward morphology-tunable mesoporous ZnO films

  Suo Tu
  Thermoelectric properties and applications of PEDOT:PSS-based conducting polymers

  Peixi Wang
  Volume phase transition behaviors of thermoresponsive hydrogels

  Christian Ludwig Weindl
  Diblock-copolymer templated Si/Ge/C thin films as anodes in Li-ion batteries

  Tianxiao Xiao
  Triboelectric nanogenerators for hybrid energy harvesters and self-powered sensing systems

- **Accomplished Master Theses**

  Tarek Azzouni
  Organic solar cells for space application

  Mrinalini Chatterjee
  The Study of N-Type PbS Colloidal Quantum Dots towards Printed Quantum Dot Solar Cells

  Jan Darsow
  Organic solar cells for space application: impact of mechanical stress and methods for enhanced perfomance

  Kin Long Fong
  In situ GIWAXS measurements on mixed halide quasi-2D perovskite films under thermal cycling

  Eric Fuchs
  Experimental Study on Interdiffusion and the Kirkendall Effect in the UMo/Al Fuel System prepared by Physical Vapor Deposition

  Mayank Garg
  Development of PEO/PVP/LiTFSI polymer electrolyte batteries for medical implants

  Tannu Garg
  Study of PEO-LLZTO Composite Electrolyte in All-Solid-State Lithium-Ion Batteries

  Kyriaki Nektaria Gavriilidou
  Synthesis and self-assembly of gold nanoparticles for optoelectronic devices

Juliane Heim
Encapsulation and shelf-life study of NIR PbS quantumn dot

Lukas Kühnemann
Development of a multi-purpose in-core irradiation device for the McMaster Nuclear Reactor

Petar Lovric
Improved surface passivation of $AgBiS_2$ quantum dots for photovoltaic application

Lorenzo Nastasi
Pushing Validation of Thermal-Hydraulic Models to Support the Conversion of FRM II

Antariksh Parichha
Optimization of electrode structures for oxide Li-Metal solid-state batteries

Antonio Prior Fernández Amat
Calculation of KERMA Coefficients for JEFF 3.3 Library with NJOY and Sensitivity Analysis using Collision History for the FRM II

Ni Lar Win Pyae
Investigating the additive impact on slot-die coated quasi-2D perovskite thin films for potential photovoltaic applications

Martin Seiter
TEM Characterization of (Cr+N) co-doped TiO2 films for photovoltaic applications

Faryal Talib
Synthesis and optimization of P-type PbS CQDs ink for optoelectronic devices: A study of spin and slot-die coating techniques

Hagen Tockhorn
Global impacts of climate change on heating and cooling energy demand of buildings

Manuel Trigueros Galdón
Characterization of neutron response of ionization chambers

Daniel Wenczel
Single-ion conducting polymers in carbonate-based electrolytes for Lithium-metal batteries

- **Accomplished Bachelor Theses**

Bendedikts Beck
Analysis of hydrated and dehydrated mixtures of glycerol-proline regarding density, viscosity for potential further use as deep eutectic solvents in cryopreservation

Julian Bischof
Protein-based biohybrid composites for aqueous zinc-ion batteries

Rami Boudache
Humidity-controlled phase behavior of phospholipids via grazing incident small angle X-ray scattering (GISAXS)

Jascha Fricker
Optische Verfahren zur In-Situ Analyse von Perowskitschichten

Alexander Hinke
Composite electrolyte with succinonitrile plasticizer forhigh-voltage lithium metal battteries

Aleksandar Iliev
Leaf cuticular structure of Crassula species and water transport

Felix Kerscher
Alginate-based dual-crosslinking thermoresponsive copolymers: A light scattering study

Parid Koroveshi
The effect of gas phase adsorption of ethanol into lamellar fluid phase lipid bilayers of DOPC

Nils Künne
Thermal stability comparison of three different organic solar cell types

Yi Lyu
Morphological investigation of self-assembled gold nanoparticles in PbS quantum dots

Adrian Margieh
Mechanosynthetische Lithiierung von Graphit durch Kugelmahlen

Xaver Meyer
Replication of solar irradiation for the extension of the emulated borehole heat exchanger with artificially-generated environmental influences

Alexander Morlang
Environmentally friendly double perovskite solar cells

Magdalena Pfaller
Perovskite solar cells for space applications

Niklas Reineke
LiF reinforced composite electrolyte for high-voltage lithium metal batteries

Victor Reisenauer
Impact of light and heat-induced degradation on photoluminescence in quasi-2D mixed Halide perovskites: A comparison of Ruddlesden-Popper and Dion-Jacobson type perovskites

Nikolaus Sefalidis
Co-solvent effects on the photovoltaic performance of printed organic solar cells

Antonio Torres Saldarriaga
Environmentally friendly perovskite materials for solar cells

Dominik Wiedenmann
Agar-based electrolytes for aqueous zinc-ion batteries

Tianrui Xu
Dynamic behaviour of azo-dye modified thermoresponsive polymers

Riccardo Zanaboni
Impact of sugars on polysaccharide conformation and viscoelasticity